BOSTON UNIVERSITY

COLLEGE OF ENGINEERING

Dissertation

VIBRATIONS OF ELASTIC STRUCTURES WITH MULTIPLE ARRAYS OF ATTACHMENTS: THEORY AND APPLICATIONS

by

DIMITAR GUEORGUIEV

M.S., Technical University - Sofia, 1994

Submitted in partial fulfillment of the

requirements for the degree of

Doctor of Philosophy

2001

UMI Number: 3002595

UMI

UMI Microform 3002595

Bell & Howell Information and Learning Company
300 North Zeeb Road
P.O. Box 1346
Ann Arbor, MI 48106-1346

Approved by

First Reader J. Gregory McDaniel

J. Gregory McDaniel, Ph.D.
Assistant Professor of Aerospace and Mechanical Engineering

Second Reader

Pierre DuPont, Ph.D.
Associate Professor of Aerospace and Mechanical Engineering

Third Reader

Paul Barbone, Ph.D.
Associate Professor of Aerospace and Mechanical Engineering

Fourth Reader

Harley Johnson, Ph.D.
Assistant Professor of Aerospace and Mechanical Engineering

Committee Chair Raymond J. Nagem

Raymond Nagem, Ph.D.
Associate Professor of Aerospace and Mechanical Engineering

I would like to thank Professor James G. McDaniel and Professor Pierre DuPont for guiding me to the area of structural acoustics and vibrations. The former was the person who opened to me the world of finite elements and its application to vibrational problems. Also I would like to thank Professor Leopold Felsen for guiding me in such important concepts as ray methods in acoustics and asymptotic approaches for wave scattering problems. Additionally, I am thankful to Professor Thomas Bifano, the students Julie Perrault and Daniel Pascual for their help on the designs of high Q MEMS resonators. For accepting to be chairman of my dissertation committee I would like to extend my gratitude to Professor Raymond Nagem.

I would like to acknowledge the lecture excellence of Professor Leopold Felsen who through discussions and homeworks made a strong impact on my understanding of acoustics. Also I would like to recognize Professors Raymond Nagem, Paul Barbone, Donald Wroblewski and Ronald Roy for their interesting lectures and discussions. I will be thankful to Fillipo Capolino for the discussions (and arguments) with him about some wave propagation periodic problems.

Before coming to Boston University I would like to thank Professors Todor Karadjov and Valeri Stoilov (Technical University - Sofia) for introducing me to the area of structural mechanics and vibrations and I will be grateful to Professor Ivan Petrov for his variational analysis lectures. Also I would like to recognize the interesting discussions which I had with Professor Mosko Aladjem (Technical University - Sofia) in his computer modeling lectures and Professor Vessela Pasheva for her computer algorithms lectures.

For introducing me in the world of mathematics I would like to thank my high school teacher Veliko Kolev. Also I will always remember the mountain hikes and bridge sessions with his group in Sofia school of mathematics.

In addition to my experience at Boston University I would like to recognize the important influence of my mother Angelina and my father Petko. Also I am thankful to my cousins Iskra and Tzonko for their help and support. Also I am grateful to my friends Vesselin and Vladimir for the time we spent together and the diverse discussions we had.

Finally, but not last, I would like to say that I will always be grateful to all my colleagues and friends at Department of Aerospace and Mechanical Engineering at Boston University. Some of them are Mario Zampolli, Preston Wilson, Irena Velikovic, Trevor Woods, Gary Dewar, Jerry Cartmell, Brian Rush, Cory Clarke, Kelly Horan, Mark Booth.

I would like to acknowledge the group of my friends at Boston who are Valentin Vullev, Kostadinka (Dida) Bizheva, Georgi Georgiev, Boriana Georgiev, Mieko Iwai.

The research presented in the dissertation was financed by National Science Foundation under Grant Number CMS-9531399 and by the U.S. Office of Naval Research. I would like to thank the two institutions which made possible my study and research at Boston University.

D.G.

VIBRATIONS OF ELASTIC STRUCTURES WITH MULTIPLE ARRAYS OF ATTACHMENTS: THEORY AND APPLICATIONS

(Order No.)

DIMITAR GUEORGUIEV

Boston University College of Engineering, 2001

Major Professor: J. Gregory McDaniel, Assistant Professor of Aerospace and Mechanical Engineering

ABSTRACT

This thesis concerns the analysis and passive control of waves that propagate in smooth elastic structures, such as beam and plates, with arrays of substructures attached at regularly spaced locations. Examples of such structures include aircraft fuselages, ship hulls, and a variety of composite materials. This thesis presents new analytical descriptions that illuminate the physics of existing structures and suggest new applications of periodic structures. A primary contribution is the derivation of Floquet wave dispersion relations that are hierarchical in form and thereby quantify the effects of individual arrays on the vibrational response of the structure. Analysis of these relations indicates when a subset of arrays may be approximated by modifying the parameters of the smooth structure and provides a method for choosing the modifications. This "partial homogenization" approach will reduce the computational burdens of numerically analyzing structural designs and will provide structural designers with a better understanding of the effects of array parameters on structural response. In contrast, an "inverse homogenization" approach is developed in which continuous portions of a structure are approximated by an array of attached

substructures. This approach is useful in constructing finite element models of composite structures from vibrational response data. These analytical contributions are illustrated by two applications of current interest. In the first, a new class of high-Q MEMS resonators is proposed in which energy is localized by periodic structures that dynamically simulate rigid structures. In the second, the inverse homogenization method is used to construct a transient model of a beam damping treatment for inclusion in a time-domain finite element model.

Contents

List of Tables

List of Figures

Chapter 1

Introduction

Engineering research often has the goal of presenting a simplified approach. applicable to a broad class of problems with different geometries and governed by different equations of motion. In this spirit. this thesis investigates the complex way in which arrays of point-attached impedances influence the propagation of waves in periodic structures. presents simplified treatment for a class of periodic problems. and describes the applications of such periodic structures. Means of extending the analysis to other geometries and loadings is also considered.

1.1 Motivation

This thesis is motivated by the fact that regularly spaced attachments dramatically affect the propagation of waves in elastic structures. Aircraft fuselages and ship hulls are two examples of such structures. An important aspect of their design of such structures involves selecting the locations and geometries of attached substructures such as ribs. and bulkheads. While their major structural role is to prevent collapse. they may also be designed to control the flow of vibrational energy in the structure. When a localized excitation is applied to a plate with arrays of regularly spaced attachments, it generates Floquet waves whose wavenumbers indicate whether the injected vibrational energy will be localized or distributed along the plate. A new analysis is presented here for understanding wave propagation in structures with multiple arrays of attachments, as modeled by an infinite plate or bar reinforced with multiple line arrays. As a first application, the design of an elastic micromechanical resonator with a high Q factor will be developed using a periodic structure as a means of vibroisolation and energy localization. In the second application, it will be shown that the periodic structure models the transverse vibrations of steel box beam with damping treatment.

1.2 Overview of doctoral thesis

The wave propagation analysis of periodic structures with multiple arrays of attachments is presented in Chapter 2. There, a generalized dispersion relation is derived and expressions for the plate response are discussed. Throughout the thesis, the term *offset* will be used to denote the smallest distance between two attachments belonging to different arrays and thus measuring the arrays' misalignment. For the case of periodic structures with offset arrays, the dispersion relations are obtained numerically and the best vibroisolating structure among the class of two array structures is selected. It is shown here that the wave propagation depends dramatically on the offset. As described in section 2.7 even small changes may lead to significant variations in attenuation.

As an application of the array attachment theory, the design of a MEMS resonator with high Q factor is considered. There, the existing uniform resonator is replaced by a resonating nonuniform periodic structure, minimizing energy flow through its boundaries. The new design is proposed in Chapter 3. The computation of the beam response is performed using a finite element model (FEM). Further, frequency-dependent expressions for the loss and Q factors of the structure are derived. On the basis of a two-dimensional FEM with quadratic elements, realistic designs are developed and proposed for manufacturing.

Chapter 4 introduces the concept of partial homogenization, by which a simplification of the structural geometry can be achieved at low frequencies upon recognizing the small scales of the problem in the considered frequency range. Asymptotic expansions up to the first order correction term for the Floquet wavenumber and the structural response at the periodic cell boundary are developed there.

As an application of the homogenization theory, a model for the damping treatment of a steel box beam is developed. On the basis of this model, an estimation for the loss factor is obtained. Array impedance of a single-array model structure and structural loss factor are obtained by implementing FEM by an optimization procedure that matches the computed beam response from the FEM with the measured data in the frequency domain. The computed response shows very good agreement with the measured data both in the frequency and time domains. The array impedance is approximated by a rational function such that the model becomes linear with reduced order. The rational function has a specific form allowing the damping treatment model to be incorporated in the existing time-domain FE codes. An alternative model for the array impedance is investigated which approximate the damping treatment by a fictitious fluid with low wave speed. The wave speed is selected such that impedance computed by this model matches with that obtained by the optimization procedure. The discussion is given in Chapter 5.

Chapter 2

Wave propagation in infinite elastic structures with multiple arrays of attachments

The analysis presented here was inspired by a history of increasingly advanced analyses for a broad variety of structures with arrays of point attachments. Analysis of the attenuation along an infinite elastic beam with pinned periodic supports was performed by Miles [1] and a dispersion relation was analytically derived, supporting Brillouin's observations of stop and pass bands in the wave propagation though periodic structures. Miles' analysis involved the solution of a difference equation derived by enforcing the boundary conditions at the pinned locations. The resulting equations for the phase and group speeds indicated alternating stop and pass bands. His analysis was extended by Lin [3]–[4] to include finite rotational impedances at the pinned locations and by Smith [5] to estimate the coupling of the beam vibrations to an ambient acoustic medium. Ungar [7] considered an infinite plate with a single beam attached to it, presenting reflection, transmission and near field effects, associated with the flexural waves, impinging on the beam side. Heckl's analysis [6] of plates supported by regularly spaced beams used Ungar's analysis [7] of the reflection and transmission of a flexural waves. By accounting for the multiple reflections and transmissions created by regularly spaced beams, equations were derived for the attenuation of flexural waves that also exhibited stop and pass band behavior. Thereafter, analyses of periodic structures have mostly employed two basic analysis methods, both of which assume time-harmonic motions of the structure.

The first method, which shall be referred to here as the *eigenvalue method*, formulates an eigenvalue problem for the attenuation constant based on the analysis of one cell of the periodic structure. The eigenvalue problem is found by applying Floquet's Theorem to the responses at the ends of the cell. Applications of Floquet's Theorem to the case of a beam with one array of attachments were described by Ungar [8] and Bobrovnitskii and Maslov [9]. Mead [10]-[13] extended the approach to any linear structure and developed insights into the locations of the stop and pass bands as well as the number of Floquet waves that propagate in a structure. Mead's method utilized a second order difference equation, describing the free motion of a piecewise periodic structure by

$$F_{r-1} + aF_r + F_{r+1} = 0, \tag{2.1}$$

where F represents the generalized force along the structure and the index r relates the corresponding quantity to the rth cell. The coefficient a is a function of the structural receptances and in the case of a perfectly periodic structure it does not depend on the index r. Note that a will be a matrix for multi-coupled structures. The relation (2.1) shows that the attachments provide nearest-neighbor coupling between the adjacent bays. Substituting the Floquet theorem,

$$F_{r+1} = e^{ikd} F_r \tag{2.2}$$

in (2.1), one obtains a dispersion equation for the Floquet wavenumber k. The development of this approach by Mead and others at the University of Southampton is summarized in [15].

The second method, which shall be referred to here as the *wavenumber method*, proceeds by taking the spatial Fourier transform of the differential equations of motion of the structure. Once in the wavenumber domain, the structural response is obtained by employing Poisson's summation formula. Each pole of the wavenumber response is known as a Floquet wavenumber and it is related to the propagation constant by a factor of $\sqrt{-1} \times$ *cell length*. Upon returning to the spatial domain, the response is found to consist of a linear combination of waves with spatially periodic coefficients in the form

$$v_n(x,t) = \Re\left\{V_n(x)\exp[-i(\omega t + k_n x)]\right\}, \tag{2.3}$$

where the number of the terms depends on the order of the ODE.

The spatially dependent amplitudes $V_n(x)$ are periodic with the same spatial period as the structure. The complex-valued constant k_n depends on frequency and is known as Floquet wavenumber. Mead showed in [12] that for an N-coupled periodic problem there will be N distinct Floquet wavenumbers. For instance, there will be a single Floquet wavenumber for the longitudinal vibrations of a beam with a longitudinal array of attachments. Early applications of the method are presented by Romanov [16], Evseev [17], and Rumerman [18].

Both methods have been applied to the analysis of structures with two arrays of attachments. The eigenvalue method was employed by Gupta [19]. His analysis revealed the appearance of "minor" stop and pass bands when a second array was added to the structure. His approach was specific to the two-array problem, however, its extension to a structure with more than two arrays is not obvious. The wavenumber analysis of a plate with two arrays of line attachments was first presented by Mace [20] and was later applied by Burroughs [22] to a cylindrical shell with two arrays of ring attachments. Recently, Cray [23] and Nuttall [24] presented procedures that render explicit expressions for the wavenumber response of a plate with multiple arrays of attachments, each one being arbitrarily shifted with respect to the others.

In this section, analytical expressions are presented that allow one to understand the relationships between the Floquet wavenumbers and the properties of the attached arrays. The excitation is taken to be a phased line force and each array is composed of identical regularly spaced attachments aligned parallel to the excitation line. Each attachment applies a line force to the plate that is proportional to its line impedance and the local plate velocity. Using the wavenumber method, a spatial Fourier transform is applied to the differential equation of motion of the structure and the Poisson summation formula is used to obtain the equation of motion in the wavenumber domain.

This approach provides simple closed form expressions for the dispersions and responses of a large class of systems. The primary restrictions on this class of structures are that each array spacing must be a multiple of the smaller array spacings and that spatial points of coincidence, where an attachment from each array resides, must exist. Restricting attention to this class allows analytic inversion to the spatial domain and reveals that the plate response is a sum of two Floquet waves that propagate in each direction. The Floquet wavenumbers, measuring attenuation along the structure, are found from a hierarchical procedure where one begins with the unstiffened plate wavenumbers and adds the effect of each array by solving a quadratic equation for the altered wavenumbers. This procedure allows one to assess the effect of each array spacing and impedance on the dispersions of waves, so that one may conceptually design a structure that either localizes or distributes energy. Extension of this analysis to a broad class of problems described by linear differential equations is straightforward. For example, the analysis could be extended to shells with rings of attachments.

2.1 Problem statement

Consider a thin elastic plate with P arrays, an example of which is shown in Figure 2.1. The plate is described by its Young's modulus E, thickness h, mass per unit area m, and Poisson's ratio ν. The midplane of the plate coincides with the xy plane, so that the y axis is into the paper.

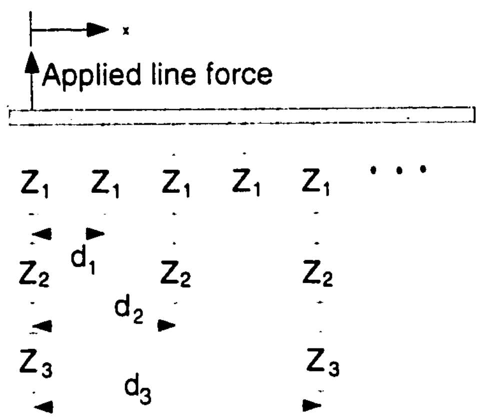

Figure 2.1: Example structure, consisting of a thin elastic plate with three arrays of line attachments. This particular arrangement is analyzed in section 2.6. The circles represent line impedances that extend along the y coordinate (into page).

A harmonic dependence in time and the y coordinate is assumed throughout this chapter, so that the total force F applied to the plate and its transverse displacement W are represented as:

$$F(x, y, t) = \Re\{f(x)\exp[i(k_y y - \omega t)]\} \text{ and} \tag{2.4}$$

$$W(x, y, t) = \Re\{w(x)\exp[i(k_y y - \omega t)]\}. \tag{2.5}$$

Lower-case variables, such as f and w, will generally be used to represent the x-dependent complex amplitude of the corresponding upper-case variables. Henceforth, all dependent variables and attachment impedances will be assumed functions of k_y and ω. This dependence is omitted for brevity.

The equation of motion of the plate with no attachments is

$$D\Delta^2 W - m\frac{\partial^2 W}{\partial t^2} = F, \text{ where} \tag{2.6}$$

$$\Delta^2 = \frac{\partial^4}{\partial x^4} + 2\frac{\partial^4}{\partial x^2 \partial y^2} + \frac{\partial^4}{\partial y^4} \tag{2.7}$$

and $D = Eh^3/[12(1-\nu^2]$. Given the assumptions in (2.4) and (2.5), this equation simplifies to

$$D\left(k_y^4 v - 2k_y^2\frac{\partial^2 v}{\partial x^2} + \frac{\partial^4 v}{\partial x^4}\right) - m\omega^2 v = -i\omega f, \tag{2.8}$$

where the complex amplitude of velocity is given by $v(x) = -i\omega w(x)$. Hysteretic damping is included in the frequency domain by allowing the Young's modulus to be complex-valued, so that $E = E_0(1 - i\eta)$ where η is the material loss factor.

Each attachment of each array is assumed to exert a line force on the plate that is linearly proportional to its velocity, the constant of proportionality being the mechanical line impedance Z_p for an attachment in the pth array. An attachment does not exert a moment on the plate. Ordering the arrays such that $d_p > d_{p-1}$, we further require that $d_p = n_p d_{p-1}$ where n_p is required to be an integer. It is also assumed that x locations exists where an attachment from each array interacts with the structure and these locations will be referred to as *points of coincidence*. The origin $x = 0$ is positioned at a point of coincidence. Each array is fully characterized by its spacing d_p and its line impedance Z_p.

The total force applied to the plate is a sum of a unit line force applied at $x = 0$, which is represented with the Dirac delta function, and the force applied by each attachment of each array,

$$f(x) = \delta(x) - \sum_{p=1}^{P} f_p(x). \tag{2.9}$$

Each of the f_p terms represents the force applied by the plate to the p^{th} array, which accounts for the minus sign preceding the summation. Each such force is expressed as

$$f_p(x) = Z^{(p)}(x)v(x), \text{ where } Z^{(p)}(x) = Z_p \sum_{n=-\infty}^{\infty} \delta(x - nd_p). \tag{2.10}$$

The spatial impedance $Z^{(p)}$ represents the ratio of forces applied by the plate to the velocity at the attachment points.

2.2 Wavenumber domain formulation

Closed-form expressions for the forced response and Floquet wave dispersion require the solution of Equation (2.6). This shall be accomplished in the wavenumber domain, which is defined by the following Fourier transform pair:

$$\tilde{g}(k) = \int_{-\infty}^{\infty} g(x)e^{-ikx}\,dx \text{ and} \tag{2.11}$$

$$g(x) = \frac{1}{2\pi} \int_{-\infty}^{\infty} \tilde{g}(k) e^{ikx} \, dk, \tag{2.12}$$

where the tilde over any variable designates the wavenumber transform of that variable throughout this thesis. Taking the Fourier transform of (2.6) yields an algebraic relation between the wavenumber velocity $\tilde{v}(k)$ and distributed loading $\tilde{f}(k)$ in terms of the plate admittance $\tilde{Y}(k)$, given by

$$\tilde{v}(k) = \tilde{Y}(k)\tilde{f}(k), \text{ where} \tag{2.13}$$

$$\tilde{Y}(k) = \frac{1}{-im\omega}\left[\frac{k_f^4}{k_f^4 - (k^2 + k_y^2)^2}\right]. \tag{2.14}$$

The wavenumber of flexural waves propagating in the plate without attachments is $k_f = \sqrt[1/4]{m\omega^2/D}$. This wavenumber is complex-valued for a damped plate and real-valued for an undamped plate.

Assuming a unit line force that is independent of k_y, the total force transforms as

$$\tilde{f}(k) = 1 - \sum_{p=1}^{P} \tilde{f}^{(p)}(k), \text{ where} \tag{2.15}$$

$$\tilde{f}^{(p)}(k) = \tilde{Z}^{(p)}(k) * \tilde{v}(k) \tag{2.16}$$

and the symbol "$*$" designates k-convolution. The Fourier transform of the pth array's impedance is

$$\tilde{Z}^{(p)}(k) = Z_p \sum_{n=-\infty}^{\infty} \exp(-iknd_p) \tag{2.17}$$

The convolution indicated in (2.16) may be simplified by Poisson's summation formula. When the general form of Possion's equation, given by (see [26], page 47)

$$\sum_{n=-\infty}^{\infty} g(nd) = \frac{1}{d} \sum_{m=-\infty}^{\infty} \tilde{g}(mk_d), \tag{2.18}$$

is specialized for the choice $g(x) = \exp(-ikx)$, we get the identity

$$\sum_{n=-\infty}^{\infty} \exp(-iknd) = k_d \sum_{n=-\infty}^{\infty} \delta(k - nk_d), \text{ where } k_d = \frac{2\pi}{d}. \tag{2.19}$$

The identity in (2.19) allows the impedance in (2.17) to be written as

$$\tilde{Z}^{(p)}(k) = k_{d,p} Z_p \sum_{n=-\infty}^{\infty} \delta(k - nk_p), \text{ where } k_{d,p} = \frac{2\pi}{d_p} \tag{2.20}$$

. Carrying out the convolution indicated in (2.16) gives

$$\tilde{f}^{(p)}(k) = \frac{Z_p}{d_p} \sum_{-\infty}^{\infty} \tilde{v}(k - nk_{d,p}). \tag{2.21}$$

The wavenumber transform of the total force acting on the plate is then

$$\tilde{f}(k) = 1 - \sum_{p=1}^{P} \frac{Z_p}{d_p} \sum_{n=-\infty}^{\infty} \tilde{v}(k - nk_{d,p}). \tag{2.22}$$

The wavenumber velocity $\tilde{v}(k)$ now follows from (2.13).

$$\tilde{v}(k) = \tilde{Y}(k) - \tilde{Y}(k) Z_p \sum_{p=1}^{P} \tilde{v}_{\Sigma,p}(k), \text{ where} \tag{2.23}$$

$$\tilde{v}_{\Sigma,p}(k) = \frac{1}{d_p} \sum_{n=-\infty}^{\infty} \tilde{v}(k - nk_{d,p}). \tag{2.24}$$

The subscript Σ, p on a quantity shall be used to identify a transformed variable, such as $\tilde{v}_{\Sigma,p}(k)$, that is summed over multiples of the pth array wavenumber $k_{d,p}$ and normalized by d_p. Equation (2.23) represents the coupling of velocities at different wavenumbers due to the different spacings of the arrays. The next section presents a method of uncoupling this equation using a generalization of a procedure presented by Mace [20].

2.3 Response in the wavenumber domain

To find values of k that satisfy (2.23), the spatial scales introduced by the arrays will be successively eliminated. The key concept that allows this elimination is that each $\tilde{v}_{\Sigma,p}(k)$ is periodic in wavenumber with period $k_{p,d}$. The procedure is to find $\tilde{v}_{\Sigma,1}(k)$ in terms of the other $\tilde{v}_{\Sigma,p}(k)$ and $v(k)$ by using the fact that any d_p is an integer multiple of d_1. This allows (2.23) to be written in terms of $\tilde{v}_{\Sigma,p}(k)$, where $p \geq 2$, and $v(k)$. Next, the $p = 2$ array is similarly treated. This process, which must begin at $p = 1$ and proceed consecutively to $p = P$, continues until all of the summed velocities are removed from the equation, at which point only $\tilde{v}(k)$ remains. The process will be illustrated here for the $p = 1$ and $p = 2$ arrays and then a general expression for $\tilde{v}(k)$ accounting for all P arrays will be presented.

The analysis is begun by replacing the wavenumber k in (2.23) by the shifted wavenumber $k - qk_{d,1}$, where q is a fixed integer, so as to obtain

$$\tilde{v}(k - qk_{d,1}) = \tilde{Y}(k - qk_{d,1}) - \tilde{Y}(k - qk_{d,1}) \sum_{p=1}^{P} \frac{Z_p}{d_p} \tilde{v}_{\Sigma,p}(k - qk_{d,1}) \qquad (2.25)$$

Since $k_{d,1}$ is an integer multiple of the wavenumbers $k_{d,p}$, the summed velocities $\tilde{v}_{\Sigma,p}(k)$ are periodic with a period of $k_{d,p}$. This observation leads to

$$\tilde{v}_{\Sigma,p}(k - qk_{d,1}) = \frac{1}{d_p} \sum_{n=-\infty}^{\infty} \tilde{v}(k - nk_{d,p} - qk_{d,1}) = \frac{1}{d_p} \sum_{n=-\infty}^{\infty} \tilde{v}(k - (n + qN_p)k_{d,p}) \quad (2.26)$$

where $N_p = d_p/d_1$ is an integer. This equation involves a shift of the summation index n by the integer amount qN_p and, since the summation is infinite, the following identity holds

$$\tilde{v}_{\Sigma,p}(k - qk_{d,1}) = \tilde{v}_{\Sigma,p}(k). \tag{2.27}$$

Summing (2.25) over q from $-\infty$ to ∞, invoking (2.27), and dividing by d_1 yields,

$$\tilde{v}_{\Sigma,1}(k) = \tilde{Y}_{\Sigma,1}(k) - \tilde{Y}_{\Sigma,1}(k) \sum_{p=1}^{P} Z_p \tilde{v}_{\Sigma,p}(k), \tag{2.28}$$

where the notation

$$\tilde{Y}_{\Sigma,1}(k) = \frac{1}{d_1} \sum_{n=-\infty}^{\infty} \tilde{Y}(k - nk_{d,1}) \tag{2.29}$$

has been introduced for convenience. Rearranging (2.28) allows $\tilde{v}_{\Sigma,1}$ to be expressed in terms of the other velocity sums

$$\tilde{v}_{\Sigma,1}(k) = \frac{\tilde{Y}_{\Sigma,1}(k)}{1 + Z_1 \tilde{Y}_{\Sigma,1}(k)} - \frac{\tilde{Y}_{\Sigma,1}(k)}{1 + Z_1 \tilde{Y}_{\Sigma,1}(k)} \sum_{p=2}^{P} Z_p \tilde{v}_{\Sigma,p}(k). \tag{2.30}$$

Substituting (2.30) into (2.23), one obtains $v(k)$ in terms of the summed velocities for the $p > 1$ arrays

$$\tilde{v}(k) = \tilde{Y}_2(k) - \tilde{Y}_2(k) \sum_{p=2}^{P} Z_p \tilde{v}_{\Sigma,p}(k) \tag{2.31}$$

with the admittance function $\tilde{Y}_2(k)$ defined as

$$\tilde{Y}_2(k) = \frac{\tilde{Y}(k)}{1 + Z_1 \tilde{Y}_{\Sigma,1}(k)}. \tag{2.32}$$

Physically, $\tilde{Y}_2(k)$ is the wavenumber impedance of the plate with the first array ($p = 1$) attached.

The $p = 2$ array is similarly treated by solving for $\tilde{v}_{\Sigma,2}$ just as we did for $\tilde{v}_{\Sigma,1}$

above. Replacing the wavenumber k in (2.31) by $k - qk_2$, where q is a fixed integer, gives

$$\tilde{v}(k - qk_{d,2}) = \tilde{Y}_2(k - qk_{d,2}) - \tilde{Y}_2(k - qk_{d,2}) \sum_{p=2}^{P} Z_p \tilde{v}_{\Sigma,p}(k - qk_{d,2}) \tag{2.33}$$

. Since $k_{d,2}$ is an integer multiple of $k_{d,p}$, the following identity holds (see (2.27)):

$$\tilde{v}_{\Sigma,p}(k - qk_{d,2}) = \tilde{v}_{\Sigma,p}(k), \text{ where } p = 2, \ldots, P \tag{2.34}$$

. Summing (2.33) over q over from $-\infty$ to ∞, invoking (2.34), and dividing both sides by d_2 yields

$$\tilde{v}_{\Sigma,2}(k) = \tilde{Y}_{\Sigma,2}(k) - \tilde{Y}_{\Sigma,2}(k) \sum_{p=2}^{P} Z_p \tilde{v}_{\Sigma,p}(k). \tag{2.35}$$

with the second summed admittance defined as

$$\tilde{Y}_{\Sigma,2}(k) = \frac{1}{d_2} \sum_{n=-\infty}^{\infty} \tilde{Y}_2(k - nk_{d,2}) \tag{2.36}$$

. Solving for the summed velocity $\tilde{v}_{\Sigma,2}$ gives

$$\tilde{v}_{\Sigma,2}(k) = \frac{\tilde{Y}_{\Sigma,2}(k)}{1 + Z_2 \tilde{Y}_{\Sigma,2}(k)} - \frac{\tilde{Y}_{\Sigma,2}(k)}{1 + Z_2 \tilde{Y}_{\Sigma,2}(k)} \sum_{p=3}^{P} Z_p \tilde{v}_{\Sigma,p}(k) \tag{2.37}$$

. Substituting (2.37) into (2.31) yields an expression for $\tilde{v}(k)$ that has the same form as (2.31) but with one more summed velocity, $\tilde{v}_{\Sigma,2}$, eliminated to give

$$\tilde{v}(k) = \tilde{Y}_3(k) - \tilde{Y}_3(k) \sum_{p=3}^{P} Z_p \tilde{v}_{\Sigma,p}(k). \tag{2.38}$$

The admittance wavenumber function $\tilde{Y}_3(k)$ is

$$\tilde{Y}_3(k) = \frac{\tilde{Y}_2(k)}{1 + Z_2\tilde{Y}_{\Sigma,2}(k)} = \frac{\tilde{Y}(k)}{(1 + Z_1\tilde{Y}_{\Sigma,1}(k))(1 + Z_2\tilde{Y}_{\Sigma,2}(k))}. \tag{2.39}$$

where $\tilde{Y}_{\Sigma,2} = \frac{1}{d_2}\sum_{n=-\infty}^{\infty} \tilde{Y}_2(k - nk_{d,2})$.

After performing similar steps until the last unknown quantity $\tilde{v}_{\Sigma,P}$ is eliminated one obtains the following expression for wavenumber velocity:

$$\tilde{v}(k) = \frac{\tilde{Y}(k)}{\tilde{Q}(k)} \tag{2.40}$$

, where $\tilde{Q}(k)$ will be referred to as the *wavenumber dispersion function.* It is periodic in wavenumber with period $k_{d,1}$ and is given explicitly by

$$\tilde{Q}(k) = [1 + Z_1\tilde{Y}_{\Sigma,1}(k)][1 + Z_2\tilde{Y}_{\Sigma,2}(k)]\ldots[1 + Z_P\tilde{Y}_{\Sigma,P}(k)] \tag{2.41}$$

The summed admittances $\tilde{Y}_{\Sigma,p}$ in (2.41) are defined by

$$\tilde{Y}_{\Sigma,p}(k) = \frac{1}{d_p}\sum_{n=-\infty}^{\infty} \tilde{Y}_p(k - nk_p). \tag{2.42}$$

They are also periodic in wavenumber with period $k_{d,p}$. In (2.42), $\tilde{Y}_p$ is the wavenumber admittance of the plate with the first $(p-1)$ arrays attached. The pth admittance satisfies the recursion relation.

$$\tilde{Y}_p(k) = \begin{cases} \tilde{Y}(k) & \text{if } p = 1 \\ \dfrac{\tilde{Y}_{p-1}(k)}{1 + Z_{p-1}\tilde{Y}_{\Sigma,p-1}(k)} & \text{if } p = 2,\ldots,P. \end{cases} \tag{2.43}$$

Note that the wavenumber velocity of the plate with no attachments is $\tilde{v}(k) = \tilde{Y}(k)$.

as one would expect from (2.14) with $\tilde{f} = 1$. The dispersion function $\tilde{Q}(k)$ takes into account the interactions of the plate with all P arrays, and the dispersion relation is simply

$$\tilde{Q}(k) = 0. \tag{2.44}$$

Note that this result is independent of the inclusion of forcing in (2.9). The above analysis could also be used to show that (2.44) must be satisfied by the unforced system in order to yield a nontrivial solution for the velocity.

One may gain confidence in equations (2.40) and (2.41) by considering a structure with P arrays all having the same spacing, d, but each array having an impedance Z_p. For this case, the structure would behave exactly like a structure with a single array of attachments with spacing d and with an impedance equal to the sum of the impedances from the P-array structure, $\sum_{p=1}^{P} Z_p$. To show this, one computes the velocity of the P-array structure by evaluating (2.40) and (2.41) for each array. The velocity of the structure with the first array is

$$\tilde{v}_1(k) = \frac{\tilde{Y}(k)}{1 + Z_1 \tilde{Y}_\Sigma(k)} \tag{2.45}$$

where the summed admittance is

$$\tilde{Y}_\Sigma(k) = \frac{1}{d} \sum_{n=-\infty}^{\infty} \tilde{Y}(k - nk_d) \tag{2.46}$$

and $k_d = 2\pi/d$. Addition of the second array results in a velocity of

$$\tilde{v}_2(k) = \frac{\tilde{Y}(k)}{1 + (Z_1 + Z_2)\tilde{Y}_\Sigma(k)}. \tag{2.47}$$

This process continues until the velocity of the structure with all P arrays is obtained.

$$\tilde{v}_P(k) = \frac{\tilde{Y}(k)}{1 + \sum_{p=1}^{P} Z_p \tilde{Y}_\Sigma(k)}. \tag{2.48}$$

Therefore, consecutive application of equations (2.40) and (2.41) gives a result which matches the physical expectation that impedances attached to the same position of the structure may be replaced by the sum of the individual impedances.

2.4 Response in spatial domain

In order to return to the spatial domain, it is necessary to take the inverse Fourier transform, defined in (2.12), of the velocity $\tilde{v}(k)$ given in (2.40). To do this by contour integration requires determination of the poles of $\tilde{v}(k)$, given by the zeros of $\tilde{Q}(k)$. This can be efficiently performed by first simplifying the function $\tilde{Q}$ after deriving closed-form expressions for each $\tilde{Y}_{\Sigma,p}$. The subsection below presents this derivation followed by contour integration of the simplified $\tilde{Q}$.

2.4.1 Closed-form expressions for the summed plate admittances

The first step of our analysis, namely the finding of $\tilde{Y}_{\Sigma,1}$, follows Mace's analysis [27] of a one-array structure. A new approach is presented here for the finding of $\tilde{Y}_{\Sigma,p}$ for $p > 2$. This approach, which is crucial to the development of closed-form solutions to the multiple-array problem, finds the $\tilde{Y}_{\Sigma,p}$ sequentially, beginning with $p = 1$ and proceeding with higher values of p. In the following treatment, $\tilde{Y}_{\Sigma,1}$ and $\tilde{Y}_{\Sigma,2}$ will be explicitly simplified and the results will be generalized to $\tilde{Y}_{\Sigma,p}$ for any p.

First, the $\tilde{Y}_{\Sigma,1}$ given in (2.29) is rewritten as

$$\tilde{Y}_{\Sigma,1}(k) = \frac{1}{d_1} \sum_{m=-\infty}^{\infty} \tilde{g}_1(mk_{d,1}), \text{ where } \tilde{g}_1(u) = \tilde{Y}(k+u) \tag{2.49}$$

and $\tilde{Y}(k)$ is given in (2.14). Poisson's summation formula, given in (2.18), is evaluated with $d = d_1$ and $g = g_1$ allowing (2.49) to be written as

$$\tilde{Y}_{\Sigma,1}(k) = \sum_{n=-\infty}^{\infty} g_1(nd_1). \tag{2.50}$$

In order to evaluate (2.50), the spatial function $g_1(x)$ must be found. Taking the inverse transform of $\tilde{g}_1(u)$ gives

$$g_1(x) = \frac{1}{2\pi} \int_{-\infty}^{\infty} e^{ixu} \tilde{Y}(k+u) du. \tag{2.51}$$

Introducing the new variable $\xi = k + u$ into (2.51), we obtain

$$g_1(x) = \frac{e^{-ixk}}{2\pi} \int_{-\infty}^{\infty} e^{ix\xi} \tilde{Y}(\xi) d\xi = e^{-ixk} v^{(0)}(x), \text{ where} \tag{2.52}$$

$$v^{(0)}(x) = \frac{1}{2\pi} \int_{-\infty}^{\infty} e^{ix\xi} \tilde{Y}(\xi) d\xi \tag{2.53}$$

is the spatial velocity response of the plate without attachments caused by the applied line force at the origin.

This integral is to be evaluated by contour integration in the complex ξ-plane, which requires determination of the residues of the integrand. The poles of the integrand satisfy the dispersion relation of the plate without attachments.

$$(k^2 + k_y^2)^2 - k_f^4 = 0. \tag{2.54}$$

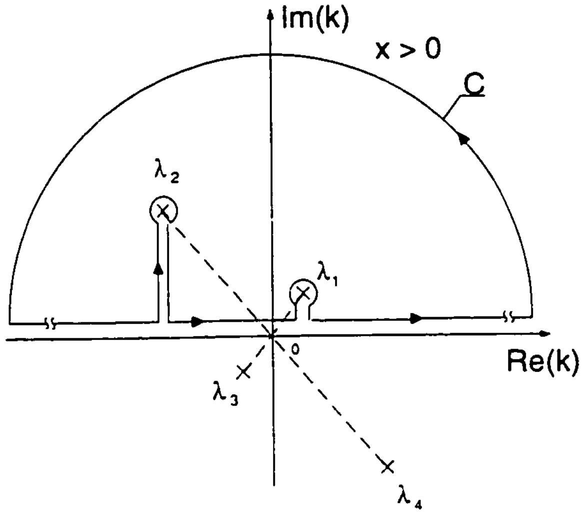

Figure 2.2: Pictorial representation of the roots of the dispersion relation for a plate with no arrays. The integration contour is also shown.

This equation has four simple roots, $k = \lambda_i$, where $i = 1, \ldots, 4$, that represent the four simple poles of the integrand in (2.53) given by :

$$\lambda_{1,2,3,4} = \pm\sqrt{\pm k_f^2 - k_y^2} \tag{2.55}$$

For a damped plate it can be observed that two of the roots lie in the upper half of the complex wavenumber plane, while the other two lie in the lower half plane, antisymmetric with respect to the first two, as shown in Figure 2.2. To find $v^{(0)}(x)$, the roots λ_1 and λ_2 are required to lie in the upper half plane and the integration contour given in Figure 2.2 is used. Applying Jordan's lemma and invoking symmetry considerations in the x-coordinate, $v^{(0)}(x)$ is found to be a sum of two waves.

$$v^{(0)}(x) = c_1 e^{i\lambda_1|x|} + c_2 e^{i\lambda_2|x|} \tag{2.56}$$

with the coefficients c_1 and c_2 given by

$$c_1 = \frac{k_f^2}{4m\omega\lambda_1} \qquad \text{and } c_2 = -\frac{k_f^2}{4m\omega\lambda_2} \tag{2.57}$$

. Substituting (2.52) into (2.50) gives

$$\tilde{Y}_{\Sigma,1}(k) = \sum_{n=-\infty}^{\infty} v^{(0)}(nd_1)e^{-ind_1k}. \tag{2.58}$$

Evaluating (2.56) at $x = nd_1$ and substituting into (2.58) gives

$$\tilde{Y}_{\Sigma,1}(k) = c_1 \sum_{n=-\infty}^{\infty} e^{-ind_1k}e^{i\lambda_1|nd_1|} + c_2 \sum_{n=-\infty}^{\infty} e^{-ind_1k}e^{i\lambda_2|nd_1|}. \tag{2.59}$$

The infinite sums given in (2.59) are evaluated with the aid of the geometric series formula

$$\sum_{n=0}^{\infty} e^{\alpha nd_1} = \frac{1}{1-e^{\alpha d_1}}. \tag{2.60}$$

where α is a parameter with $\Re(\alpha) < 0$. The first sum in (2.59) reduces to

$$\sum_{n=-\infty}^{\infty} e^{-ind_1k}e^{i\lambda_1|nd_1|} = \sum_{n=0}^{\infty} e^{ind_1(\lambda_1-k)} + \sum_{n=1}^{\infty} e^{ind_1(\lambda_1+k)}. \tag{2.61}$$

Identifying $\alpha = \lambda_1 \pm k$ in (2.59) further simplifies this result to

$$\sum_{n=-\infty}^{\infty} e^{-ind_1k}e^{i\lambda_1|nd_1|} = \frac{1}{1-e^{i(\lambda_1-k)d_1}} + \frac{1}{1-e^{i(\lambda_1+k)d_1}} - 1. \tag{2.62}$$

Using the identities

$$\frac{e^{-i\lambda d_1} + e^{i\lambda d_1}}{2} = \cos(\lambda d_1): \qquad \frac{e^{-i\lambda d_1} - e^{i\lambda d_1}}{2} = -i\sin(\lambda_1 d_1) \tag{2.63}$$

with $\lambda = \lambda_{1,2}$ and rearranging, gives

$$\sum_{n=-\infty}^{\infty} e^{-ind_1 k} e^{i\lambda_q |nd_1|} = \frac{-i \sin \lambda_q d_1}{\cos \lambda_q d_1 - \cos k d_1}, \text{ where } q = 1, 2. \tag{2.64}$$

Substituting (2.64) into (2.59) yields

$$\tilde{Y}_{\Sigma,1}(k) = A_1 \frac{\sin(\lambda_1 d_1)}{\cos(\lambda_1 d_1) - \cos(k d_1)} + B_1 \frac{\sin(\lambda_2 d_1)}{\cos(\lambda_2 d_1) - \cos(k d_1)}. \tag{2.65}$$

where the constants A_1 and B_1 are given by

$$A_1 = \frac{k_f^2}{4im\omega\lambda_1} \text{ and } B_1 = -\frac{k_f^2}{4im\omega\lambda_2}. \tag{2.66}$$

Next, the application of this procedure to $Y_{\Sigma,2}$ is summarized. Recalling that

$$\tilde{Y}_{\Sigma,2}(k) = \frac{1}{d_2} \sum_{n=-\infty}^{\infty} \tilde{Y}_2(k + nk_{d,2}), \text{ where} \tag{2.67}$$

$$\tilde{Y}_2(k) = \frac{\tilde{Y}(k)}{1 + Z_1 \tilde{Y}_{\Sigma,1}(k)} \text{ and } k_{d,2} = \frac{2\pi}{d_2}. \tag{2.68}$$

As before, $Y_{\Sigma,2}$ is rewritten as

$$Y_{\Sigma,2}(k) = \frac{1}{d_2} \sum_{m=-\infty}^{\infty} \tilde{g}_2(mk_{d,2}), \text{ where } \tilde{g}_2(u) = \tilde{Y}_2(k + u). \tag{2.69}$$

Following the steps in (2.49)–(2.52) leads to

$$g_2(x) = \frac{e^{-ixk}}{2\pi} \int_{-\infty}^{\infty} \frac{e^{ix\xi} \tilde{Y}(\xi)}{1 + Z_1 \tilde{Y}_{\Sigma,1}(\xi)} d\xi = e^{-ixk} v^{(1)}(x). \tag{2.70}$$

where

$$v^{(1)}(x) = \frac{1}{2\pi} \int_{-\infty}^{\infty} \frac{e^{ix\xi} \tilde{Y}(\xi)}{1 + Z_1 \tilde{Y}_{\Sigma,1}(\xi)} d\xi \tag{2.71}$$

is the velocity due to a unit line force acting on the plate with only the $p = 1$ array attached.

To obtain an explicit expression for $v^{(1)}$ by contour integration, we must first determine the zeros of the denominator in the integrand of (2.71). These zeros are given by the roots of

$$1 + Z_1 \tilde{Y}_{\Sigma,1}(k) = 0, \tag{2.72}$$

which is the dispersion relation for the plate with only the first array attached. This relation has been presented by others (see, for example [8]). Using the closed-form expression for $\tilde{Y}_{\Sigma,1}$ in (2.65), the zeros of (2.72) are found to be the roots of the following quadratic equation in $\cos(kd_1)$:

$$\cos^2(kd_1) + a_1 \cos(kd_1) + b_1 = 0. \tag{2.73}$$

The coefficients are

$$a_1 = -\cos(\lambda_1 d_1) - \cos(\lambda_2 d_1) - Z_1 \frac{k_f^2}{4im\omega\lambda_1} \sin(\lambda_1 d_1) + Z_1 \frac{k_f^2}{4im\omega\lambda_2} \sin(\lambda_2 d_1) \tag{2.74}$$

$$b_1 = \cos(\lambda_1 d_1)\cos(\lambda_2 d_1) + Z_1 \frac{k_f^2}{4im\omega\lambda_1} \sin(\lambda_1 d_1)\cos(\lambda_2 d_1) - Z_1 \frac{k_f^2}{4im\omega\lambda_2} \sin(\lambda_2 d_1)\cos(\lambda_1 d_1). \tag{2.75}$$

Equations (2.73)-(2.75) agree with the dispersion relation presented by Ungar [7] for a beam with one array of attached impedances.

Let ξ_1 and ξ_2 be the two roots of (2.73). Then the roots that satisfy the dispersion relation (2.72) are generated by the equations

$$\cos(kd_1) = \xi_{1,2} \tag{2.76}$$

$$\text{where } \xi_{1,2} = \frac{-a_1 \pm \sqrt{a_1^2 - 4b_1}}{2}. \tag{2.77}$$

These roots are repetitive since $\cos(kd_1) = \cos(kd_1 + 2n\pi)$, and they represent simple poles in the integrand of (2.71). There are exactly two roots, $k_1^{(1)}$ and $k_2^{(1)}$, in the strip defined by

$$k_{d,1} > \Re(k) \geq 0 \text{ where } \Im(k) \geq 0. \tag{2.78}$$

In the present work, this region of the complex wavenumber plane is defined as the *fundamental zone* for the plate with the first array. Accordingly,

$$\cos(k_{1,2}^{(1)} d_1) = \xi_{1,2}, \text{ where } \frac{2\pi}{d_1} > \Re(k_{1,2}^{(1)}) \geq 0, \text{ where } \Im(k_{1,2}^{(1)}) \geq 0. \tag{2.79}$$

All roots of the dispersion relation (2.72) are given by those in (2.79) subject to the $nk_{d,1}$ shift mentioned earlier.

To calculate $v^{(1)}$ in (2.71), the residue theorem is used with the integration contour given in Figure 2.3. After applying Jordan's lemma and invoking symmetry in the x-coordinate, the spatial velocity $v^{(1)}(x)$ is cast in the following form:

$$v^{(1)}(x) = 2\pi i \sum_{n=-\infty}^{\infty} \frac{1}{2\pi} \frac{\tilde{Y}(k_1^{(1)} + nk_{d,1})}{Z_1 \tilde{Y}'_{\Sigma,1}(k_1^{(1)} + nk_{d,1})} \exp\left((k_1^{(1)} + nk_{d,1})|x|\right) + \text{similar term with } k_2^{(2)}. \tag{2.80}$$

where the notation

$$\tilde{Y}'_{\Sigma,1}(k) = \frac{d\tilde{Y}_{\Sigma,1}(k)}{dk} \tag{2.81}$$

has been introduced for convenience.

Upon recognizing that (see (2.65))

$$\tilde{Y}'_{\Sigma,1}(k + nk_{d,1}) = \tilde{Y}'_{\Sigma,1}(k). \tag{2.82}$$

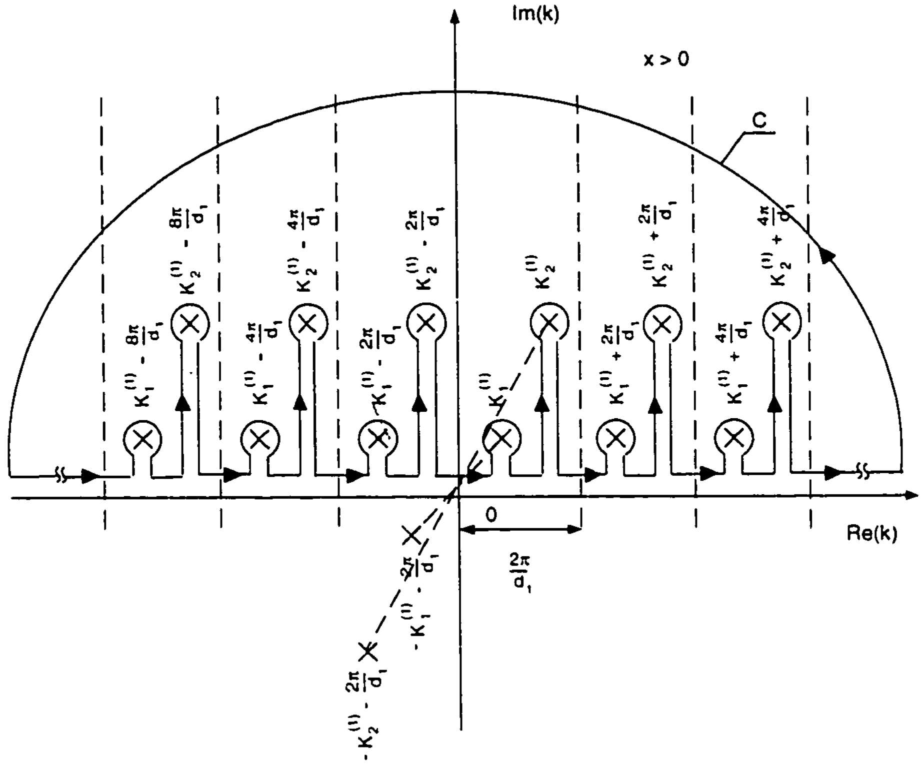

Figure 2.3: Pictorial representation of the roots of the dispersion relation for a plate with one array of attachments.

(2.80) is written as

$$v^{(1)}(x) = W_1^{*(1)}(x)e^{ik_1^{(1)}|x|} + W_2^{*(1)}(x)e^{ik_2^{(1)}|x|} \tag{2.83}$$

where $W_{1,2}^{*(1)}(x)$ are periodic functions with period d_1 and are given by

$$W_q^{*(1)}(x) = \frac{i}{Z_1 \tilde{Y}_{\Sigma,1}^{*\prime}(k_q^{(1)})} \sum_{n=-\infty}^{\infty} \tilde{Y}^{*}(k_q^{(1)} + nk_{d,1})e^{ink_1|x|}, \text{ where } q = 1, 2. \tag{2.84}$$

The superscript (1) in (2.84) means that the corresponding quantities are related to the problem where only the first array ($p = 1$) is attached to the plate.

When $x = 0$, one has

$$W_q^{(1)}(0) = \frac{id_1\tilde{Y}_{\Sigma,1}(k_q^{(1)})}{Z_1\tilde{Y}'_{\Sigma,1}(k_q^{(1)})}, \text{ where } q = 1, 2 \tag{2.85}$$

Using the Poisson summation formula in (2.18) and $\tilde{g}_2(u) = \tilde{Y}_2(k+u)$ gives

$$\tilde{Y}_{\Sigma,2}(k) = \sum_{n=-\infty}^{\infty} v^{(1)}(nd_2)e^{-ind_2k} \tag{2.86}$$

Combining (2.83) and (2.86) and observing that

$$W_q^{(1)}(nd_2) = W_q^{(1)}(nn_2d_1) = W_q^{(1)}(0); \quad q = 1, 2, \text{ where } n_2 = \frac{d_2}{d_1} \tag{2.87}$$

leads to

$$\tilde{Y}_{\Sigma,2}(k) = W_1^{(1)}(0)\sum_{n=-\infty}^{\infty} e^{-ind_2k}e^{ik_1^{(1)}|nd_2|} + W_2^{(1)}(0)\sum_{n=-\infty}^{\infty} e^{-ind_2k}e^{ik_2^{(1)}|nd_2|}, \tag{2.88}$$

with the constants $W_{1,2}^{(1)}(0)$ given in (2.85). This is the desired expression for $\tilde{Y}_{\Sigma,2}(k)$.

To obtain a closed form expression for $\tilde{Y}_{\Sigma,2}$, the infinite sum in (2.88) must be evaluated. Following the procedure of Equation 2.60 – 2.64 yields

$$\tilde{Y}_{\Sigma,2}(k) = A_2\frac{\sin(k_1^{(1)}d_2)}{\cos(k_1^{(1)}d_2) - \cos(kd_2)} + B_2\frac{\sin(k_2^{(1)}d_2)}{\cos(k_2^{(1)}d_2) - \cos(kd_2)}, \tag{2.89}$$

where

$$A_2 = \frac{d_1\tilde{Y}_{\Sigma,1}(k_1^{(1)})}{Z_1\tilde{Y}'_{\Sigma,1}(k_1^{(1)})} \qquad B_2 = \frac{d_1\tilde{Y}_{\Sigma,1}(k_2^{(1)})}{Z_1\tilde{Y}'_{\Sigma,1}(k_2^{(1)})}. \tag{2.90}$$

Equations (2.89) and (2.90), when compared with (2.65) and (2.66), have a structure that allows generalization to any $\tilde{Y}_{\Sigma,p}$, for $p = 1, 2, \ldots, P$, by induction. Specifically, the results for the pth array are related to those of the $(p-1)$th array. Referring to

(2.65) and (2.89), the summed admittance is written as

$$\tilde{Y}_{\Sigma,p}(k) = A_p \frac{\sin(k_1^{(p-1)} d_p)}{\cos(k_1^{(p-1)} d_p) - \cos(kd_p)} + B_p \frac{\sin(k_2^{(p-1)} d_p)}{\cos(k_2^{(p-1)} d_p) - \cos(kd_p)}, \text{ where } p = 2, \ldots, P \tag{2.91}$$

with the constants A_p and B_p found by induction of (2.90),

$$A_p = \begin{cases} \dfrac{k_f^2}{4im\omega\lambda_1} & \text{if } p = 1 \\ \dfrac{d_{p-1}\tilde{Y}_{\Sigma,p-1}(k_1^{(p-1)})}{Z_{p-1}\tilde{Y}'_{\Sigma,p-1}(k_1^{(p-1)})} & \text{if } p = 2, \ldots, P \end{cases} \tag{2.92}$$

$$B_p = \begin{cases} -\dfrac{k_f^2}{4im\omega\lambda_2} & \text{if } p = 1 \\ \dfrac{d_{p-1}\tilde{Y}_{\Sigma,p-1}(k_2^{(p-1)})}{Z_{p-1}\tilde{Y}'_{\Sigma,p-1}(k_2^{(p-1)})} & \text{if } p = 2, \ldots, P \end{cases} \tag{2.93}$$

The $k_{1,2}^{p-1}$ are the two Floquet wavenumbers of the plate with the first $p-1$ arrays attached. They lie in the fundamental zone $\Re(k) > (2\pi/d_p)$ and $\Im(k) \geq 0$ and they are simple poles of the dispersion equation, where

$$\tilde{Q}(k) = [1 + Z_1\tilde{Y}_{\Sigma,1}(k)][1 + Z_2\tilde{Y}_{\Sigma,2}(k)]\ldots[1 + Z_p\tilde{Y}_{\Sigma,p}(k)] \tag{2.94}$$

To justify the above, we refer to (2.72)-(2.78). The generalization of (2.72) is given by

$$1 + Z_p\tilde{Y}_{\Sigma,p}(k) = 0 \tag{2.95}$$

2.5 General recursive dispersion relations

The zeros of (2.95) are the roots of the following quadratic equation with respect to $\cos(kd_p)$ (compare to (2.72) - (2.78)):

$$\cos^2(kd_p) + a_p\cos(kd_p) + b_p = 0. \tag{2.96}$$

The values of k that satisfy this equation are the Floquet wavenumbers of the waves that propagate in the structure with p arrays. The coefficients a_p and b_p, which are obtained using the closed form expression for $\tilde{Y}_{\Sigma,p}$ from the previous step, are given by

$$a_p = -\cos(k_1^{(p-1)}d_p) - \cos(k_2^{(p-1)}d_p) - Z_pA_p\sin(k_1^{(p-1)}d_p) - Z_pB_p\sin(k_2^{(p-1)}d_p). \tag{2.97}$$

$$\begin{aligned} b_p = \cos(k_1^{(p-1)}d_p)\cos(k_2^{(p-1)}d_p) + Z_pA_p\sin(k_1^{(p-1)}d_p)\cos(k_2^{(p-1)}d_p) + \\ Z_pB_p\sin(k_2^{(p-1)}d_p)\cos(k_1^{(p-1)}d_p). \end{aligned} \tag{2.98}$$

Then, from (2.91) and (2.96),

$$1 + Z_p\tilde{Y}_{\Sigma,p}(k) = \frac{[\cos(kd_p) - \cos(k_1^{(p)}d_p)][\cos(kd_p) - \cos(k_2^{(p)}d_p)]}{[\cos(kd_p) - \cos(k_1^{(p-1)}d_p)][\cos(kd_p) - \cos(k_2^{(p-1)}d_p)]} \tag{2.99}$$

Using (2.99) recursively for $p = 1, 2, \ldots P$, $\tilde{Q}$ will acquire the form

$$\tilde{Q}(k) = \frac{[\cos(kd_p) - \cos(k_1^{(p)}d_p)][\cos(kd_p) - \cos(k_2^{(p)}d_p)]}{[\cos(kd_1) - \cos(\lambda_1d_1)][\cos(kd_1) - \cos(\lambda_2d_1)]}, \tag{2.100}$$

which is useful for inversion to the spatial domain.

2.5.1 Inversion of the response to the spatial domain

Using the closed-form expressions in (2.100) with $p = P$, the dispersion function $\tilde{Q}(k)$ is

$$\tilde{Q}(k) = \frac{\Phi(k)}{\Psi(k)}, \tag{2.101}$$

where $\Phi(k)$ and $\Psi(k)$ are

$$\Phi(k) = [\cos(kd_P) - \cos(k_1^{(P)}d_P)][\cos(kd_P) - \cos(k_2^{(P)}d_P)] \tag{2.102}$$

$$\Psi(k) = [\cos(kd_1) - \cos(\lambda_1 d_1][\cos(kd_1) - \cos(\lambda_2 d_1)]. \tag{2.103}$$

Here, $k_{1,2}^{(P)}$ are the Floquet wavenumbers of the plate with all P arrays attached and they are computed using (2.96) with $p = P$. Since the quadratic equation in (2.96) has recursive coefficients, then in order to obtain the Floquet wavenumbers of the P-array problem, we have to compute first the wavenumbers $k_{1,2}^{(1)}$, then $k_{1,2}^{(2)}$ and so on until $k_{1,2}^{(P)}$. In this way, we adjust the wavenumbers as each array is added to the structure.

To evaluate the spatial velocity $v(x)$ by Fourier inversion (see 2.12), the residue theorem is applied to the wavenumber velocity of the P-array problem whose velocity in the wavenumber domain is

$$\tilde{v}(k) = \frac{\tilde{Y}(k)}{\tilde{Q}(k)}. \tag{2.104}$$

The deformed integration contour is shown in Figure 2.4.

Using Jordan's lemma, recalling that all poles are simple, and taking into account the physical symmetry in the x-coordinate gives

$$v(x) = \sum_{r=1}^{2}\sum_{n=-\infty}^{\infty} i\frac{\Psi(k_r^{(P)} + nk_{d,P})\tilde{Y}(k_r^{(P)} + nk_{d,P})}{\Phi'(k_r^{(P)} + nk_{d,P})}\exp[(k_r^{(P)} + nk_{d,P})|x|]. \tag{2.105}$$

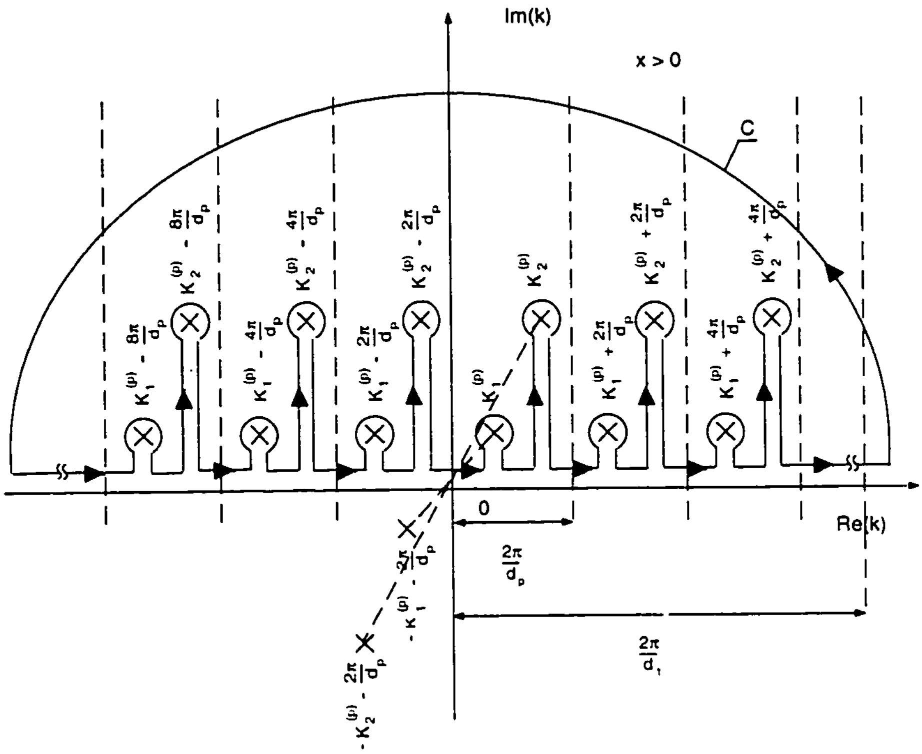

Figure 2.4: Pictorial representation of the roots of the dispersion relation for a plate with P arrays of attachments.

where $\Phi'(k) \equiv d\Phi/dk$. Since

$$\Phi'(k + \frac{2\pi n)}{d_P}) = \Phi'(k). \tag{2.106}$$

the spatial velocity of the above multiple array problem can be cast in the following form:

$$v(x) = W_1(x)e^{ik_1^{(P)}|x|} + W_2(x)e^{ik_2^{(P)}|x|} \tag{2.107}$$

with the newly defined quantities

$$W_q(x) = \frac{i}{\Phi'(k_q^{(P)})} \sum_{n=-\infty}^{\infty} \Psi\left(k_q^{(P)} + nk_{d,P}\right) \tilde{Y}\left(k_q^{(P)} + nk_{d,P}\right) e^{ink_{d,P}|x|}, \text{ where } q = 1, 2. \tag{2.108}$$

We observe that $W_q(x)$ is periodic with the largest array spacing d_P. Thus, each of the two terms in (2.107) satisfies the Floquet theorem cited in the introduction. For comparison to the eigenvalue analysis method, note that the propagation constants are related to the Floquet wavenumbers by

$$\mu_q = ik_q^{(P)} d_P, \text{ where } q = 1, 2. \tag{2.109}$$

Thus, $\Re(\mu_q)$ measure attenuation in the x direction along the plate.

A closed-form expression for the spatial velocity at the cell boundaries, defined as $x = nd_P$ where $n = 0, \pm 1, \pm 2, \ldots$, follows from (2.107),

$$v(nd_P) = W_1(0)e^{ik_1^{(P)}|n|d_P} + W_2(0)e^{ik_2^{(P)}|n|d_P}. \tag{2.110}$$

The expressions for the constant $W_{1,2}(0)$ are obtained following the procedure in (2.80)-(2.85), which yields

$$W_q(0) = \frac{id_P \tilde{Y}_{\Sigma,P}(k_q^{(P)})}{Z_P \tilde{Y}'_{\Sigma,P}(k_q^{(P)})}, \text{ where } q = 1, 2 \tag{2.111}$$

and $\tilde{Y}'_{\Sigma,P}(k) = d\tilde{Y}_{\Sigma,P}(k)/dk$.

The observation that the spatial velocity consists of two wave terms with two different propagation constants agrees with Mead's [12] observation that there are two propagation constants in piecewise periodic structures on flexible supports. Also, it can be shown that one of the propagation constants is purely negative real with magnitude increasing with frequency. Thus, one of the velocity terms represents a strongly decaying wave that becomes negligible at high frequencies. When the imaginary part of the wavenumber is small, the energy injected by the harmonic force passes freely through the structure with very little attenuation. Those frequency bands for which this is true are known as *pass bands.* Likewise, when the imaginary part of the wavenumber is large, energy is confined and the frequency lies in a *stopband*.

2.6 Example system — a three-array structure

In this section, the Floquet wavenumbers are evaluated for a three-array structure and compared to finite element predictions computed using Mead's equations [12]. For ease of finite element computations, a beam was modeled instead of a plate. The results derived above are applicable to a beam by replacing the bending rigidity D by $EI/(\rho A)$, replacing the line impedances with point impedances, replacing line forces by point forces, and replacing m by ρA. Recalling Figure 2.1, the attachments in all arrays were taken as point masses, with each mass equal to the mass of the beam contained within a length d_1. The parameters of the beam were $E = 2 \times 10^{11}$ Pa, $\rho = 7800$ kg/m^3, $\nu = 0.3$, and $\eta = 0.01$. The beam had a square cross section with thickness $h = 0.01$ m. As a test of the derived dispersion relations, several comparisons were made to numerical calculations based on Mead's equations. To evaluate these equations, a finite element model was developed for one periodic section of the beam. A representative comparison is shown for a three-array structure in Figure 2.5, which contains a plot of the imaginary part of the Floquet wavenumber of the propagating wave. Differences between the two dispersion curves, which were very small for the considered examples, were attributed to numerical implementations of the two approaches.

A plot of the imaginary parts of the Floquet wavenumbers for the propagating wave is given in Figure 2.6 for a structure with one, two, and three arrays attached to the beam. This ordering coincides with the sequential ordering of the dispersion given by (2.96)–(2.98). Large values of the imaginary part indicate high attenuation of a wave along the structure. The real parts of the propagating Floquet wavenumbers in Figure 2.7 demonstrate that, consistent with one-array structures, the real part of the wavenumber (i.e. the spatial frequency) varies little within the stop bands.

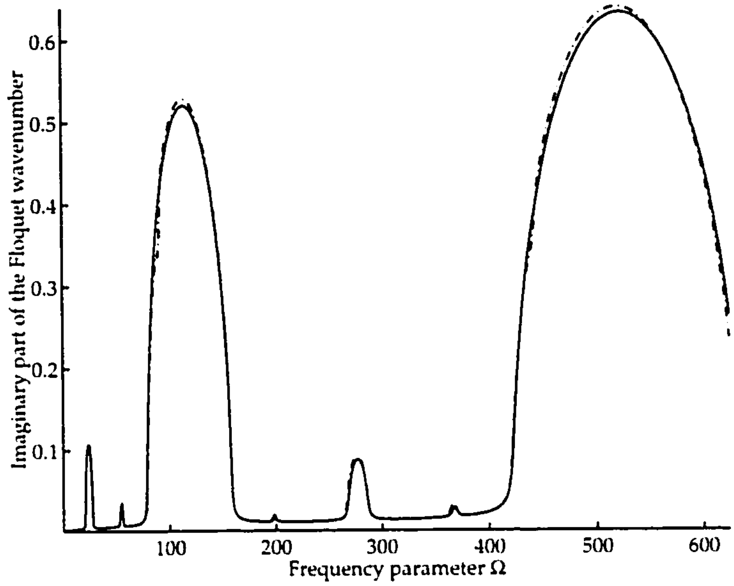

Figure 2.5: Imaginary part of the propagating Floquet wavenumber, $\Im(k)$, versus normalized frequency, Ω, for a beam with three arrays of attachments. The array spacings (in meters) are $d_1 = 1$, $d_2 = 2$, and $d_3 = 4$. Computed from (2.73) - - -; Computed by Mead's equations and a finite element model —.

The addition of each array alters the dispersion of the wave in a complex way. To see this, compare Figure 2.6 with the Floquet wavenumbers of the three corresponding one-array structures plotted in Figure 2.8. From these figures, it is clear that the stop and pass band features of the individual arrays are not linear (that is, additive).

For example, note that the large stop band above $\Omega = 400$ in Figure 2.6 is very similar to that of the one-array structure with spacing $d = 1$m shown in Figure 2.8. For this stop band, the addition of the other arrays has not significantly changed the attenuation. However, the addition of the other arrays produces smaller stop bands that are visible in Figure 2.6 near $\Omega = 275$. These stop bands may not be predicted from the corresponding one-array structures in Figure 2.8.

In order to understand the effects of stop and pass bands on the velocity at the drive-point ($x = 0$), Figure 2.9 shows the contribution of the propagating wave to the

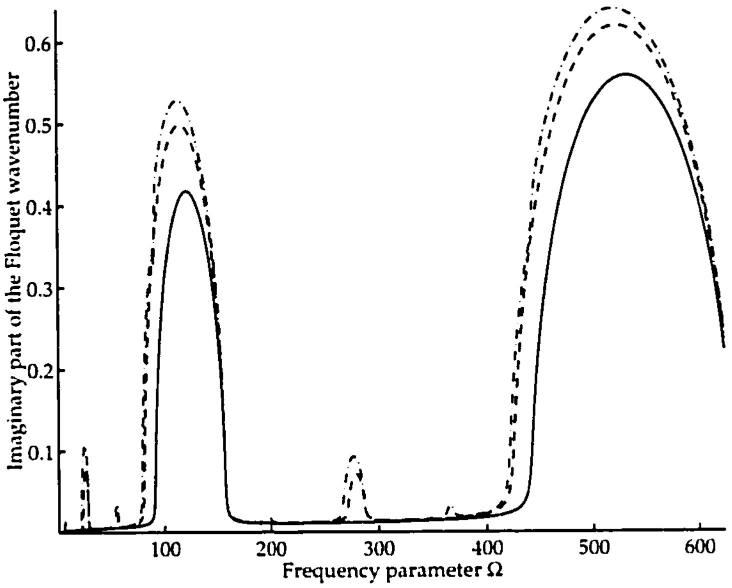

Figure 2.6: Imaginary part of the propagating Floquet wavenumber, $\Im(k)$, versus normalized frequency, Ω, for a beam with one, two, and three arrays of attachments. The array spacings for the three cases (in meters) are $d_1 = 1$; $d_1 = 1$ and $d_2 = 2$; $d_1 = 1$, $d_2 = 2$, and $d_3 = 4$. One array —; Two arrays - - -; Three arrays - · -.

velocity magnitude for the structures indicated in Figure 2.8. The velocity maxima occur as the Floquet wavenumber passes through cutoff from a pass band to a stop band, approaching infinity with the decrease of the loss factor. The minima occur as one moves from a stop band to a pass band with the velocity magnitude approaching zero with the decrease of the loss factor.

Figure 2.10 depicts the velocity due to the propagating and evanescent waves at two positions away from the drive-point. As anticipated, strong attenuation in the stop bands and weak attenuation in the pass bands correlates with the magnitude of the imaginary part of the propagating Floquet wavenumbers plotted in Figure 2.8.

Further, the frequencies at which the structure exhibits resonance-like behavior shall be referred to *"resonance"* frequencies and those for which the response exhibits minima shall be denoted as *"antiresonance"* frequencies. For a single array problem

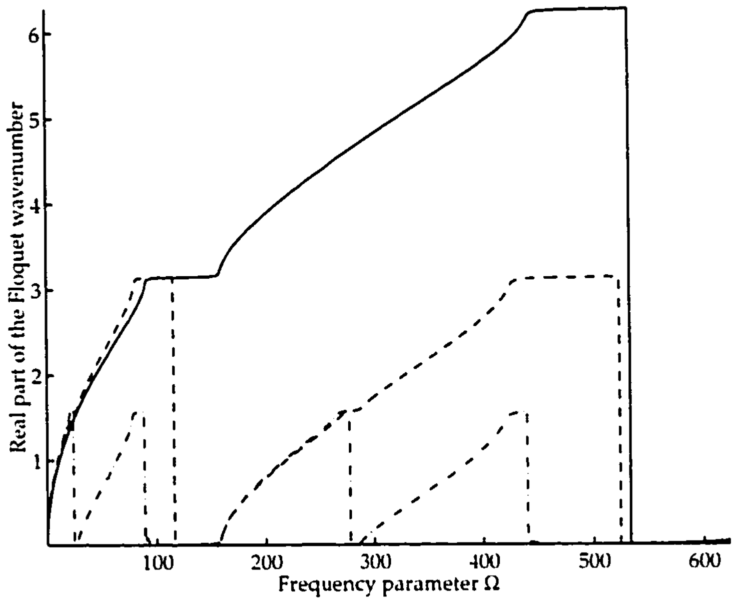

Figure 2.7: Real part of the propagating Floquet wavenumber $\Re(k)$ versus normalized frequency Ω for a beam with one, two, and three arrays of attachments. The array spacings for the three cases (in meters) are $d_1 = 1$; $d_1 = 1$ and $d_2 = 2$; $d_1 = 1$, $d_2 = 2$, and $d_3 = 4$. One array —; Two arrays - - -; Three arrays - · -.

it can be shown that the minima are determined by

$$\sin(k_f d) = 0 \tag{2.112}$$

and the maxima are roots of the equation

$$\sin(k_1 d) = 0 \tag{2.113}$$

where k_1 denotes the propagating Floquet wavenumber, k_f is the flexural wavenumber and d is the array spacing. A discussion about the "resonance" and "antiresonance" frequencies of infinite periodic structures is given by Mead [14]. Note that unlike "antiresonance", the "resonance" frequencies depend on the array impedance in a complex way. Recalling the fact that the energy flow through a given point of the

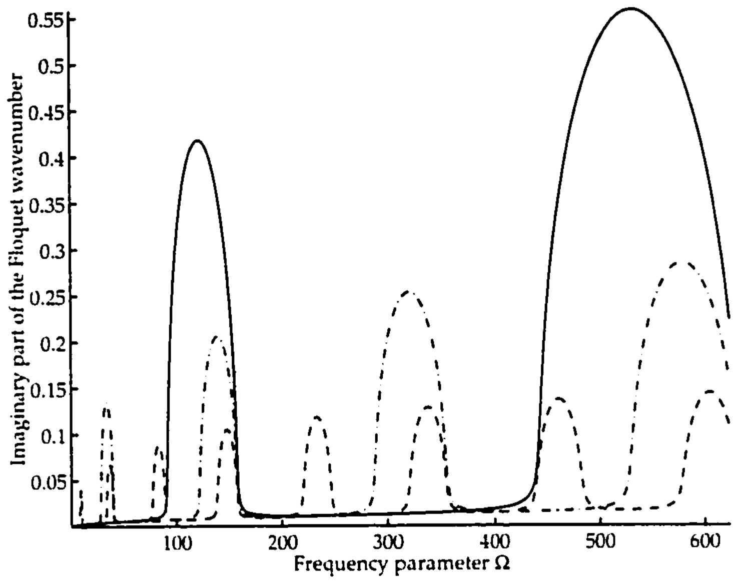

Figure 2.8: Imaginary part of the propagating Floquet wavenumber, $\Im(k)$, versus normalized frequency, Ω, for a beam with one array of attachments. Three array spacings are shown corresponding to $d_1 = 1$, 2, and 4 meters. $d = 1$m —; $d = 2$m - · -; $d = 4$m - - -.

structure is proportional to the real part of the velocity at this point, it can be demonstrated that the energy flow exhibits a peak at the "resonance" frequency and after that it plunges into a steep minimum extending through the stop band.

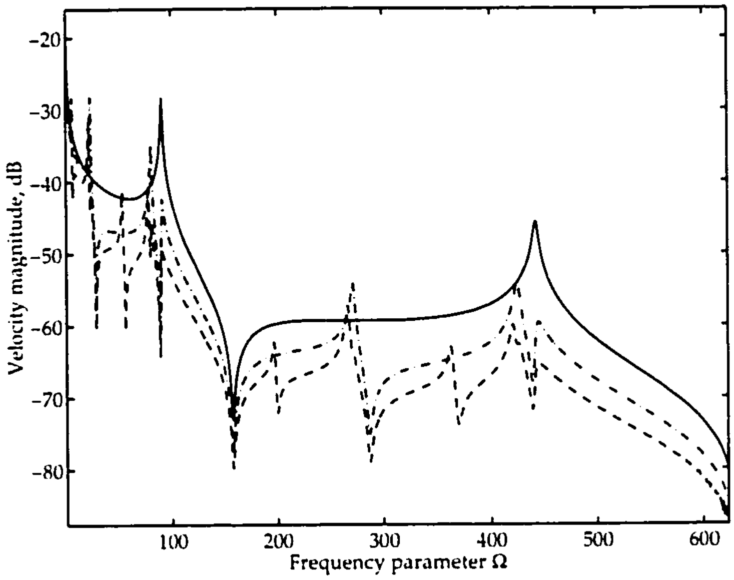

Figure 2.9: Drive-point velocity magnitude due to the propagating wave versus normalized frequency, Ω, for a beam with one, two, and three arrays of attachments. The array spacings for the three cases (in meters) are $d_1 = 1$; $d_1 = 1$ and $d_2 = 2$; $d_1 = 1$, $d_2 = 2$, and $d_3 = 4$. One array —; Two arrays - · -; Three arrays - - -.

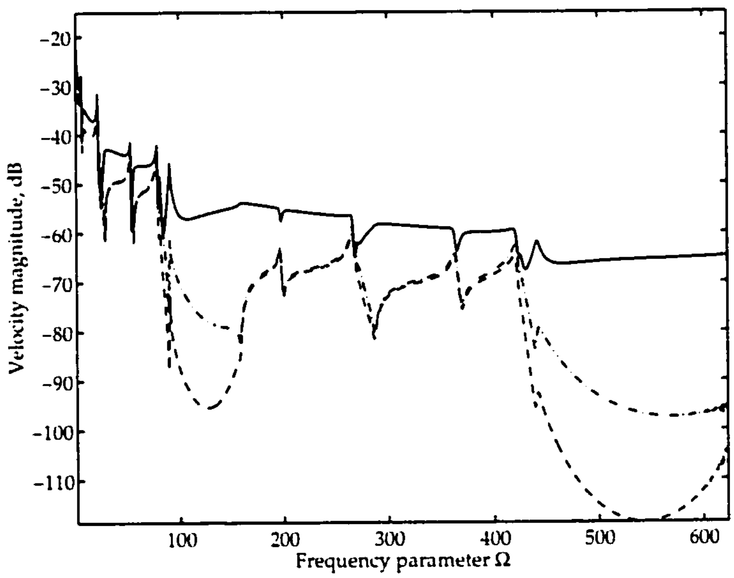

Figure 2.10: Velocity magnitude due to the propagating and evanescent versus normalized frequency, Ω, for a beam with three arrays of attachments, evaluated at various positions in the structure. At origin —; At $x = 4$m - · -; At $x = 8$m - - -.

2.7 Infinite elastic structures with offset arrays

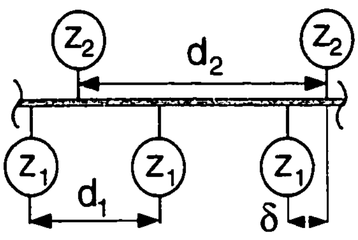

Figure 2.11: Periodic structure with two arrays with spacings ratio $d_1/d_2 = 1/2$ and offset

In the analysis presented above, the arrays were assumed to be perfectly aligned. However structural attenuation depends on the offset between the attached arrays, defined as the smallest distance between two attachments belonging to different arrays. The offset, δ, is shown in Figure 2.11. Moreover, structures with offset arrays may be better vibroisolators than those with perfectly aligned arrays. Relevant questions are how the array offset influences the structural wave propagation and which periodic structure among a class of multiarray structures with given design parameters is the most efficient energy isolator. In [25], Cray discusses a string supported by offset arrays of attachments and provides an explicit solution for the response in the wavenumber domain for the case of two offset arrays. In [23] the same author studied acoustic radiation from infinite plate with two array of attachments. These works have illustrated the complex ways in which sets of offset arrays interact with each other and the master structure. Consider the same multiarray problem but now the arrays can be offset with respect to each other as it is shown in Figure 2.11

Design parameters could be array spacing, offset or total amount of mass per unit length of the structure and many design problems constrain these parameters. Assuming that the design goal is to maximize attenuation another question which arises is how exactly the goal function should be defined. In this study, varying the array geometry and offset, the following different goal functions are minimized:

- average attenuation over a given frequency band:

- fraction of frequency band in which attenuation is higher than 3 dB (interval criterion).

Three example structures with two attached arrays are studied with spacing ratios 1/1, 1/4, and 2/3. All three structures are chosen to have the same amount of mass per unit length and array attachments, modeled as pure masses. The normalized offset is varied over given frequency band.

The attenuation is computed by evaluating the dispersion relation of the structure which is cast in determinant form following Mead's approach.

$$|A(\omega,\delta)\mu^2 + B(\omega,\delta)\mu + C(\omega,\delta)| = 0 \tag{2.114}$$

where ω is the excitation frequency, δ is the array offset, and μ is the structural propagation constant defined in (2.109). For bicoupled problems A, B, and C are 2×2 matrices such that $C = A^T$. In order to avoid numerical instability that arises in analytic beam models, A, B, and C are obtained by the finite element method using Euler-Bernoulli beam elements. For details on the derivation of the dispersion relation and the formulation of the Euler-Bernoulli element see Appendices A and B.

Figure 2.12 shows attenuation of a two-array structure with offset. The arrays have equal spacings. The horizontal coordinate is the offset between arrays and the vertical coordinate is the normalized frequency. Bright spots represent regions with high attenuation. Each vertical line represents the attenuation of a two array structure with a particular geometry in the given frequency range. Thus one can directly compare two-array structures with different offsets and judge which is the best vibroisolating structure: It will be that offset which crosses as many bright regions as possible.

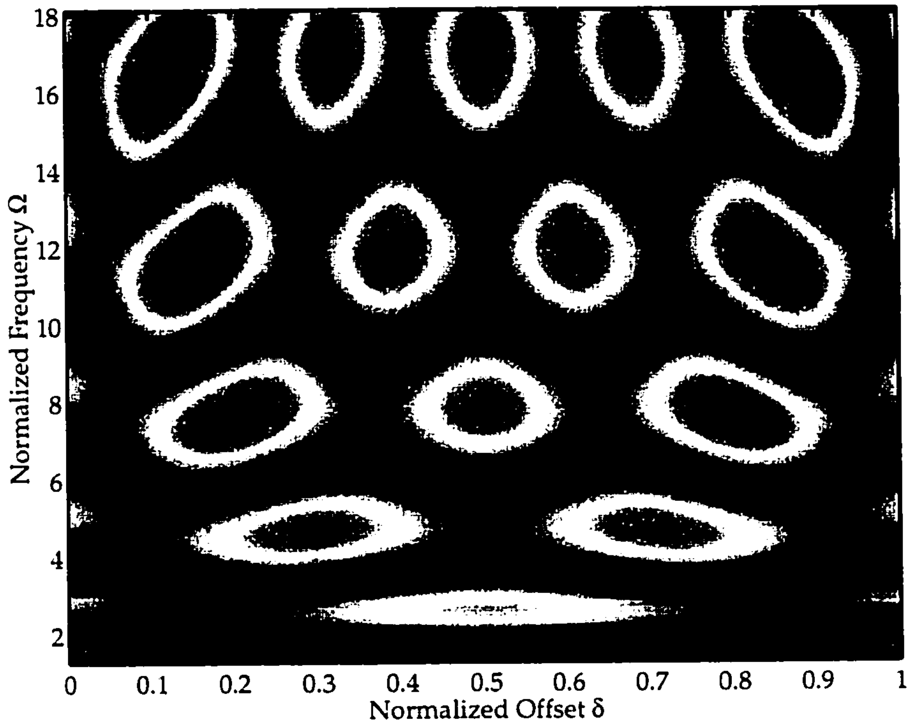

Figure 2.12: Attenuation of offset two-array structure. The bright spots represent regions of high attenuation and the dark spots correspond to areas of low attenuation

The interval criterion is defined as the ratio of the number of frequencies I_μ for which the attenuation is larger than μ dB over the total number of considered frequencies I_{tot}

$$L_\mu(\delta) = \frac{I_\mu(\delta)}{I_{tot}}. \tag{2.115}$$

The average attenuation criterion is defined as

$$\mu_{av} = \frac{\sum_{k=1}^{N} \mu_k}{N}. \tag{2.116}$$

where N is the number of discrete frequencies in the considered range.

The results in Figures 2.13 and 2.14 show that the structure which is the most efficient vibroisolator depends on the goal function. For instance, in Figure 2.13 the interval criterion is plotted for three structures with spacings ratios 1/1, 2/3, and 1/4. The plot shows that the best vibroisolating structure over the given normalized frequency range $0 < \Omega < 20$ will be that with equal array spacings and normalized offset between the arrays equal to 0.2 (see Figure 2.15). Analogously with the average attenuation criterion the best performance is achieved by structure with spacing ratio 1/4 and offset 0.5.

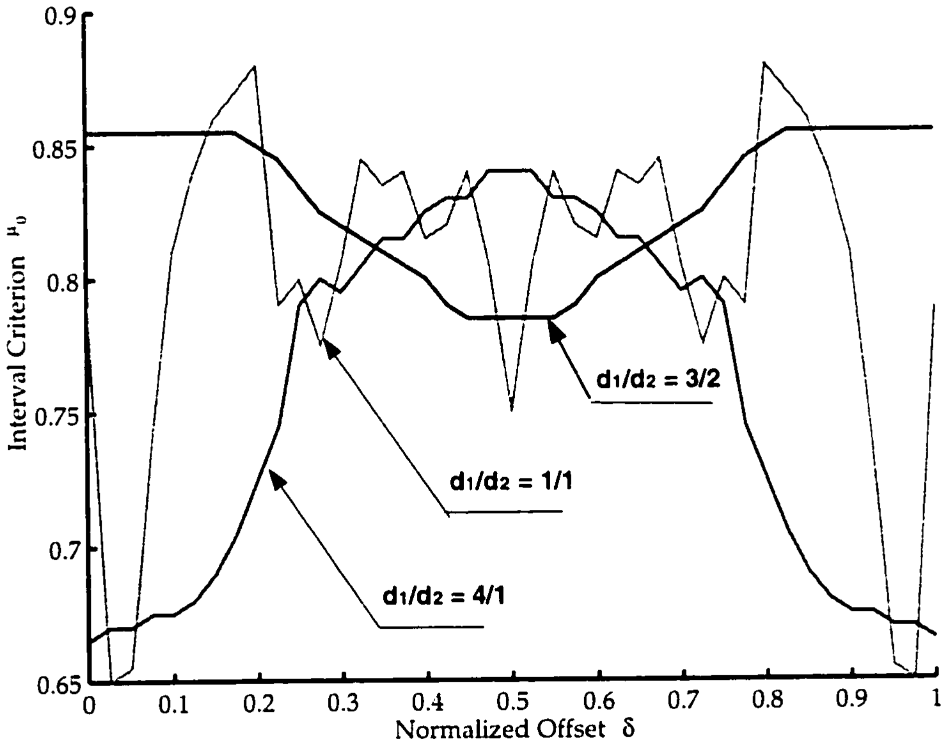

Figure 2.13: Interval criterion for two-array structures

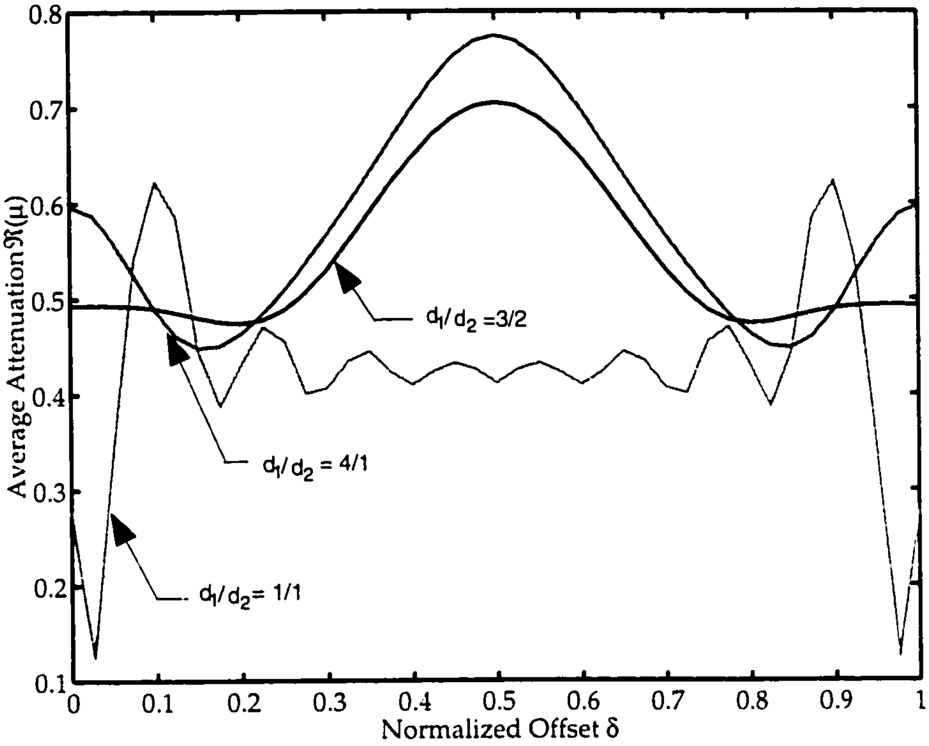

Figure 2.14: Average attenuation criterion for two-array structures

a) According to average attenuation criterion

b) According to interval criterion

Figure 2.15: Performance of best vibroisolating structure

2.8 Chapter summary

In contrast to prior work that considered only one- and two-array structures, a general analytical solution is presented for the wavenumber and spatial velocities of a plate with an arbitrary number of attached arrays. While prior analyses of two-array structures resulted in algebraically complex expressions, one appealing feature of the results presented in this chapter is their simplicity. In particular, the Floquet wavenumbers are obtained by analyzing the bare plate first, and then treating the attachment of each array in turn according to their relative spacing. As each array is added to the structure, a quadratic equation is solved for the Floquet wavenumbers.

Another appealing feature of the analysis is its easy extensibility to other geometries and loadings. For example, the analysis could be extended to thin cylindrical shells with arrays of ring attachments by expanding the shell velocities in Fourier series about the circumference of the shell. The Fourier harmonic number would then assume the role of the plate wavenumber k_y in the analysis presented here. The essential steps in the analysis would be repeated and the Floquet wavenumbers $k_p^{(1,2)}$ would describe propagation down the axis of the shell. Similarly, extensions to attachments that apply forces and moments in more than one direction would magnify the algebra but would otherwise be straightforward.

An example was presented in which the best vibroisolating structure among the class of two arrays structures is selected. For this purpose a finite element model was utilized and different cost functions were evaluated, varying the array geometry and offset. It was shown that the wave propagation depends dramatically on the offset and even small changes may lead to significant variations in attenuation.

Chapter 3

Application of dispersion analysis to the design of high Q MEMS resonators

Vibrational design of structures focuses on the tendency of a structure to either localize, transmit, reject or absorb energy. While in some applications perfect transmission is desirable, in many engineering problems energy localization is sought. This chapter demonstrates that the theory developed in Chapter 2 can be used for this purpose. As an example, consider the problem of designing a MEMS resonator for use as a high Q filter. Given limited material choices, the effective damping of the structure is largely determined by its geometry (assuming that the device is operated in vacuum). In this case the device must allow sufficient energy injection into the structure (usually by electrostatics) while simultaneously minimizing energy loss through the structure's supports.

For many applications in the communications area, stable oscillating signals used for frequency synchronization and sampling are needed. The most important parameter influencing frequency stability is the Q factor of the resonating microdevice. At present, the existing technology still relies on off-chip dielectric resonators and discrete elements, providing the necessary high-Q parameters [31]. Since these resonators interface with the integrated electronics on board level, they consume a sizeable portion of the system area. The newest trend, allowing further miniaturization and portability in this kind of technology, is to create high Q resonating microdevices which can be integrated at the chip level. The working frequencies of such devices often lie in the gigahertz range. A thorough discussion on the topic is provided in Nguyen [31].

The idea of designing microelectromechanical resonating devices with high Q factors through the attachment of vibrating substructures is not new (see for instance, Tang [29]). On the basis of lumped-parameter mechanical circuits, band-pass filters with Q factors over 80,000 in vacuum have been designed (Nguyen [32]).

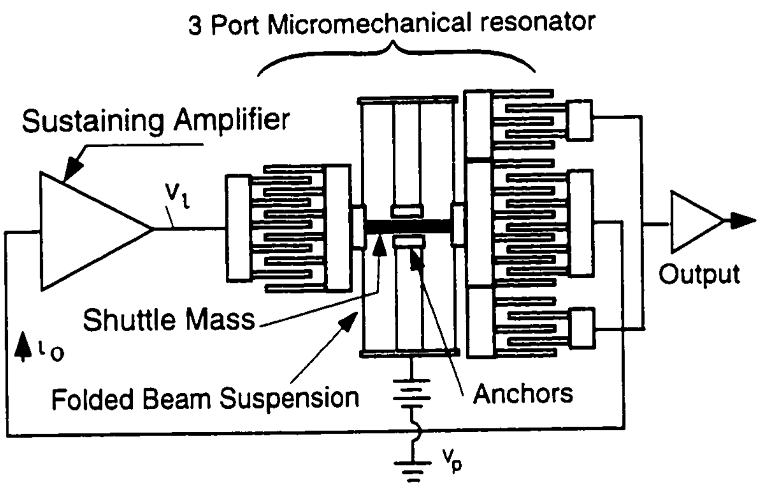

Figure 3.1: Schematic of a microresonator with comb transducers and folded beams.

Figure 3.1 depicts an existing design of a micromechanical resonator, fully integrated with sustaining CMOS electronics. This design, which is widespread among MEMS community [33], achieves a Q factor of 40,000 in a vacuum under pressures less than about 50 mtorr. In order to increase the frequency stability against supply voltage variations, a micromechanical resonator is utilized by a comb transducer and a folded beam as an elastic element. The microresonator consists of a shuttle mass suspended 2 μm above the substrate by folded elastic beams which are anchored in the center. The shuttle mass is free to move in the longitudinal direction, parallel to the plane of silicon layer where the resonance frequency of this single degree of freedom resonator is determined by the material properties and the beam geometry. Excitation of the microresonator is achieved by supplied *dc* voltage V_P and *ac* excitation v_i applied across one of the comb capacitors. This creates a force component between the electrode and resonator proportional to the product $V_p v_i$ and at the frequency of v_i. The vibration of the elastic element creates a time-varying capacitor $C_0(x, t)$ generating current

$$i_0 = V_P \frac{\partial C_0}{\partial x} \frac{\partial x}{\partial t} \tag{3.1}$$

on the output transducer.

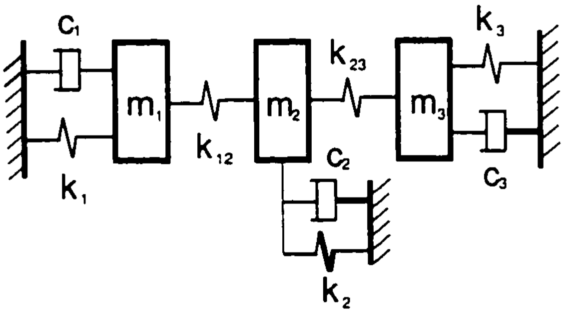

Figure 3.2: Equivalent lumped parameter model for a mechanical filter with high Q factor

For improvement of the frequency characteristics of micromechanical filters and for creating a flat high-Q band, coupled microresonators are used. Each one consist of three comb-transduced oscillators, connected by coupling beams as shown in Figure 3.2 (see Wang [33]). If the microresonator is required to operate at a higher frequency, elastic elements with smaller masses are needed and as a result folded-beam resonators used in the filter in Figure 3.1 are not applicable. Currently, high frequency microresonators are designed on the basis of clamped-clamped beam microelements as shown in Figure 3.3.

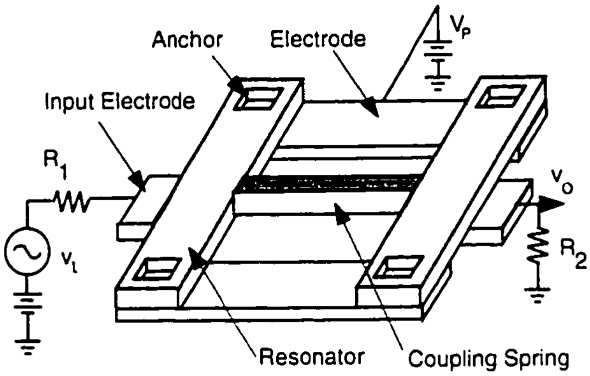

Figure 3.3: Schematic of microresonator, consisting of two coupled beams

Two beams with clamped ends are coupled mechanically by a soft spring, all suspended 0.1-0.2 μm above the substrate. Conductive polysilicon strips are placed below the central regions of each beam and serve as capacitive transducer electrodes, inducing vibrations in a direction perpendicular to the substrate. The device is excited capacitively by a signal voltage applied to the input electrode. The output is taken at the other end of the structure also via capacitive transduction. For a properly designed mechanical filter, if the frequency is inside the filter working frequency range maximal vibrations on both beams should be achieved. Here the working frequency range denotes the interval where the optimal performance and highest Q factor is achieved. In this literature, instead of *working frequency range* the term *passband* is used. In our discussion, we will not use the former to avoid confusion with the pass band of the periodic structure.

In the new design approach, presented in this chapter, the vibrating element of high frequency microresonator is constructed as an elastic beam with finite arrays of lumped or distributed masses, added at the ends, forming a nonuniform periodic structure. For modeling purposes, the structure is subject to general impedance boundary conditions at the ends. A finite element model for the computation of its frequency response is developed. Using this model, the velocity response of an example structure with 25-element arrays is computed and the presence of stop bands at the ends is investigated, limiting significantly the energy loss at the boundaries for any frequency inside the stop bands. For comparison, the velocity response of an uniform beam with equal total mass is obtained and it is determined that the energy flow at the boundaries is much higher at the stop band frequencies.

The periodic element is tuned such that it vibrates inside its stop band, thereby making the structural vibration independent of the imposed boundary conditions. As a consequence, the structural loss factor will approach the material loss factor inside the stop band. In the following sections, appropriate resonating frequency, element dimensions, and array spacings shall be selected such that the element can be fully integrated in the comb-transduced micromechanical resonator. Figure 3.4 depicts the

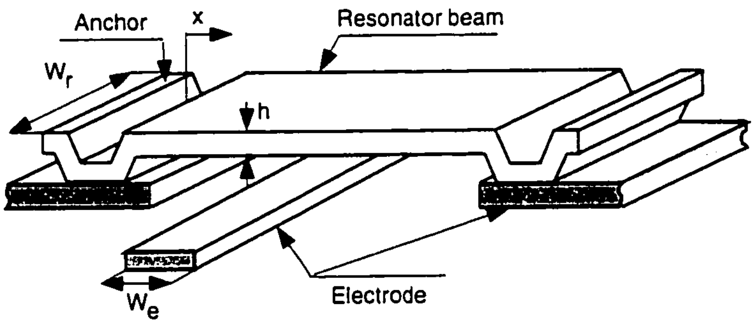

Figure 3.4: Beam microresonator with clamped ends

existing design of a high frequency resonator in which an elastic polysilicon beam with clamped ends is driven electrostatically. The model which shall be considered is shown on Figure 3.5.

3.1 Problem statement

In this section, the phenomenon of energy localization due to the presence of periodic structures at the resonator ends is discussed. For this purpose, a simplified one-dimensional FEM of the resonator is considered. On both sides of a uniform elastic beam two arrays of attachments are added, as shown in Figure 3.5, forming a periodic structure with a uniform smooth interior. The arrays are represented by their point impedances, where the attachments shall be modeled as pure masses having impedance

$$Z = -i\omega M, \tag{3.2}$$

with M denoting the attached mass.

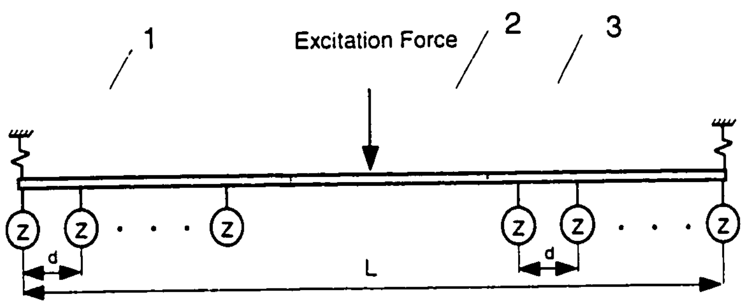

Figure 3.5: Proposed new design with high Q factor. 1 – isolating part; 2 - resonating part

The beam is subjected to general impedance boundary conditions at its ends. If the beam is harmonically excited, the wave propagation through it will be hindered at the ends if the excitation frequency lies in the stop band of the periodic structure. In terms of the loss factor, one shall be able to achieve a resonating structure with very small loss factor (i.e., high Q factor) since the energy cannot flow freely through the boundaries because of the attached constraints. To show this, the nonuniform periodic model will be compared with a uniform beam with equal total mass.

In Figure 3.6, the velocity magnitude at the end point is plotted for both the proposed nonuniform periodic design and the equivalent uniform resonator with equal mass. The nondimensional frequency, given by

$$\Omega = \omega d^2 \sqrt{\frac{EI}{m}}, \tag{3.3}$$

is varied inside the stop band of the periodic structure. Here, d is the array spacing, E is Young's modulus , I is inertial moment, and m is mass per unit length of the uniform beam. A steep decrease in the end point velocity magnitude of the periodic model is observed if the excitation frequency is within the stop band, confirming the energy localization inside the structure.

In Figure 3.7, the velocity magnitude at the drive point of the two structures is shown. Observe that several resonance frequencies are present inside the stop band. The structure will be designed to resonate in any of these frequencies, thereby achieving high Q factor.

In the remainder of this chapter, the connection between the energy localization phenomenon and the structural Q factor will be formalized and an explicit expression for the structural loss factor will be sought. A high-fidelity 2D FE model of the resonator will be developed and an efficient design rendering a high Q factor will be selected. The design parameters (resonating frequency, array spacing, rib's mass) are chosen such that the new design can operate in a selected resonance frequency and can be fully integrated at the chip level.

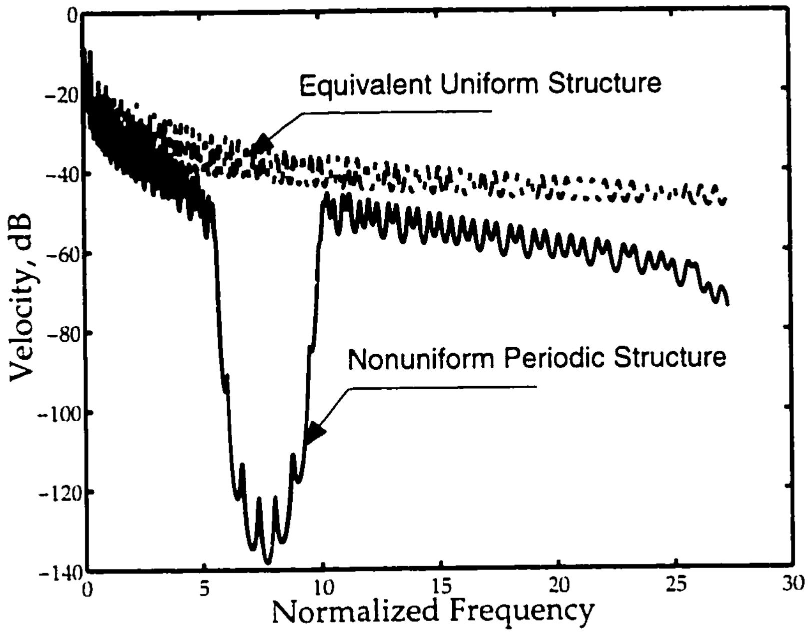

Figure 3.6: Comparison between the end point velocity magnitudes in dB of the periodic nonuniform structure and equivalent uniform beam

3.2 Energy relations in a vibrating elastic structure

The nodal force vector in the system is given through the global impedance matrix and nodal velocity

$$\{f\} = [Z_{st}]\{v\} \tag{3.4}$$

Here, the impedance matrix is rewritten as a combination of real and imaginary parts

$$[Z_{st}] = [R] + i[X] \tag{3.5}$$

The real part of the impedance matrix is used to compute the dissipated power

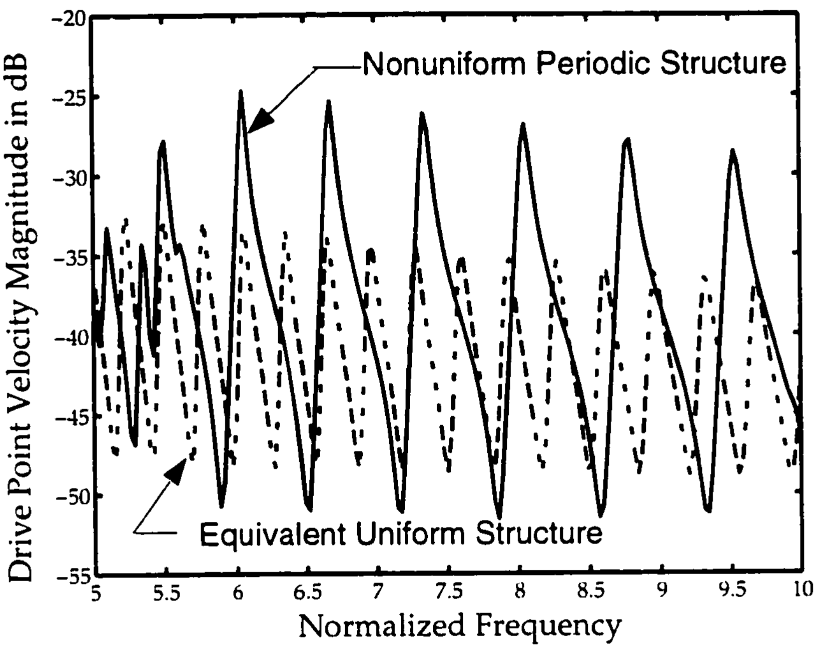

Figure 3.7: Comparison between the drive point velocity magnitudes in dB of the periodic nonuniform structure and equivalent uniform beam inside the periodic structure stop band

per cycle.

$$\Phi = \frac{1}{2}\{v\}^{*}[R]\{v\} \tag{3.6}$$

Here $\{v\}$ denotes the complex amplitudes of velocity, composed of the nodal variables corresponding to the structural DOF. $\{v\}^{*}$ denotes the Hermitian transpose of $\{v\}$. The imaginary part of the impedance matrix can be expressed as

$$[X] = \frac{1}{\omega}[K] - \omega[M] \tag{3.7}$$

where $[K]$ and $[M]$ denote the global stiffness and mass matrices of the system. The average kinetic energy per cycle for the vibrating system is determined as

$$T = \frac{1}{4}\Re\{v\}^{*}[M]\{v\} \tag{3.8}$$

The potential energy per cycle stored in the system is expressed in terms of the global stiffness matrix (see [34], Chapter 4 for instance)

$$U = \frac{1}{4}\{w\}^{*}[K]\{w\} - \{w\}^{*}f \tag{3.9}$$

where $\{w\}$ is the global displacement vector given with $\{w\} = i\omega\{v\}$. The loss factor of a vibratory system is determined as the energy dissipated per cycle over the total vibratory energy stored in the system. Thus we obtain the following expression for the structural loss factor η.

$$\eta = \frac{\Phi}{\omega(T+U)} \tag{3.10}$$

The Q factor is related to the loss factor by

$$Q = \frac{1}{\eta} \tag{3.11}$$

The dissipated energy per cycle includes the total energy loss and can be written as a sum of the following three terms, denoting three different dissipative mechanisms (see [38])

$$\Phi = \Phi_a + \Phi_b + \Phi_i \tag{3.12}$$

The Φ_a denotes the viscous and acoustic dissipation. Φ_b corresponds to the boundary dissipation, and Φ_i is the internal dissipation inside the resonator. In our study, we assume that the structure vibrates in perfect vacuum, neglecting all viscous forces due to fluid coupling. Under this assumption, the internal dissipation of the polysilicon resonator is usually small compared to the boundary damping, so a decrease of the boundary dissipation Φ_b will lead to significant increase of the Q factor.

3.3 Simplified approach for designing high Q MEMS resonators

An important question which arises in this chapter is how one can choose reasonable design parameters before using a computationally expensive high-fidelity model. We shall use the analysis from Chapter 2 to answer this question.

Let us consider the following problem: a high-Q resonator with periodic design has to be constructed given a resonance frequency ω_r and stop band width Δ. The thickness t, height h, and the material properties (Young's modulus E, mass per unit length m, material loss factor η) of the resonator beam are also given (see Figure 3.8). The resonator shall be modeled with Euler-Bernoulli beam theory, under the assumption that the wavelengths are large compared to the beam thickness. The ribs are modeled as point attachments.

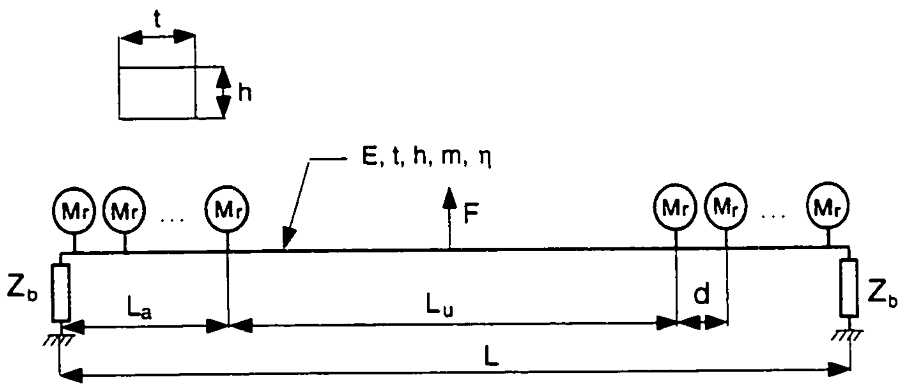

Figure 3.8: Dimensions of high Q resonator

The design parameters are assumed to be

- array spacing, d
- the mass of the rib, M_r
- the length of the uniform section, L_u
- the number of ribs on each side, N_r

In this section, a simplified procedure for determining the design parameters is described. It consists of the following three main steps :

1. Selecting the array spacing;
2. Selecting the length of the uniform section;
3. Selecting the number of ribs on each side.

3.3.1 Selecting the array spacing and the mass of the rib

The width of the stop band and the attenuation inside the stop band depends on the array spacing d and the rib's mass M_r. Given the resonance frequency ω_r one can place the maximum attenuation at ω_r and cover the desired stop band width by selecting appropriate values of d and M_r.

The frequency of maximum attenuation can be determined from the dispersion relation of the infinite beam with single array of attachments (see Equation (2.72)) which is

$$1 + Z\tilde{Y}_{\Sigma}(\mu) = 0. \tag{3.13}$$

Here, the summed wavenumber admittance $\tilde{Y}_{\Sigma}(\mu)$ is expressed in terms of the nondimensional parameter $\Omega = k_f d$ and the propagation constant μ

$$\tilde{Y}_{\Sigma}(\mu) = \frac{\Omega}{4Z_m}\left[\frac{\sin(\Omega)}{\cos(\Omega) - \cosh(\mu)} - \frac{\sinh(\Omega)}{\cosh(\Omega) - \cosh(\Omega)}\right]; \quad Z_m = -i\omega md \tag{3.14}$$

Using the approximation $\cosh(\Omega) \sim \sinh(\Omega) \sim \frac{e^{\Omega}}{2}$ simplifies Equation (3.14) to

$$\tilde{Y}_\Sigma(\mu) = \frac{\Omega}{4Z_m}\left[\frac{\sin(\Omega)}{\cos(\Omega) - \cosh(\mu)} - \frac{1}{1 - e^{-\Omega}\cosh(\mu)/2}\right] \tag{3.15}$$

Further, assuming that

$$1 \gg \frac{e^{-\Omega}\cosh(\mu)}{2} \tag{3.16}$$

leads to a simplified form of the dispersion relation (3.13)

$$\cosh(\mu) = \cos(\Omega) - \frac{\Omega\zeta}{4 + \Omega\zeta}\sin(\Omega) \quad \text{where} \quad \zeta = \frac{M_r}{md}. \tag{3.17}$$

Note that the contribution of the evanescent waves is eliminated in (3.17), which gives a reasonable approximation inside the first stop band.

The maximum attenuation inside the stop band is determined from the condition

$$\frac{d\mu}{d\Omega} = 0. \tag{3.18}$$

Differentiating (3.17) with respect to Ω and substituting the result in (3.18) gives the following transcendental equation:

$$\tan(\Omega) = g(\Omega) \;\; \text{where } g(\Omega) = -\frac{\Omega\zeta(4 + \Omega\zeta)}{(4 + \Omega\zeta)^2 + 4\zeta}. \tag{3.19}$$

From this we find the frequency where the attenuation reaches its maximum. Writing (3.19) as a polynomial with respect to ζ gives

$$c_2\zeta^2 + c_1\zeta + c_0 = 0 \tag{3.20}$$

where

$$c_2 = \Omega^2 \tan(\Omega) + \Omega^2$$

$$c_1 = 8\Omega \tan(\Omega) + 4\tan(\Omega) + 4\Omega$$

$$c_0 = 16\tan(\Omega) \tag{3.21}$$

The positive root of (3.20) is

$$\zeta = \frac{-c_1 + \sqrt{c_1^2 - 4c_2c_0}}{2c_2} \tag{3.22}$$

from which the normalized impedance ζ can be determined, given the nondimensional parameter Ω, corresponding to maximum attenuation.

One can show that the beginning and end of the stop band occurs when

$$\sinh(\mu) = 0, \tag{3.23}$$

Using (3.17), (3.23) can be transformed into the following system

$$\begin{cases} \sin(\Omega) = 0 \\ \tan(\Omega) = h(\Omega) \quad \text{where} \quad h(\Omega) = -\frac{\Omega\zeta(4+\Omega\zeta)}{4(2+\Omega\zeta)} \end{cases} \tag{3.24}$$

The first equation gives the stop band ends and the second one corresponds to the beginning of the stop band. Accordingly, the frequencies of the ends of the stop band are given by

$$\omega_e = \frac{n^2\pi^2}{d^2}\sqrt{\frac{EI}{m}}, \quad n = 1, 2, \ldots \tag{3.25}$$

where the index n denotes the stop band number.

Given the resonance frequency ω_r and stop band width Δ, the array spacing d

can be determined from

$$\omega_e = \omega_r + \frac{\Delta}{2}. \tag{3.26}$$

Assuming that the resonator oscillates in the first stop band we obtain

$$d = \frac{\pi(EI/m)^{1/4}}{\sqrt{\omega_r + \Delta/2}}. \tag{3.27}$$

The mass of the rib M_r is selected such that the frequency of maximal attenuation ω_{ma} coincides with the resonance frequency ω_r. For this purpose, (3.22) is utilized with $\Omega = \left(\frac{m\omega^2}{EI}\right)^{1/4} d$ to get

$$M_r = md\left[\frac{-c_1 + \sqrt{c_1^2 - 4c_2c_0}}{2c_2}\right]\Bigg|_{\omega=\omega_r} \tag{3.28}$$

3.3.2 Selecting the length of the uniform section

Once we have chosen the spacing d and rib mass M_r we need to select the length of the uniform section L_u. Inside the stop band the velocity decays very fast once it reaches the end of the uniform section. Therefore as a first order approximation the uniform section can be assumed clamped at its ends as shown on Figure 3.9

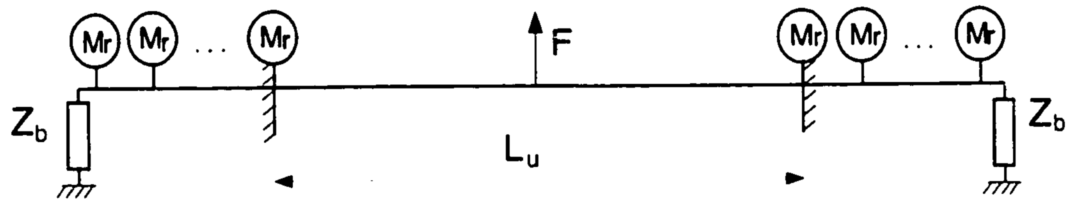

Figure 3.9: Clamping the ends of the uniform section

The resonances of the beam on clamped supports are given as

$$\omega_{cl} = \sqrt{\frac{EI}{m}\frac{\alpha_n{}^2}{L_u{}^2}} \tag{3.29}$$

where α_n is a positive root of the transcendental equation

$$\cos(\alpha)\cosh(\alpha) - 1 = 0 \tag{3.30}$$

The solution of (3.30) is given in tabular form in Table 3.1

n	α_n	$\alpha_n{}^2$
1	4.73004	22.3733
2	7.85320	61.6728
3	10.9956	120.903
4	14.1372	199.859
5	17.2788	298.556
$n > 5$	$\frac{(2n+1)}{2}\pi$	$\frac{(2n+1)^2}{4}\pi^2$

Table 3.1: Solution of the transcendental equation (3.30)

The length of the uniform section L_u is determined from

$$\omega_{cl} = \omega_r \tag{3.31}$$

for some positive root of (3.30).

From the approximate analysis we obtain

$$L_u = \alpha_n \left[\frac{EI}{m\omega_r{}^2}\right]^{1/4}. \tag{3.32}$$

3.3.3 Selecting the number of ribs on each side

Obtaining a smooth flat stop band is important because it allows for robustness in manufacturing. This goal will be achieved only if the rib number N_r is sufficiently large. Therefore it is necessary to obtain a lower bound, N_{min}, such that if

$$N_r > N_{min} \tag{3.33}$$

the structural loss factor η approaches the material loss factor η_m. In order to obtain an estimate for N_{min}, we shall employ the Floquet theorem. Neglecting the Floquet waves reflected from the corners, the velocity amplitude at the resonator end, v_2, can be related to the velocity at the end of the uniform section

$$v_1 = e^{N_r \Re(\mu)} v_2, \tag{3.34}$$

where $\Re(\mu)$ is the attenuation of the periodic structure. Then

$$N_r = \frac{\log(v_1/v_1)}{\Re(\mu)}. \tag{3.35}$$

Inside the stop band v_1/v_2 is a large number. One can define a constant $C(\epsilon)$ such that

$$v_1/v_2 > C \qquad \text{whenever } |\eta - \eta_m| < \epsilon. \tag{3.36}$$

Then we obtain the desired estimation N_{min} in terms of the engineering constant $K = \log(C)$

$$N_{min} = \frac{K}{\Re(\mu)} \tag{3.37}$$

For engineering purposes K can be chosen between 5.5 and 6.5, which corresponds to velocity reduction in the range 48 dB - 56 dB.

3.4 Two-dimensional FEM of a high Q MEMS resonator

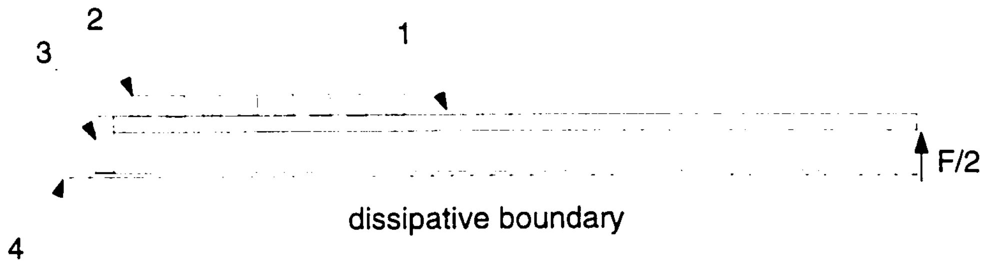

Figure 3.10: High fidelity two-dimensional FE model of high Q MEMS resonator. 1 - main body of the resonator, 2 - resonator rib, 3 - resonator support, 4 - substrate layer.

Figure 3.10 depicts a FE model of a high Q resonator, based on plane stress 2D solid elements space. Due to symmetry only half of the structure is modeled.

The elements approximate the stress with a linear function and have quadratic element shape functions (also known as Turner-Clough elements). For details about the form of the element stiffness and mass matrices see the Appendix C.

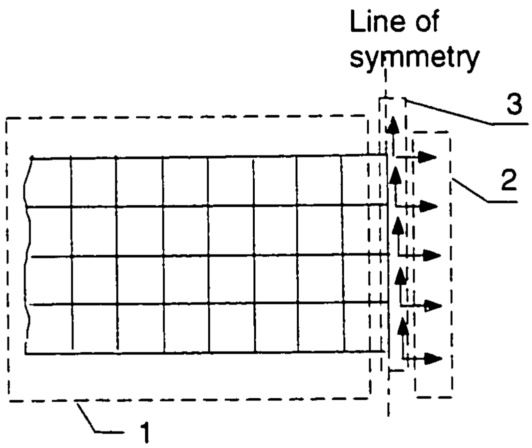

Figure 3.11: Partition of the resonator DOF. 1 – DOF related to subscript 1, 2 – DOF related to subscript 2, 3 – DOF related to subscript 3

The global mass and stiffness matrices are assembled by using the package $CALFEM^{TM}$ [40]. The frequency response of the system is computed by

$$\{v\} = [Z]^{-1}\{f\} \tag{3.38}$$

where $[Z_{st}]$ is the global impedance matrix, $\{v\}$ is the global velocity vector, and $\{f\}$ is the global force vector. Note that since the excitation frequencies are very high, a large number of solid elements is necessary and inverting the impedance matrix requires significant computational time. In order to simplify the problem, we partition the global impedance matrix as

$$[Z] = \begin{bmatrix} Z_{11} & Z_{12} & Z_{13} \\ Z_{21} & Z_{22} & Z_{23} \\ Z_{31} & Z_{32} & Z_{33} \end{bmatrix} \tag{3.39}$$

where the subscript index 1 denotes the degrees of freedom associated with one half of the structure, 2 represents the horizontal DOF at the line of symmetry, and 3 - the vertical DOF at the line of symmetry (see Figure 3.11). With Equation (3.39) we have the following equation of motion for half of the system

$$\begin{bmatrix} Z_{11} & Z_{12} & Z_{13} \\ Z_{21} & Z_{22} & Z_{23} \\ Z_{31} & Z_{32} & Z_{33} \end{bmatrix} \begin{Bmatrix} v_1 \\ v_2 \\ v_3 \end{Bmatrix} = \begin{Bmatrix} 0 \\ R_2 \\ R_3 \end{Bmatrix} + \begin{Bmatrix} 0 \\ 0 \\ F_e \end{Bmatrix} \tag{3.40}$$

Here R_2 is the vector of horizontal reaction forces and R_3 is the vector of vertical reaction forces at the line of symmetry and F_e is the excitation force vector applied to the half of the structure and it has the form

$$F_e = \begin{Bmatrix} F/2 \\ 0 \\ \vdots \\ 0 \end{Bmatrix} \tag{3.41}$$

Because of the structural and loading symmetry v_2 and R_3 are equal to zero. Then, the system (3.40) transforms to

$$\begin{bmatrix} Z_{11} & Z_{13} \\ Z_{31} & Z_{33} \end{bmatrix} \begin{Bmatrix} v_1 \\ v_3 \end{Bmatrix} = \begin{Bmatrix} 0 \\ F_e \end{Bmatrix} \tag{3.42}$$

(3.43)

$$R_2 = Z_{21}v_1 + Z_{23}v_3 \tag{3.44}$$

With Equation (3.44) the unknown velocity vectors v_1 and v_3 are determined as

$$v_1 = -Z_c{}^{-1}Z_{13}Z_{33}{}^{-1}F_e; \quad v_3 = Z_{33}{}^{-1}(I + Z_{31}Z_c{}^{-1}Z_{33}{}^{-1})F_e \tag{3.45}$$

where the condensed impedance matrix for half of the structure Z_c is given as

$$Z_c = Z_{11} - Z_{13}Z_{33}{}^{-1}Z_{31} \tag{3.46}$$

3.4.1 Description of dissipative boundary condition

In order to model realistically the connection of the resonator with the outer world, a dissipative boundary shall be introduced. Since the substrate is very large compared to the resonator size, a reasonable approximation would be a boundary extending

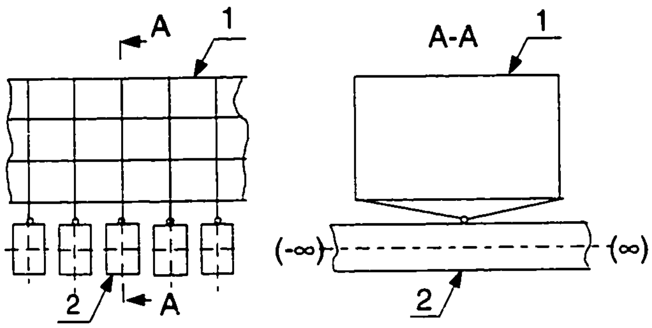

Figure 3.12: Dissipative boundary of high Q MEMS resonator. 1 - substrate layer, 2 - infinite beam

infinitely in one or more dimensions. In the literature, different models of dissipative infinite boundaries are developed (see [35], [36], [37]). In the present problem, infinite elastic beams are attached to each transverse degree of freedom of the foundation layer as shown in Figure 3.12. Thus, the elastic foundation model stretches infinitely in both directions away from the resonator. Note that this type of all-absorbing boundary is an idealization but nevertheless it demonstrates the applicability of the periodic design. The infinite beams have equal dimensions and material properties as the resonator - Young's modulus, material density, material loss factor.

The drive-point impedance of the infinite beam is given as

$$Z_{dp} = \frac{4m_b\omega}{(1+i)k_f} \tag{3.47}$$

, where m_b is the mass per unit length and $k_f = \left(\frac{m_b\omega^2}{EI}\right)$ is the flexural wavenumber of the infinite beam. Each drive point impedance is added to the corresponding location of the global impedance matrix.

3.5 Numerical examples

In this section we will illustrate the design approach through appropriate example structures and will consider two dimensional models of high Q resonators.

3.5.1 Example illustrating the simplified approach for high Q resonator design

To illustrate the procedure in section 3.3, let us consider the following example :

A high MEMS resonator has to be designed to oscillate at frequency $\omega_r = 375$ MHz and have a high Q factor in the interval Δ = 275 - 475 MHz. Such resonators, usually are built from polysilicon, have the following material properties:

- Young's modulus $E = 1.61 \times 10^{11}$ N/m^2
- mass density $\rho = 2330$ kg/m^3
- Poisson ratio $\nu = 0.22$
- polysilicon loss factor $\eta = 10^{-5}$

The height and width of the cross section are chosen to be typical of such devices in the literature:

- height $h = 2 \times 10^{-6}$ m
- thickness $t = 4 \times 10^{-6}$ m

The array spacing d is computed by using (3.27) which gives 3.977×10^{-6} m. We round it up to the closest integer and choose $d = 4 \times 10^{-6} m$. The mass of the rib is computed with (3.28), which gives $M_r = 8.19 \times 10^{-14}$ kg (corresponding to $\zeta = 1$). The length of the uniform cross section is obtained by using Equation (3.32). We select three different values of the parameter α (see (3.30)) to obtain three possible values for the length of uniform section summarized in Table 3.2

In Figure 3.13, the first stop band is shown for a periodic structure with the

Design type	α	Uniform section length L_u	Ribs number N_r	Total length L
1	4.73004	$6.8446 \times 10^{-6}\ m$	16	$135 \times 10^{-6}\ m$
2	10.9956	$16 \times 10^{-6}\ m$	16	$144 \times 10^{-6}\ m$
3	17.2788	$25 \times 10^{-6}\ m$	16	$153 \times 10^{-6}\ m$

Table 3.2: Three different designs of high Q resonators

chosen spacing d and ribs mass M_r. In Figure 3.14 the drive point velocity is plotted

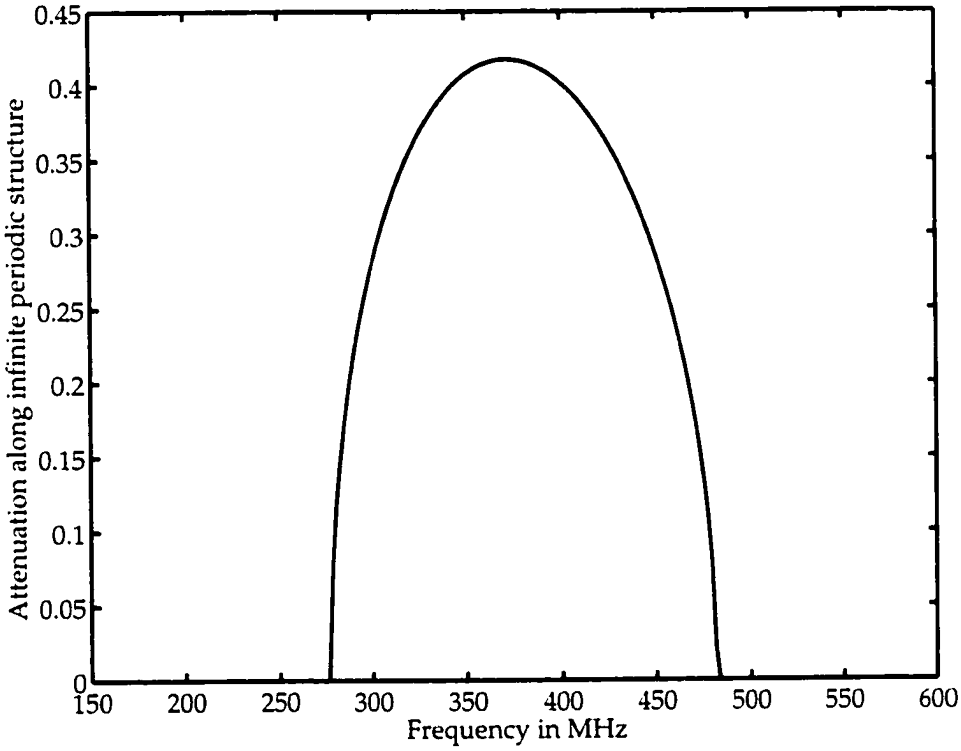

Figure 3.13: Attenuation along infinite periodic structure

for a high Q resonator with design type 1. In Figure 3.15 the structural loss factor for design type 1 is plotted and compared with that of the clamped ends model.

One can observe, as expected, that the natural frequency is close to the frequency of highest attenuation. The deviation $\Delta\omega$ of the resonating frequency ω_r from the frequency of highest attenuation is due to the clamped ends approximation. In fact, the ends of the uniform section are not perfectly rigid which results in the difference

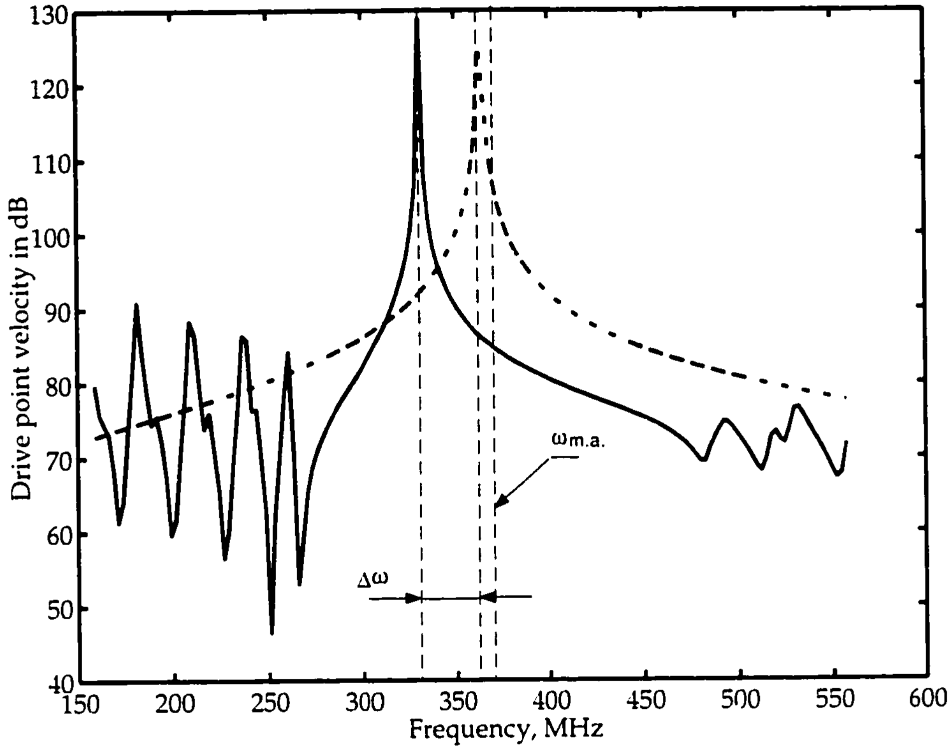

Figure 3.14: Drive point velocity of a high Q resonator with design type 1. Resonator with periodic design —: Equivalent uniform structure with clamped ends - - -

$\Delta\omega$. The clamped ends approximation leads to accurate results if the ratio of uniform section length over array length, Lu/L_a, is large enough. This can be observed after comparison of Figure 3.14 with Figure 3.16 for design type 2 and Figure 3.17 for design type 3.

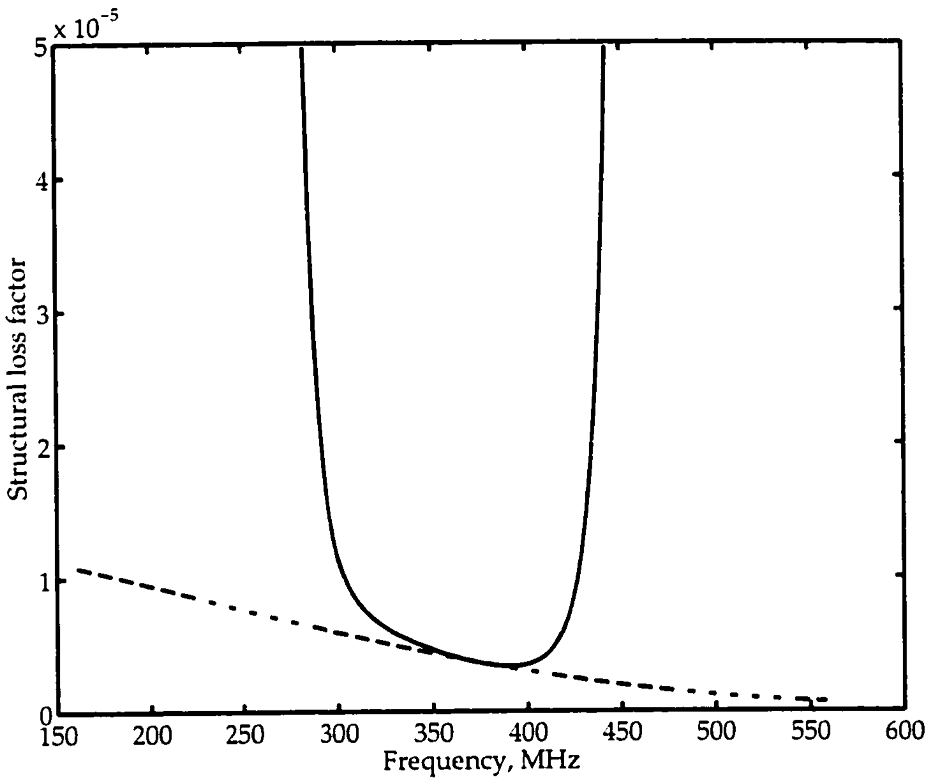

Figure 3.15: Structural loss factor of a high Q resonator with design type 1. Resonator with periodic design —: Equivalent uniform structure with clamped ends - - -

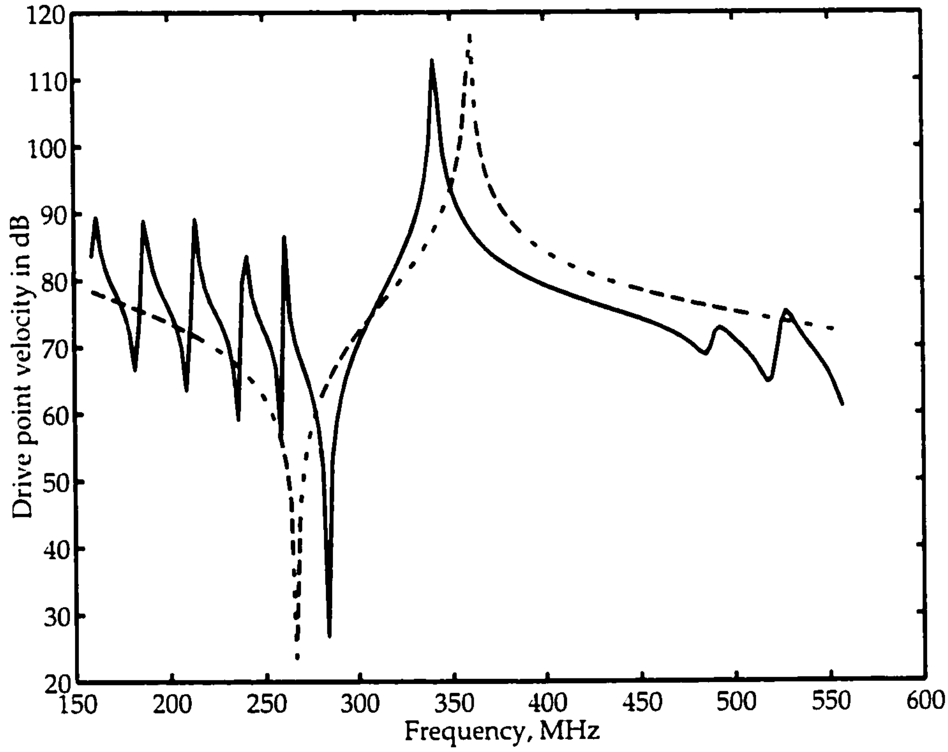

Figure 3.16: Drive point velocity of a high Q resonator design type 2. Resonator with periodic design —: Equivalent uniform structure with clamped ends - - -

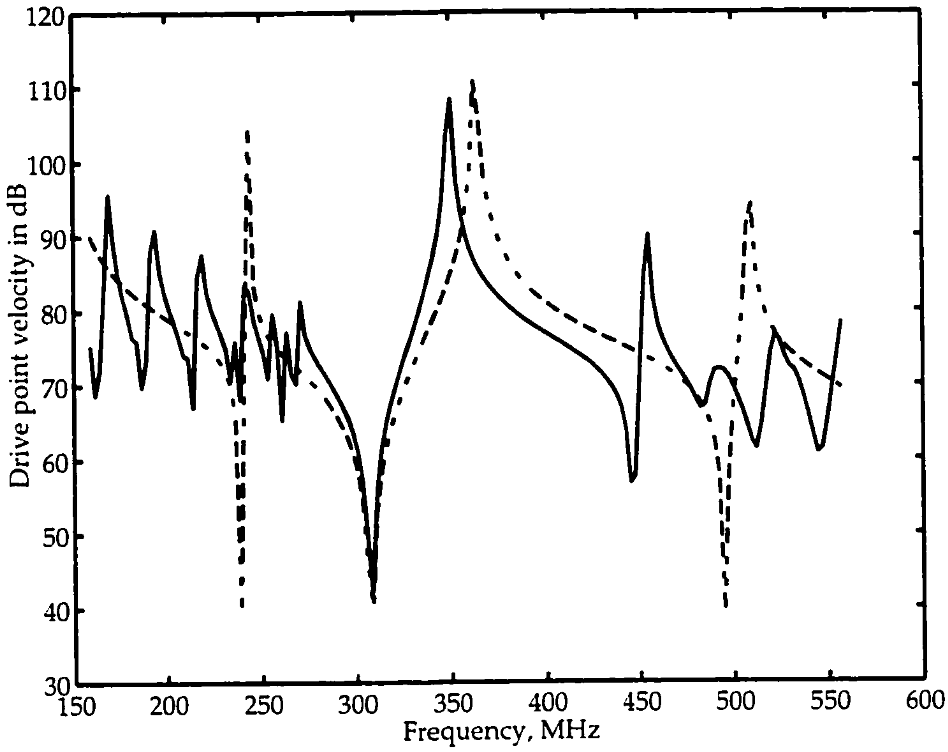

Figure 3.17: Drive point velocity of a high Q resonator with design type 3. Resonator with periodic design —: Equivalent uniform structure with clamped ends - - -

The number of ribs per side is computed by using (3.37). With the value 5.5 for the engineering constant K we obtain $N_{min} = 13$ and for $K = 6.5$ we get $N_{min} = 16$. In Figure 3.18, the structural loss factor is plotted for design type 3, varying the rib number N_r. One can see that, indeed, $N_r = 16$ is a good choice.

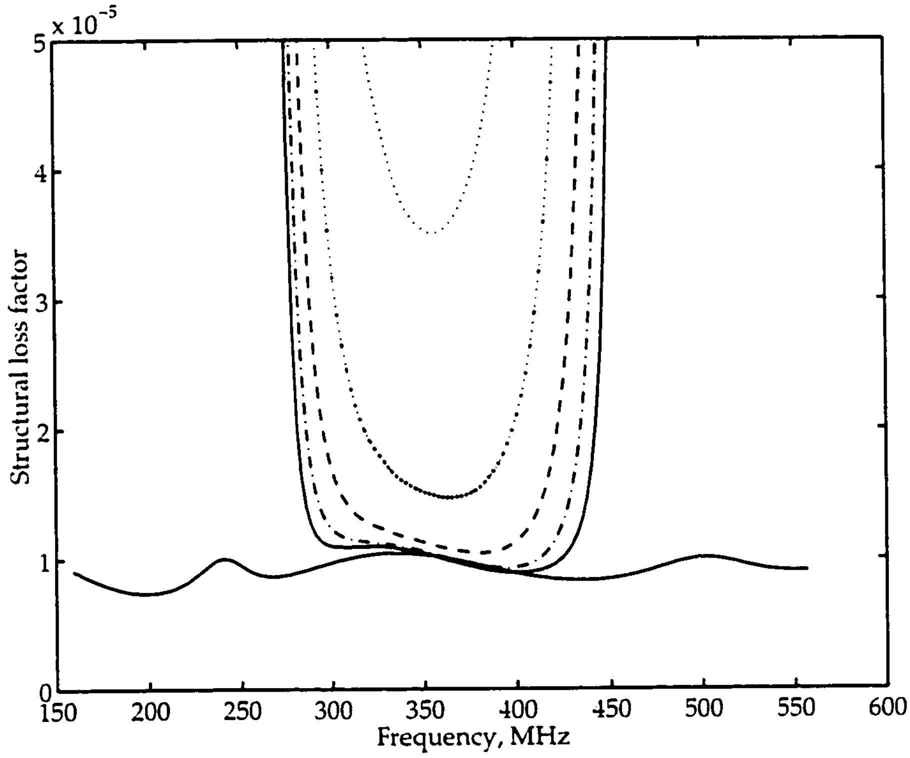

Figure 3.18: Structural loss factor for different number of ribs. 18 ribs per side —: 16 ribs per side -·-: 14 - - -: 12 ribs per side ...◦...: 10 ribs per side .... The flat line varying around the value 10^{-5} refers to the resonator with free ends.

3.5.2 Two-dimensional finite element models for high Q resonators

In this section we will consider several example structures, helping us to understand the physics of the high frequency behavior of resonators with different designs. A critical modeling issue is that all of the ribs have dimensions comparable to the wavelength which necessitates two-dimensional (2D) finite element modeling. The periodic design types are denoted as *long section*, *short section*, *long ribs*, *tin cover*, and *top and bottom*. In *long section* and *short section* long and short uniform sections are presented, in *long rib* the effect of longer polysilicon ribs is studied, and in *tin cover long section*, a tin cover is added to the top of each rib for a resonator with long polysilicon section. This increases the mass of the rib substantially. After each design type an integer will be added denoting the number of ribs per side for the considered resonator. For example, *tin cover long section 8* will denote a resonator with 8 ribs per side, long uniform section and *Sn*-cover on the top of the ribs. A periodic design is studied with ribs on the top and bottom surfaces of the resonator body, denoted as *top and bottom*. In this case two integers will be added for the number of the top ribs and bottom ribs accordingly. Thus *top and bottom short section 9 10* denotes resonator with 9 ribs on the top and 10 ribs on the bottom and short uniform section. Additionally, design type *uniform long* is considered which does not have ribs and it is used for performance comparison.

The parameters of the periodic designs which are varied are summarized in Table 3.3. The resonator dimensions are shown in Figure 3.19. For all resonators, the height h is equal to 2 μm, the spacing d_1 is equal to 4 μm, the length of the anchor

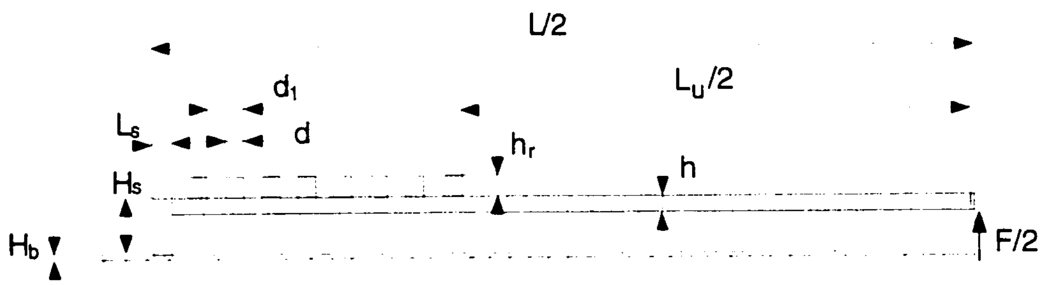

Figure 3.19: Dimensions of high Q MEMS resonator

DESIGN	L_u, μm	h_r, μm	N_r, ribs/side
long section 6	168	1.5	6
long section 7	168	1.5	7
long section 8	168	1.5	8
long section 9	168	1.5	9
long section 10	168	1.5	10
long section 11	168	1.5	11
short section 5	18	1.5	5
short section 6	18	1.5	6
short section 7	18	1.5	7
short section 8	18	1.5	8
short section 9	18	1.5	9
short section 10	18	1.5	10
short section 11	18	1.5	11
long ribs 8	50	4	8
tin cover long section 8	168	1.5	8
top and bottom short section section 9 10	18	1.5	9/10

Table 3.3: Periodic design types for high Q MEMS resonators

L_s is equal to 2 μm, their total length L is given with

$$L = L_u + N_r d_1 + L_s. \tag{3.48}$$

Periodic design *long section 8*

The geometry of this design type is shown in Figure 3.20. To test the convergence of

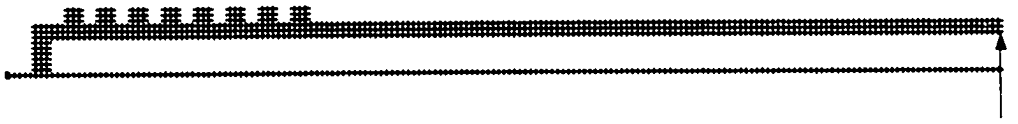

Figure 3.20: Design *long section 8* with 2476 *DOF*, 828 elements and element size 0.67 μm × 0.67 μm

the FE model three different meshes are considered - coarse mesh with 2476 DOF, element size 0.67 μm × 0.67 μm, fine mesh with 3278 DOF, element size 0.5 μm × 0.67 μm, and very fine mesh with 4080 DOF, element size 0.4 μm × 0.67 μm. The drive point velocity of the structure computed with the very fine mesh is compared with that of the fine mesh in Figure 3.21, indicating convergence of the model. In 3.22 the structural loss factor is shown, computed by (3.10). It approaches the loss factor of the polysilicon in the interval 355 MHz - 445 MHz, which represents the stop band of the periodic structure. Very good agreement is observed when the latter is compared with Figure 3.23, showing the stop band in the case when the same periodic structure is approximated as an Euler-Bernoulli beam, extending infinitely in both directions (see Figure 3.24). Note that there are five resonance frequencies within the flat portion of the loss factor. The fact that the resonator may operate and achieve high Q in any of the stop band resonance frequencies allows one to build a switchable high Q resonator. In Figure 3.25 a resonator with free ends is shown to investigate absence of boundary dissipation. In this case the loss factor fluctuates around the material loss factor as shown in Figure 3.26. As in the 1D structural model, the velocity near the resonator ends exhibits distinct stop band behavior as shown in Figure 3.27.

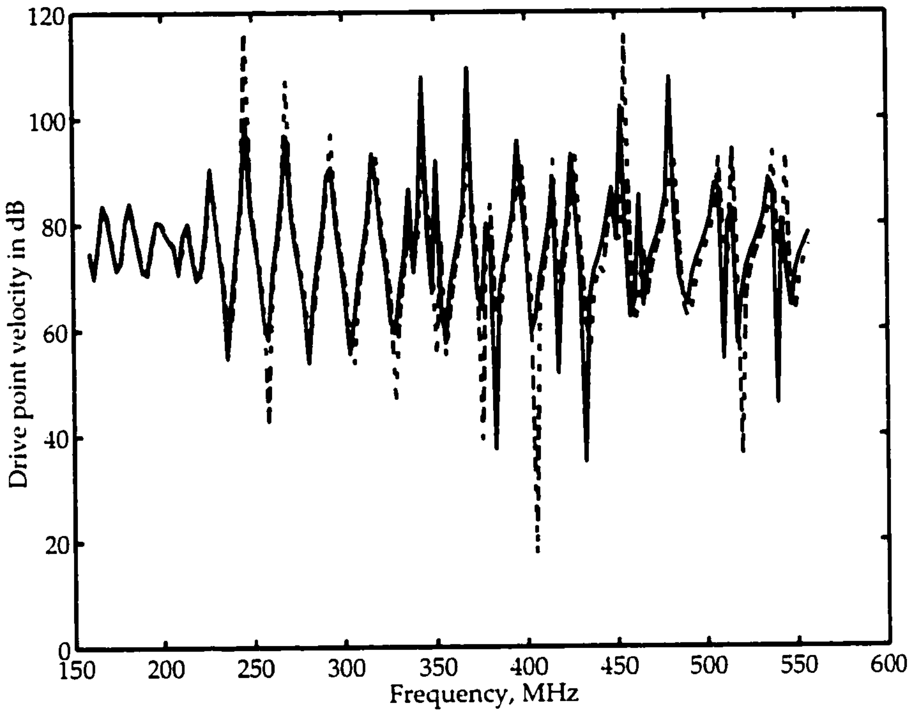

Figure 3.21: Drive point velocity of design *long section 8* for two different meshes. 4080 *DOF* (element size 0.4 μm × 0.67 μm) — : 3278 *DOF* (element size 0.5 μm × 0.67 μm) - - -

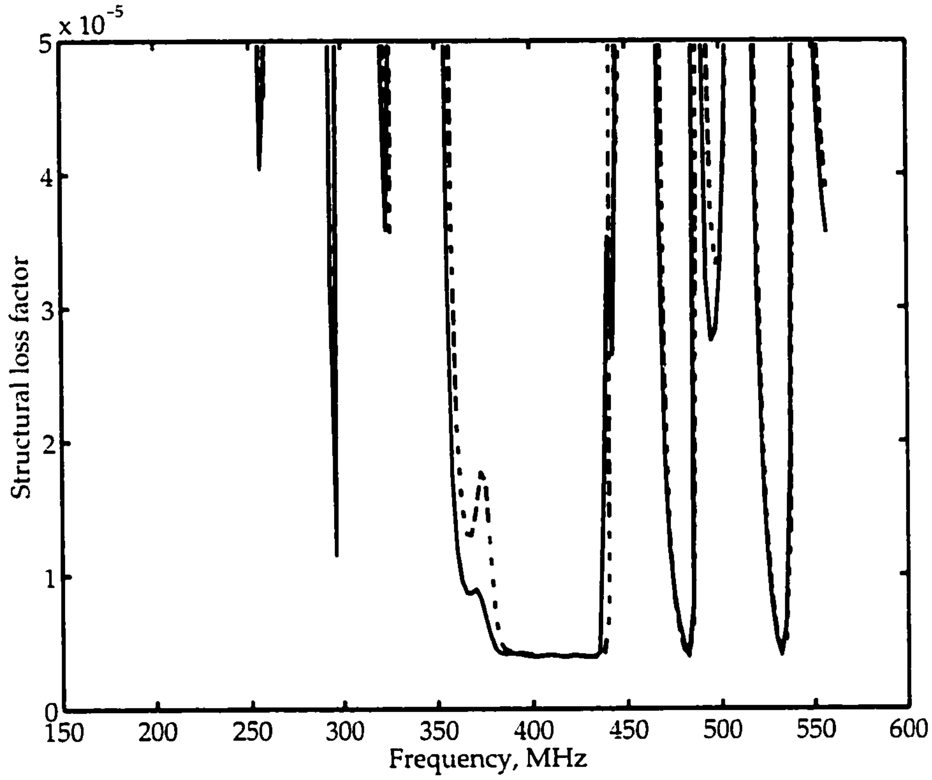

Figure 3.22: Structural loss factor of design *long section 8* for two different meshes. 4080 DOF (element size 0.4 μm × 0.67 μm) —: 3278 DOF (element size 0.5 μm × 0.67 μm) - - -

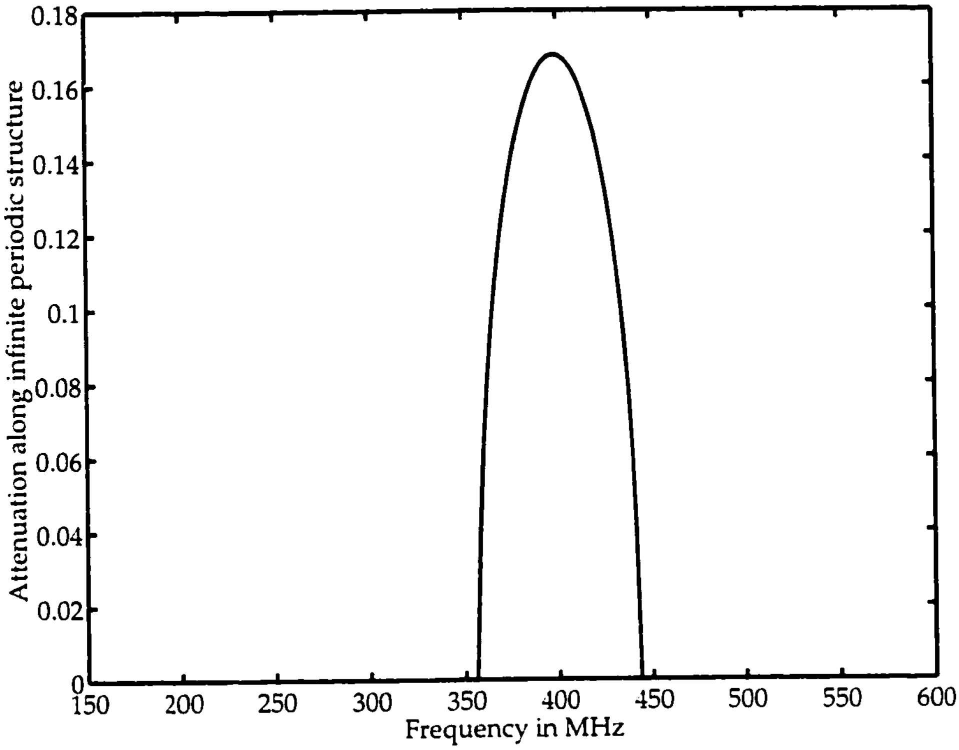

Figure 3.23: First stop band of the corresponding infinite elastic structure with $d = 2$ μm and $d_1 = 4$ μm

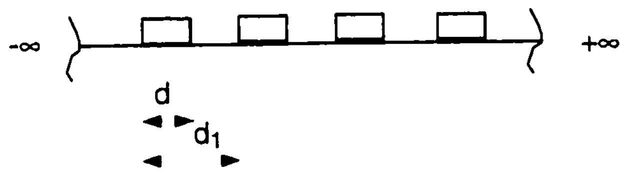

Figure 3.24: Euler-Bernoulli approximation for evaluating the stop band

Figure 3.25: Resonator with free ends

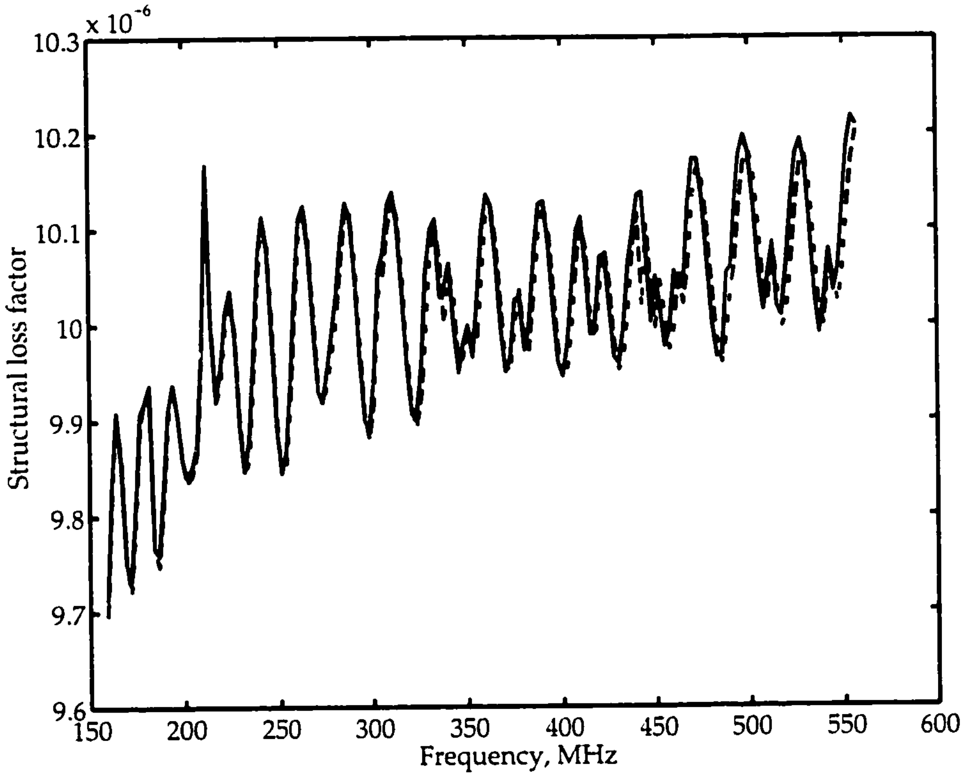

Figure 3.26: Structural loss factor of design *long section 8* for two different meshes. The resonator is disconnected from the supports and has free end boundary conditions. 4080 *DOF* (element size 0.4 μm × 0.67 μm) —: 3278 *DOF* (element size 0.5 μm × 0.67 μm) - - -.

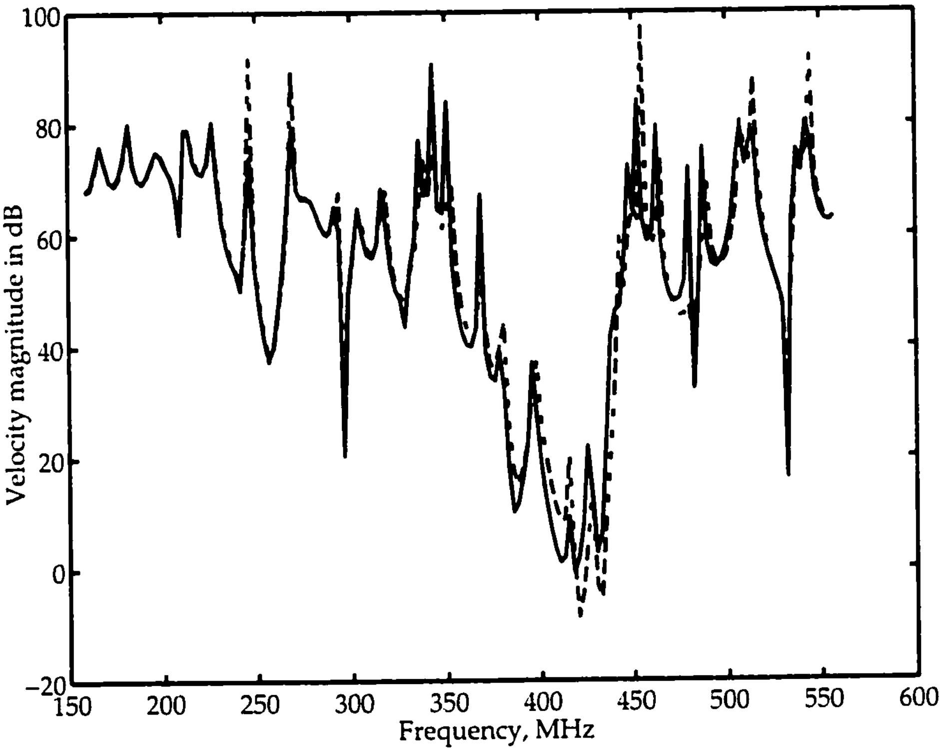

Figure 3.27: Velocity magnitude in dB at 6 μm away form the support corner. Computed for design *long section 8* with two different meshes. 4080 DOF (element size 0.4 μm × 0.67 μm) —; 3278 DOF (element size 0.5 μm × 0.67 μm) - - -.

Periodic design *long ribs 8*

In this design, the height of the rib is doubled and the length of the resonator is halved compared to the type *long section*. Thus, a more compact resonator with heavier ribs achieves the same attenuation and comparable Q factors. Figure 3.28 illustrates the *long ribs 8* design type for a mesh with 2508 *DOF*. In Figure 3.29,

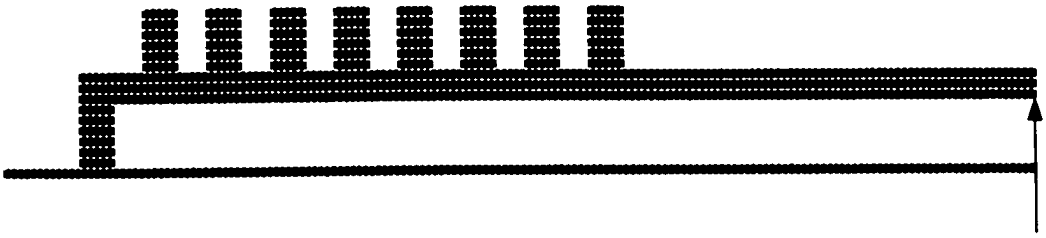

Figure 3.28: Design *long rib* with 2508 *DOF*, 885 elements and element size 0.4 μm $\times$ 0.67 μm.

the convergence of the drive point velocity is shown for two different meshes. In Figure 3.30, the structural loss factor is shown and one observes that the stop band for this design lies in the interval 452 MHz - 540 MHz. Note that the stop band for this design is larger than that for *long section 8*, which is due to the increased rib weight. In Figure 3.31, the stop band of a periodic structure, extending infinitely in both directions, is plotted assuming identical geometry at that of *long ribs 8*. The stop band, predicted by this infinite model differs from the stop band of the resonator. A possible explanation is related to the fact that the rib is modeled as pure (distributed) mass in the infinite model which does not match the problem physics for this frequency range.

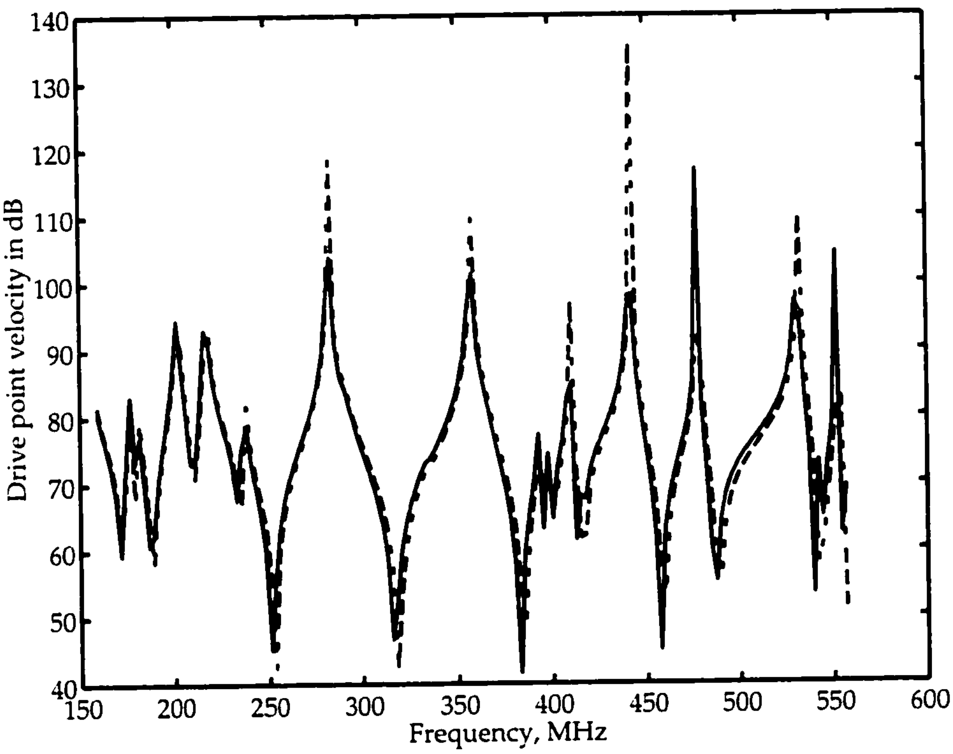

Figure 3.29: Drive point velocity of design *long rib* for two different meshes. 2508 *DOF* (element size 0.4 $\mu m \times 0.67$ μm) —: 2030 *DOF* (element size 0.5 $\mu m \times 0.67$ μm) - - -.

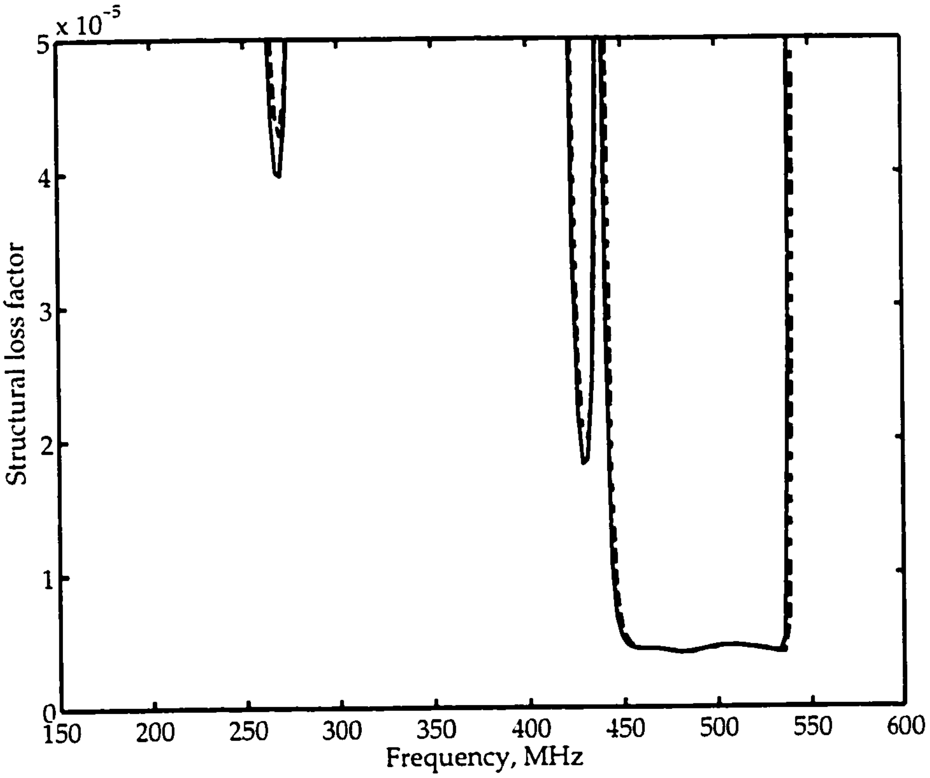

Figure 3.30: Structural loss factor of design *long rib* for two different meshes. 2508 DOF (element size 0.4 μm × 0.67 μm) —: 2030 DOF (element size 0.5 μm × 0.67 μm) - - -

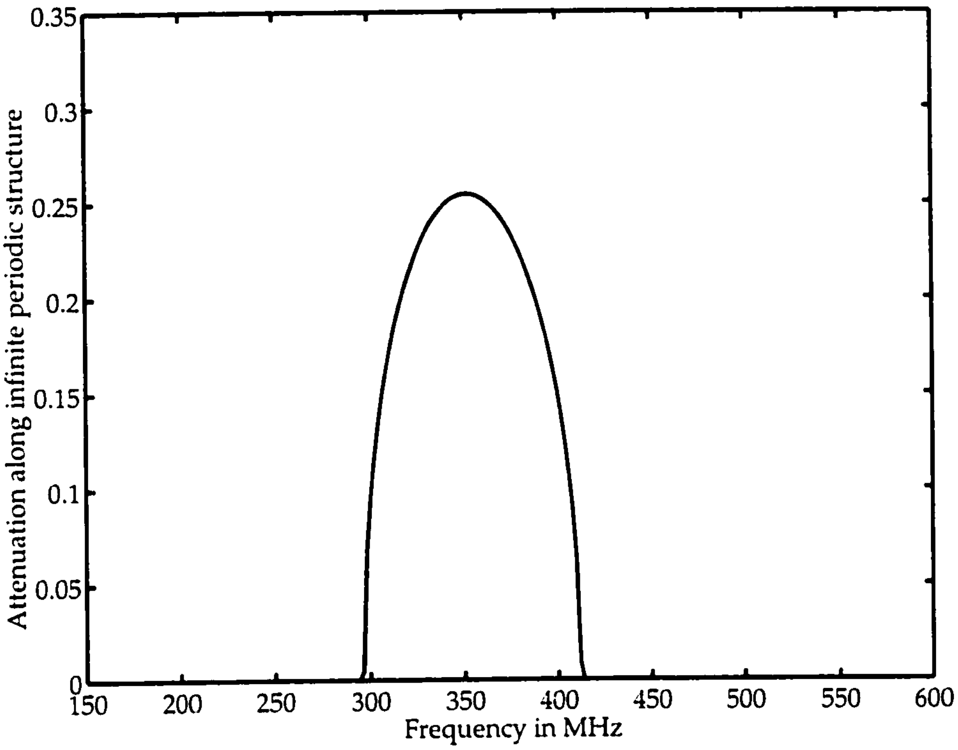

Figure 3.31: First stop band of the corresponding infinite elastic structure with $d = 2$ μm and $d_1 = 4$ μm

Periodic design with tin cover *tin cover long section 8*

In this design type, a 0.4 μm tin cover is deposited on the top of each rib, increasing twice the total mass of the ribs compared to design type *long section.* The reason this is done is to investigate the possibility of achieving a broad stop band by lumping additional mass and keeping the rib dimensions the same.

In Figures 3.32 and 3.33, the structural loss factor and the drive point velocity magnitude are plotted. It is observed that additional resonances rise inside the stop band which are due to the presence of lumped mass. Those "new" resonances facilitate the wave propagation inside the stop band instead of preventing it, which degrades the performance and lowers the Q.

Uniform design *uniform long*

This design was analyzed for comparison to new design approach. Three different meshes were considered - - coarse mesh with 2284 DOF, element size 0.67 $\mu m \times 0.67$ μm, fine mesh with 3038 DOF, element size 0.5 $\mu m \times 0.67$ μm, and very fine mesh with 3792 DOF, element size 0.4 $\mu m \times 0.67$ μm (see Figure 3.34). The convergence of the drive point velocity for the fine versus very fine mesh is shown in Figure 3.35. The structural loss factor is shown in Figure 3.36.

Periodic design with ribs on top and bottom *top and bottom long section 8*

In this particular design, ribs are attached on the top and the bottom of the main resonator body. This kind of structure represents a realistic model taking into account the possible limitations in the existing MEMS technology. The ribs on the bottom of the resonator body appear as a result of the etching technology used for shaping the ribs on the top surface.

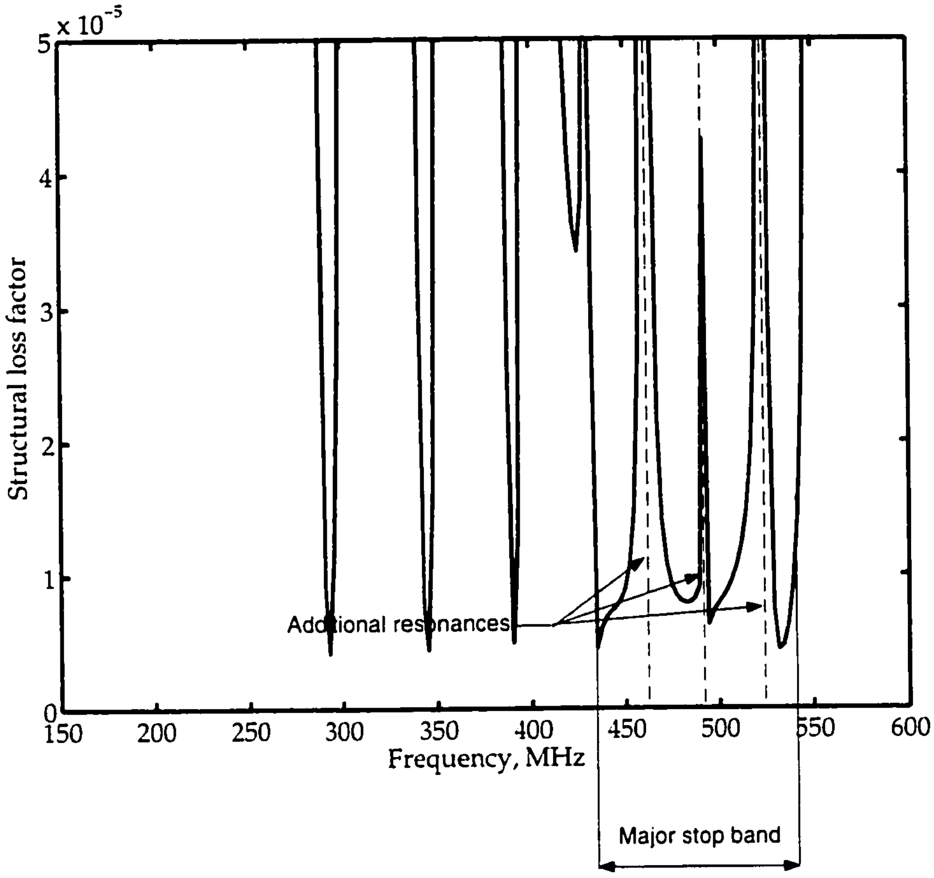

Figure 3.32: Structural loss factor of design *tin cover long section 8* for a mesh with 4080 DOF (element size 0.4 μm × 0.67 μm).

In Figure 3.37 the structural geometry and dimensions are shown. In Figures 3.38 and 3.39, the structural loss factor and velocity magnitude are shown. Compared to the previous designs adding a second array of ribs on the bottom leads to a wider stop band and larger flat region in frequency with a high Q.

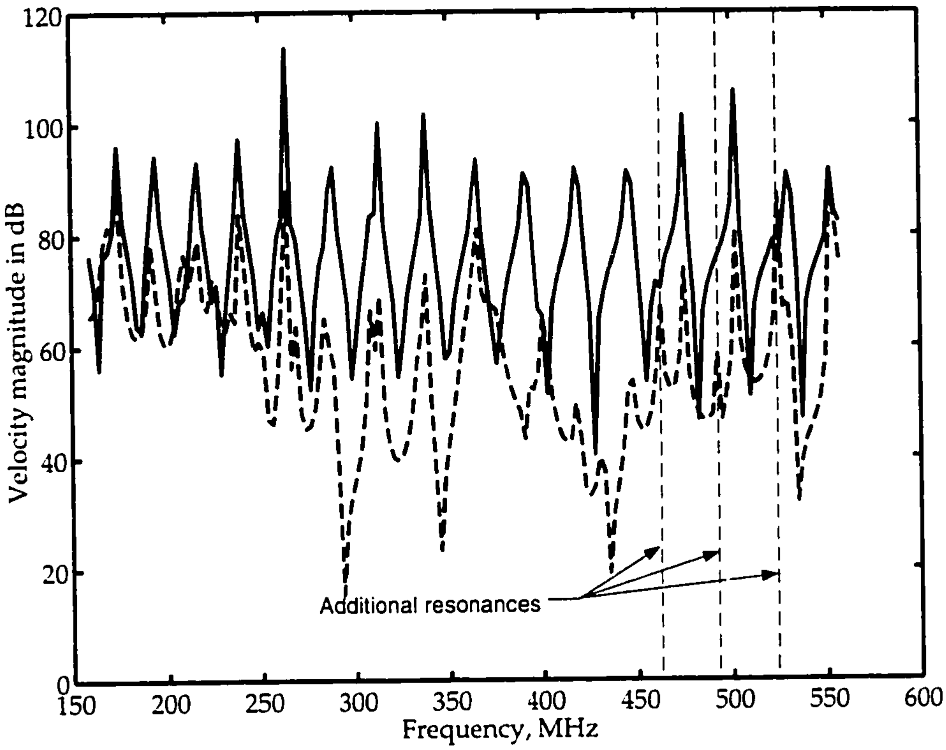

Figure 3.33: Drive point velocity magnitude —: Velocity magnitude at 6 μm away from the support corner – – –. Design type is *tin cover long section 8* for a mesh with 4080 *DOF* (element size 0.4 μm × 0.67 μm).

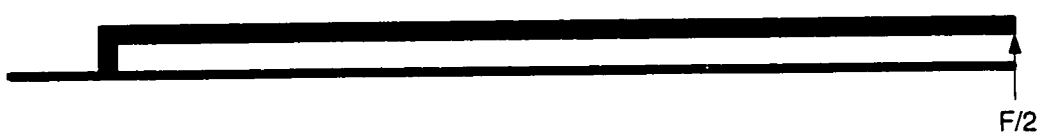

Figure 3.34: Design type *uniform long* with 3792 *DOF*, 1260 elements and element size 0.4 μm × 0.67 μm

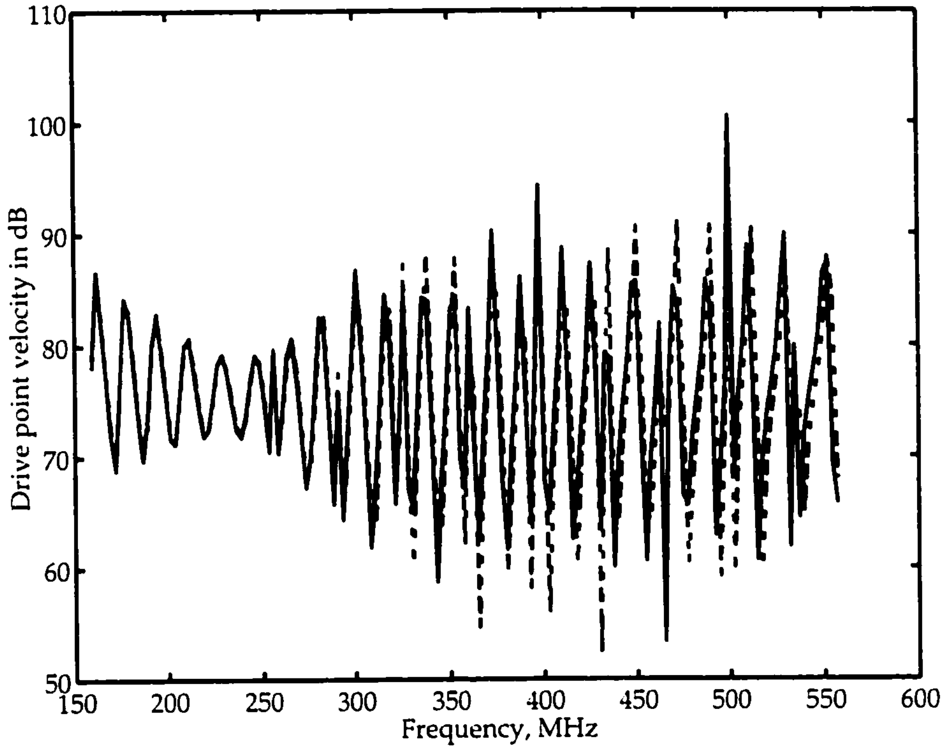

Figure 3.35: Drive point velocity in dB of design *uniform long* for two different meshes. 3792 *DOF* (element size 0.4 μm × 0.67 μm) —: 3038 *DOF* (element size 0.5 μm × 0.67 μm) - - -.

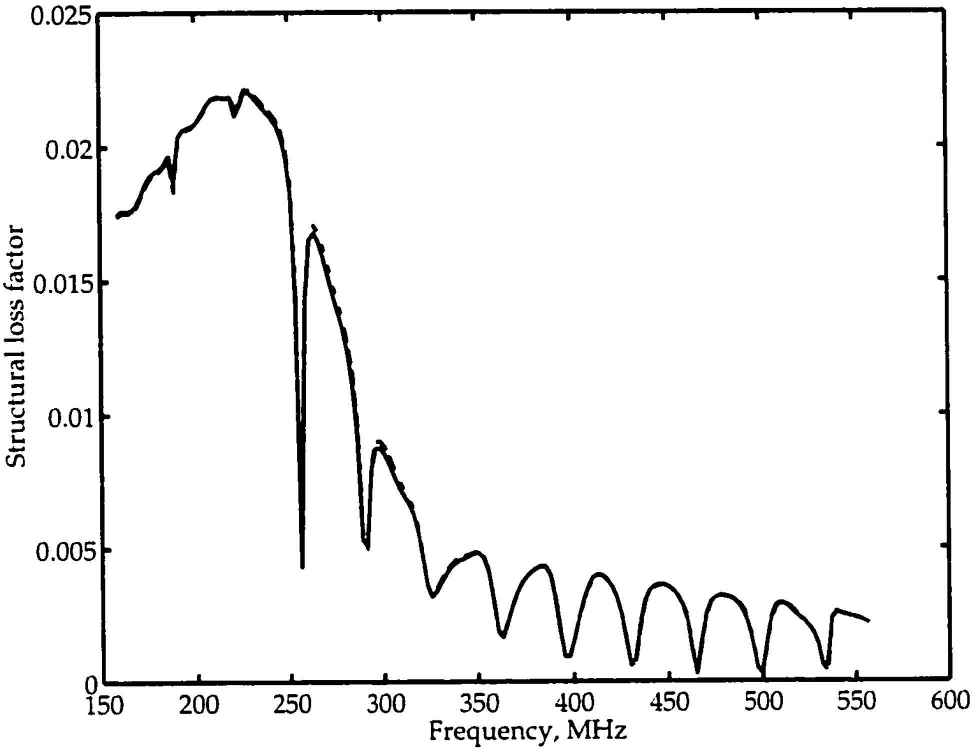

Figure 3.36: Structural loss factor of design *uniform* for two different meshes. 3792 DOF (element size 0.4 μm × 0.67 μm) —: 3038 DOF (element size 0.5 μm × 0.67 μm) – – –.

Figure 3.37: Resonant structure with 9/10 ribs on top/bottom. 2816 DOF, 1018 elements and element size 0.33 μm × 0.67 μm

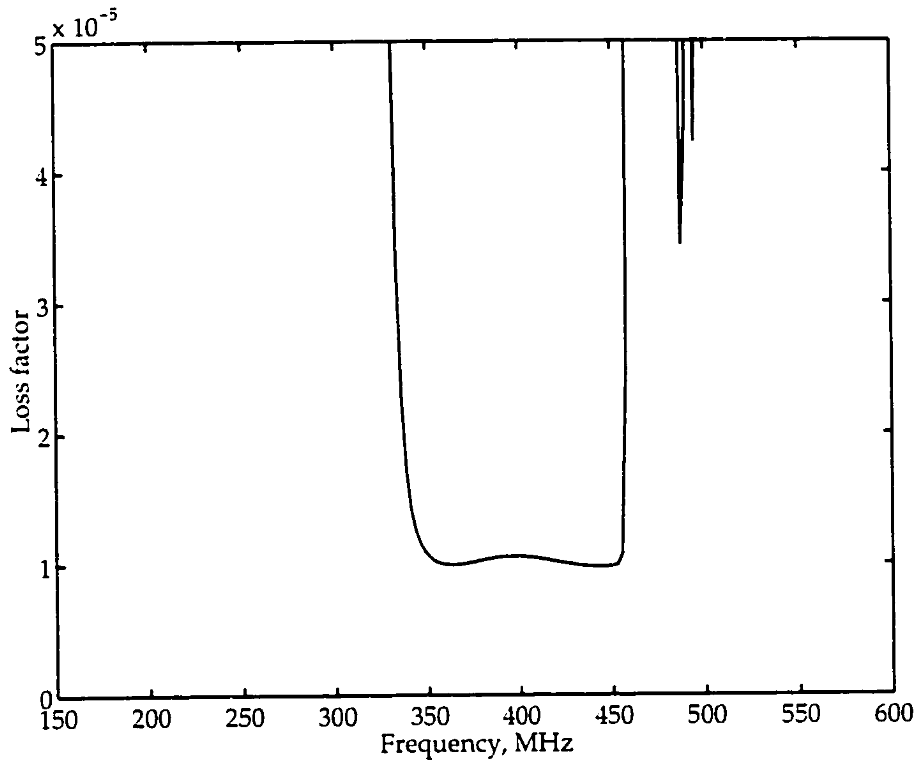

Figure 3.38: Structural loss factor for the resonant structure with 9/10 ribs on top/bottom

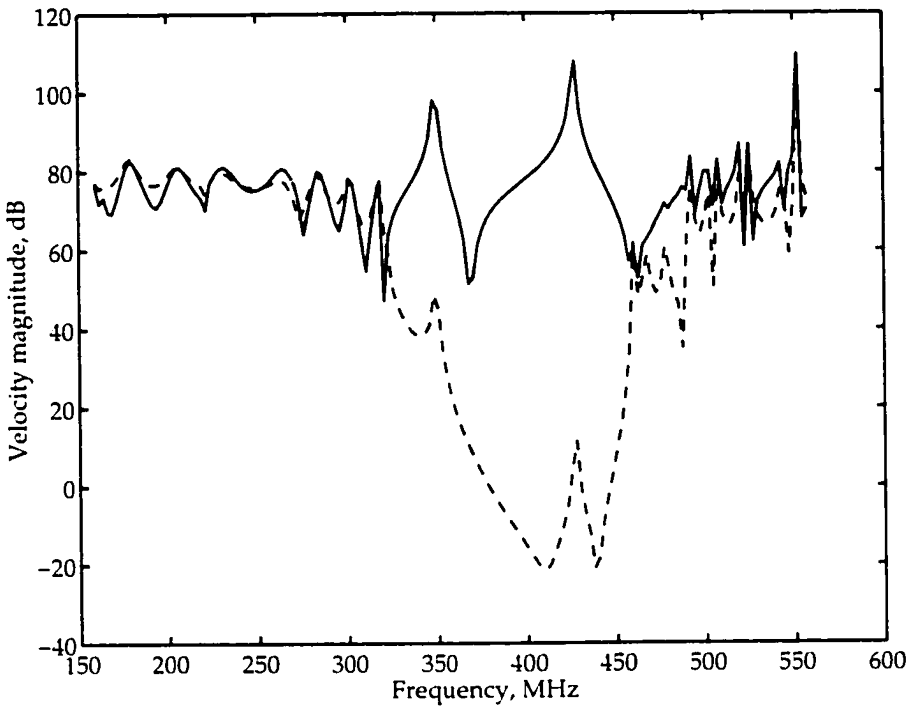

Figure 3.39: Velocity magnitude for the resonant structure with 9/10 ribs on top/bottom. Drive point velocity magnitude —; Velocity magnitude 3.33 μm away from the support corner - - -

The relation between the ribs number and the stop band length

The effect of the rib number, N_r, was also investigated. Two groups of resonators were considered - long uniform section (*long section 6–long section 11* and short uniform section (*short section 5–short section 11*). The rib number for each of the considered groups was varied.

The geometries of the resonator groups with long bodies are shown in Figures 3.40 – 3.45. Note that all of these have the same length of the uniform section

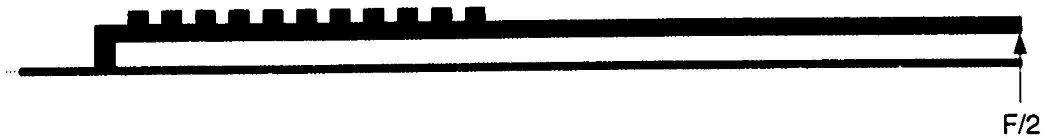

Figure 3.40: Design type *long section 11*, 4560 DOF, 1548 elements and element size 0.4 μm × 0.67 μm

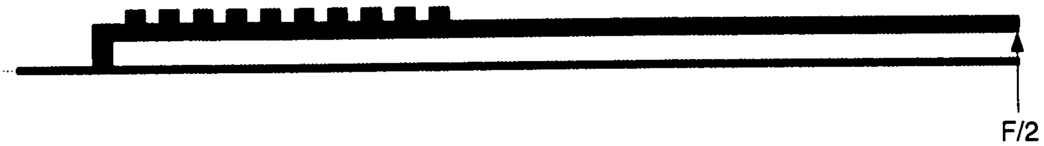

Figure 3.41: Design type *long section 10*, 4400 DOF, 1492 elements and element size 0.4 μm × 0.67 μm

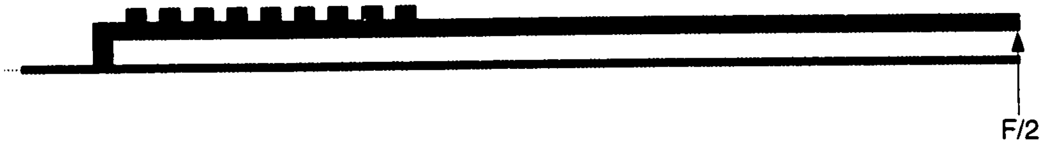

Figure 3.42: Design type *long section 9*, 4244 DOF, 1437 elements and element size 0.4 μm × 0.67 μm

(see Table 3.3). The rib's height is 1.5 μm for all structures. The total length of the resonator with 11 ribs per side is 132 μm and that of a resonator with 6 ribs per side is 112 μm. The variation of the structural loss factor with respect to the rib

Figure 3.43: Design type *long section 8*, 4080 DOF, 1380 elements and element size 0.4 μm × 0.67 μm

Figure 3.44: Design type *long section 7*, 3920 DOF, 1324 elements and element size 0.4 μm × 0.67 μm

number is shown in Figure 3.46. From this figure it is observed that the zone where the structural loss factor is minimal broadens with increase of the rib number. For instance, in the case of 5 ribs the minimal loss factor zone is between 425 MHz and 475 MHz and for 11 ribs per side the zone spreads within 390 MHz and 480 MHz.

The drive point velocity for resonators with different rib numbers is shown in Figure 3.47. It is observed that inside the major stop band (380 MHz - 480 MHz) the structural response does not depend on the rib number. This is observed if both the number of ribs and their masses are large enough. The same observation is approximately true for certain frequencies within the range 250 MHz - 340 MHz, suggesting the presence of minor stop band(s) in this frequency interval. In Figure 3.48 the drive point versus end point velocity (4 μm away from the support end) are shown. The presence of a major stop band within 400 MHz - 500 MHz is confirmed. Also, minor stop bands are observed in the intervals 250 MHz - 270 MHz, 300 MHz - 315 MHz, and 315 MHz - 325 MHz.

The geometries of resonators with short designs are shown in Figures 3.49 – 3.55. The length of the uniform section for all considered short designs is $L_u = 18$ μm

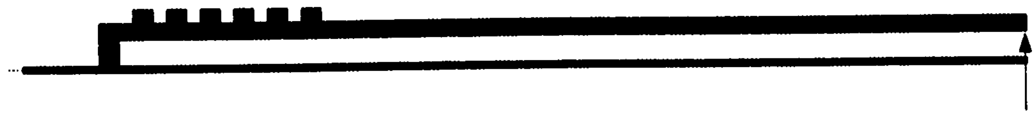

Figure 3.45: Design type *long section 6*, 3760 DOF, 1268 elements and element size 0.4 μm × 0.67 μm

(see Table 3.3). The length of the short design with 11 ribs is 56 μm and that with 5 ribs per side is 32 μm. The loss factors for resonators with different rib numbers are shown in Figure 3.56. The conclusions from the long designs regarding the rib number and width of the stop band may be drawn here. The drive point velocity of the short designs is shown in Figure 3.57 and as expected it is found that the response does not depend on the ribs number inside the major stop band (395 MHz - 475 MHz).

Realistic modeling of the ribs, fabricated using MUMPs™ technology, used at Boston University

An important task is to develop a realistic design which can be manufactured using the existing MUMPs™ technology at Boston University. For this purpose the software L – Edit™ was utilized and it was found that the conventional rectangular-shaped ribs cannot be built using the MUMPs™ technology. Thus specially T-shaped ribs were used as shown on Figure 3.58. The height of the main resonator body and the total height of the ribs are fixed to 2 μm and 2.25 μm accordingly which is determined by the the thickness of the $POLY1$, $POLY2$, and sacrificial oxide layers. Additionally, a constraint is imposed on the total length of the resonator - the latter cannot be longer than 600 μm due to possible stiction effects. The resonator has total length L equal to 544 μm, length of the uniform section L_u equal to 36 μm, and spacing d - 36 μm. It is observed a resonance at 13 MHz inside the stop band

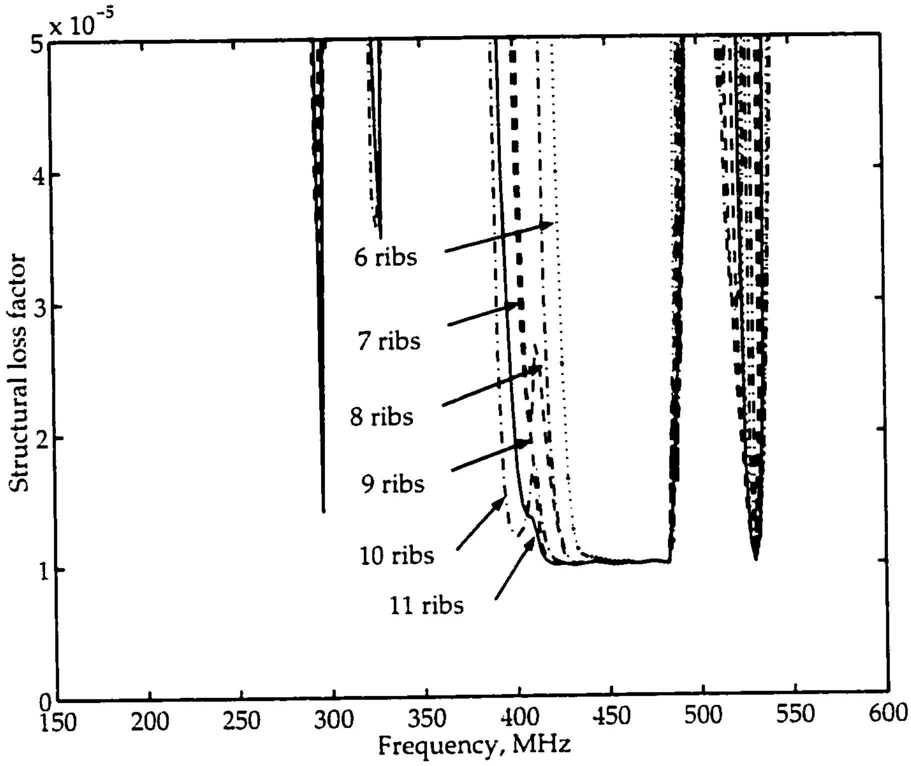

Figure 3.46: Structural loss factor for resonant structures with different rib number per side. 11 ribs per side —: 10 ribs per side -·-: 9 ribs per side - -: 8 ribs per side -·-: 7 ribs per side - -: 6 ribs per side ...

lying between 11 MHz and 19 MHz. Result from computation of such a realistic rib design is shown in Figure 3.59.

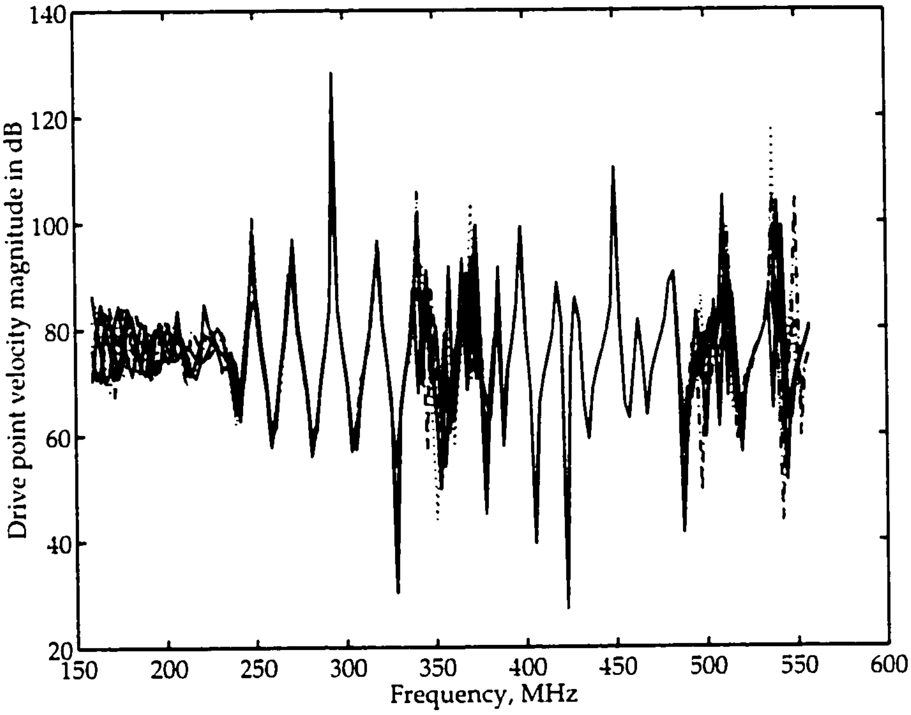

Figure 3.47: Drive point velocity for resonant structures with different rib numbers per side. 11 ribs per side —: 10 ribs per side -·-: 9 ribs per side - -: 8 ribs per side -·-: 7 ribs per side - -: 6 ribs per side …

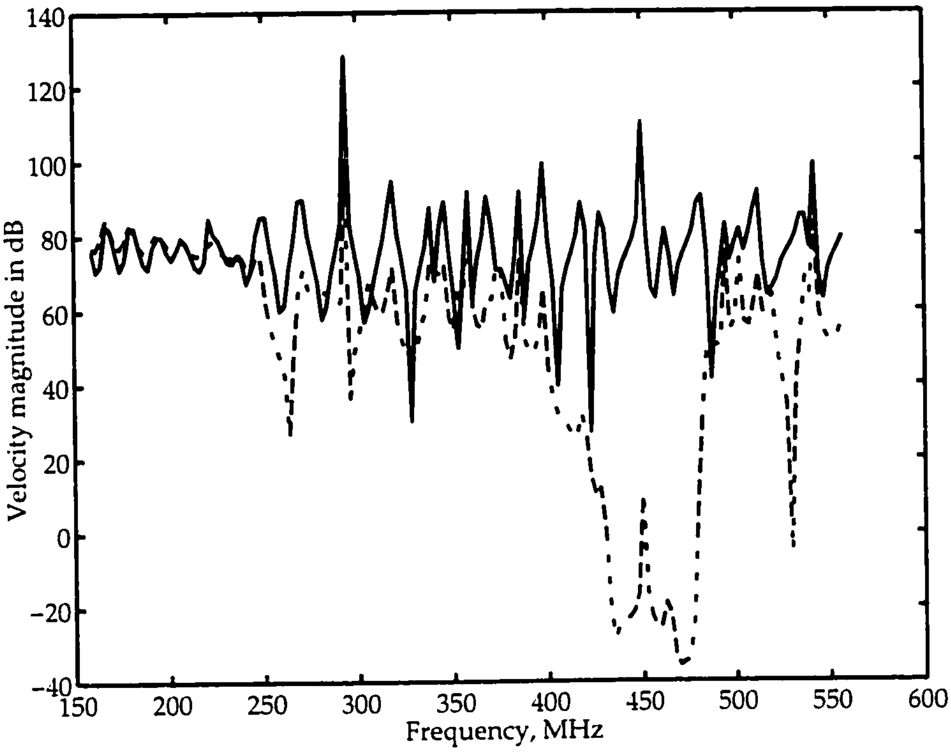

Figure 3.48: Velocity magnitude in dB. Drive point —; Velocity at 4 μm away from the support end - - -

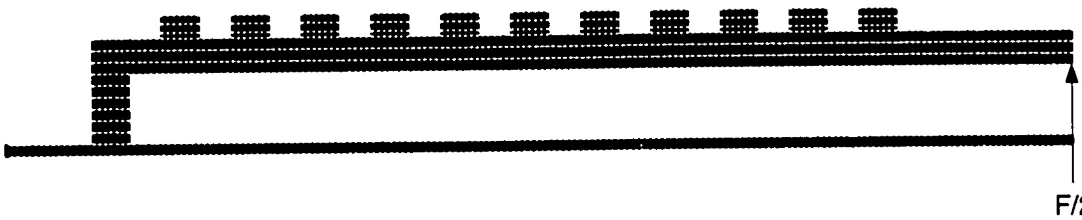

Figure 3.49: Design type *short section 11*, 2628 *DOF*, 923 elements and element size 0.33 μm × 0.67 μm

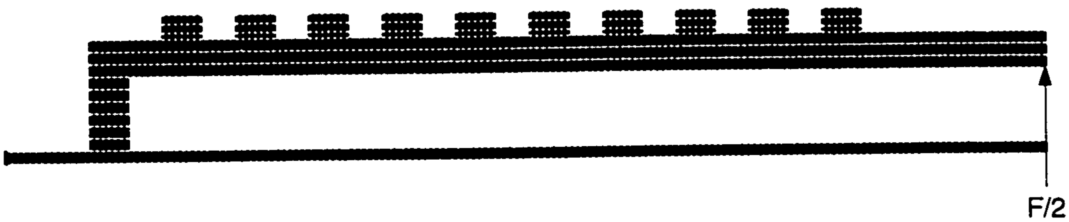

Figure 3.50: Design type *short section 10*, 2438 *DOF*, 856 elements and element size 0.33 μm × 0.67 μm

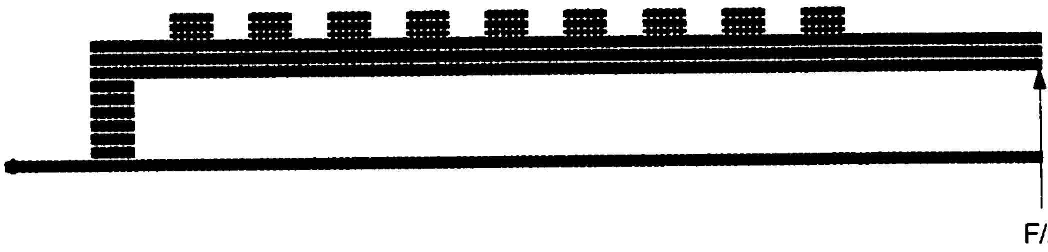

Figure 3.51: Design type *short section 9*, 2248 *DOF*, 789 elements and element size 0.33 μm × 0.67 μm

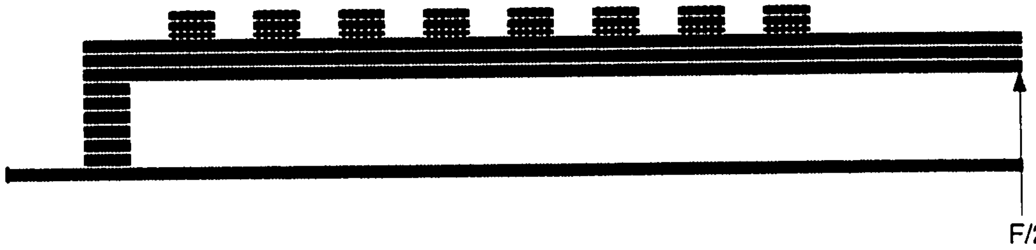

Figure 3.52: Design type *short section 8*, 2058 *DOF*, 722 elements and element size 0.33 μm × 0.67 μm

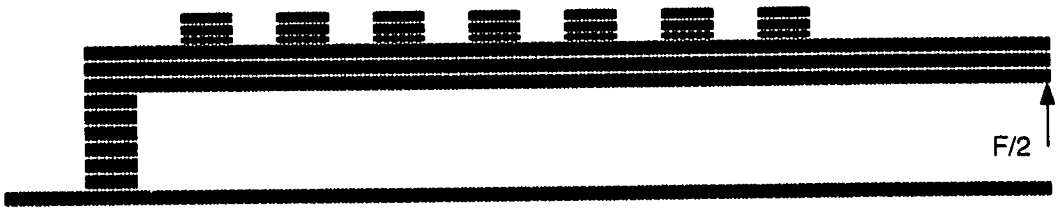

Figure 3.53: Design type *short section 7*, 1864 *DOF*, 654 elements and element size 0.33 μm × 0.67 μm

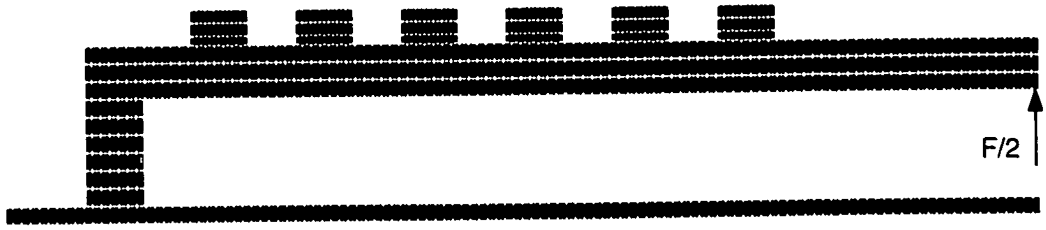

Figure 3.54: Design type *short section 6*, 1674 *DOF*, 587 elements and element size 0.33 μm × 0.67 μm

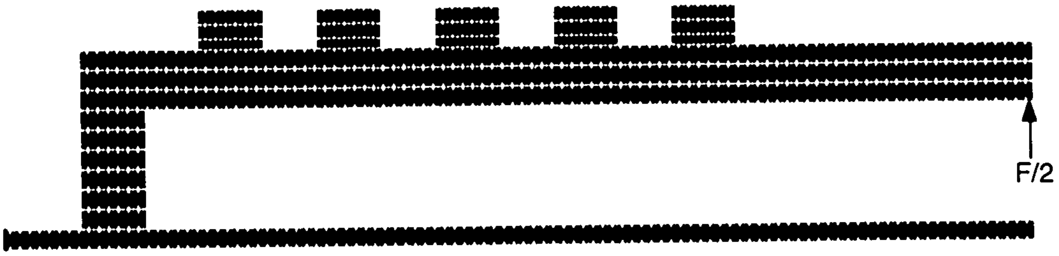

Figure 3.55: Design type *short section 5*. 1484 *DOF*. 520 elements and element size 0.4 μm × 0.67 μm

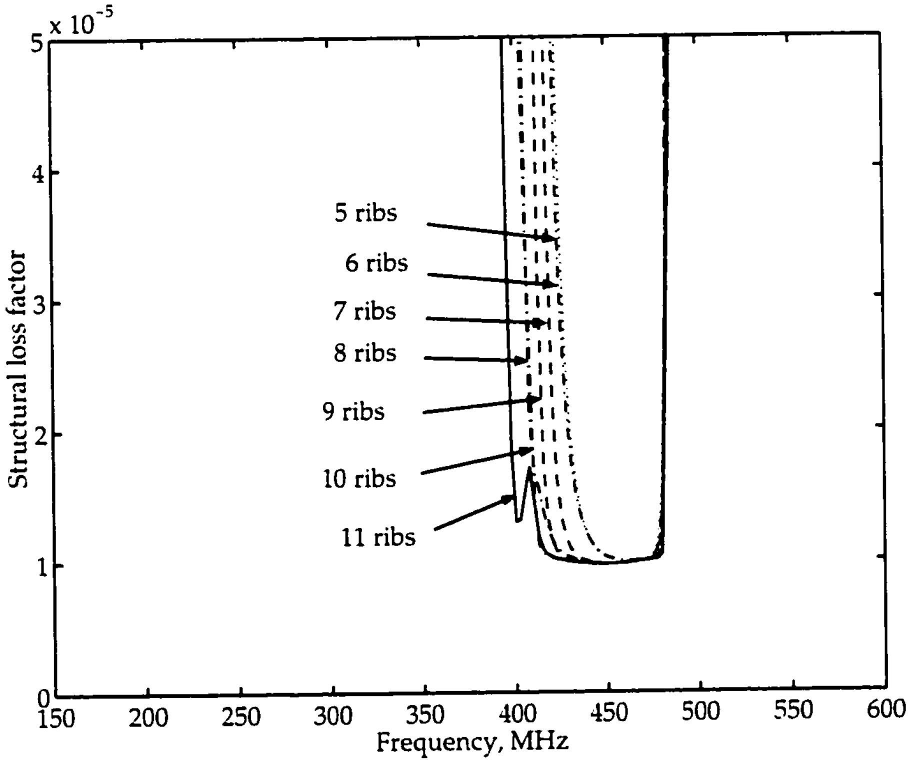

Figure 3.56: Structural loss factor for resonant structures with different rib number per side. Drive point velocity for resonant structures with different rib numbers per side. 11 ribs per side —; 10 ribs per side -·-; 9 ribs per side - - -; 8 ribs per side -·-; 7 ribs per side - - -; 6 ribs per side -·-; 5 ribs per side ...

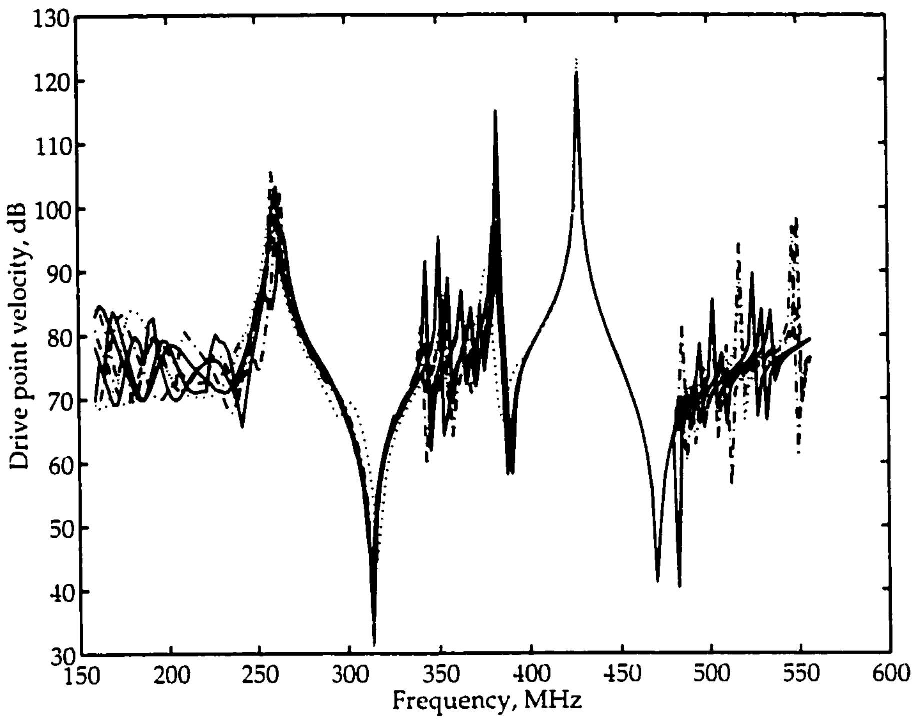

Figure 3.57: Drive point velocity magnitude for resonant structures with different rib number per side. 11 ribs per side —: 10 ribs per side -·-: 9 ribs per side - - -: 8 ribs per side -·-: 7 ribs per side - - -: 6 ribs per side -·-: 5 ribs per side ...

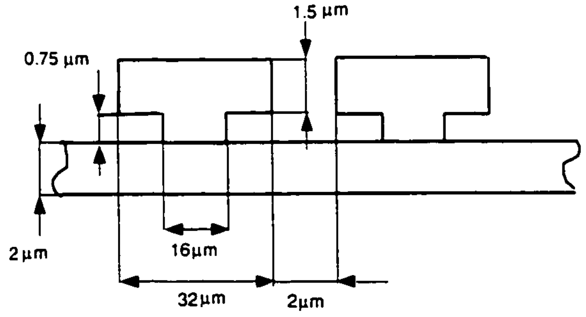

Figure 3.58: Realistic model for the ribs of high Q resonator using MUMPs^{TM} technology

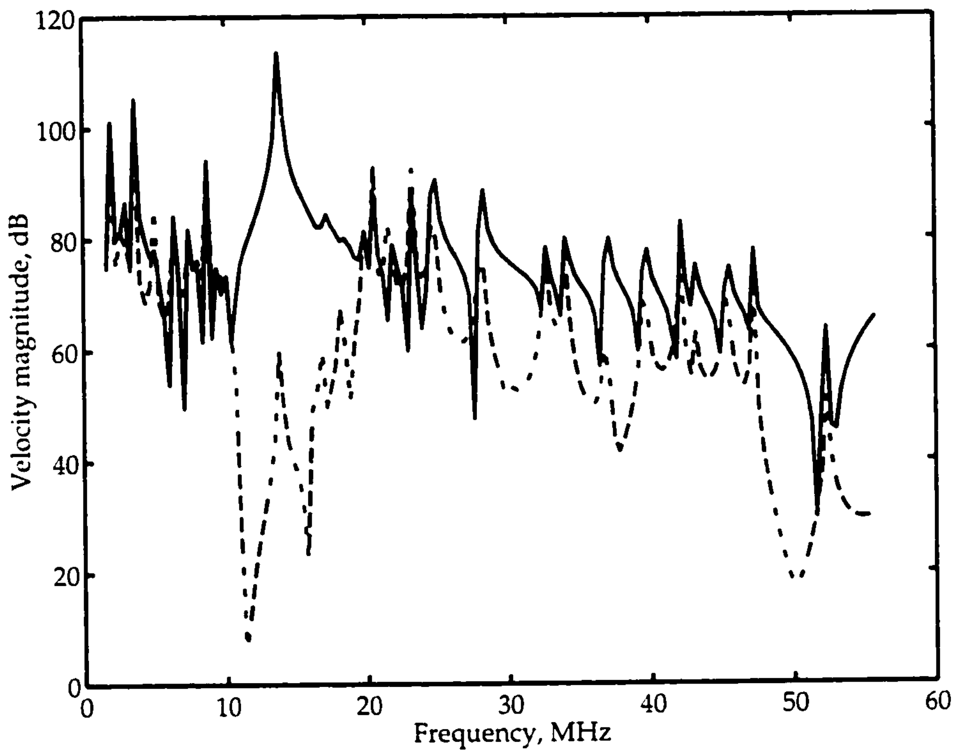

Figure 3.59: High resonator with realistic rib design. Drive point velocity magnitude —: Velocity magnitude 3.33 μm away from the support corner - - -

3.6 Manufacturing of high Q MEMS resonators with periodic design

High Q resonators are currently designed and manufactured using Multi-User MEMS Processes or MUMPs^{TM}. The MUMPs^{TM} process is a three-layer polysilicon surface micromachining process having flexibility and versatility necessary for the multi-user environment. The process begins with 100 mm n-type silicon wafers. The surfaces of the wafers are heavily doped with phosphorus in order to prevent or reduce charge feedthrough to the substrate from the electrostatic device on the surface. Next, a 600 nm low-stress LPCVD (low pressure chemical vapor deposition) silicon nitride layer is deposited on the wafers as an electrical isolation layer. This is followed directly by the deposition of a 500 nm LPCVD polysilicon film - POLY0 (see Figure 3.60).

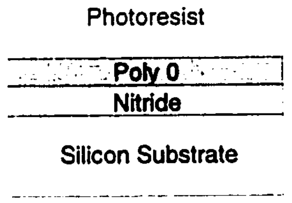

Figure 3.60: Starting surface of the wafer on the basis of which the resonators are created

POLY0 is then patterned by photolithography, a process that includes the coating of the wafers with photoresist, exposure of the photoresist with the appropriate mask and developing the exposed photoresist to create the desired etch mask for subsequent pattern transfer into the underlying layer.

In Figure 3.61 a MEMS resonator is shown fabricated by MUMPs^{TM} technology. It has a uniform design and it will serve for comparison with the newly developed periodic designs. A 0.52 μm metal layer is deposited over POLY0 and etched such

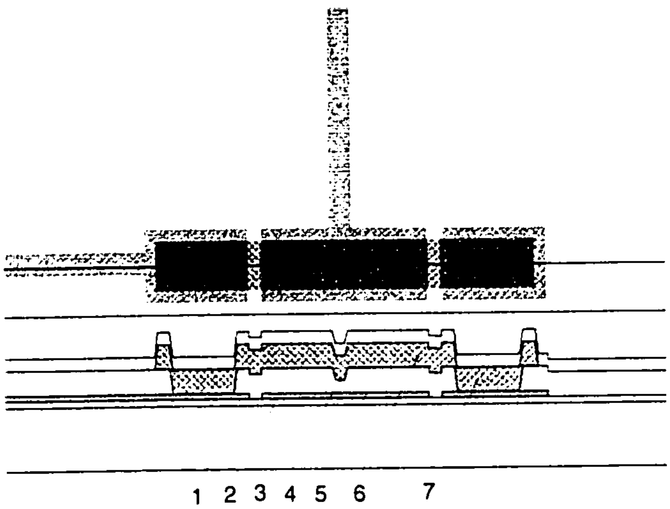

Figure 3.61: MEMS resonator fabrication by MUMPs^{TM} technology: Layers: 1-NITRIDE: 2-POLY0: 3-METAL: 4-DIMPLES: 5-First Oxide: 6-POLY1: 7-ANCHOR1

that it provides a wiring for the resonator. A 2.0 μm phosphosilicate sacrificial layer is deposited over POLY0 by LPCVD. This layer, known as First Oxide, is removed at the end of the process to free the first mechanical layer of polysilicon (POLY1). The sacrificial layer is lithographically patterned with the DIMPLES mask such that dimples with nominal depth are created. The wafers are then patterned with third mask layer ANCHOR1 and reactive ion etched. This step provides anchor holes that will be filled by POLY1 layer. After etching ANCHOR1, the first structural layer of polysilicon (POLY1) is deposited at a thickness of 2.0 μm. A thin (0.2 μm) layer is deposited over the polysilicon and the wafer is annealed reducing the net stress in POLY1 layer.

In Figure 3.62 a resonator with T-shaped rib design is shown. Resonators with three different lengths are designed by using the software layer editor L – Edit^{TM}. This design type allows simple computational modeling but is relatively hard to fabricate. In Figure 3.63, a resonator with side ribs is fabricated in three different

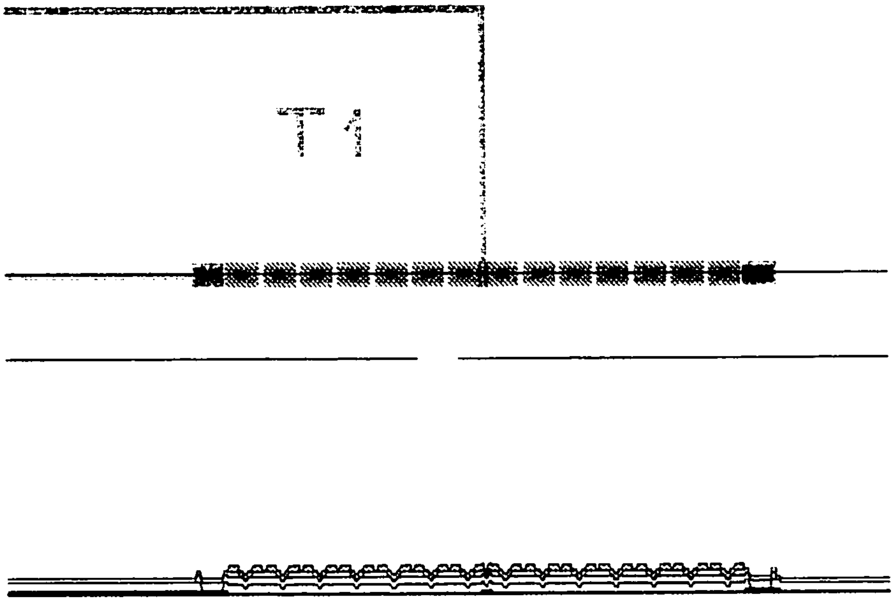

Figure 3.62: High Q resonator with T-shaped ribs design

lengths. This design type is easily manufactured and has heavy ribs, rendering a high attenuation inside the stop band. In Figure 3.64, a combined design is shown having T-shaped and side ribs.

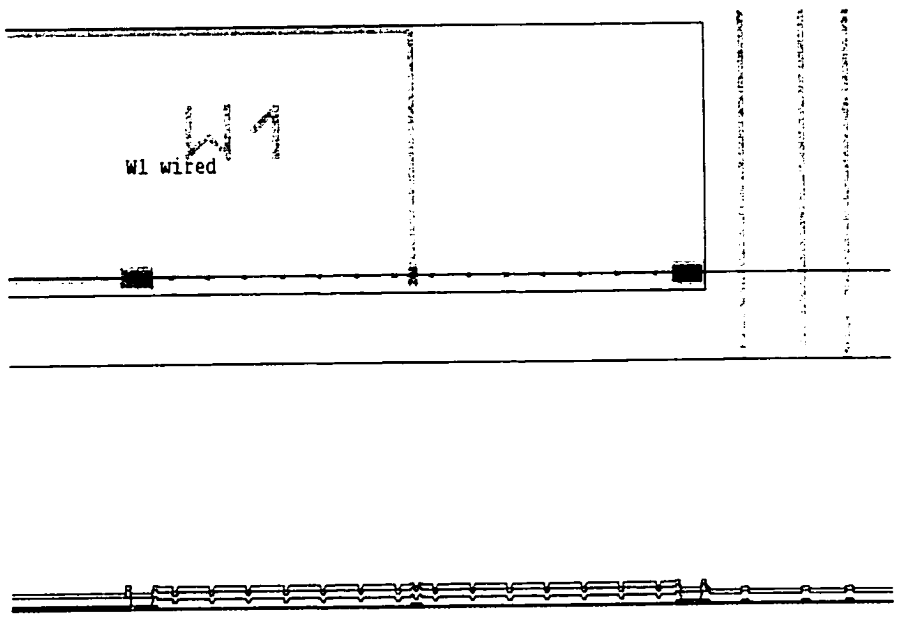

Figure 3.63: High Q resonator with side ribs design

This design has the heaviest ribs among all considered types and will be fabricated in five different lengths. In Figure 3.65, a resonator with corrugated surface is shown.

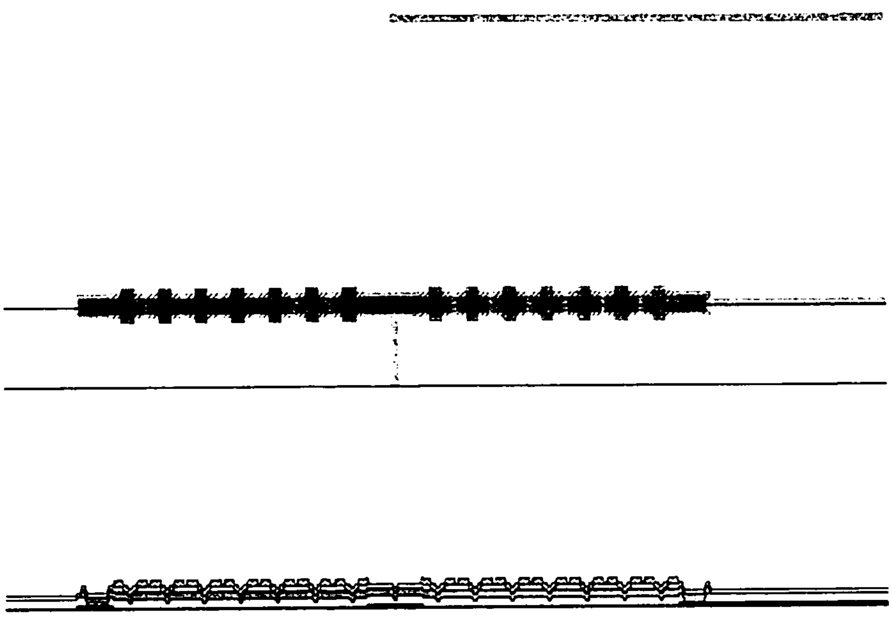

Figure 3.64: High Q resonator with combined design

This design type is easily fabricated and can be analyzed by simple 2D FE model but has very light rib due to the limitation of the MUMPs™ technology. In Figure 3.66, the whole 144-pin design pad is shown with the five resonator types. Each resonator, wired separately, will be excited independently from the others such that the response at the center of the resonator body will be measured. In future work by others, the performance of all five design types at the resonance shall be compared and the Q factor shall be measured by using standard technique.

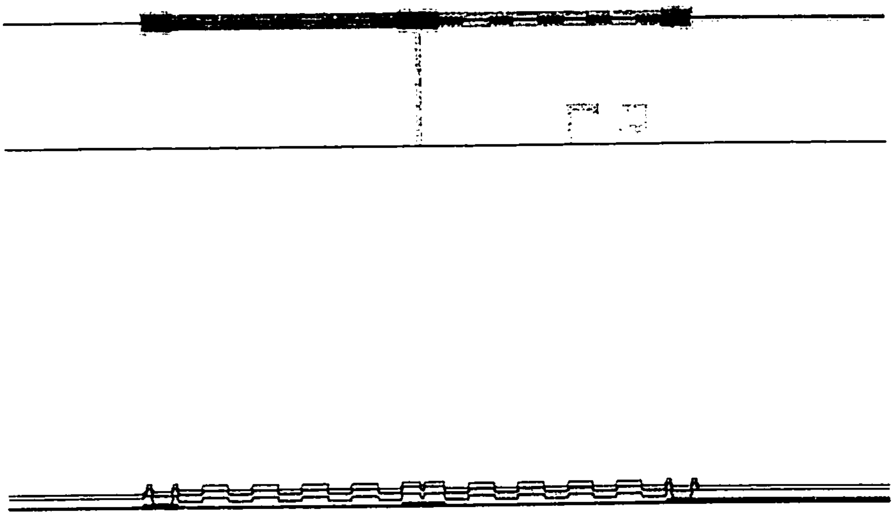

Figure 3.65: High Q resonator with corrugated design

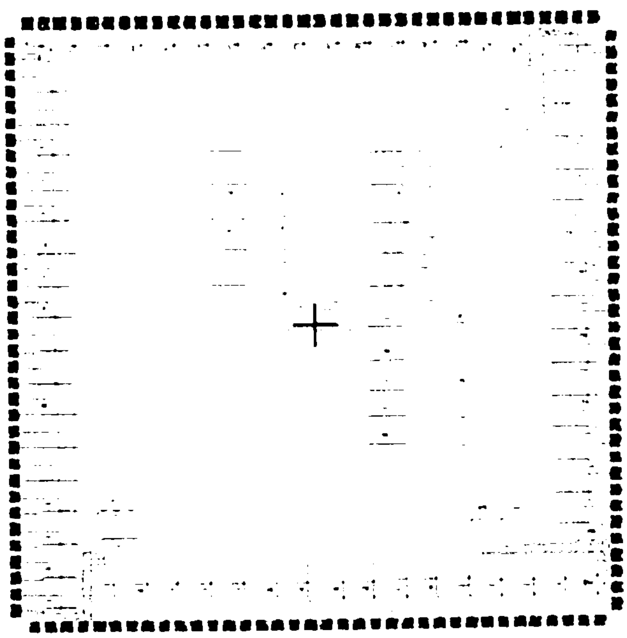

Figure 3.66: Integral circuit pad with high Q MEMS resonator designs

3.7 Chapter summary

New periodic designs of MEMS resonators with high Q factor are proposed and shown to offer significant promise. The design exploits the wave attenuation mechanisms that were analytically investigated in Chapter 2. The analysis of the beam response is performed on the basis of a finite element model. The connection between the energy localization phenomenon and the structural Q factor is formalized. On the basis of 2D FE model structures with different rib geometries and spacing ratios are studied for fabrication and testing. It is shown that certain materials added to the structure, such as tin, can worsen significantly the performance of the resonator by damping the insulation more than silicon. The effect of the rib's length and height on the performance of the resonators are demonstrated through examples. A simplified design procedure for obtaining optimal design is described on the basis of the analysis in section 3.3. The design parameters, determined with this procedure are the resonating frequency, the array spacing, and the dimensions of the structure. Realistic designs, fully integrated on chip level for high Q MEMS resonators are developed.

Chapter 4

Partial homogenization of infinite elastic structures with multiple arrays of attachments

When predicting the dynamic response of a structure, engineers often make choices about the amount of detail to include in the analysis. Typical details include ribs, stringers, welds, and bolted connections. While the inclusion of detail leads to more accurate results, it also increases the computational expense of the predictions. These considerations have led to "homogenization" – a process of approximating the effects of structural details on the dynamic response by adjusting the parameters of the homogeneous portion of the structure. This chapter presents a new approach to homogenization in which certain details are homogenized, based on consideration of their spatial patterns and dynamic properties, while other details are treated exactly.

Homogenization techniques have arisen in many contexts and the following brief survey is intended to put the present work in context and to suggest possible applications. While homogenization techniques have been developed for nonperiodic structures, this survey will focus on periodic structures. For further background on the analytical approaches and for more comprehensive discussions of applications, the reader is referred to the paper by Morgan and Babuska [56] and to texts devoted to the subject [45, 54, 60, 51].

Several papers describe homogenization of structural details for static analysis. These include the homogenization of cavities in torsion of bars [46], holes in plate buckling [47], and thickness variations in plate flexure [48]. Kolpakov *et al.* [62] present a technique for homogenizing variations in the circular cross-section of an elastic bar, resulting in separate equations for torsion, flexure, and compression. Meguid *et al.* [61] discuss the homogenization of periodic reinforcements in composite materials. Castillero *et al.* [63] present an electrostatic homogenization technique for laminated piezoelectric materials.

Homogenization techniques to approximate the propagation of waves through periodic media were pioneered by Born and Huang [41]. In considering wave propagation through three-dimensional crystal lattices, they expanded displacements in terms of Floquet waves [2] and obtained relations for the periodic amplitudes. By requiring nontrivial amplitudes, a dispersion relation was obtained. The wavelength was assumed to be large, allowing long wave expansions for the Floquet amplitudes and frequency. The leading order coefficients of these expansions were found by inserting them into the dispersion and amplitude relations. This approach was simplified by Behrens [42] using symmetry of composites that are piecewise periodic in one direction. The author generalized this approach, investigating composites that are piecewise periodic in two dimensions [43] and three dimensional periodic structures [44].

Santosa and Vogelius [55] studied the vibrations of a three dimensional periodic structure, that satisfied a Dirichlet condition on the boundary. There, the authors constructed a homogenized problem and derived asymptotic expansions for the eigenvalues up to the second order term, assuming that the periodicity of the microstructure is small enough.

Other work on complete homogenization of generalized elliptic boundary value problems with periodic coefficients was done by Conca [57] and Allaire *et al.* [59].

Potel *et al.*. [52] investigated plane wave propagation in a multilayered medium, employing a Floquet formalism and exploring the frequency range in which the homogenization is relevant. Meisenholder [53] considered sound transmission through a three-dimensional periodic structure formed by in-plane periodic plates attached together. The author formulates a general procedure for low frequency homogenization of the periodic system to an equivalent uniform medium and obtained the effective elastic constants.

Norris [50] examined the low frequency vibrations of elastic plate with rapidly varying thickness. He applied the Floquet theorem and assumed an asymptotic series expansion for the response, thereby deriving an expansion for the dispersion relation. He also showed that the first term in the dispersion relation expansion approximates the periodic structure with an equivalent uniform plate and the second non-zero term introduces a correction to this approximation, recognizing two parameters which control the approximation accuracy: the frequency and the period.

In this chapter, an arbitrary number of arrays of point-attached impedances with different spacings are added to an uniform elastic bar, forming a periodic structure with complex geometry. The partial homogenization concept developed here differs from the previously described techniques in two important aspects:

- the periodic structure is homogenized to a different periodic structure with simpler geometry for which an analytical solution is available;

- attachment impedance influences the homogenization and controls the homogenization error.

Moreover, the attachment impedance, frequency, and the array spacings are shown to justify the selective homogenization for a part of the periodic structure, smearing the less important details and keeping the critical features of the periodic structure.

The partial homogenization concept is expected to reduce the computational efforts of analyzing complex periodic structures for which analytical solutions are not available, provided that the basic cell is decomposed conveniently into periodic cells with smaller scales. The idea of partial homogenization should be applicable to a broad variety of structures described by linear differential equations. To the author's best knowledge, the partial homogenization concept, extending the notion of complete homogenization of periodic structures, has not been previously proposed or applied to the area of structural wave propagation.

The multiarray problem considered here allows analytical solution and is chosen for illustration of the partial homogenization concept for one- and two-array problems. Asymptotic expansions are derived for the Floquet wavenumber and drive-point velocity utilizing the exact solution. The leading order term of each quantity corresponds to a new effective structure with partially homogenized periodic cell. The higher order homogenization effects are captured through the second order term in the expansions, thereby obtaining a bound for the homogenization error. It is shown that the higher-order terms in the asymptotic expansions become singular in certain frequencies unlike complete homogenization. The partial homogenization concept is generalized for a P-array problem and a three-array example is included with a hierarchy of homogenized structures. Additional examples are discussed which illustrate the influence of different parameters on the homogenization error.

4.1 Problem Statement

Let us return to the multiple-array structures of Chapter 2. For simplicity, now the medium will be taken as a viscoelastic bar in longitudinal motion. The discussion applies for the flexural vibrations of beam which is governed by fourth order equation of motion, resulting in additional evanescent terms. By considering the simpler second order equation (4.1) we may clearly present a methodology of partial homogenization reducing the derivation procedure significantly.

Applications of the analysis to other analogous systems will be described at the end of this section.

The bar is represented by its cross-sectional area A_b, Young's modulus E, and mass per unit length m. Hysteretic damping is included by allowing the Young's modulus to be complex such that $E = E_0(1 - i\eta)$, where η is the loss factor.

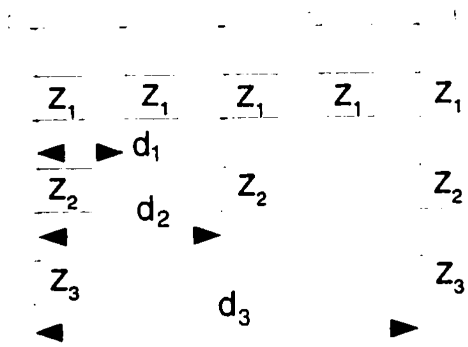

Figure 4.1: Three array periodic structure with spacings ratio $d_1/d_2/d_3 = 1/2/4$

The equation of motion governing the bar's longitudinal displacement $U(x,t)$ is

$$m\frac{\partial^2 U}{\partial t^2} - EA\frac{\partial^2 U}{\partial x^2} = Q(x,t), \tag{4.1}$$

where $Q(x,t)$ represents the longitudinal force distribution applied to the bar. This distribution contains forces exerted by the attached structures as well as externally applied force distributions. Assuming time-harmonic motion with an $e^{-i\omega t}$ dependence and using lower-case variables to denote the complex amplitudes of the time-dependent quantities, Equation 4.1 becomes

$$\frac{d^2 v}{dx^2} + {k_b}^2 v = \frac{{k_b}^2}{i\omega m} q(x) \tag{4.2}$$

where $v(x)$ is the complex amplitude of the bar velocity and $k_b = \omega\sqrt{m/EA_b}$ is the bar wavenumber. The quantity $q(x)$ represents the distributed longitudinal forces applied by the attached structures to the bar.

Each array is represented by the point impedance Z_p of each attachment and its spacing d_p, where $p = 1, \ldots, P$. The impedance Z_p is defined as the ratio of force to velocity in the same direction, where the force is applied to the attachment and the velocity is evaluated at the attachment point. Note that impedance Z_p will depend on the excitation frequency ω. As in Chapter 2, the spacing of the p^{th} array is required to be an integer multiple of the $(p-1)^{\text{th}}$ array spacing, such that $d_p = n_p d_{p-1}$. The total distributed force applied to the bar is therefore

$$q(x) = \delta(x) - v(x)\sum_{p=1}^{P} Z_p(\omega) \sum_{n=-\infty}^{\infty} \delta(x - nd_p). \tag{4.3}$$

Fourier transforming Equations (4.2) and (4.3) using the convention

$$\tilde{f}(k) = \int_{-\infty}^{\infty} f(x) e^{-ikx} dx \tag{4.4}$$

$$f(x) = \frac{1}{2\pi}\int_{-\infty}^{\infty} \tilde{f}(k) e^{ikx} dx \tag{4.5}$$

leads to

$$\tilde{v}(k) = -\sum_{p=1}^{P} Z_p \tilde{Y}(k) \sum_{m=-\infty}^{\infty} \tilde{v}(k - mk_{d,p}) \quad . \tag{4.6}$$

where the spacing wavenumber of the p^{th} array is

$$k_{d,p} = \frac{2\pi}{d_p} \tag{4.7}$$

and the wavenumber admittance of the unstiffened bar is

$$\tilde{Y}(k) = \frac{k_b^2}{i\omega m(k^2 - k_b^2)} \tag{4.8}$$

. Using the technique developed previously one can show that the dispersion relation of the P-array problem becomes

$$\cos(k_p d_p) = \cos(k_{p-1} d_p) + Z_p a_p \sin(k_{p-1} d_p). \tag{4.9}$$

Here, k_p represents the Floquet wavenumber of the structure with p arrays, defined to be in the strip

$$0 < \Re\{k_p d_p\} \leq 2\pi; \qquad 0 \leq \Im(k_p d_p); \qquad p \geq 1. \tag{4.10}$$

It is a root of $(p-1)$-array dispersion relation which can be obtained from Equation (4.9) if $p \geq 2$. The coefficient a_p is proportional to the velocity at the origin of the p-array structure with unit force applied at point of coincidence and is given by

$$a_p = \begin{cases} \dfrac{k_b}{2i\omega m} & \text{when } p = 1 \\[2ex] \dfrac{\cos(k_{p-1} d_{p-1}) - \cos(k_{p-2} d_{p-1})}{Z_{p-1} \sin(k_{p-1} d_{p-1})} & \text{when } p \geq 2 \end{cases} \tag{4.11}$$

Also of interest is the bar velocity due to an applied unit force. For simplicity, we shall evaluate the velocity at the boundaries of periodic cells of length d_1, where

d_1 is the largest array spacing. Furthermore, the applied force is assumed to act at the junction of two cells. For a bar with p attached arrays, this velocity is given by

$$v_p(nd_p) = ia_{p+1}e^{ik_p|n|d_p}. \tag{4.12}$$

where $n = 0$ represents the point at which the force is applied. Note that (4.12) is valid only if the force is applied at a point of coincidence which is defined in Chapter 2.

Also note that Equation (4.9) is a dispersion relation where only the previous step result is involved: it is solved by starting first with $p = 1$ and computing k_1 which is the Floquet wavenumber of the bar with attached first array only. Using this result one can obtain k_2 and so on until all P arrays are included.

Let us consider the P-array problem described previously. A new fictitious periodic structure is to be constructed excluding the 1st, 2nd,...,Qth arrays ($Q \leq P$) from the P array structure and prescribing a new mass per unit length, m_Q, of the unstiffened bar. The questions which arise are:

1) what effective mass per unit length m_Q has to be prescribed:

2) what will be the error of such an approximation.

In this chapter we show that the Floquet wavenumber (and also the response at the cell boundary) of the P array structure can be expanded in a power series of nondimensionalized frequency $k_b d_1$. The leading order term in such an expansion is the Floquet wavenumber of the reduced multiarray structure with a modified mass per unit length to account for the excluded arrays. The Floquet wavenumber of the reduced periodic structure will approach asymptotically that of the P array bar with decreasing frequency. In a given frequency range, the first Q arrays can be homogenized into the bar and effectively excluded from consideration, thus reducing the number of equations which have to be solved recursively.

Moreover, a hierarchy of reduced multiarray structures can be constructed such that the Floquet wavenumber of each converges asymptotically to the exact result. The frequency range of the approximation increases as the number of homogenized arrays increases. For instance, the first member of such a hierarchy will be the structure with all arrays homogenized (i.e. $Q = P$); its wavenumber will approximate the exact Floquet wavenumber over the shortest frequency range compared to other members of the hierarchy. Throughout this section subscript indices in the form P, Q shall relate the corresponding quantity to the reduced periodic structure formed by homogenization of Q arrays from the original P array problem.

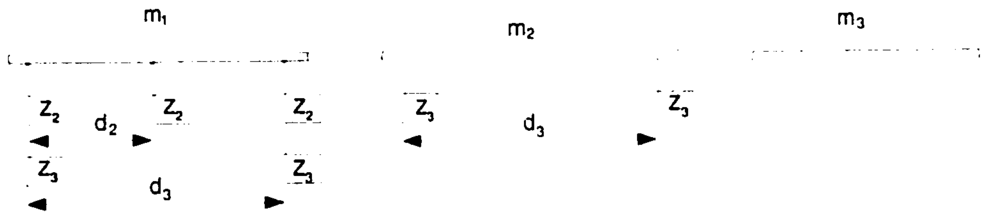

Figure 4.2: Hierarchy of partially homogenized structures

In Figure 4.2, a hierarchy of homogenized structures is shown for the three-array problem described above. The structure has the first array homogenized, the middle structure has the first and second arrays homogenized, and the right structure has all arrays homogenized. The best approximation of the original three-array structure will obtained by using the structure with homogenized first array and the worst approximation will be observed when all arrays are completely homogenized (the right structure). The notion of a partial homogenization of periodic structure with multiple scales can be extended for a broad class of periodic problems for which closed form dispersion relations do not exist, as demonstrated later in this chapter. In the analysis below the attachments will be considered as pure masses and all expansions are obtained on the basis of this assumption.

4.2 Homogenization of a structure with one array

In this section we will illustrate the method for a structure with one array. Using Equation (4.9) with $P = 1$ and omitting the array index gives the dispersion relation of the single array periodic structure

$$\cos(kd) = \cos(k_b d) + \frac{Zk_b}{2\omega mi}\sin(k_b d) \tag{4.13}$$

For convenience, we define the normalized frequency of the periodic structure as

$$\Omega = k_b d \tag{4.14}$$

and the normalized array impedance

$$\zeta = \frac{Z}{-i\omega md}. \tag{4.15}$$

Physically, ζ is the attachment impedance normalized by the impedance of the bar mass between two attachments. For the case of pure mass attachments considered here, Z has the form:

$$Z = -i\omega M \tag{4.16}$$

where M is the attachment mass. Thus, in this case, ζ will be positive real.

Equation (4.13) is nondimensionalized as

$$\cos(kd) = \cos(\Omega) - \frac{\zeta}{2}\Omega\sin(\Omega). \tag{4.17}$$

We seek values of the nondimensional wavenumber kd which satisfy Equation (4.17) for low frequencies. For this purpose, we will expand the terms in the right-hand side of Equation (4.17) in Taylor series up to Ω^4, as shown below

$$\sin(\Omega) \sim \Omega - \frac{\Omega^3}{6} + \mathcal{O}\left[\Omega^5\right] : \quad \cos(\Omega) \sim 1 - \frac{\Omega^2}{2} + \frac{\Omega^4}{24} + \mathcal{O}\left[\Omega^6\right] \tag{4.18}$$

Further, let us define

$$\Omega_1 = \Omega\sqrt{1+\zeta} \tag{4.19}$$

Then Equation (4.17) can be approximated as

$$kd \sim \cos^{-1}\left[1 - B{\Omega_1}^2\right] \tag{4.20}$$

where B is on the order of 1 and it is given as

$$B = \frac{1}{2} - \frac{1+2\zeta}{(1+\zeta)^2}\frac{{\Omega_1}^2}{24} + \mathcal{O}\,[\Omega_1]^4 . \tag{4.21}$$

Now we shall obtain an explicit expansion for kd that reveals the physics of the homogenization process. The inverse trigonometric function in Equation (4.20) is evaluated by using the following expansion

$$\cos^{-1}(1 - B{\Omega_1}^2) \sim \sqrt{2}B^{1/2}\Omega_1 + \frac{1}{6\sqrt{2}}B^{3/2}{\Omega_1}^3 + \frac{3}{80\sqrt{2}}B^{5/2}{\Omega_1}^5 + \mathcal{O}\left[B^{7/2}{\Omega_1}^7\right] . \tag{4.22}$$

where $B{\Omega_1}^2$ is small quantity. Next, we seek approximation for each of the three terms on the right-hand side of (4.22). Using the expansion (D.1) in Appendix D gives series expression for the first term in (4.22)

$$\sqrt{2}\Omega_1 B^{1/2} \sim \Omega_1 - \frac{1+2\zeta}{24(1+\zeta)^2}{\Omega_1}^3 + \mathcal{O}\left[{\Omega_1}^5\right] \tag{4.23}$$

Analogously one obtains expansion for $\frac{1}{6\sqrt{2}}B^{3/2}{\Omega_1}^3$ shown in Equation (D.2) in Appendix D. Note that $B^{5/2}{\Omega_1}^5$ term in Equation (4.22) will contribute only with Ω^5 and higher order terms and will not contribute to the leading and second order terms in the expansion (D.2). It is important to understand that the expansion holds only if the nondimensional parameter Ω_1 is small enough because the homogenization error is controlled by the magnitude of Ω_1.

Finally, the powers of Ω_1 and ${\Omega_1}^3$ are collected, giving

$$kd \sim \Omega_1 + K{\Omega_1}^3 + \mathcal{O}\left[{\Omega_1}^5\right] \tag{4.24}$$

where

$$\Omega_1 = k_b d\sqrt{1+\zeta}; \qquad K = \frac{\zeta^2}{24(1+\zeta^2)} \tag{4.25}$$

Physically, the quantity Ω_1/d represents the structural wavenumber of an unstiffened bar with with mass per unit length $m_1 = m(1+\zeta_1)$. This structure can be interpreted as one with a homogenized array of attachments. The nondimensional parameter Ω_1 is normalized frequency related to the homogenized single array problem. As ζ increases, more terms will be needed in order to homogenize the array onto the bar.

The velocity response is evaluated at the origin of the single array structure from Equation (4.12) with $p = 1$ and $n = 0$. Using Equation (4.11) with $p = 2$, one can show that

$$a_2 = \frac{1}{-i\omega m\zeta d}\frac{\cos(kd) - \cos(\Omega)}{\sin(kd)} \tag{4.26}$$

With the assumption of small Ω_1 one can expand a_2 in series of Ω_1. The details of the derivation are shown in Appendix D, (D.4) - (D.13). Using Equation (D.13) in (4.26), the following expression for a_2 is obtained

$$a_2 \sim \alpha + A{\Omega_1}^2 + \mathcal{O}\left[{\Omega_1}^4\right] \tag{4.27}$$

where

$$\alpha = \frac{1}{2i\sqrt{mEA_b(1+\zeta)}}; \qquad A = \frac{\zeta(4+3\zeta)}{48i\sqrt{mEA_b}(1+\zeta)^{5/2}} \tag{4.28}$$

The leading term α is recognized as the coefficient given by Equation (4.11) with $p = 1$ related to equivalent unstiffened bar with effective distributed mass $m_1 = m(1+\zeta)$.

Using Equations (4.27) and (4.12) with $p = 1$ and $n = 0$, the low frequency expansion for the velocity response at the origin of the single array structure becomes

$$v_1(0) \sim \nu + V{\Omega_1}^2 + \mathcal{O}\left[{\Omega_1}^4\right] \tag{4.29}$$

where

$$\nu = \frac{1}{2\sqrt{m_1 EA_b}}; \qquad V = \frac{\zeta(4+3\zeta)}{48\sqrt{mEA_b}(1+\zeta)^{5/2}} \tag{4.30}$$

Physically, ν represents the spatial velocity at the origin of an equivalent uniform bar with mass per unit length $m_1 = m(1+\zeta)$.

Note that the effective mass per unit length of the equivalent structure will be positive real in the case when the attachments are modeled as pure masses. However, it will be frequency dependent and real, positive or negative, in the case of attached springs, and complex in the case of damped attachments.

The first two terms in the asymptotic expansions (4.24) and (4.29) approximate the corresponding exact quantities if the nondimensional parameter $\Omega_1 = \Omega\sqrt{1+\zeta}$ is small enough.

4.3 Homogenization of the first array in two array periodic structure

Using Equation (4.9) with $P = 2$, the dispersion relation of the two array problem becomes

$$\cos(k_2 d_2) = \cos(k_1 d_2) + Z_2 a_2 \sin(k_1 d_2) \tag{4.31}$$

Defining the spacing ratio n_2 as

$$n_2 = \frac{d_2}{d_1} \tag{4.32}$$

and using Equation (4.24), we obtain

$$k_1 d_2 \sim \Omega_1 n_2 + \frac{n_2 {\zeta_1}^2}{24(1+\zeta_1)^2}{\Omega_1}^3 + \mathcal{O}\left[{\Omega_1}^5\right]. \tag{4.33}$$

Our goal is to obtain the first two terms of the Ω-expansion of the Floquet wavenumber of the two array problem.

Denoting

$$\epsilon_1 = \frac{n_2 {\zeta_1}^2}{24(1+\zeta_1)^2}\Omega^3 \tag{4.34}$$

and using Equation (4.33), we obtain

$$\cos(k_1 d_2) \sim \cos(\Omega_1 n_2)\cos(\epsilon_1) - \sin(\Omega_1 n_2)\sin(\epsilon_1) + \mathcal{O}\left[{\Omega_1}^5\right]. \tag{4.35}$$

In general, $n_2\Omega_1$ is not necessarily a small quantity because the spacing ratio can be large. Therefore, in Equation (4.35) we may not expand the corresponding trigonometric functions of $\Omega_1 n_2$ as Taylor series with only a few terms. Since we look only for the first two terms in the Floquet wavenumber expansion, we can make the approximation

$$\sin(\epsilon_1) \sim \epsilon_1; \qquad \cos(\epsilon_1) \sim 1 \tag{4.36}$$

Note that if we include more terms in Equation (4.36) they will contribute only to terms involving Ω^6 and higher powers. Therefore, we have

$$\cos(k_1 d_2) \sim \cos(\Omega_1 n_2) - \sin(\Omega_1 n_2)\epsilon_1 + \mathcal{O}\left[{\Omega_1}^5\right] \quad \text{and} \tag{4.37}$$

$$\sin(k_1 d_2) \sim \sin(\Omega_1 n_2) + \cos(\Omega_1 n_2)\epsilon_1 + \mathcal{O}\left[{\Omega_1}^5\right]. \tag{4.38}$$

Introducing the normalized impedance related to the second array

$$\zeta_2 = -i\omega m n_2 d_1 \tag{4.39}$$

and substituting Equation (4.27), (4.37), and (4.38) in (4.31), we obtain

$$\cos(k_2 d_2) \sim \cos(\Omega_1 n_2) - \frac{\gamma_2 \Omega_1 n_2}{2}\sin(\Omega_1 n_2) + C{\Omega_1}^3 + \mathcal{O}\left[{\Omega_1}^5\right]. \tag{4.40}$$

where the expression for C is given with Equation (D.14) in Appendix D and we have used the notation

$$\gamma_2 = \frac{\zeta_2}{1+\zeta_1} = \frac{Z_2}{-i\omega m_1 d_2}. \tag{4.41}$$

Let us consider a one-array structure with mass per unit length $m_1 = m(1 + \zeta_1)$, array spacing d_2, and array impedance Z_2, so that the structural wavenumber becomes $k_b\sqrt{1+\zeta_1}$. This structure, which can be considered as a two-array structure with homogenized first array, is expected to approximate the actual structure if the nondimensional parameter Ω_1 is small enough. Let the Floquet wavenumber of the homogenized structure, normalized by the spacing of the second array, be denoted by the quantity κ_1. Then, using Equation (4.28), the dispersion relation of this structure can be cast in the form

$$\cos(\kappa_1) = \cos(\Omega_1 n_2) - \frac{\gamma_2 \Omega_1 n_2}{2} \sin(\Omega_1 n_2) \tag{4.42}$$

This may be obtained from Equation (4.13) by substituting m, d_1, and Z_1 with m_1, d_2, Z_2. Using Equation (4.42) in (4.40), the last transforms to

$$\cos(k_2 d_2) = \cos(\kappa_1) + C\Omega_1{}^3 + \mathcal{O}\left[\Omega_1{}^5\right]. \tag{4.43}$$

Using the expansion (D.15) in Appendix D with $\alpha = \cos(k_{2,1} d_2)$ and $z \sim C\Omega^3 + \mathcal{O}\left[\Omega^5\right]$ gives an expression for the Floquet wavenumber,

$$k_2 d_2 \sim \kappa_1 + K_1 \Omega_1{}^3 + \mathcal{O}\left[\Omega_1{}^5\right] \tag{4.44}$$

where K_1 is given with Equation (D.16) in Appendix D. Thus, the structure with homogenized first array is a reasonable approximation of the original two-array structure provided that the nondimensional parameter Ω_1 is small enough.

Note that the expansion in Equation (D.15) will be divergent whenever $\alpha = 1$, which is

$$\sin(\kappa_1) = 0. \tag{4.45}$$

In the next section it will be shown that the roots of Equation (4.45) represent the "resonance" and "antiresonance" frequencies of the homogenized structure. Consequently, all terms except the leading term κ_1 in the expansion Equation (4.44) will become singular or close to singular at the "resonance" and "antiresonance" frequencies of the homogenized structure (depending on the material damping). Therefore if we want to use the first few terms in Equation (4.44) as a low frequency approximation of the two array problem, we have to require that the drive point frequency is away from the "resonance" and "antiresonance" frequencies of the homogenized structure.

Note that increasing the magnitude of ζ_1 will decrease the approximation range. Since $\Omega_1 n_2$ is generally large, this is also true for κ_1. It cannot be expanded as Taylor series keeping only few terms. This defines a domain (Ω, ζ_1) in which the asymptotic expression is a reasonable approximation.

Now let us reconsider the velocity and evaluate

$$a_3 = \frac{d_2}{Z_2} \frac{\bar{Y}_{\Sigma,2}(k_2)}{\bar{Y}'_{\Sigma,2}(k_2)} \tag{4.46}$$

from Equation (4.12). Using Equation (4.46), we get

$$a_3 = \frac{1}{-i\zeta_2 m\omega d_2} \frac{\cos(k_2 d_2) - \cos(k_1 d_2)}{\sin(k_2 d_2)}. \tag{4.47}$$

Using the expansion (4.44) similarly in (D.4) and (D.5) one can show

$$\cos(k_2 d_2) \sim \cos(\kappa_1) - \sin(\kappa_1) K_1 \Omega_1{}^3 + \mathcal{O}\left[\Omega_1{}^5\right]. \tag{4.48}$$

$$\sin(k_2 d_2) \sim \sin(\kappa_1) + \cos(\kappa_1) K_1 \Omega_1{}^3 + \mathcal{O}\left[\Omega_1{}^5\right]. \tag{4.49}$$

Now we will find expansion for a_3. Using Equation (D.12) in Appendix D, we have

$$\frac{1}{\sin(k_2 d_2)} \sim \frac{1}{\sin(\kappa_1)}\left(1 - \frac{\cos(\kappa_1)}{\sin(\kappa_1)} K_1 \Omega_1{}^3 + \mathcal{O}\left[\Omega_1{}^5\right]\right) \tag{4.50}$$

After substitution of Equations (4.35), (4.48), and (4.50) in (4.47), we get

$$a_3 \sim \alpha_1 + A_1 \Omega_1{}^2 + \mathcal{O}\left[\Omega_1{}^4\right], \tag{4.51}$$

where

$$\alpha_1 = \frac{1}{-i m_1 \omega n_2 d_1 \gamma_2} \frac{\cos(\kappa_1) - \cos(\Omega_1 n_2)}{\sin(\kappa_1)}. \tag{4.52}$$

The coefficient A_1 is given in Appendix D with (D.17). Then the velocity at the origin of the two array structure is

$$v_2(0) \sim \nu_1 + V_1 \Omega_1{}^2 + \mathcal{O}\left[\Omega_1{}^4\right], \tag{4.53}$$

where

$$\nu_1 = \frac{1}{m_1 \omega n_2 d_1 \gamma_2} \frac{\cos(\kappa_1) - \cos(\Omega_1 n_2)}{\sin(\kappa_1)}. \tag{4.54}$$

Here, the coefficient V_1 is given with

$$V_1 = i A_1. \tag{4.55}$$

Comparing (4.53) with (4.26), the leading term in (4.53) represents the velocity of the origin of the discussed earlier single array structure given with $m_1 = m(1 + \zeta_1)$, d_2, and Z_2. Since $\Omega_1 n_2$ is not necessarily small if Ω_1 is small, ν_1 may not be represented with a truncated Taylor series.

4.4 "Resonance" and "antiresonance" frequencies of the two array structure with first array homogenized

Using Equation (4.42), the drive point velocity of the homogenized structure given in (4.54) can be transformed to

$$\nu_1 = \frac{1}{2\sqrt{m_1 E A_b}} \frac{\sin(\Omega_1 n_2)}{\sin(\kappa_1)}. \tag{4.56}$$

Using the identity $\sin(\kappa_1) = \pm\sqrt{1-\cos^2(\kappa_1)}$, we obtain

$$\sin(\kappa_1) = \sin(\Omega_1 n_2)\left\{\cos(\Omega_1 n_2)\gamma_2\Omega_1 n_2 - \left[\left(\frac{\gamma_2\Omega_1 n_2}{2}\right)^2 - 1\right]\sin(\Omega_1 n_2)\right\} \tag{4.57}$$

and therefore

$$\nu_1 \sim \frac{\sqrt{\sin(\Omega_1 n_2)}}{\sqrt{\cos(\Omega_1 n_2)\gamma_2\Omega_1 n_2 - \left[\left(\frac{\gamma_2\Omega_1 n_2}{2}\right)^2 - 1\right]\sin(\Omega_1 n_2)}}. \tag{4.58}$$

From Equation (4.58), we deduce that the drive point velocity approaches zero for zero loss factor if and only if

$$\sin(\Omega_1 n_2) = 0 \tag{4.59}$$

The roots of the latter are the "antiresonance" frequencies of the periodic structure. Again from Equation (4.58) it follows that the drive point velocity approaches infinity (depending on the loss factor) if and only if

$$\tan(\Omega_1 n_2) = \frac{\gamma_2 \Omega_1 n_2}{\left(\frac{\gamma_2 \Omega_1 n_2}{2}\right)^2 - 1}. \tag{4.60}$$

The roots of Equation (4.60) represent the "resonance" frequencies, of the periodic structure. It can be shown that in the case when γ_2 is purely imaginary, (4.60) does not have real roots and "resonance" frequencies do not exist. This is the case when the first array is modeled with pure masses or pure springs and the second array is modeled with pure dashpots. Also from Equation (4.57) we observe that the roots of the equation

$$\sin(\kappa_1) = 0 \tag{4.61}$$

are either "resonance" or "antiresonance" frequencies as described in the previous paragraph.

4.5 Homogenization of both arrays in a two array periodic structure

If the frequency range is small enough and the spacing ratio n_2 is not large, then $\Omega_1 n_2$ and κ_1 are small quantities and the trigonometric functions of these parameters can be expanded as truncated Taylor series. Thus the second array can be homogenized onto the bar allowing additional simplification of the expansions for the Floquet wavenumber and the velocity response.

Comparing the nondimensionalized dispersion relation Equation (4.42) with Equation (4.17) we obtain $\Omega_1 n_2$-expansion of κ_1 by using Equation (4.24) with γ_2 and $\Omega_1 n_2$

instead of ζ_1 and Ω,

$$\kappa_1 \sim \sqrt{1+\zeta_1+\zeta_2}\Omega_1 n_2 + \frac{\zeta_2^2}{24\sqrt{1+\zeta_1+\zeta_2}}\Omega_1 {n_2}^3 + \mathcal{O}\left[(\Omega_1 n_2)^5\right]. \tag{4.62}$$

Now we expand the term K_1 in the right side of Equation (4.44). Using

$$\cos(\Omega_1 n_2) \sim 1 - \frac{\Omega_1 {n_2}^2}{2} + \mathcal{O}\left[(\Omega_1 n_2)^4\right] \qquad \sin(\Omega_1 n_2) \sim \Omega_1 n_2 - \frac{\Omega_1 {n_2}^3}{6} + \mathcal{O}\left[(\Omega_1 n_2)^5\right]. \tag{4.63}$$

we simplify Equation (D.14) keeping only $(\Omega_1 n_2)$ and $(\Omega_1 n_2)^3$ terms. This results in Equation (D.18) of Appendix D). Let us define

$$\Omega_2 = \sqrt{1+\zeta_1+\zeta_2} n_2 \Omega \tag{4.64}$$

and

$$\epsilon_2 = n_2^3 \frac{\zeta_2^2}{24\left(1+\zeta_1+\zeta_2\right)^2}{\Omega_2}^3 \tag{4.65}$$

Then using Equation (4.62), we have

$$\sin(\kappa_1) \sim \sin(\Omega_2) + \cos(\Omega_2)\epsilon_2 + \mathcal{O}\left[(\Omega_1 n_2)^5\right] \tag{4.66}$$

Now let us assume that the parameter Ω_2 is so small that the sine and cosine in (4.66) can approximated by the first and second terms as

$$\cos(\Omega_2) \sim 1 - \frac{{\Omega_2}^2}{2} + \mathcal{O}\left[{\Omega_2}^4\right] \qquad \sin(\Omega_2) \sim \Omega_2 - \frac{{\Omega_2}^3}{6} + \mathcal{O}\left[{\Omega_2}^5\right] \tag{4.67}$$

Note that the assumption for small Ω_2 implies smallness of $\Omega_1 n_2$. Thus the small parameter which controls the approximation accuracy will be Ω_2 and not $\Omega_1 n_2$. Consequently, all series in this section will be expanded in terms of Ω_2.

Using (4.67) in (4.66) leads to

$$\sin(\kappa_1) \sim \Omega_2 \left[1 + \frac{{\Omega_2}^2}{24} \left(\frac{\zeta_2^2}{1+\zeta_1+\zeta_2} - 4n_2 \right) + \mathcal{O}\left[{\Omega_2}^4\right] \right]. \tag{4.68}$$

With Equation (4.66) and Equation (4.68) and using Equation (D.12) as before, K_1 simplifies to Equation (D.19) in Appendix D.

Since we want to retrieve only the first two terms (Ω_2 and ${\Omega_2}^3$) in the Floquet wavenumber expansion, we need to consider only the leading term in Equation (D.19) (see Equation (4.44)). Therefore we can approximate

$$K_1 \sim \frac{n_2}{24} \frac{\zeta_1^2 + 2\zeta_1\zeta_2}{\sqrt{1+\zeta_1+\zeta_2}}. \tag{4.69}$$

Substituting (4.69) and (4.62) into (4.44) leads to the final result for the Floquet wavenumber when both arrays are homogenized.

$$k_2 d_2 \sim \kappa_2 + K_2 {\Omega_2}^3 + \mathcal{O}\left[{\Omega_2}^5\right], \tag{4.70}$$

where

$$\begin{aligned} \kappa_2 &= \Omega_2 = \Omega n_2 \sqrt{1+\zeta_1+\zeta_2}; \\ K_2 &= n_2 \frac{\zeta_1^2 + 2\zeta_1\zeta_2 + n_2\zeta_2^2}{24\left(1+\zeta_1+\zeta_2\right)^2} \end{aligned} \tag{4.71}$$

Here, κ_2 is the normalized wavenumber of the two array structure with both array homogenized and is equal to the bar wavenumber $\omega\sqrt{\dfrac{m(1+\zeta_1+\zeta_2)}{EA_b}}$ of unstiffened bar with mass per unit length $m_2 = m(1+\zeta_1+\zeta_2)$.

In order to obtain a more accurate expression for κ_2 and to increase the approximation range of the latter, higher order terms, such as ${\Omega_2}^5$ and ${\Omega_2}^7$, have to be included in Equation (4.70). They represent higher order homogenization effects and can be obtained including more terms in the expansions (4.62) and (4.63).

The velocity at the origin of the two array structure can be expanded in a similar way. To do so, we use the expansion in Equation (4.53) and additionally require Ω_2 to be small quantities. Thus, Ω_2-expansions of all involved trigonometric functions of κ_2 can be computed and, after some algebra, one gets

$$v_2(0) \sim \nu_2 + V_2{\Omega_2}^2 + \mathcal{O}\left[{\Omega_2}^4\right]. \tag{4.72}$$

where

$$\begin{aligned} \nu_2 &= \frac{1}{2\sqrt{mEA_b}(1+\zeta_1+\zeta_2)} \\ V_2 &= \frac{3\zeta_1^2 + n_2^2\zeta_2(4+3\zeta_2) + 2\zeta_1\left[2+(1+2n_2^2)\zeta_2\right]}{48n_2^2\sqrt{mEA_b}(1+\zeta_1+\zeta_2)^3}. \end{aligned} \tag{4.73}$$

The leading order term, ν_2, represents the velocity at the origin of equivalent unstiffened bar with effective mass $m_2 = \sqrt{1+\zeta_1+\zeta_2}m$, which takes into account the homogenization of the both arrays. Note that the derivation of these asymptotic expansions relies on the assumption that $\Omega_2 = k_b d_2\sqrt{1+\zeta_1+\zeta_2}$ is small. If the magnitude of the normalized impedances ζ_1 and ζ_2, or the spacing ratio n_2 are increased, then $k_b d_2$ has to be small enough to approximate the exact result with the first two terms in Equation (4.70) and Equation (4.72). This observation can be confirmed by looking at V_2 in Equation (4.73). If we increase the magnitude of ζ_1, ζ_2 or n_2, the magnitude of the latter terms become comparable to the first term and these terms have to be included. In the limiting case when either some of the arrays represent rigid supports or the second array has infinite spacing, homogenization of both arrays is not possible.

4.6 Extension to the general case

Let us extend our discussion to the general case of a P array structure with the first Q arrays homogenized ($Q \leq P$). The normalized impedance of the pth array is defined by

$$\zeta_p = \frac{Z_p}{-i\omega m d_p}; \qquad p = 1, \ldots, P. \tag{4.74}$$

. Note that for the case of pure mass attachments, considered here, Z_p can be expressed as

$$Z_p = -i\omega M_p \tag{4.75}$$

where M_p is the mass of an attachment from the pth array. Thus ζ_p is positive real.

A nondimensional frequency, related to the reduced structure is defined as

$$\Omega_Q = k_b d_Q \sqrt{1 + \sum_{r=1}^{Q} \zeta_r} \tag{4.76}$$

and the mass per unit length of the reduced structure is

$$m_Q = m \left[1 + \sum_{r=1}^{Q} \zeta_r \right]. \tag{4.77}$$

Further, we denote the Floquet wavenumber and the velocity response at the origin of the reduced structure by κ_Q and ν_Q. Since this multiarray problem is described by recursive equations corresponding to the number of attached arrays, this approach can be applied to the general P-array problem. The asymptotic expansions up to the first and second term for the Floquet wavenumber and the velocity response at the origin have the form

$$k_P d_P \sim \kappa_Q + K_Q \Omega_Q{}^3 + \mathcal{O}\left[\Omega_Q{}^5\right] \tag{4.78}$$

and

$$v_P(0) \sim \nu_Q + V_Q \Omega_Q{}^2 + \mathcal{O}\left[\Omega_Q{}^4\right]. \tag{4.79}$$

These expansions can be developed by assuming that Ω_Q is a small parameter and by approximating trigonometric functions of Ω_Q as truncated Taylor series, keeping only the first several terms. Note that the smallness of Ω_Q implies the smallness of Ω_{Q-1}.

The leading term in (4.78) and (4.79) will asymptotically approach the exact quantity if Ω_Q is small. In other words, the waves propagating through the structure will not "see" a given array of attachments if the frequency is small enough, and the array spacing and the array impedances are not too large. The correction terms K_Q and V_Q in the expansions (4.78) and (4.79), in general, depend on the frequency and tend to constant values in the low frequency limit, so that

$$\lim_{\Omega_Q \to 0} K_Q = const_1;$$
$$\lim_{\Omega_Q \to 0} V_Q = const_2; \qquad Q = 1, \ldots, P \tag{4.80}$$

Further, it can be shown that if $P > Q$ there is a discrete set of frequencies at which the higher order terms become large and the asymptotic expansions are not convergent in a small interval around those frequencies. The size of the interval depends on the structural loss factor. Moreover, it can be shown that at those frequencies the structural response of the corresponding homogenized structure with a reduced number of arrays tends either to infinity or to zero. Those are recognized to be the "resonance" and "antiresonance" frequencies of the corresponding homogenized structure with a reduced number of arrays.

4.7 Examples

Throughout the examples, the bar material is assumed to be steel with Young's modulus $E = 2.11 \times 10^{11}$ N/m^2, cross-sectional area $A_b = 10^{-4}m$, and loss factor $\eta = 0.01$. The structure has spacing $d = 1m$ and the attachment is modeled as pure mass equal to that of the uniform bar with length d. Figure 4.3 shows the imaginary part of the Floquet wavenumber expansion for a structure with one array of attachments. We see that adding the second term in the asymptotic expansion

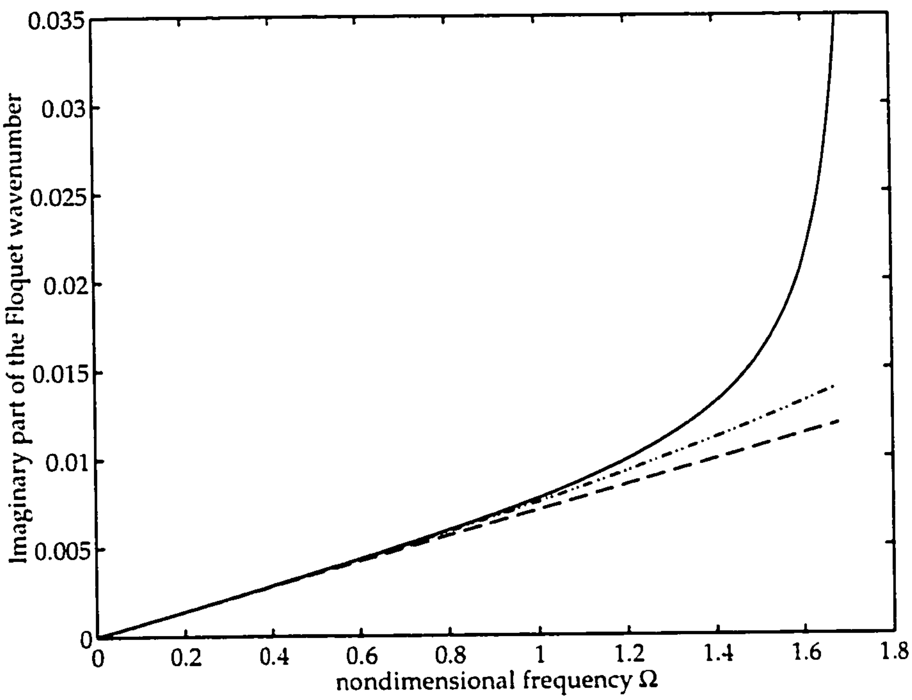

Figure 4.3: The imaginary part of the Floquet wavenumber for a single array structure with unit spacing. Exact solution —: First term in the wavenumber expansion - - -: First and second term in the latter -·-

improves the approximation. The same is true for the real part of the Floquet wavenumber as shown in Figure 4.4. The drive point velocity magnitude of the structure is shown in Figure 4.5. The leading order behavior with respect to the

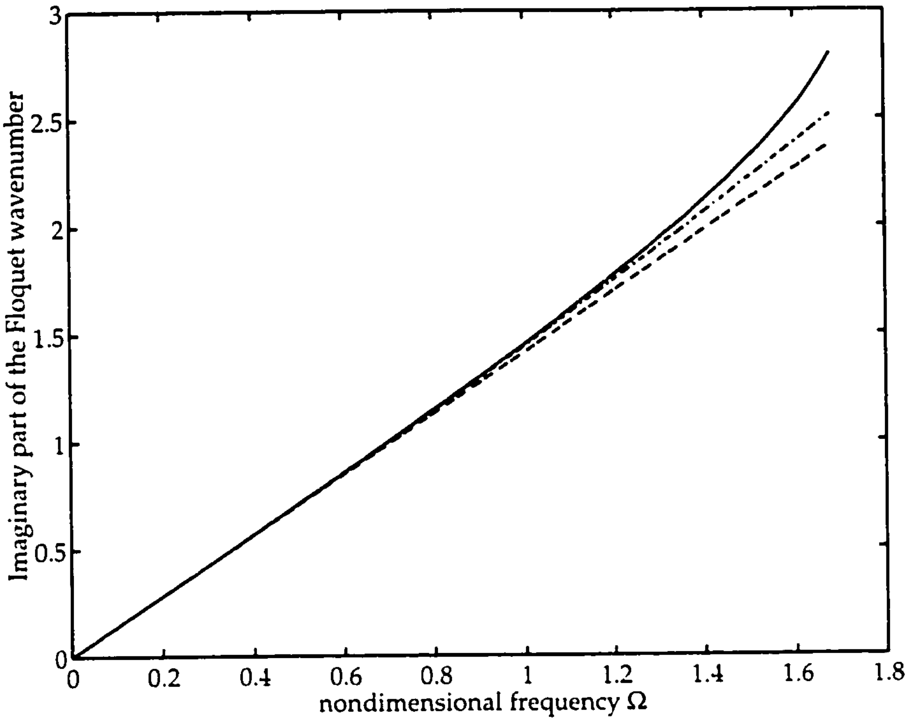

Figure 4.4: The real part of the Floquet wavenumber for a single array structure with unit spacing. Exact solution —; First term in the wavenumber expansion - - -; First and second term in the latter -· -

velocity is the constant $\frac{1}{2}[m(1+\zeta_1)EA_b]^{-1/2}$. Figure 4.6 depicts the normalized error in wavelength, defined as

$$\epsilon_{n.e.w.} = \left|\frac{\lambda_e - \lambda_a}{\lambda_e}\right|; \qquad \lambda = \frac{2\pi}{\Re(k)} \tag{4.81}$$

Here λ_e and λ_a denote the wavelength computed by the exact and homogenization solution accordingly. Varying the phase and the magnitude of the normalized impedance the highest wavelength error is plotted in the frequency interval $1. \Omega_{max}$. There are two sets of contour plots in the figure for two different frequency ranges $\Omega \in (0, 0.5)$ and $\Omega \in (0, 1)$. Not surprisingly, the lower values for the normalized impedance magnitude result in higher wavelength error for the longer frequency

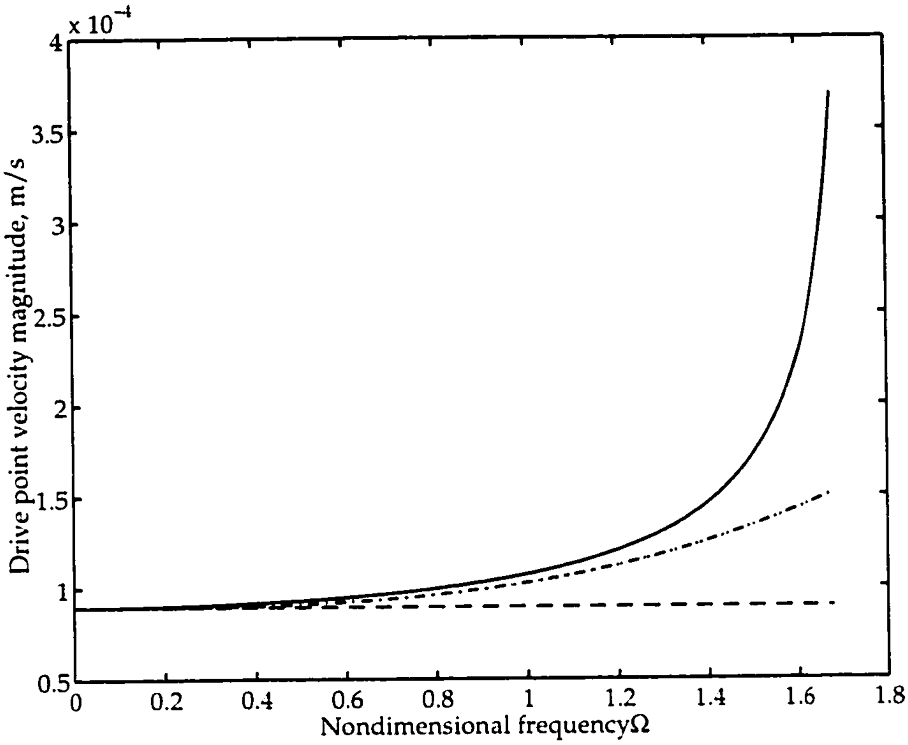

Figure 4.5: The drive point velocity magnitude for a single array structure with unit spacing. Exact solution —: First term in the wavenumber expansion - - -: First and second term in the latter -·-

range. Regions are observed where higher impedance magnitudes result in small wavelength error. For instance, for Ω_{max} normalized impedance phase between 0.5 and 1 radians.

Figure 4.7 shows the normalized error in attenuation given by

$$\epsilon_{n.e.a.} = \left| \frac{\Im(k_e) - \Im(k_a)}{\Im(k_e)} \right| . \tag{4.82}$$

Here, k_e and k_a denote the Floquet wavenumber computed by the exact and homogenization solution accordingly. Again, a region is observed where the error is not sensitive to the impedance magnitude (for instance, normalized impedance phase

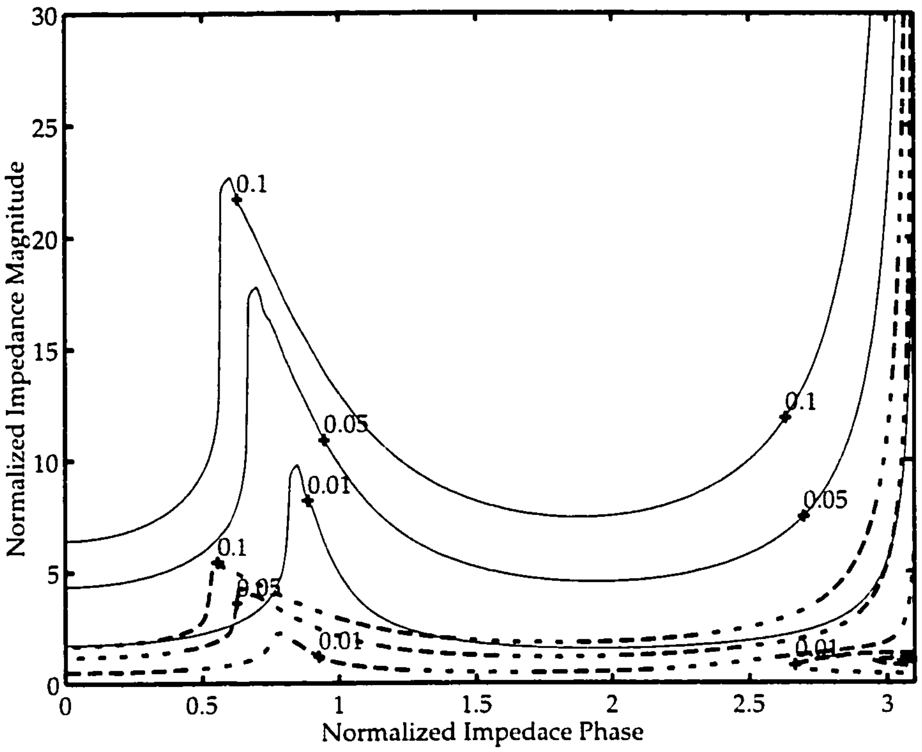

Figure 4.6: Normalized error in wavelength for a single array structure with unit spacing. $\Omega_{max} = 0.5$ —: $\Omega_{max} = 1$ - - -

between 1.6 and 2 radians for $\Omega_{max} = 1$).

Figure 4.8 shows the normalized error in wavelength for two array structure. The error is between the exact solution and the solution with homogenized first array. As before, there are two sets of contour plots for two different frequency ranges. In this case, complex curves of constant error are observed that resemble those of a single-array structure.

Figure 4.9 depicts the normalized error in wavelength for a two-array structure. Two different spacing ratios are compared - $d_1/d_2 = 1/6$ and $d_1/d_2 = 1/2$. Again, regions exist where the error is less sensitive with respect to the impedance magnitude

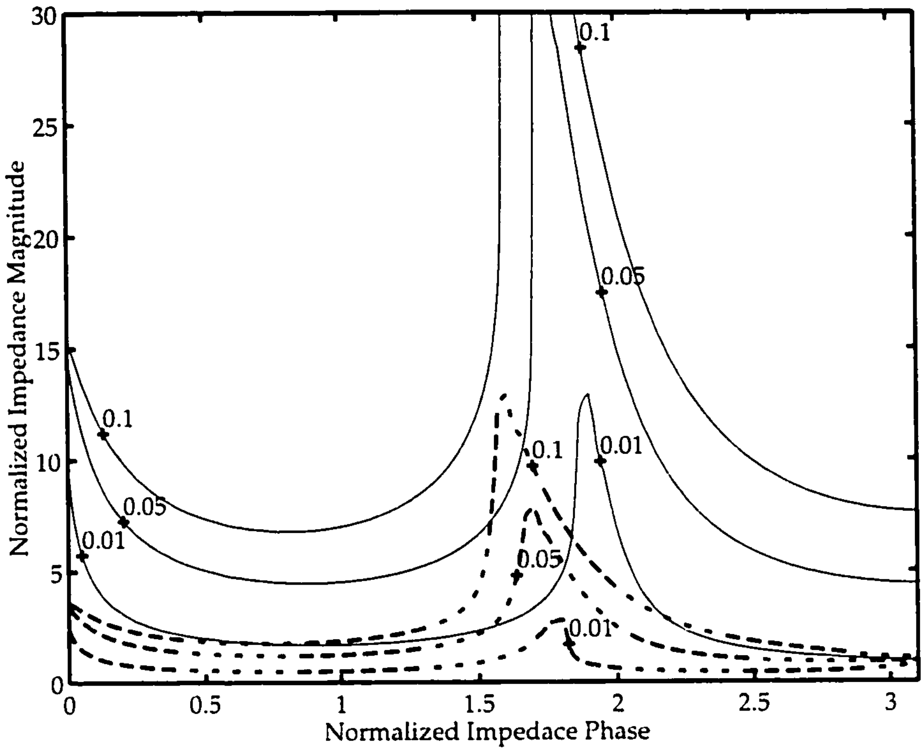

Figure 4.7: Normalized error in attenuation for a single array structure with unit spacing. $\Omega_{max} = 0.5$ —: $\Omega_{max} = 1$ - - -

(for instance, between 0.5 and 1 radians and between 2.7 and π radians).

Figure 4.10 presents the imaginary part of the Floquet wavenumber plotted for three different types of impedances: pure mass ($\zeta = 1$), pure dashpot ($\zeta = \frac{i}{\Omega}$), and pure spring ($\zeta = \frac{-1}{\Omega^2}$). The structure has two arrays with spacing ratio $d_1/d_2 = 1/6$. The exact solution for this structure is compared to the case when the first array is homogenized. It is observed that the homogenization technique renders accurate results for the dashpot and mass impedance provided that the normalized frequency is sufficiently low. For the spring impedance, the homogenization concept does not produce converging result in the low frequency region. Similar observations can be made for the response of the structure shown in Figure 4.11. Figure 4.12 shows the imaginary part of the Floquet wavenumber for a two-array structure with spacing

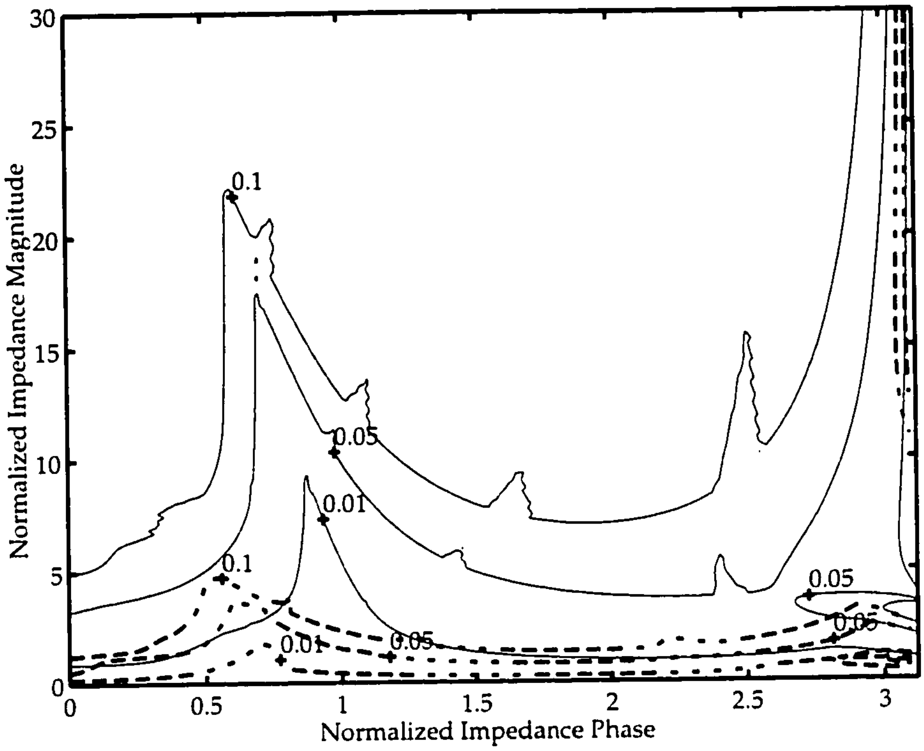

Figure 4.8: Normalized error in wavelength for two array structure with spacing ratio $d_1/d_2 = 1/6$. $\Omega_{max} = 0.5$ —; $\Omega_{max} = 1$ - - -

ratio $d_1/d_2 = 1/2$ and with the impedances modeled as pure masses. The array with the smallest spacing is homogenized.

A comparison is made between the asymptotic expansion with leading order term only and with the first and second order terms. The second term improves the approximation. In this particular example, the second order homogenization effects have significant contribution in the region of the minor stop band ($0.75 < \Omega < 1.1$). Note that spikes can be seen due to the second term in the frequencies $\Omega = 0.78$, $\Omega = 1.1$, and $\Omega = 1.6$, which are the "resonance" and "antiresonance" frequencies of the structure with homogenized first array. Better approximation of the two term expansion is also observed in the real part of the Floquet wavenumber shown in Figure 4.13 and drive point velocity magnitude in Figure 4.14. As before, spikes due to the

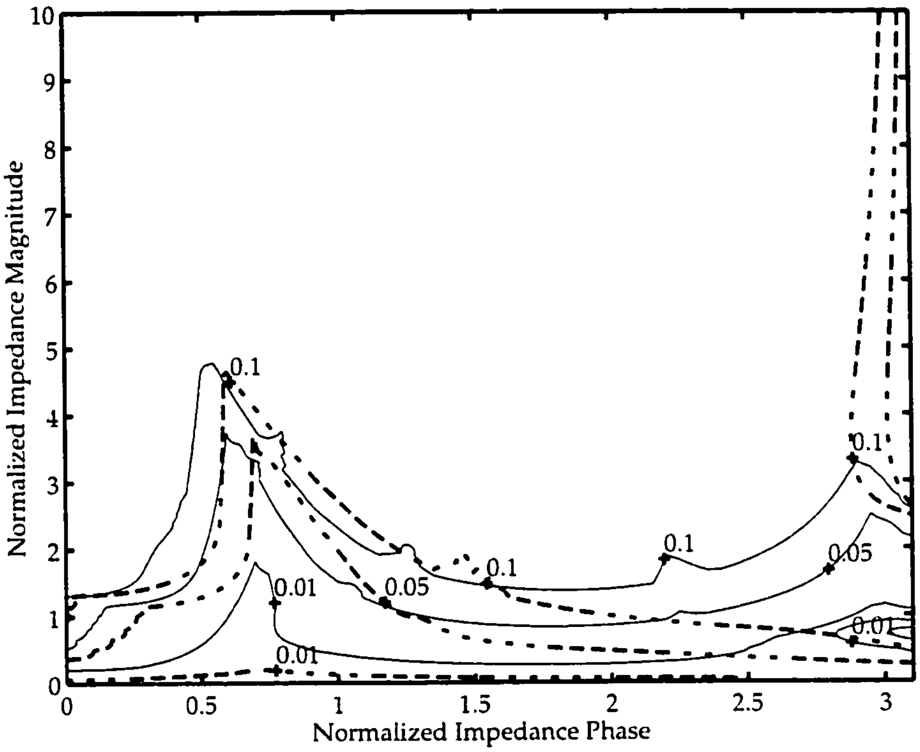

Figure 4.9: Normalized error in wavelength for two array structure with normalized frequency $\Omega_{max} = 1$. $d_1/d_2 = 1/6$ —; $d_1/d_2 = 1/2$ - - -

second order term are observed around $\Omega = 0.78$, $\Omega = 1.1$, and $\Omega = 1.6$. In Figure 4.15, the imaginary part of the Floquet wavenumber is computed for the hierarchy of homogenized structures shown in Figure 4.16. The structure with homogenized first array approximates stop bands due to the second ($0.58 < \Omega < 1.1$) and the third array ($0.35 < \Omega < 0.48$ and $1.2 < \Omega < 1.3$) but it does not approximate the stop band due to the array with smallest spacing ($\Omega > 1.33$).

Partial homogenization can be applied in multiperiodic problems for which there is not analytical solution, replacing computational procedure with simple analytical expansions valid in some low frequency region. In this regard, let us reconsider the arrays with offset from section 2.7 In Figure 4.17, two-array structures with spacings $d_1 = 1m$, $d_2 = 6m$ are depicted. The first one has an offset of $1/3\ m$ between the

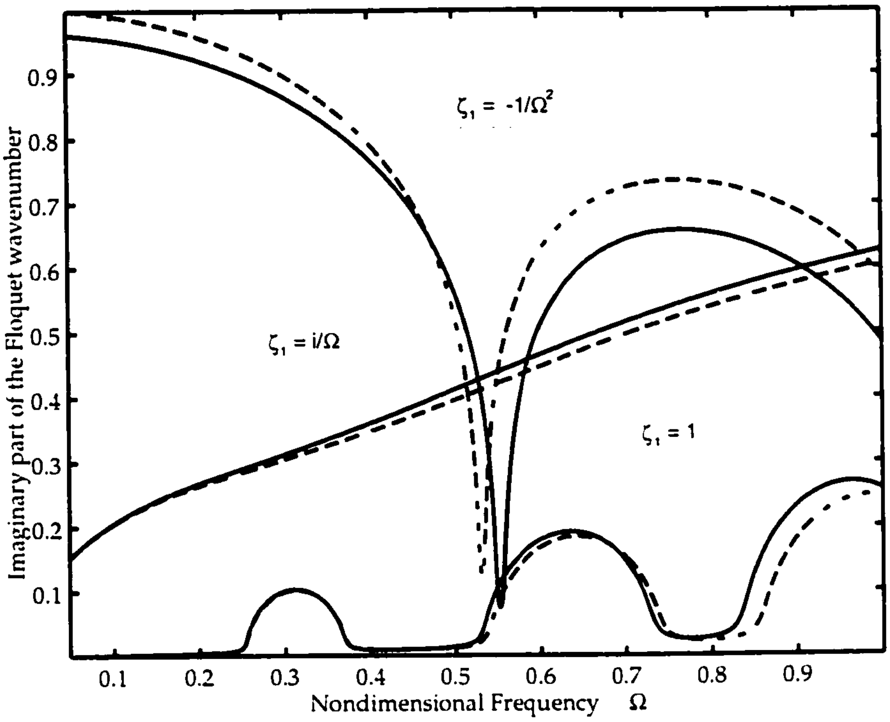

Figure 4.10: Imaginary part of the Floquet wavenumber of two array structure with spacing ratio $d_1/d_2 = 1/6$. Exact solution —: The first term in the wavenumber expansion with homogenized first array - - -

arrays and in the second one the arrays are perfectly aligned. There is a frequency range in which the waves propagating through the structure do not "see" the array with the smaller spacing but still recognize the array with larger spacing. In this frequency range, one can homogenize the first array and use an equivalent one array structure as a reasonable approximation. This will reduce the costs of modeling the homogenized array. The homogenized structure is depicted in the bottom of Figure 4.17. As shown in Figures 4.18 – 4.19, both two array structures have similar behavior and the offset does not affect dispersion for values of the nondimensional frequency $\Omega < 0.4$. In this frequency range, the partially homogenized structure, shown on the bottom in Figure 4.17, approximates well the two array structure. One can see that homogenizing the first array causes the major stop band (starting approx. at

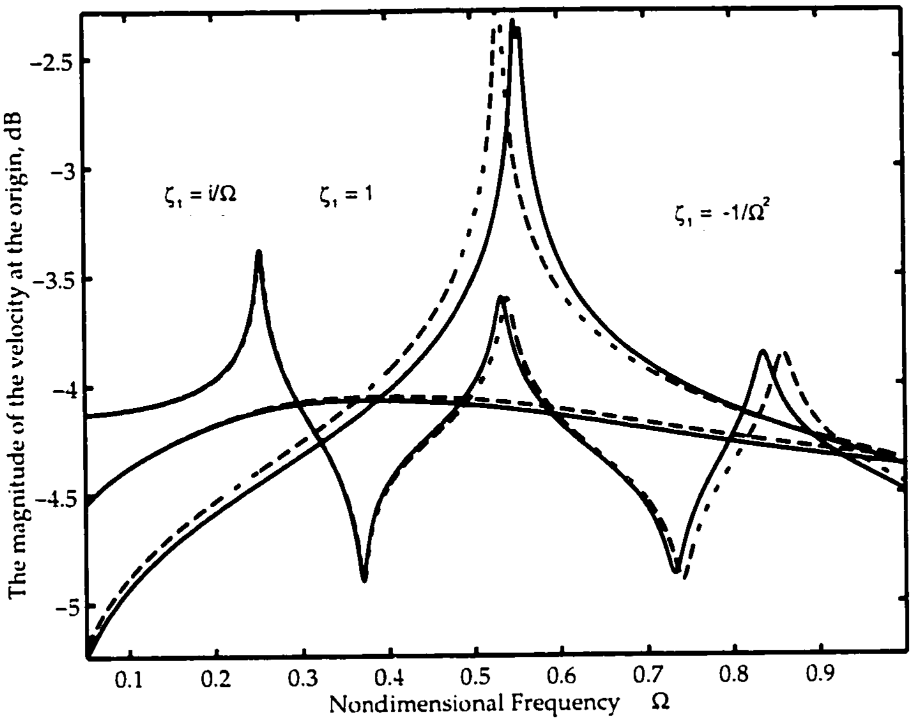

Figure 4.11: Magnitude of drive point velocity of two array structure with spacing ratio $d_1/d_2 = 1/6$. Exact solution —: The first term in the wavenumber expansion with homogenized first array - - -

$\Omega = 1.7$) to disappear but retains the minor stop bands in $0.2 < \Omega < 1.6$. This is due to the fact that the major stop band is caused by the presence of the first array and the minor stop bands are associated with the second array with larger spacing.

Finally, the choice of which array to homogenize depends on the homogenization range and on the array spacing and impedance. The homogenization of a particular array will remove features of the waves dispersion, such as stop and pass bands, that are associated with it. For instance, in the two-array problem considered before we can homogenize the second array and keep the first array. Figure 4.20 presents the imaginary part of the Floquet wavenumber for three different ratios $\frac{\zeta_1}{\zeta_2}$. Homogenization of the second array is a good approximation around the major stop band (which is due to the first array) and when the normalized impedance of the first array is

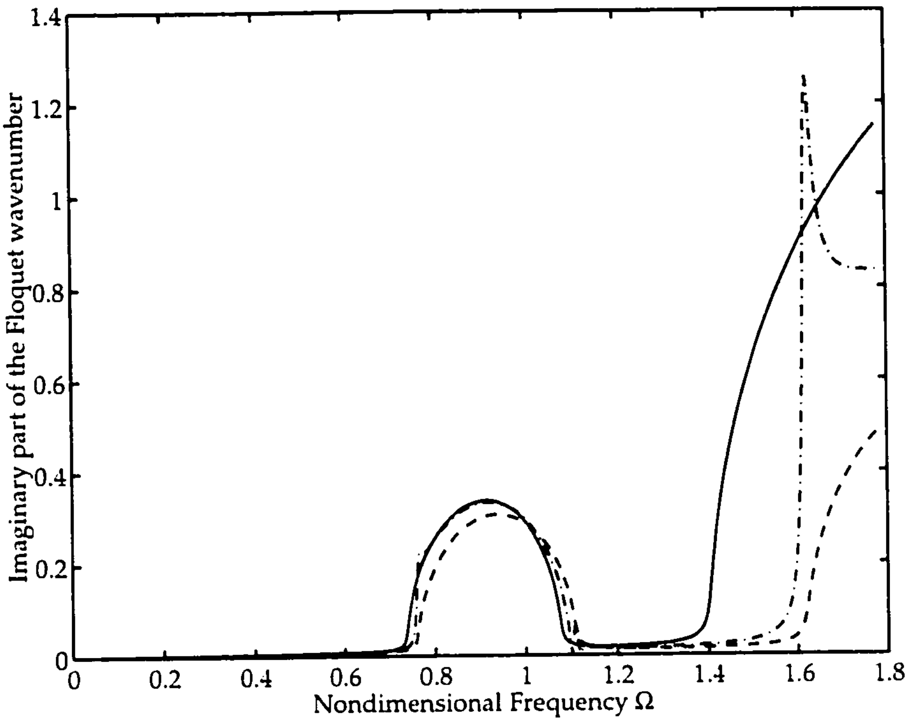

Figure 4.12: Imaginary part of the Floquet wavenumber of two array structure with spacing ratio $d_1/d_2 = 1/2$. Exact solution —: The first term in the wavenumber expansion - - -: The first and second term in the latter -·-

much higher than that of the second array, $\frac{\zeta_1}{\zeta_2} \gg 1$. Note that in this case the minor stop bands are not retained by the approximation: the latter become negligible with the increase of $\frac{\zeta_1}{\zeta_2}$. Figure 4.21 depicts the homogenization of the second array in two-array structures with offset, confirming the discussion above.

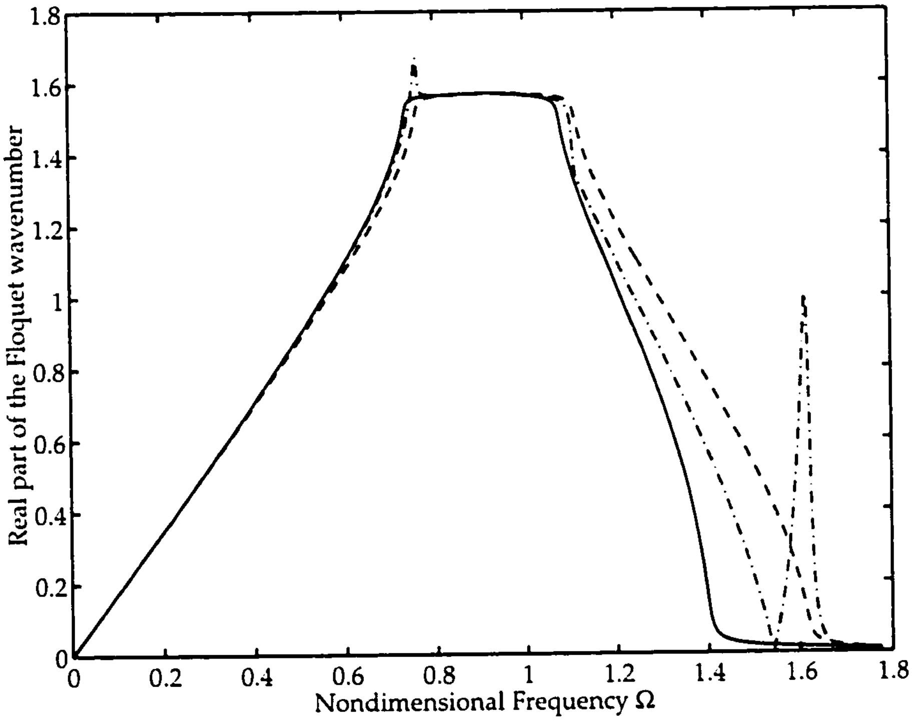

Figure 4.13: Real part of the Floquet wavenumber of two array structure with spacing ratio $d_1/d_2 = 1/2$. Exact solution —: The first term in the wavenumber expansion - -: The first and second term in the latter -·-

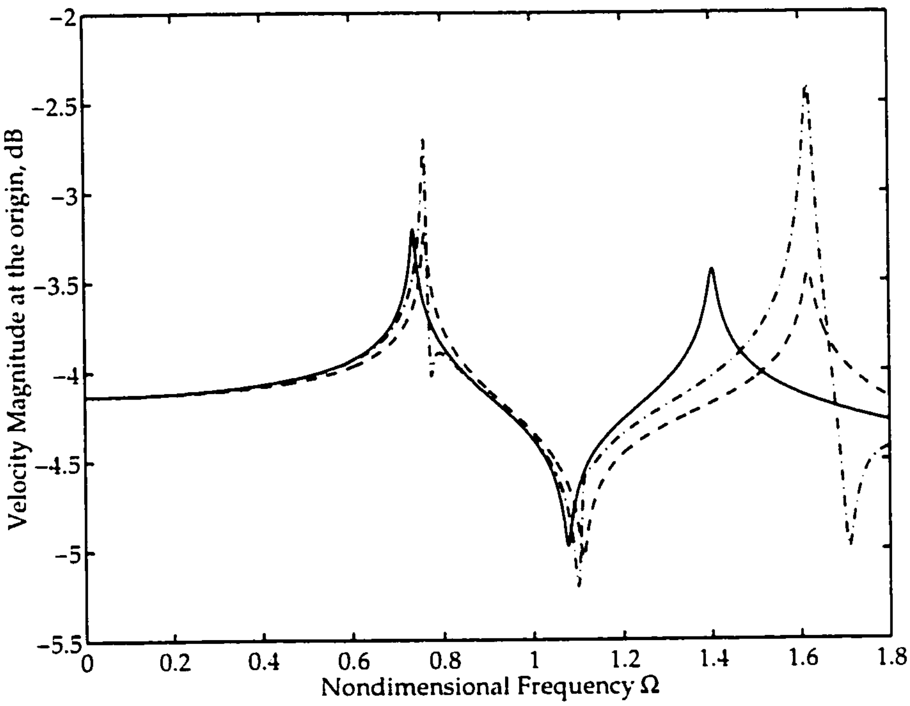

Figure 4.14: Drive point velocity magnitude of two array structure with spacing ratio $d_1/d_2 = 1/2$. Exact solution —: The first term in the wavenumber expansion - - -: The first and second term in the latter -·-

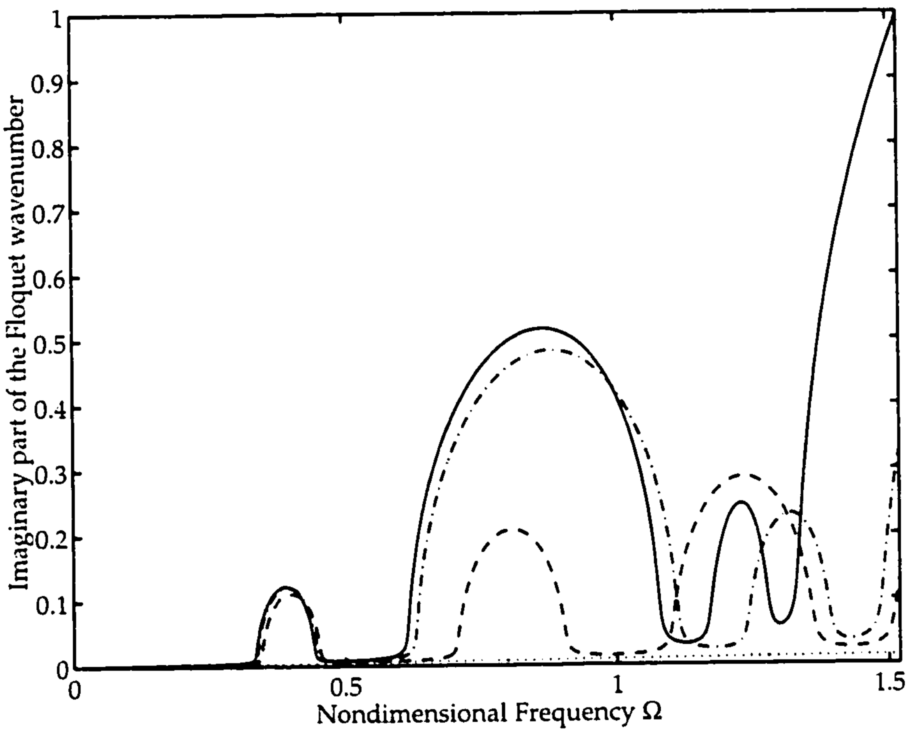

Figure 4.15: Imaginary part of the Floquet wavenumber of three array structure with spacing ratio $d_1/d_2/d_3 = 1/2/4$ and aligned arrays. Exact solution of three array structure —: Homogenized first array - - -: Homogenized first and second array -·-: Homogenized all three arrays ...

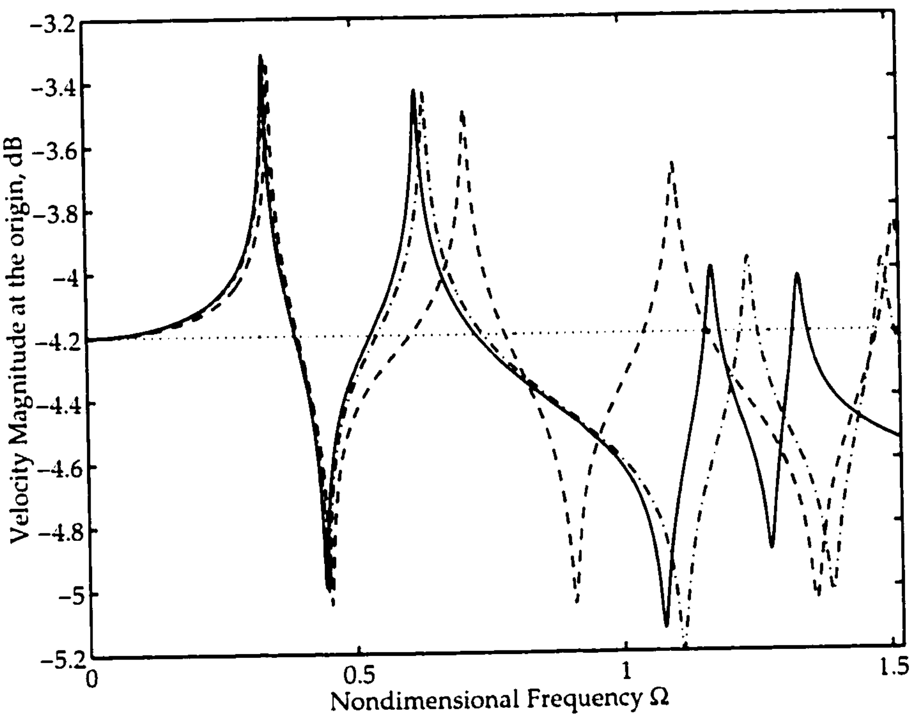

Figure 4.16: Magnitude of the drive point velocity of three array structure with spacing ratio $d_1/d_2/d_3 = 1/2/4$ and aligned arrays. Exact solution of three array structure —; Homogenized first array - - -; Homogenized first and second array -·-; Homogenized all three arrays ...

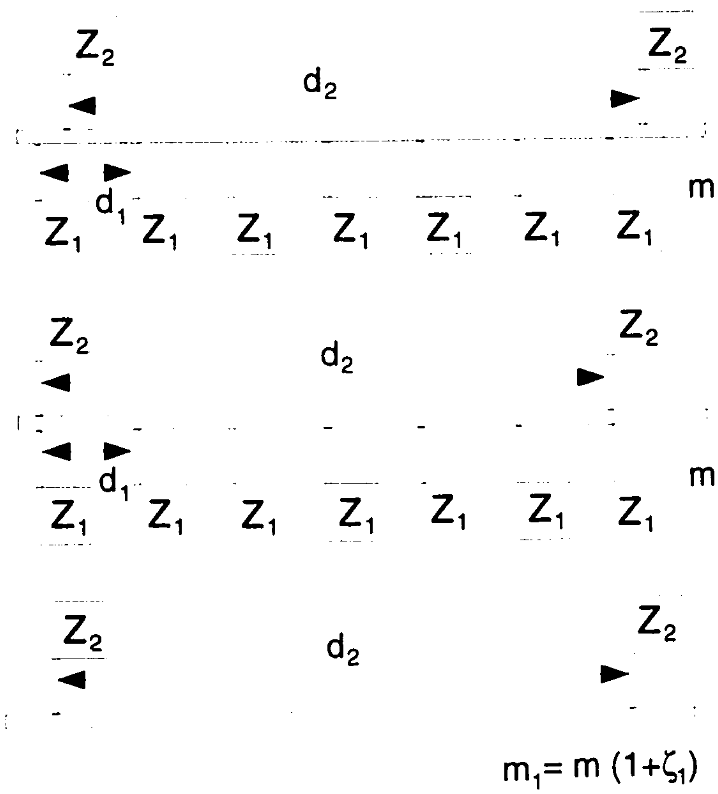

Figure 4.17: Comparison between two array structures and corresponding homogenized structure

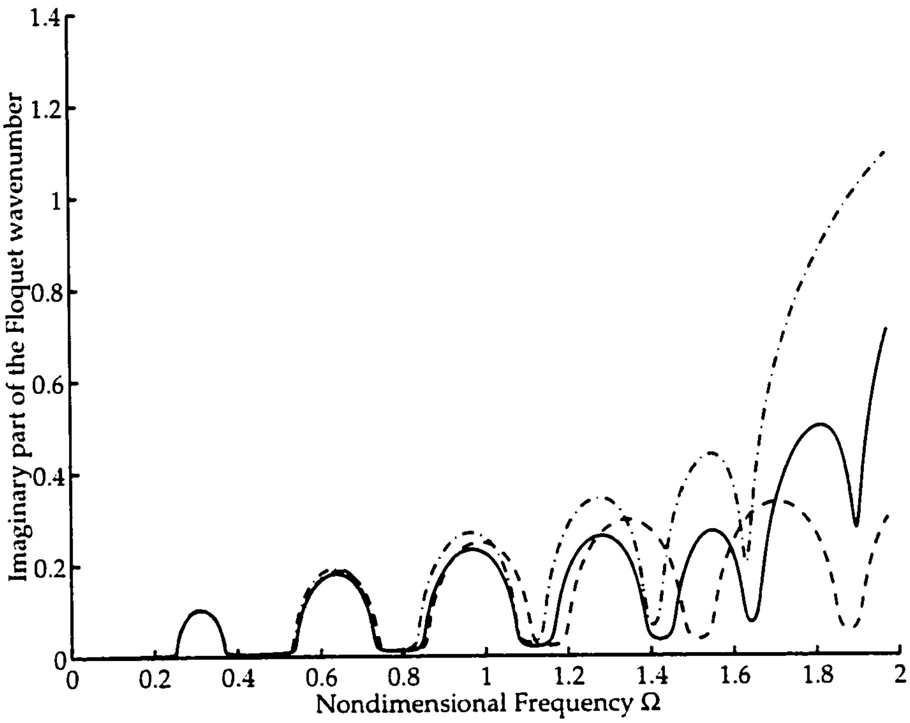

Figure 4.18: Imaginary part of the Floquet wavenumber for two array structures with spacing ratio $d_1/d_2 = 1/6$. Array offset 1/3 —: Array offset 0 -·-: Homogenized first array - - -.

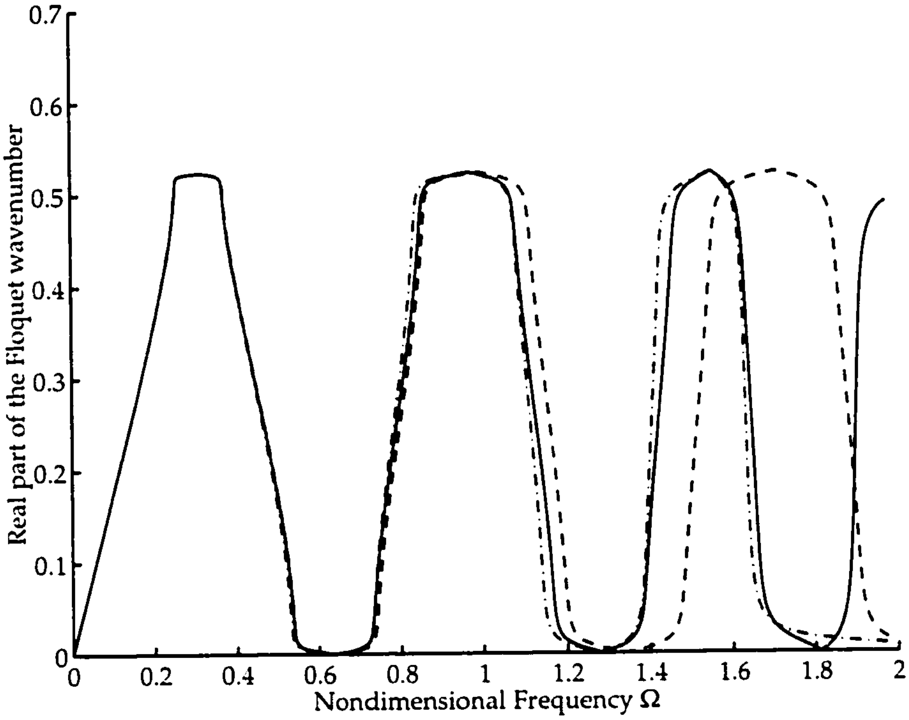

Figure 4.19: Real part of the Floquet wavenumber for two array structures with spacing ratio $d_1/d_2 = 1/6$. Array offset 1/3 —: Array offset 0 -·-: Homogenized first array - - -.

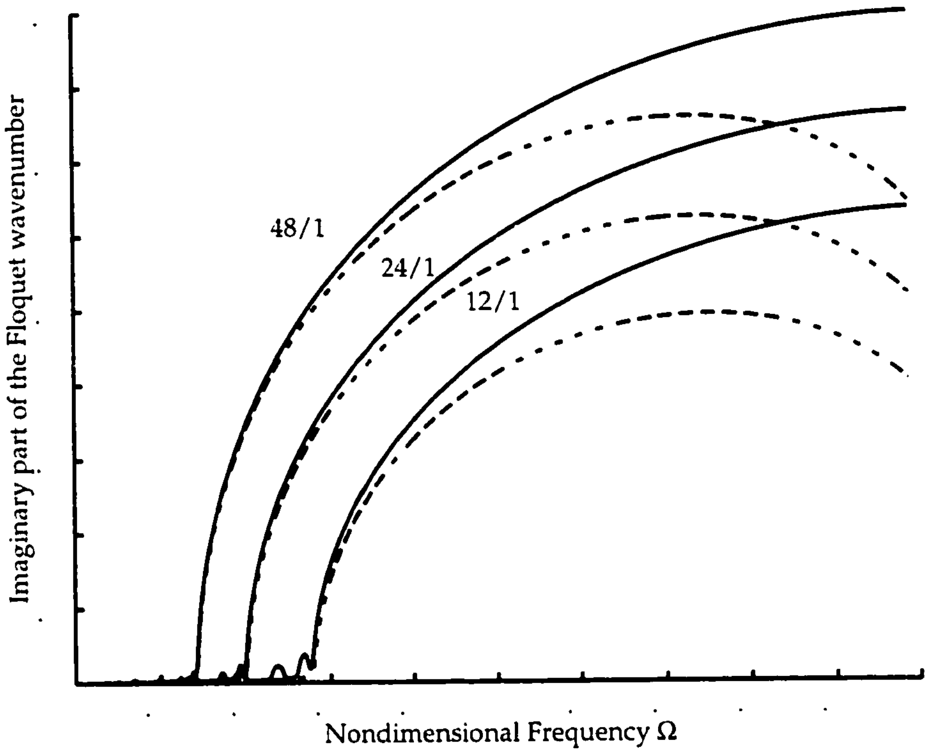

Figure 4.20: Two-array problem with homogenized second array while keeping the first array. The spacings ratio is $d_1/d_2 = 1/6$ and there is no offset between the arrays. Each set of curves corresponds to a different value of the ratio $\frac{\zeta_1}{\zeta_2}$. The exact solution —: The homogenized structure - - -.

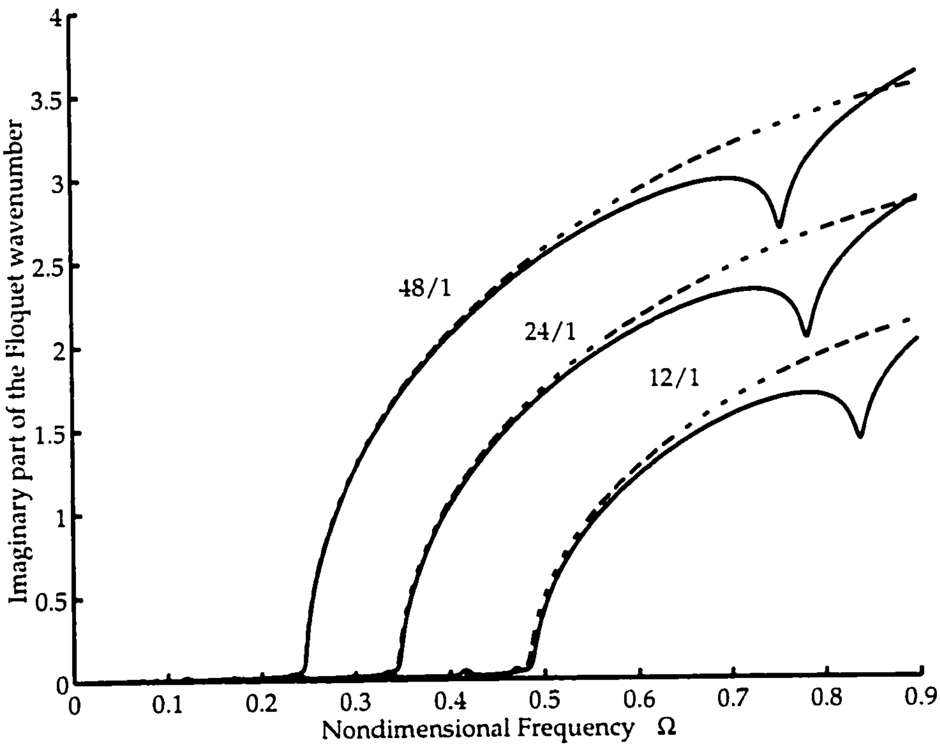

Figure 4.21: Two-array problem with homogenized second array while keeping the first array. The spacings ratio is $d_1/d_2 = 1/6$ and the array offset is 1/3. Each set of curves corresponds to a different value of the ratio $\frac{\zeta_1}{\zeta_2}$. The exact solution —: The homogenized structure - - -.

4.8 Chapter summary

Asymptotic expansions for the Floquet wavenumber and the response at the drive point for the considered single and two-array problems are obtained.

For the case when the periodic structure is partially homogenized. the higher-order terms become large at the "resonance" and "antiresonance" frequencies of the reduced structure. A nondimensional parameter. Ω_Q. is identified whose smallness guarantees the approximation. The homogenization error depends on the normalized frequency and array impedance. The special cases of spring and dashpot impedances are considered through examples and it is observed that the derived expressions give good approximations if the normalized frequency is sufficiently low.

The asymptotic expansions. derived for attached mass impedances. are applied to examples with attached spring and dashpot impedances. The resutls from these examples indicate that the derived expansions provided good approximations for small stiffness and dashpot impedances at sufficiently low frequencies.

For a multiarray structure. a hierarchy of such approximations can be constructed in which the leading order term related to a fictitious periodic structure with a reduced number of arrays. Homogenizing more arrays results in a smaller frequency range of approximation. The concept of partial homogenization introduced for this particular class of periodic problems is expected to simplify the geometry and thus reduce the computational efforts in other complex periodic structures for which the exact analytic solution is not known *a priori*.

Chapter 5

Application of homogenization theory to damping models

A broad variety of problems in the aerospace, marine, and automotive industries require damping treatments that reduce structural vibrations. Motivations include avoiding detection, minimizing hazard to the operation of mechanical or electronic systems, or reducing adverse effects on the operator. One such damping treatment is the use of small viscoelastic beads to substantially increase the damping of hollow truss-like structures [74]. It is known that in a beam with granular filling the damping in the structure can be modeled through a frequency-dependent loss factor, as experimentally demonstrated by House [75]. This chapter illustrates how the theory of Chapter 2 can be used to estimate the loss factor from experimental data.

Predicting the response of a complex structure with damping treatments is often based on a FEM analysis. However, including the effects of these materials in the model can be difficult for two reasons. First, constitutive models of the damping material and its coupling to the structure may not be available. Second, existing numerical codes may not provide the functionality to include such a model if it does exist. The method described in this chapter will be used to incorporate the granular fill in the existing transient FE models based on *in situ* measurements of a beam with damping treatment. The method uses data collected in an experiment in which a thin box beam, filled with small viscoelastic beads is subject to an impact force and the accelerations along the beam are measured in specified locations. The granular fill is modeled as an array of point-attached impedances in the frequency domain, where the frequency-dependent array impedances are obtained by fitting the measured data with the model response.

The inverse homogenization approach has been discussed in the literature [68] - [69]. In [68], Sigmund *et al.* formulate and implement a procedure for constructing linear elastic materials with prescribed material properties. An inverse homogenization problem is formulated as an optimization problem finding the interior topology of a base cell such that the cost is minimized and the constraints are defined by the prescribed constitutive parameters. In [69], inverse homogenization is considered for two-phase viscoelastic composites and, as in the previous paper it is formulated as a topology optimization problem. The cost function in the paper is defined such that microstructures are found that exhibit improved stiffness and damping characteristics within the specified frequency range.

After applying the inverse homogenization method and obtaining the frequency-dependent array impedance, we need to model the latter with appropriate mechanical system in order to incorporate the granular fill in the existing time domain codes. For this purpose we consider two models

In the first model, the damping treatment is approximated with an array of mechanical substructures, composed of masses, dashpots and springs. This is achieved by fitting the array impedance with a passive and stable rational function in frequency domain. Using this approximation, the damping treatment is introduced at the structural level through element mass, stiffness, and damping matrices. By using dissipation coordinates, internal to each finite element with damping treatment [87], a general description of frequency dependent damping treatment behavior is presented. The array impedance in the frequency domain is approximated by a rational function as

$$Z(\omega) = \frac{a_0 + a_1\omega + \ldots + a_M\omega^M}{b_0 + b_1\omega + \ldots + b_N\omega^N} \tag{5.1}$$

where the coefficients a_n and b_n can be computed by several techniques: for example, Pade approximations [82], [81] and maximum likelihood estimation methods [83]. The latter approach, employed here, predicts the parameters of a linear dynamic system given with its transfer function and subject to noisy input signal ([83]). For this purpose, it is necessary to know *a priori* the probability density function of the measurement noise. The likelihood function, representing the probability of realizing the measured data with a set of parameters, is constructed given the noise probability density function. The cost function, defined on the basis of the likelihood function, can be minimized by using least square algorithms and thereby an estimation of the system parameters can be obtained.

The second frequency-domain model which is considered in this chapter represents the damping treatment as a fluid with low sound speed. Models representing the granular fill as homogeneous medium with low sound speed are developed already in the literature ([79], [75]). According to the proposed fluid model, the granular fill in a section of the beam is replaced by a fluid column moving vertically with the transversal velocity of the beam at this location. On the basis of an acoustic model for the motion of the fluid an expression is derived for the array impedance which will approximate the array impedance for selected values of the sound speed of the "beads" fluid. The advantage of this model is that it is physics-based and it is expected to describe accurately the complex fill dynamics without significant computation efforts.

After obtaining approximations for the array impedance in frequency domain, the damping treatment model will be incorporated in existing finite element codes. In [87], McTavish *et al.* discuss a method for incorporating viscoelastic effects into standard transient FEM codes. A second order equation for the motion of linear viscoelastic system is presented in which the mass, stiffness and damping matrices are constructed on the basis of those for a purely elastic system augmented by additional dissipation coordinates. The method preserves the definiteness properties usually associated with finite element matrices. A similar approach introducing additional dissipation coordinates is considered in [88] and [90]. A higher order viscoelastic beam theory is presented in [89] modeling the material as a Maxwell solid and allowing convenient finite element formulation.

All previously described methods require knowledge of the constitutive relations for the viscous material. The new periodic model, representing the damping treatment as an array of equally spaced impedance attachments (shown on Figure 5.2) will be incorporated in the existing transient FEM codes only on the basis of *in situ* measurements. This impedance may also be used to estimate the frequency-dependent loss factor of the damped structure.

5.1 Experimental system

In this section, the use of granular fill material in box beams is studied as a means to enhance their damping under both steady and transient loading. While some effort has been made to obtain physics-based models (see [79] and [78]), the appropriate model is still open to debate. Furthermore, many time-domain codes for computing transient response can represent only proportional damping, which is clearly inappropriate for this application. In such a case, the concept of homogenization can be used to obtain a satisfactory solution. The problem can be solved in two parts. First, experiments on a single member of the structure are used to develop a model of the damped member as a combination of the undamped member plus one or more arrays of attached impedances. Time-domain representations of these impedances can then be incorporated in the transient FEM codes as state dependent forces applied to the element nodes.

Inverse homogenization of a thin metal beam with rectangular cross section filled with small viscoelastic particles is investigated. In an experiment conducted at the Naval Surface Warfare Center [71], a box beam was hung by two bungee cords, modeling free end boundary conditions and was subjected to a shock excitation at the end as shown in Figure 5.1. Structural acceleration was measured at 13 equally spaced locations along the beam and on the basis of the collected data, an estimation for the structural damping is sought. Experiments were classified based on which side of the rectangular cross section the blow was applied. Each class consists of a set of different trials ordered by increasing force magnitude. McDaniel *et al.* demonstrated in [76] that the complex wavenumbers, amplitudes, and loss factor of a mechanically excited damped beam can be determined from a small array of accelerometers at any frequency of excitation. Their approach used an iterative scheme that minimized

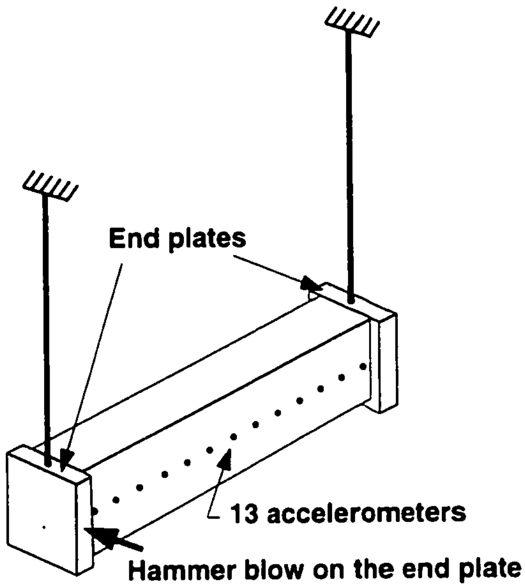

Figure 5.1: Beam schematic

the error between the wave description and the measured responses by adjusting the complex wavenumbers and amplitudes. In [77], the same author introduced the wave approach for estimating the loss factor of a steel box beam with damping treatment over a broad frequency band. In that work, expressions for the wave and modal estimates of the loss factor were derived by expressing the transient response as a sum of wave and modal solutions, where the wave solution incorporates the nonhomogeneous boundary conditions and the modal solution takes into account the nonhomogeneous initial conditions. The wave solution was composed as a combination of flexural and evanescent waves with frequency dependent coefficients, satisfying nonhomogeneous boundary conditions,

$$V(x,\omega) = c_1(\omega)e^{ik(\omega)x} + c_2(\omega)e^{ik(\omega)(L-x)} + c_3(\omega)e^{-k(\omega)(L-x)} + c_4(\omega)e^{-k(\omega)x}. \quad (5.2)$$

Here, $k(\omega)$ is the wavenumber of the beam with the damping treatment. The loss factor is estimated by solving an overdetermined system of algebraic equations with respect to $k(\omega)$ and the complex wave coefficients $c_n(\omega)$ using the measured beam response at n locations along the beam. A similar procedure for identification of the material properties of an axially impacted elastic bar with viscoelastic treatment on the basis of strain measurements is described by Hillstrom [80].

5.2 Impedance array model for the granular fill

A frequency-domain model for the thin elastic beam with granular filling is considered. For this purpose, an array of point impedances, each having impedance Z, is attached to the empty beam (see Figure 5.2).

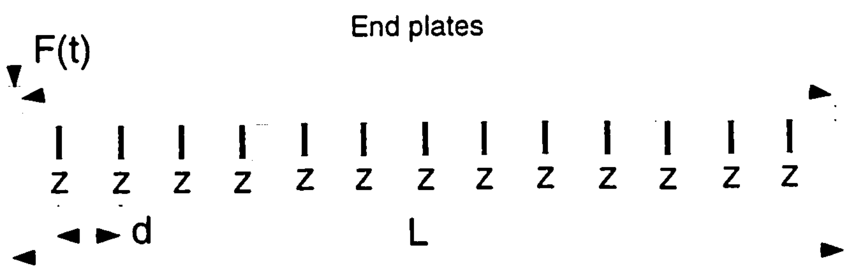

Figure 5.2: Proposed periodic model for damping estimation of beam with granular fill

The beam with attached array is described by the Euler-Bernoulli equation

$$\frac{EI}{-i\omega}\frac{d^4 v}{dx^4} - i\omega m_{empty} v = F(\omega)\delta(x) - Z(\omega)\sum_{n=1}^{N}\delta(x-d)v; \quad d = \frac{L}{N-1} \tag{5.3}$$

subject to the boundary conditions

$$\left.\frac{d^2 v}{dx^2}\right|_{x=0} = -\frac{i\omega Z_r}{EI}\left.\frac{dv}{dx}\right|_{x=0}; \quad \left.\frac{d^3 v}{dx^3}\right|_{x=0} = \frac{i\omega Z_t}{EI} v|_{x=0} \tag{5.4}$$

$$\left.\frac{d^2 v}{dx^2}\right|_{x=L} = \frac{i\omega Z_r}{EI}\left.\frac{dv}{dx}\right|_{x=L}; \quad \left.\frac{d^3 v}{dx^3}\right|_{x=L} = -\frac{i\omega Z_t}{EI} v|_{x=L} \tag{5.5}$$

$$(5.6)$$

Here, Z_t and Z_r denote the transverse and rotational impedance of the end cap mass, expressed by

$$Z_t = -i\omega M_c, \qquad Z_r = -i\omega J_c, \tag{5.7}$$

where M_c is the end cap mass and J_c is the end cap moment of inertia. N is the number of attachments and d is the spacing of the periodic structure. Our goal is to estimate $Z(\omega)$ where given are the parameters of the empty beam and the measured accelerations of the filled beam.

The measured accelerations are transformed to the frequency domain by Fourier transform using the notation

$$a(\omega) = \int_{-\infty}^{\infty} A(t)e^{-i\omega t}dt \tag{5.8}$$

Accordingly, the velocity in the frequency domain is given as

$$v(\omega) = \frac{a(\omega)}{-i\omega} \tag{5.9}$$

The model response is computed by two alternative methods - using a wave approach and a finite element model. Using the wave model, the flexural response of the beam with attached array consists of four Floquet waves - two propagating and two evanescent

$$v(x) = c_1(\omega)e^{ik_1x} + c_2(\omega)e^{-ik_1x} + c_3(\omega)e^{ik_2x} + c_4(\omega)e^{-ik_2x} \tag{5.10}$$

Here, k_1 is the propagating Floquet wavenumber and k_2 is the evanescent Floquet wavenumber (mostly imaginary). At low frequencies, the array can be completely homogenized into the beam and the Floquet wavenumbers can be computed using the homogenization theory from Chapter 5

$$k_1 = k_e(1+\zeta)^{1/4} + \mathcal{O}[\Omega^5]; \qquad k_2 = ik_e(1+\zeta)^{1/4} + \mathcal{O}[\Omega^5]; \qquad \zeta = \frac{Z}{i\omega md}; \qquad \Omega = k_e d \tag{5.11}$$

where $k_e = \left(\frac{m\omega^2}{EI}\right)^{1/4}$ is the empty beam wavenumber, ζ is the normalized array impedance, m is the mass per unit length of the empty beam and d is the array spacing. The coefficients $C_1, \ldots, C_4$ depend on the frequency ω and are obtained by satisfying the boundary conditions. Expressions for them are supplied in Appendix E.

With the finite element model, the beam response is obtained in terms of structural and array impedance matrices $[Z_{st}]$ and $[Z_{att}]$

$$\{v\} = ([Z_{st}] + [Z_{att}])^{-1}\{f\}, \tag{5.12}$$

where $\{v\}$ is the nodal velocity vector and $\{f\}$ is the nodal force vector. Here, the structural impedance matrix $[Z_{st}]$ is given by

$$[Z_{st}] = \frac{[K] - \omega^2[M]}{-i\omega}, \tag{5.13}$$

where $[K]$ and $[M]$ are the stiffness and mass matrices for the empty beam. The array impedance matrix, $[Z_{att}]$, is diagonal and has the array impedances, Z, at the transverse degrees-of-freedom where the data is collected (see Figure 5.2).

The material properties of the empty beam are determined by comparing the structural responses of the empty beam in the frequency and time domains. On the basis of the measured data the empty beam finite element model shows reasonable agreement at early times with the experimental data and, in the frequency domain, the response magnitude is aligned very well with the data. This is shown in Figure 5.9.

Using a standard optimization procedure, the attachment impedance is adjusted so that structural response matches the measured data at the locations given in Figure 5.1 for each frequency. The computation procedure is built on the basis of a one dimensional Euler-Bernoulli model. The response is computed by the wave model and using the finite element method. The results of the two methods show very good agreement in the frequency range considered (see Figure 5.15).

The loss factor is related to the wavenumber by

$$\eta_h = \frac{\Im(k_1{}^4)}{\Re(k_1{}^4)} \tag{5.14}$$

An alternative way to evaluate the structural loss factor is to use the fact that the loss factor is the ratio of the dissipated power per cycle Φ over the stored power in the system per cycle Π.

$$\eta_p = \frac{\Phi}{\Pi} \tag{5.15}$$

For this purpose, we will formulate finite element approach and solve the equation of motion. The dissipated power in the system per cycle is given by

$$\Phi = \frac{1}{2}\{v\}^*[R]\{v\} \tag{5.16}$$

where the dissipation matrix $[R]$ is the real part of the structural impedance matrix. In the case of the empty beam model, the structural impedance matrix is simply a combination of the mass and stiffness matrices as shown in Equation (5.12).

If damping treatment is present then the dissipation matrix is computed as

$$[R] = \Re\{[Z_{st}] + [Z_{att}]\} \tag{5.17}$$

where Z_{st} is the structural impedance of the empty beam and $[Z_{att}]$ is a diagonal matrix with the array impedance on the main diagonal.

The total power stored in the system per cycle is the sum of the power stored in the structural mass and stiffness as shown below

$$\Pi = \frac{1}{4}\omega\{v\}^{*}[M]\{v\} + \frac{1}{4}\frac{\{v\}^{*}[K]\{v\}}{\omega} \tag{5.18}$$

Note that the additional mass and stiffness of the damping treatment is not taken into account in the loss factor evaluation with Equation (5.15).

Agreement between these alternative approaches (modal analysis, half power, wavenumber method) is observed in Figure 5.17. Figure 5.12 shows the drive point velocity magnitude in the frequency domain, computed by using the periodic model of Equation (5.3) and the measured data, transformed by FFT.

The optimization code, used in this analysis, is $Matlab^{TM}$ *fminsearch*, which impelements the simplex direct search method [85]. The error function which is minimized is the normalized mean square error, given by

$$\epsilon = \frac{1}{13}\sum_{n=1}^{13}\frac{|v_n{}^{(data)} - v_n{}^{(fem)}|^2}{|v_n{}^{(data)}|^2}. \tag{5.19}$$

where $v_n{}^{(data)}$ is the measured beam velocity at nth location and $v_n{}^{(fem)}$ is that obtained by the FE periodic model. Using Equation (5.19) the optimal array impedance Z_{att} for each frequency is estimated. Figure 5.3 shows the error contours and the optimized array impedance for a particular frequency.

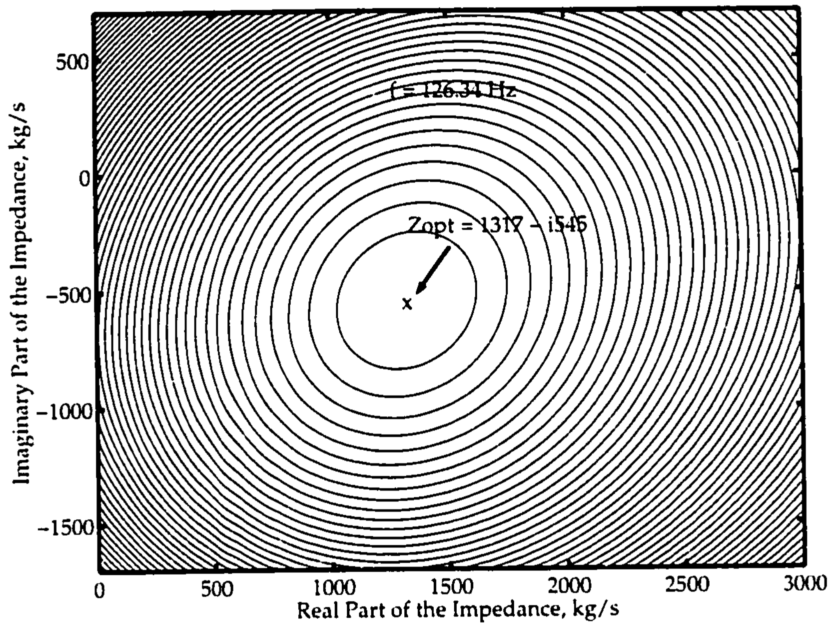

Figure 5.3: Contour plot of normalized mean square error and optimal value of the array impedance found by the optimization procedure $fminsearch$

5.3 Rational fit for the array impedance and time domain implementation

In this section, a rational function approximation is sought for the array impedance. The rational fit is assumed to have the following form:

$$Z_{rf}(\omega) = c + \sum_{n=1}^{N} \frac{r_n}{s - p_n} + \sum_{n=1}^{N} \frac{r_n^*}{s - p_n^*} \text{ where } s = i\omega. \tag{5.20}$$

The coefficients r_n^* and p_n^* represent the complex conjugates of r_n and p_n. Thus the function has $2N$ poles and residues in conjugate pairs so that it is real-valued in time domain. The poles must lie in the left-half of the s-plane, which prevents the array impedance from being unstable. An additional restriction, guaranteeing passivity, is that the zeros of the rational fit have to be in the left-half of the s-plane (see [91]).

The coefficients r_n, p_n and c are obtained by minimizing the error function

$$\epsilon_{rf} = \sum_{k=1}^{n} W_k \left| Z(\omega_k) - Z_{r.f.}(\omega_k) \right|^2 \tag{5.21}$$

where Z is the array impedance, computed by the optimization procedure and the sum is over the discrete set of frequencies. W_k is a weighting function that filters out regions with low signal-to-noise ratios. The best results were obtained with a linear combination of two Gaussian distributions such that the first two modes coincide with the local maxima of the weighting function.

$$W_k = \frac{\exp\left[-\frac{(\omega_k - \bar{\omega}_1)^2}{2}\right]}{4{\sigma_1}^2} + \frac{\exp\left[-\frac{(\omega_k - \bar{\omega}_2)^2}{2}\right]}{4{\sigma_2}^2}. \tag{5.22}$$

This resulted in better time-domain fits because the transient responses were dominated by these modes. The rational fit was obtained with the built-in $Matlab^{TM}$ procedure *invfreqs* following the equation error method based on Levi [86]. The results for the rational fit of array impedance are discussed in the next section.

Now let us see how the impedance representation in Figure 5.2 can be incorporated in transient finite element analyses. For this purpose (5.20) is written in the following form

$$Z(s) = C + \sum_{n=1}^{N} \alpha_n \frac{s + 2\hat{\gamma}_n \hat{\omega}_n}{s^2 + 2\hat{\zeta}_n \hat{\omega}_n s + \hat{\omega}_n^2} \tag{5.23}$$

where

$$\alpha_n = 2\Re(r_n); \quad \hat{\omega}_n = |p_n|; \quad \hat{\zeta}_n = -\frac{\Re(p_n)}{|p_n|}; \quad \hat{\gamma}_n = -\frac{\Re(r_n)\Re(p_n) + \Im(r_n)\Im(p_n)}{2\Re(r_n)|p_n|} \tag{5.24}$$

Let us introduce N new variables

$$z_1 = \frac{\hat{\omega}_1^2}{s^2 + 2\zeta_1\hat{\omega}_1 s + \hat{\omega}_1^2}, \quad \ldots \quad , z_N = \frac{\hat{\omega}_N^2}{s^2 + 2\zeta_N\hat{\omega}_N s + \hat{\omega}_N^2}. \tag{5.25}$$

These variables correspond to additional degrees of freedom, taking into account the effect of the damping treatment to the empty beam (see [88], [87]). Then the equation of motion of the system in the s-domain can be written in the following expanded form

$$\left(s^2[M_{aug}] + s[D_{aug}] + [K_{aug}]\right)\begin{bmatrix} q \\ z_1 \\ \vdots \\ z_N \end{bmatrix} = \begin{bmatrix} f \\ 0 \\ \vdots \\ 0 \end{bmatrix}. \tag{5.26}$$

In this form, the augmented mass, damping, and stiffness matrices $[M_{aug}]$, $[D_{aug}]$, and $[K_{aug}]$ are given as

$$[M_{aug}] = \begin{bmatrix} M & 0 & \ldots & 0 \\ 0 & \frac{\alpha_1}{\hat{\omega}_1^2}I & \ldots & 0 \\ \vdots & \vdots & \ddots & \vdots \\ 0 & 0 & \ldots & \frac{\alpha_N}{\hat{\omega}_N^2}I \end{bmatrix} \tag{5.27}$$

$$[D_{aug}] = \begin{bmatrix} CI & -2(\hat{\gamma}_1 - \hat{\zeta}_1)I & \ldots & -2(\hat{\gamma}_N - \hat{\zeta}_N)I \\ 0 & \frac{\alpha_1\hat{\zeta}_1}{\hat{\omega}_1}I & \ldots & 0 \\ \vdots & \vdots & \ddots & \vdots \\ 0 & 0 & \ldots & \frac{\alpha_N\hat{\zeta}_N}{\hat{\omega}_N}I \end{bmatrix} \tag{5.28}$$

$$[K_{aug}] = \begin{bmatrix} K + \sum \alpha_k I & -\alpha_1 I & \dots & -\alpha_1 I \\ -\alpha_1 I & \alpha_N I & \dots & 0 \\ \vdots & \vdots & \ddots & \vdots \\ -\alpha_N I & 0 & \dots & \alpha_N I \end{bmatrix} \tag{5.29}$$

where I is the identity matrix.

If we require

$$\hat{\gamma}_n = \hat{\zeta}_n \tag{5.30}$$

for all n, then the damping matrix will be symmetric. In this case each term

$$Z_n = \frac{s + 2\hat{\zeta}_n \hat{\omega}_n}{s^2 + 2\hat{\zeta}_n \hat{\omega}_n s + \hat{\omega}_n^2} \tag{5.31}$$

in Equation (5.23) represents the impedance of an oscillator with mass $\frac{\alpha_n}{\hat{\omega}_n}$, spring stiffness α_n, and dashpot $\alpha_n \frac{2\hat{\zeta}_n}{\hat{\omega}_n}$. Thus the array impedance may be approximated as oscillators connected in parallel as shown in Figure 5.4.

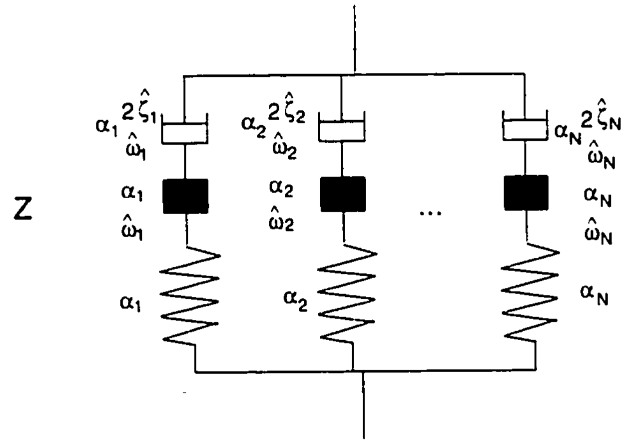

Figure 5.4: Mini-oscillator approximation for the array impedance

5.4 Fluid model for the array impedance

In this section, a fluid model for the beads will be developed by treating the granular fill as a one-dimensional fluid and the corresponding drive-point impedance will be derived. For this purpose, the beam is partitioned into discrete sections and the damping treatment inside each section is replaced with an acoustic fluid. Further, the following simplifying assumptions are made:

- a section does not influence the motion of the others i.e. they are uncoupled;
- the fluid inside each section is in vertical motion only;
- walls do not move relative to each other.

Let us consider one section of the beam with fluid density ρ_f, sectional area A_f, length L_f, and speed of sound inside the fluid c_f as shown in Figure 5.5.

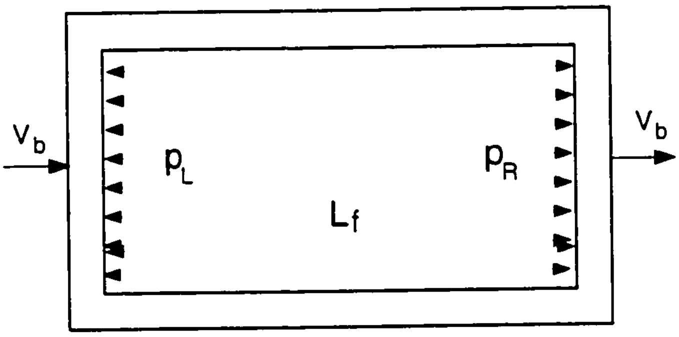

Figure 5.5: Section of the beam filled with fluid

The array impedance is given by

$$Z = \frac{(p_r - p_l)A_f}{v_b} \tag{5.32}$$

The wave solution for the velocity of the fluid is

$$v(x) = F_v e^{ikx} + B_v e^{-ikx}; \qquad k = \frac{\omega}{c_f}. \tag{5.33}$$

Upon satisfying the boundary conditions

$$v(0) = v_b; \qquad v(L) = v_b. \tag{5.34}$$

the wave coefficients F_v and B_v are obtained as

$$F_v = \left(\frac{1 - e^{-ikL}}{2i\sin(kL)}\right) V_b; \qquad B_v = -\left(\frac{1 - e^{-ikL}}{2i\sin(kL)}\right) V_b. \tag{5.35}$$

Using the Euler's momentum equation,

$$-\rho_f \frac{\partial V}{\partial t} = \frac{\partial P}{\partial x} \tag{5.36}$$

and assuming harmonic time dependence in the form $V(x,t) = v(x)e^{i\omega t}$ leads to a differential equation for the fluid pressure $p(x)$:

$$\frac{dp}{dx} = i\omega\rho v \tag{5.37}$$

. Using Equation (5.33) in Equation (5.37) leads to the following expression for the pressure in the fluid:

$$p(x) = \rho c F_v e^{ikx} - \rho c B_v e^{-ikx} \tag{5.38}$$

Substitution of Equation (5.38) in Equation (5.32) gives the final result

$$Z = i2\rho_f c_f A_f \frac{1 - \cos(kL_f)}{\sin(kL_f)} \tag{5.39}$$

Equation (5.39) is the expression which will be used to approximate the array impedance in the frequency domain. For this purpose a complex sound speed c_f will be varied so that the impedance in (5.39) agrees with the impedance found from the data.

5.5 Numerical results

5.5.1 Empty beam response and material properties

The exact parameters of the empty beam were initially unknown. To determine them, the nominal parameters were varied to achieve the best agreement between data and finite element model. The resulting parameters are given in Table 5.1. The

Material Property	Symbol	Estimated Value
Inertial moment	I_y	$6.3 \times 10^{-5}\ m^4$
Inertial moment	I_z	$2.77 \times 10^{-5}\ m^4$
Young's modulus	E	$1.83 \times 10^{11}\ Pa$
Loss factor	η	0.005
Material density	ρ	$7809\ kg/m^3$
Cross-section area	A	$7.5 \times 10^{-3}\ m^2$
Beam's length	L	$4.87\ m$
End cap mass	M_c	$9\ kg$

Table 5.1: Material properties of empty beam

frequency-domain agreement for 3 points on the beam is shown in Figures 5.6-5.8. The corresponding agreement in time domain is shown in Figures 5.9 - 5.11.

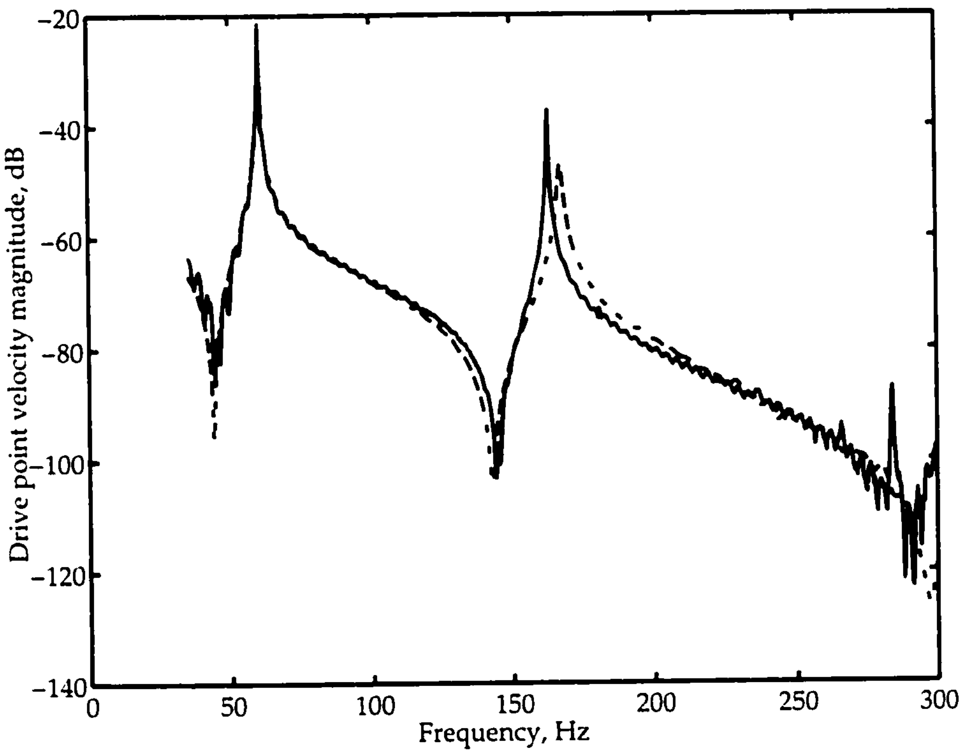

Figure 5.6: Drive point velocity magnitude for empty beam for trial 9. Measured data —: FEM - - -

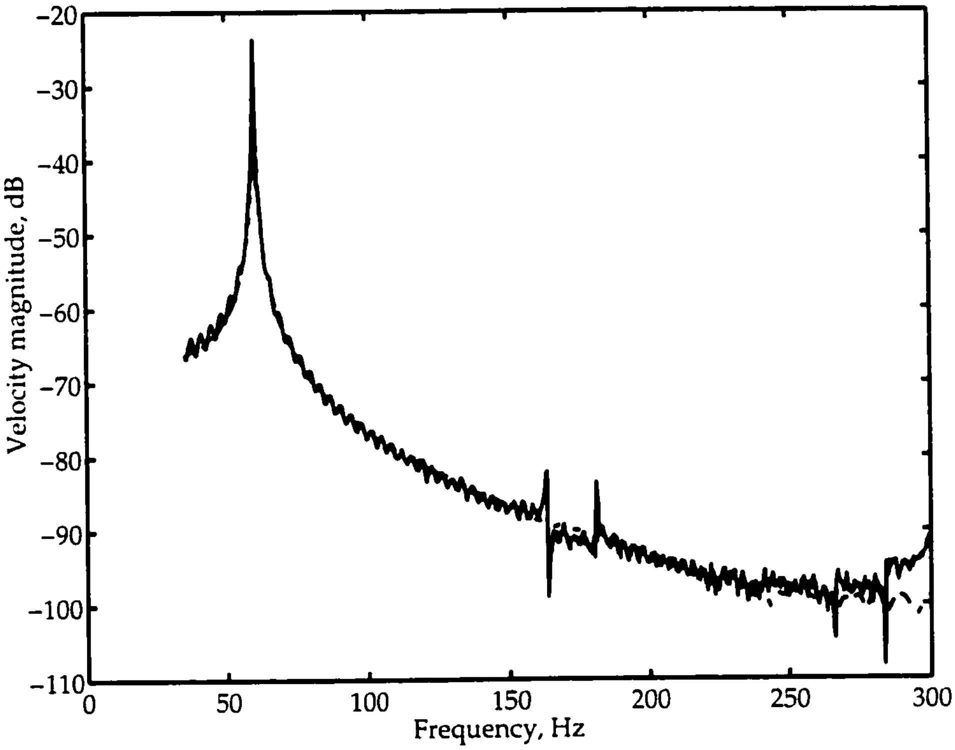

Figure 5.7: Velocity magnitude at the center for empty beam for trial 9. Measured data —; FEM - - -

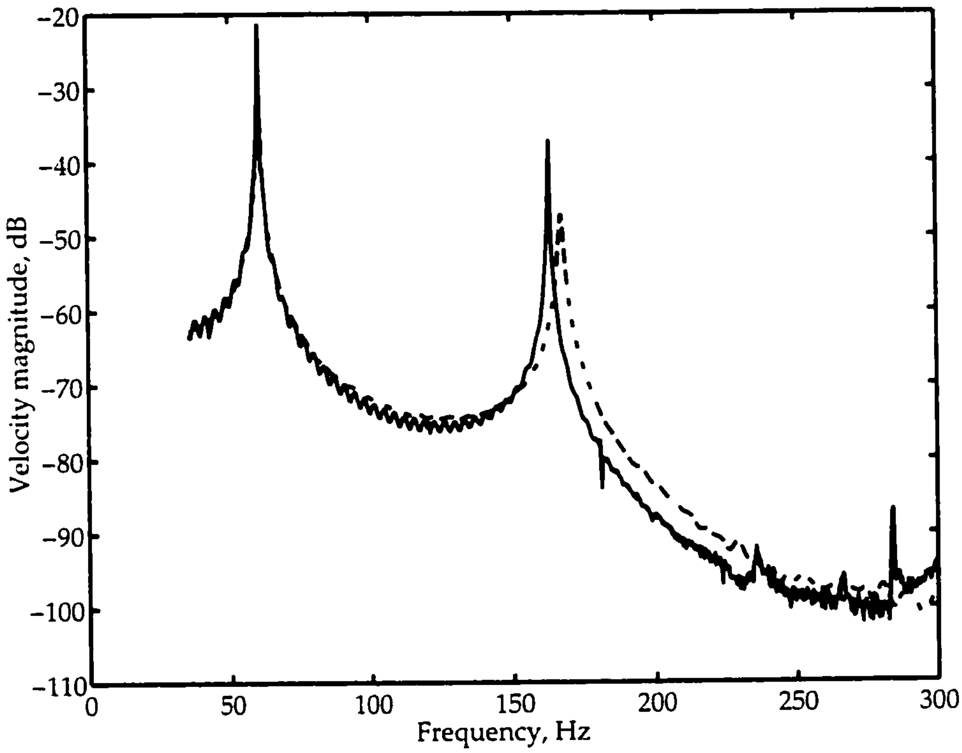

Figure 5.8: Velocity magnitude at the end for empty beam for trial 9. Measured data —: FEM - - -

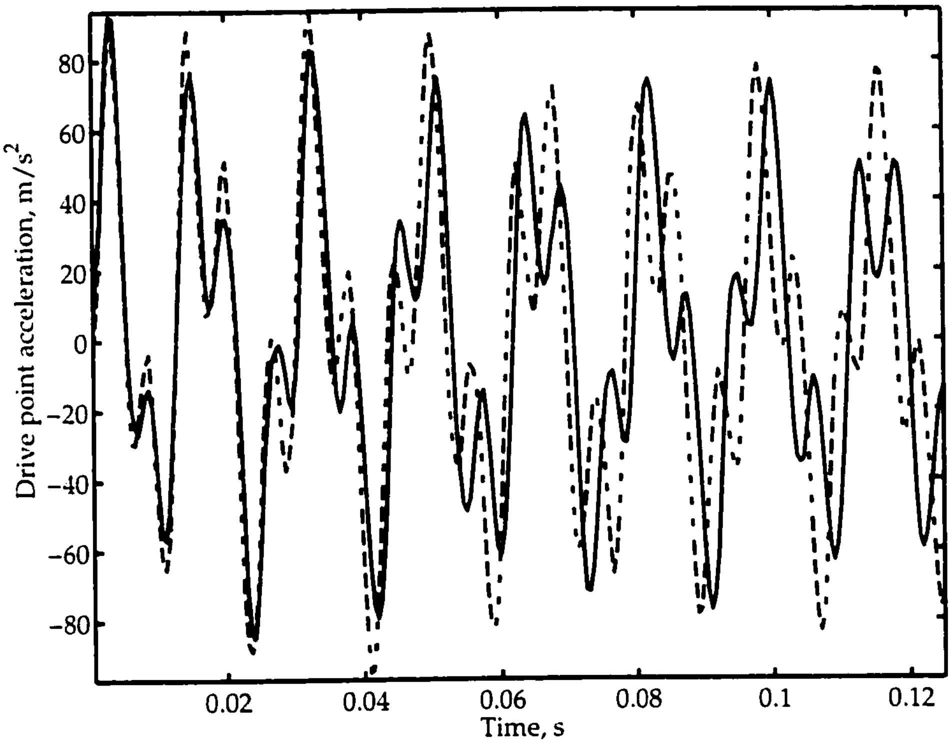

Figure 5.9: Drive point acceleration for the empty beam for trial 9. Measured data —: FEM - - -

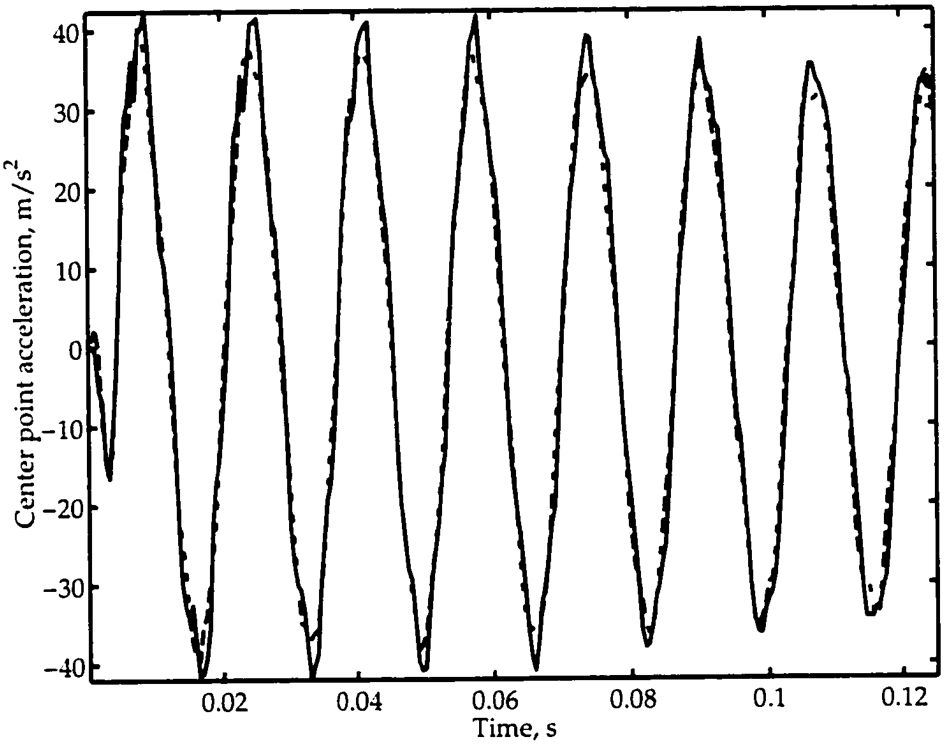

Figure 5.10: Center point acceleration for the empty beam for trial 9. Measured data —: FEM - - -

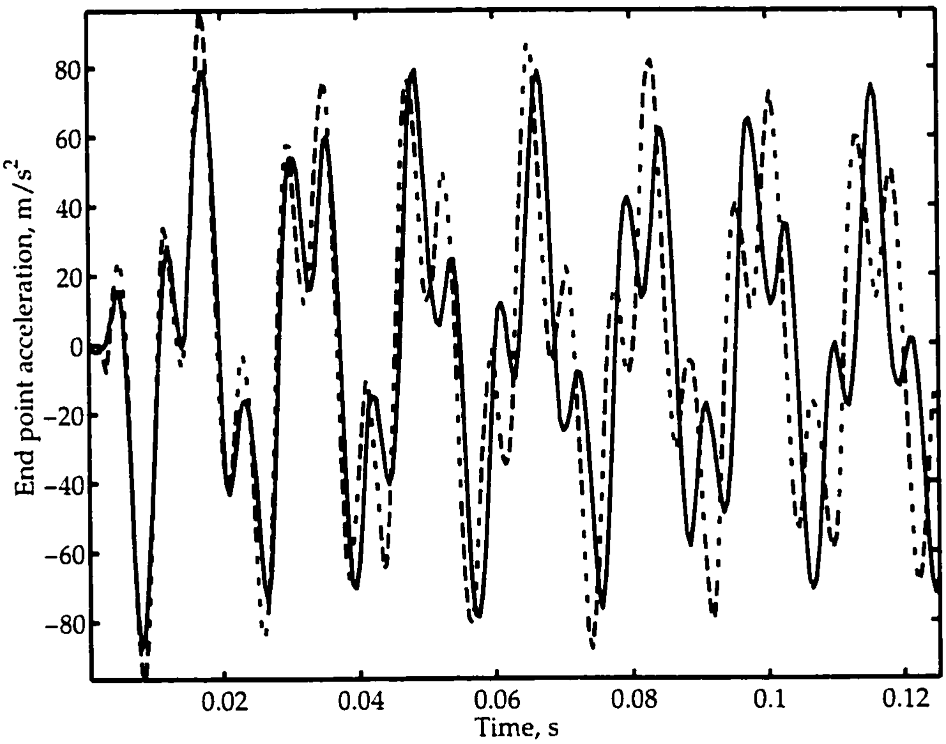

Figure 5.11: End point acceleration for the empty beam for trial 9. Measured data —: FEM - - -

5.5.2 Results from the optimization procedure

In Figures 5.12–5.14, the velocity magnitude is shown for trial 9 with the excitation force applied to the short side of the cross section. We observe that the model matches the measured data quite well in frequency domain.

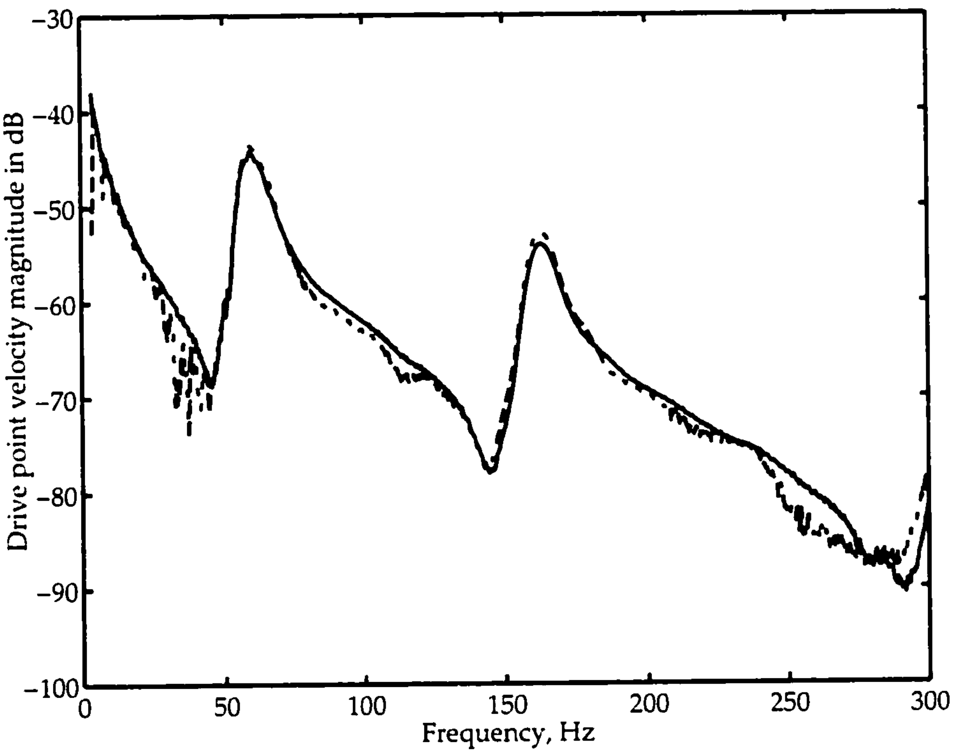

Figure 5.12: Drive point velocity magnitude for trial 9. Measured data —: Result from the optimization procedure - - -.

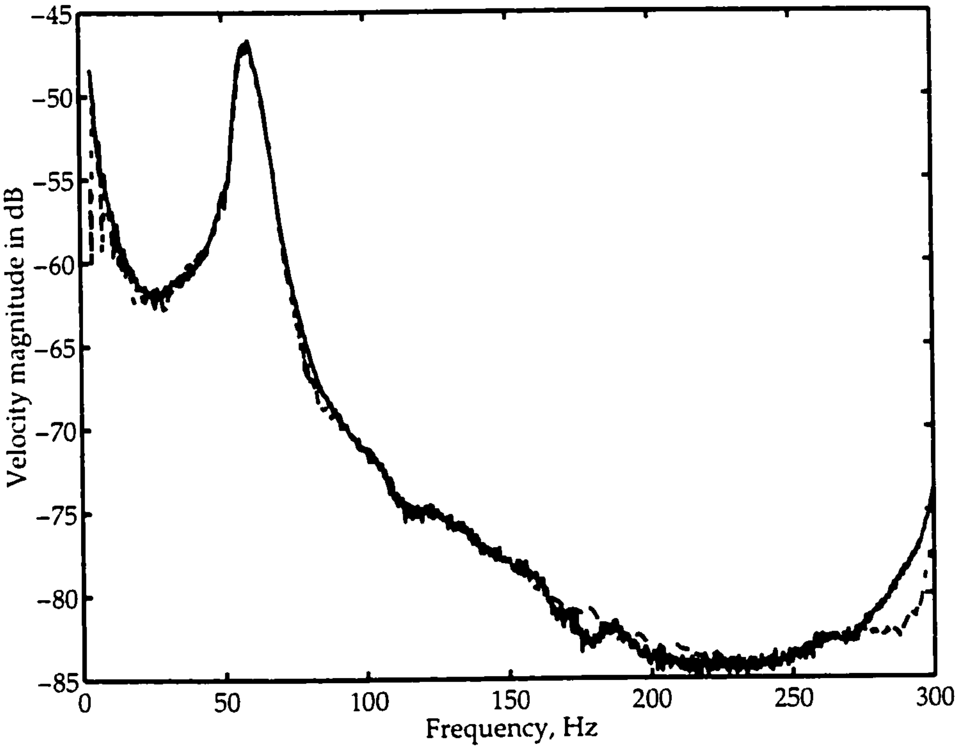

Figure 5.13: Velocity magnitude at the center for trial 9. Measured data —: Result from the optimization procedure - - -.

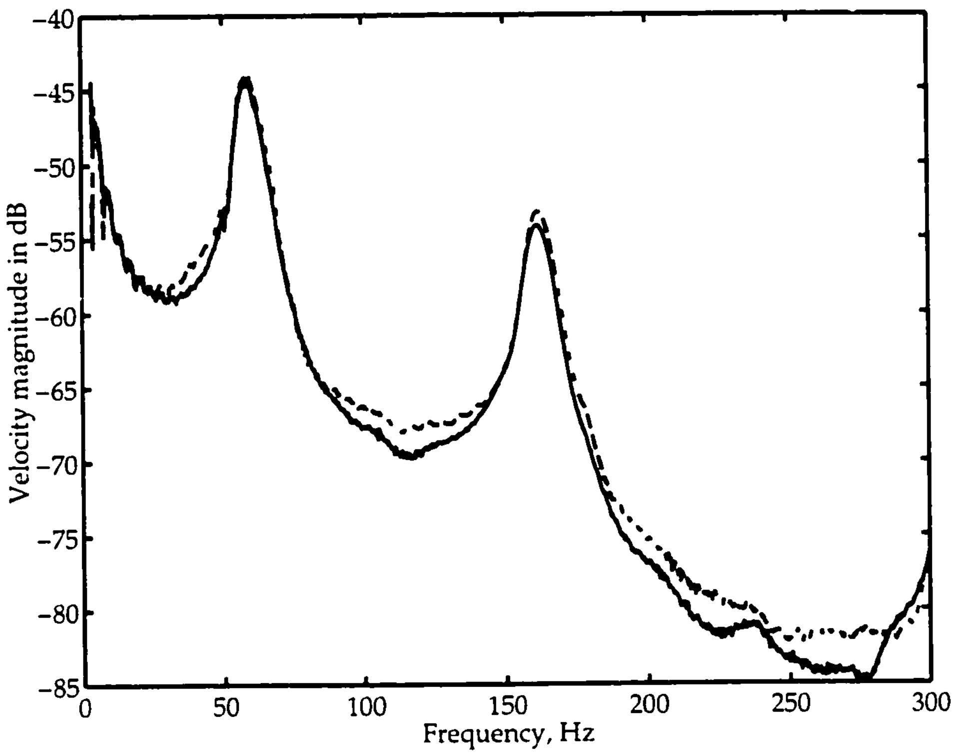

Figure 5.14: Velocity magnitude at the end for trial 9. Measured data —: Result from the optimization procedure - - -.

Figure 5.15 depicts the array impedance obtained by using the wave and finite elements models. It is observed that the two differ negligibly in the frequency band, which confirms the result accuracy. Figure 5.16 shows the normalized mean square error that was minimized by the optimization procedure. The error increases more than 20 per cent for frequencies larger than 220 Hz and lower than 10 Hz indicating that the model is incapabale of matching data in these ranges. Figure 5.17 shows the loss factor computed by Equation (5.14) (homogenization theory) and by the power flow ratio (Equation (5.15)). In the interval 100 - 150 Hz, the loss factor computed by the power flow ratio is higher than that from homogenization theory. This could be explained by the fact that the mass and stiffness of the damping treatment are not taken into account in the expression for the total power stored in the system per

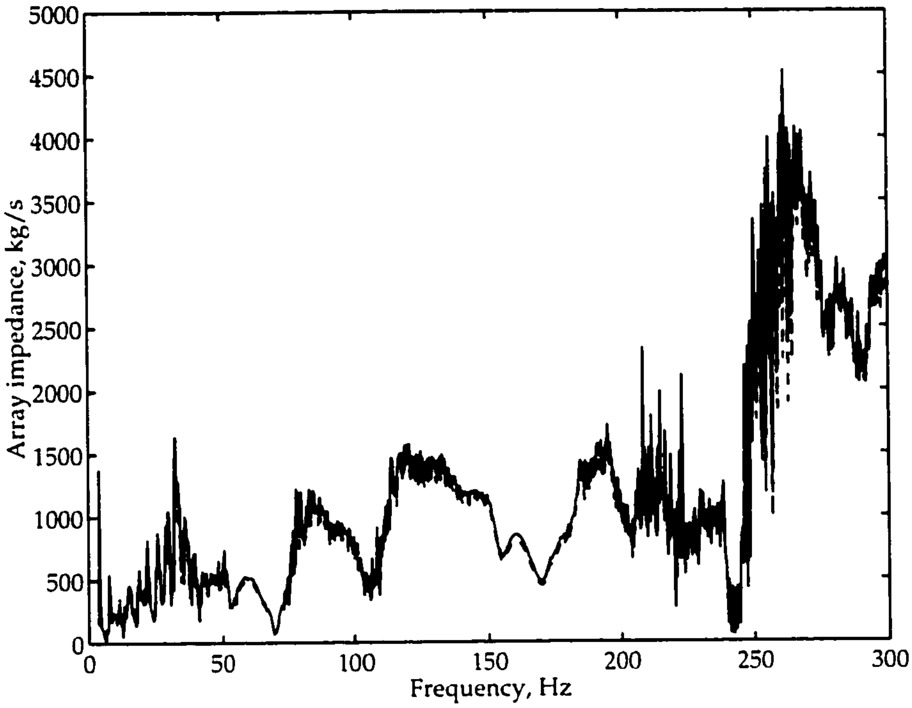

Figure 5.15: Array impedance magnitude for trial 9. FEM approach —: Wave approach - - -.

cycle (Equation (5.18)). which in turn gives a higher loss factor. Figures 5.18–5.20 depict the acceleration in time domain for the same trial. A good match is observed between the measured data and the model.

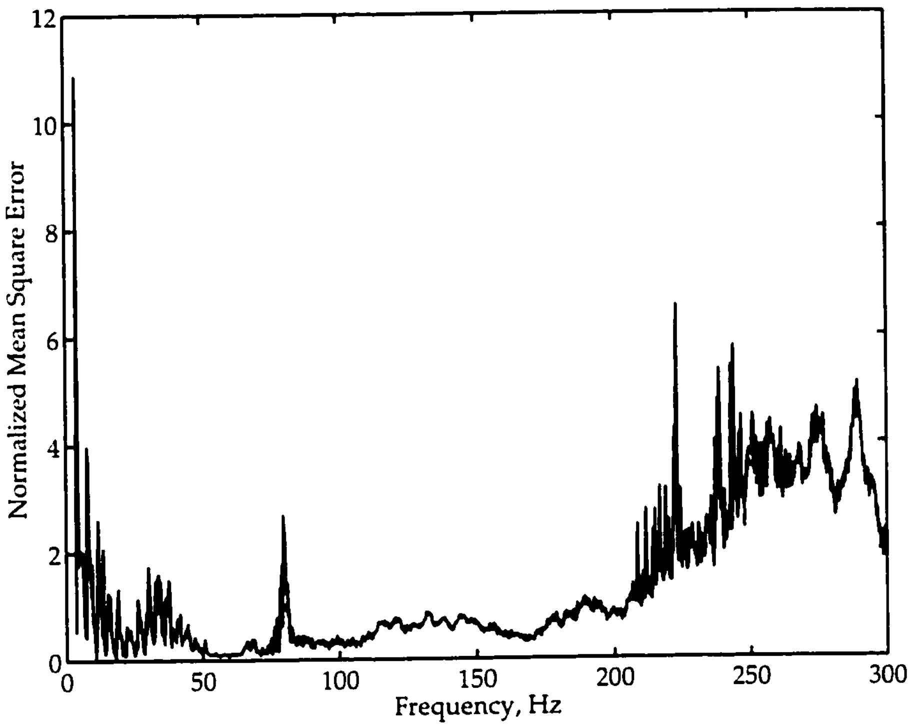

Figure 5.16: Normalized mean square error for trial 9. FEM approach —: Wave approach - - -.

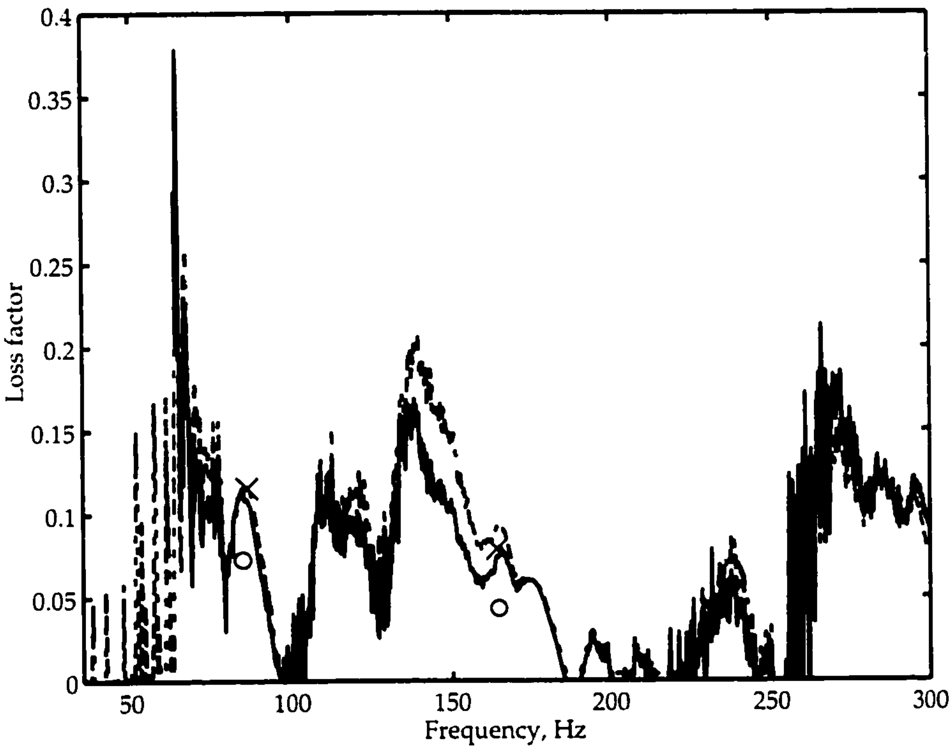

Figure 5.17: Loss factor of the structure obtained on the basis of the array impedance for trial 9. Computed by using the homogenization theory —: Computed by using the dissipated and the stored energies - - -: Half power ×: Modal analysis o.

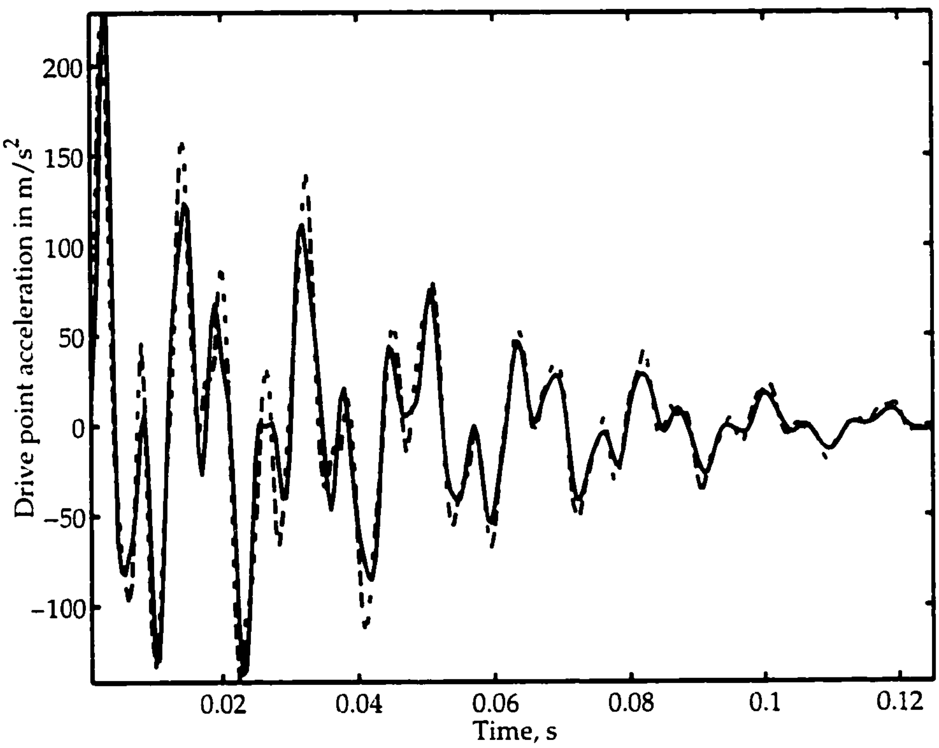

Figure 5.18: Drive point acceleration for trial 9. Measured data —: Result of the optimization procedure - - -.

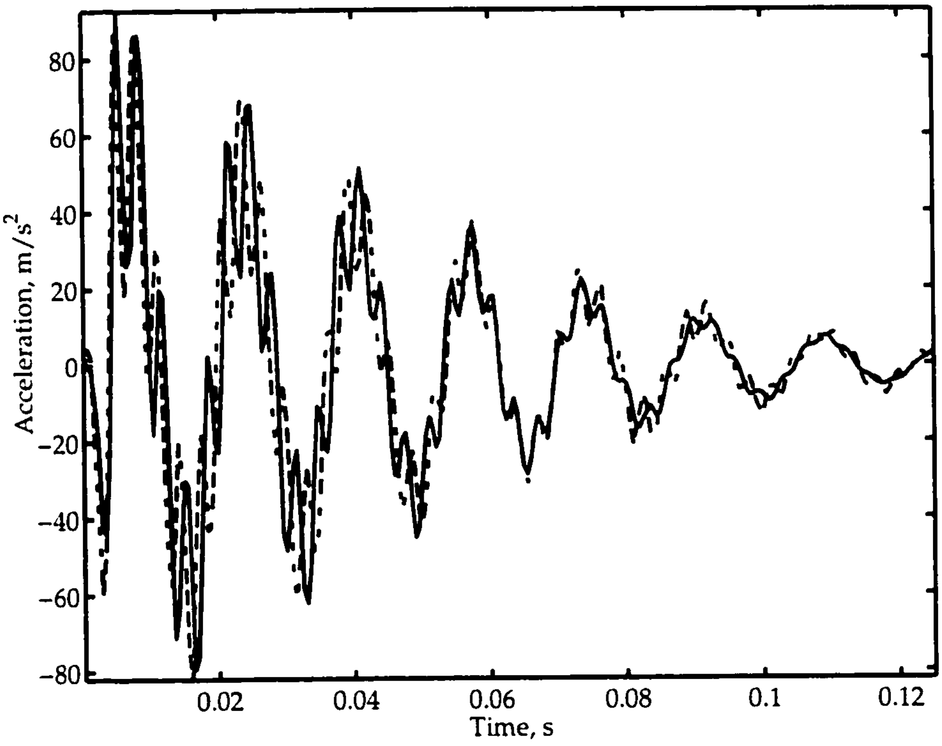

Figure 5.19: Acceleration at the center for trial 9. Measured data —: Result of the optimization procedure – – –.

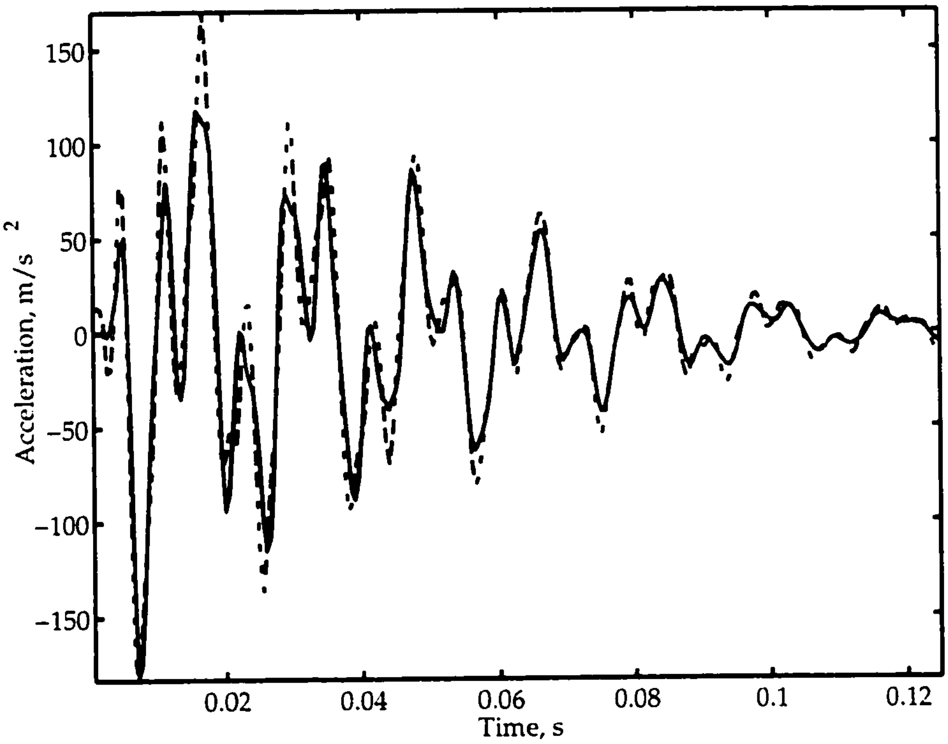

Figure 5.20: Acceleration at the end for trial 9. Measured data —: Result of the optimization procedure - - -.

5.5.3 Comparison of different trials and nonlinearity issues

There were 13 different trials for each of the two experiment types. The trials can be ordered in increasing magnitude of the impact force for trial 9. Figure 5.21 shows the excitation force trial 9. In Figure 5.22, a linearity test is conducted showing the ratio of maximum acceleration versus maximum force for each trial. Note that this graph would be a straight line if the data was linear. Trial 0 does not fit with the other data and it is therefore excluded from the trial set. On the basis of the results we conclude that a that there is a slight nonlinear behavior for the experiment trials with lower impact force. Figures 5.23-5.24 show the array impedance for different

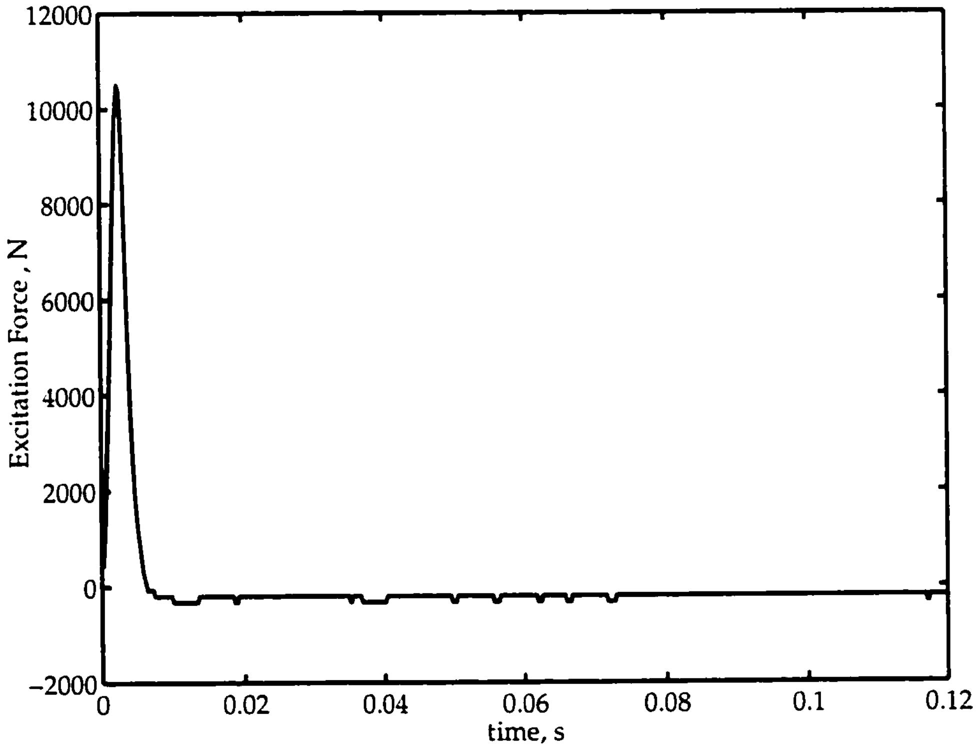

Figure 5.21: Excitation force for trial 9.

trials. Both array magnitude and phase are similar for the selected trials 12, 9, 7, and 6, which are high and middle impact trials. However, the low impact experiment

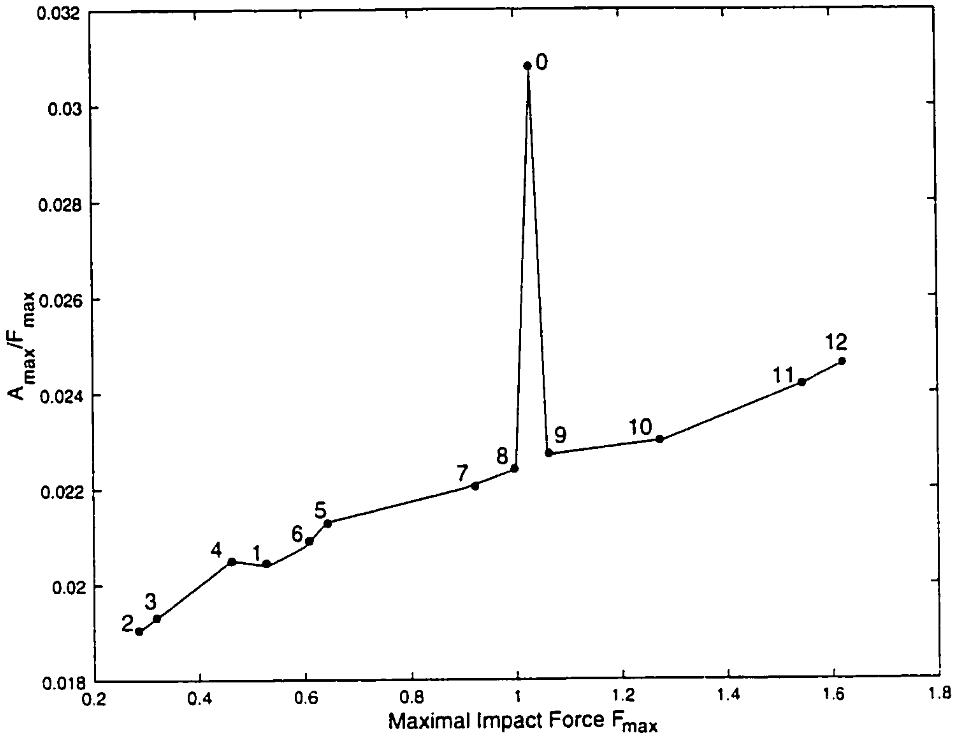

Figure 5.22: The ratio of maximal acceleration / maximal impact force versus maximal impact force for different trials.

trials do not agree, which can be explained by the observed nonlinear behavior.

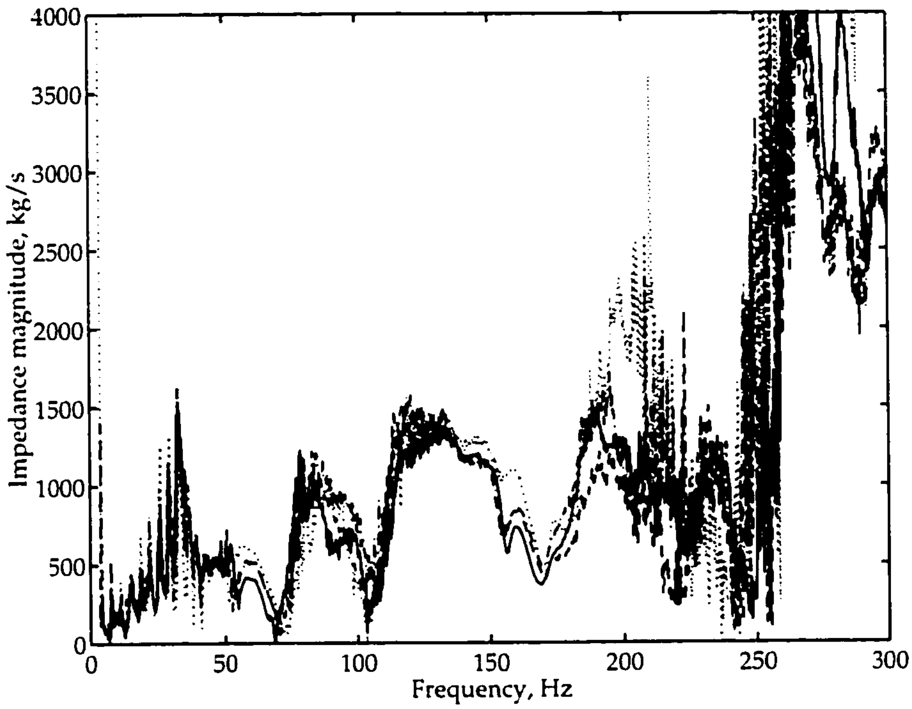

Figure 5.23: Impedance magnitude in radians for different trials. Trial 12 —: Trial 9 -·-: Trial 7 - - -: Trial 6 ....

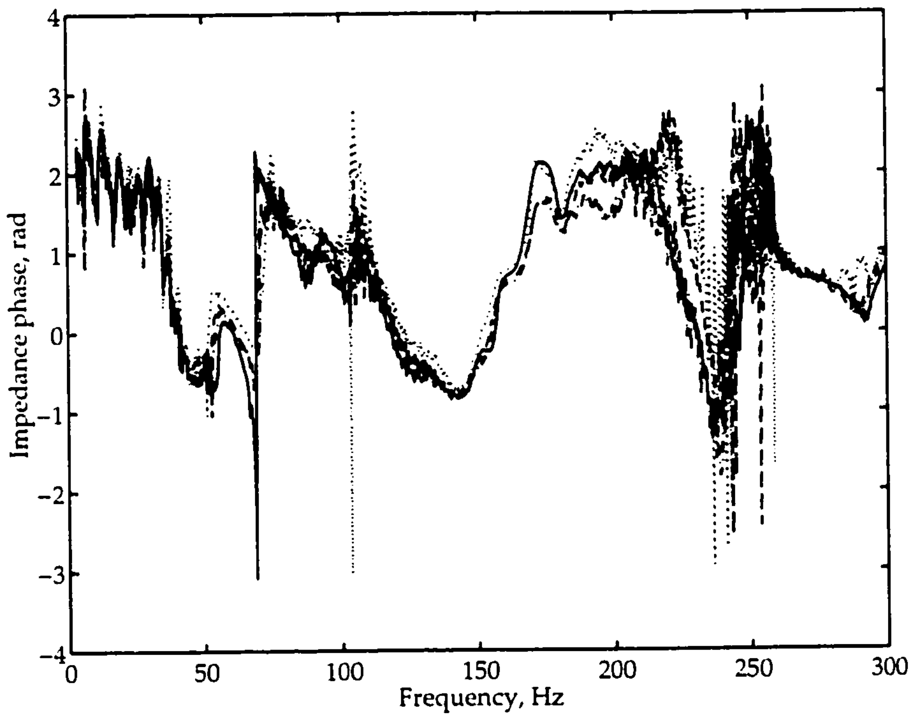

Figure 5.24: Impedance phase in radians for different trials. Trial 12 —: Trial 9 -·-: Trial 7 - - -: Trial 6 ....

5.5.4 Results for rational approximation of the array impedance

In this section, the results from a particular rational fit are discussed. Figures 5.25 and 5.26 show magnitude and phase of the array impedance for trial 9. For this

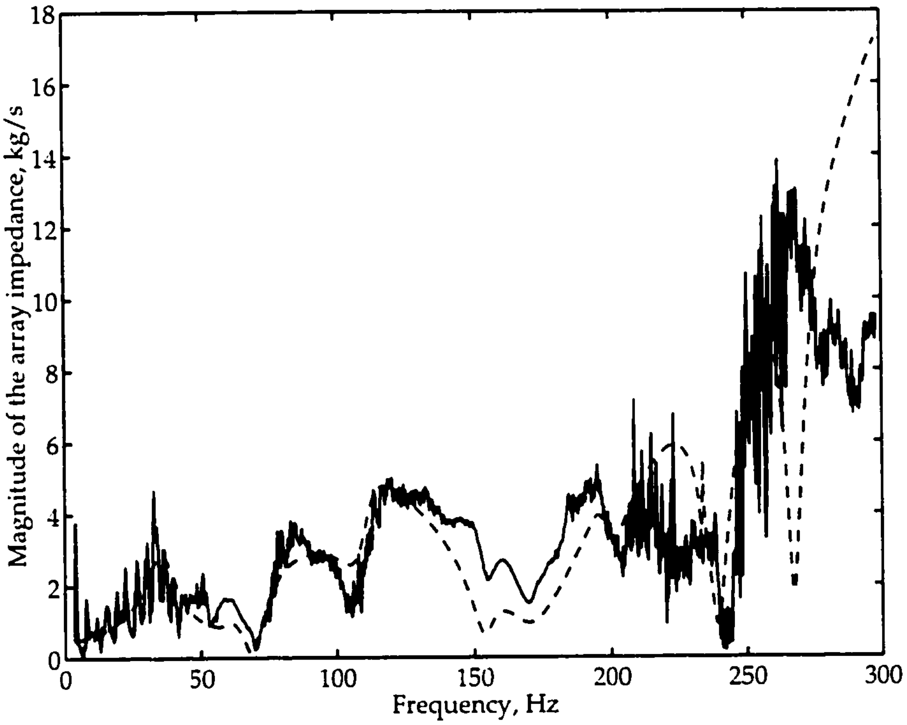

Figure 5.25: Magnitude of the array impedance, trial 9. Result from the optimization procedure —: Rational fit - - -

particular fit, a rational function is found in the form shown in Equation (5.20) with $N = 11$. Figures 5.27 and 5.28 show that poles of the function are in the left side of the complex s-plane thus fulfilling the stability requirement. Note that there are zeros which lie on the right side of the complex s-plane, which violates the passivity of the array impedance.

Note that around the second and first resonances (60 Hz and 160 Hz) this rational fit has smaller values for the impedance magnitude compared to the result from the optimization procedure. This, in turn, will lead to inaccuracy in the beam response.

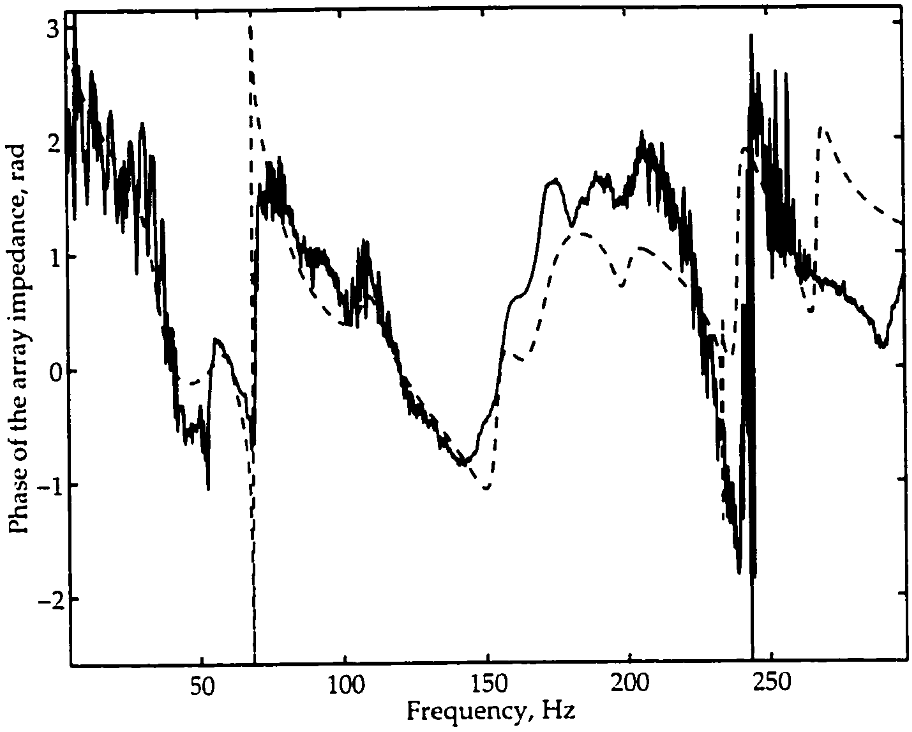

Figure 5.26: Phase of the array impedance. trial 9. Result from the optimization procedure —: Rational fit - - -

At present. better rational approximations have been sought but not found due to the following issues:

- the passivity and stability requirements impose additional constraints leading to increase of the computation time of the optimization procedure:

- the simple mechanical models for the array impedance such as mini-oscillators connected in parallel or in series did not lead to a satisfactory approximation. In future work. these issues should be resolved by using better optimization procedures and choosing more general physics-based models for the granular fill.

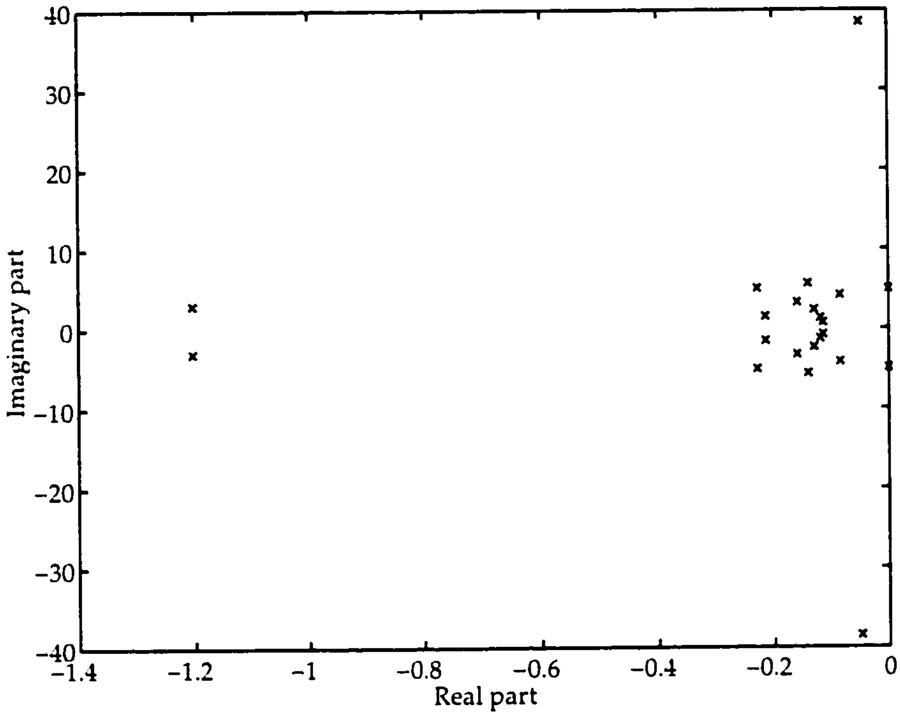

Figure 5.27: Poles of the rational fit in the complex s-plane

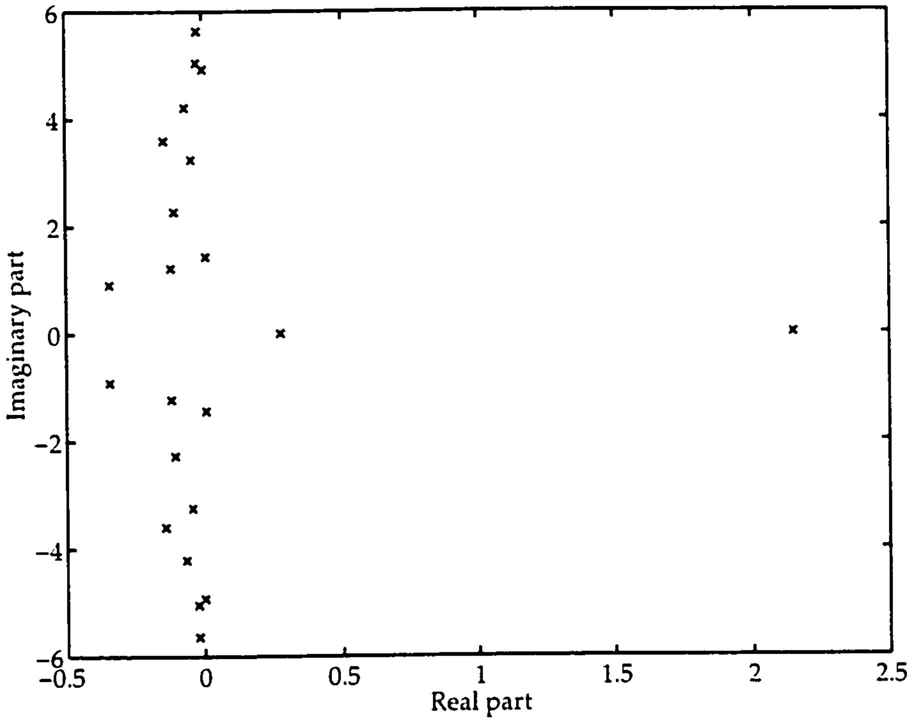

Figure 5.28: Zeros of the rational fit in the complex s-plane

5.5.5 Results from fluid model approximation of the array impedance

In this section, a fluid model for the beads is discussed and compared to the array impedance. The fluid properties that resulted in a match to data are summarized in Table 5.2. Figures 5.29 and 5.30 show the corresponding magnitude and phase

Material Property	Symbol	Used Value
Speed of sound in the beads fluid	c	$12.5 + i1.5\ m/s$
Fluid density	ρ_f	$588\ kg/m^3$
Cross-section area for the section	A_f	$6.19 \times 10^{-2}\ m^2$
Section length	L_f	$0.254\ m$

Table 5.2: Properties of the wave beads model

of the array impedance. for trial 9. which will be used to illustrate the model.

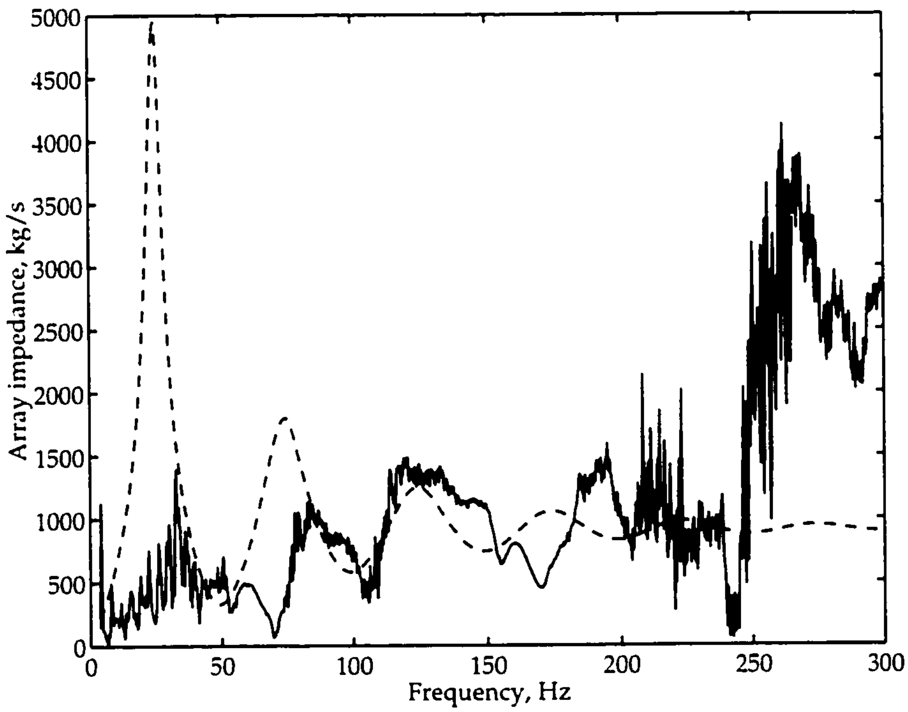

Figure 5.29: Magnitude of the array impedance. trial 9. Result from the optimization procedure —: Wave beads model - - -

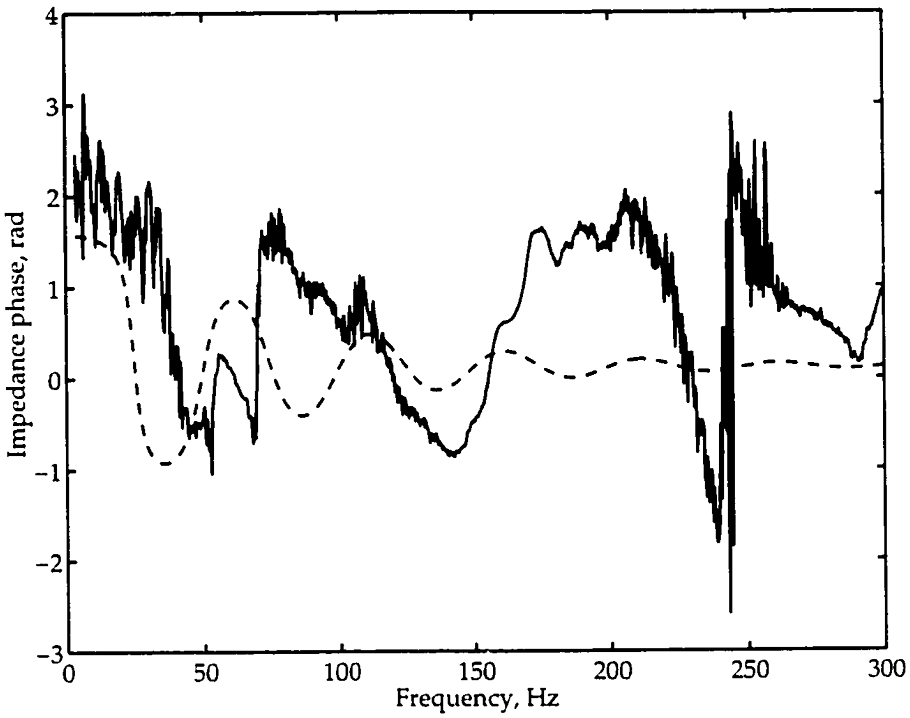

Figure 5.30: Phase of the array impedance, trial 9. Result from the optimization procedure —; Wave beads model - - -

We observe that the impedance obtained by the fluid model cannot approximate well the array impedance obtained by the optimization procedure because of the complicated frequency dependance of the latter (see Figure 5.29). The fluid falls into resonance near the frequencies 40 Hz, 90 Hz, 140 Hz and 190 Hz where the drive point impedance becomes small.

From the plots of the array impedance, one can conclude that a single fluid column is not sufficient to describe fully the complex nature of the granular fill impedance. Moreover, in order to develop an accurate model of the damping treatment the validity of the experimental data and the accuracy of the optimization procedure in the off-resonance regimes have to be understood better.

5.5.6 Model limitations at higher frequencies

There is a significant mismatch in the data measured at different locations in the plane of the cross section (see Figure 5.31) when the beam is subjected to damping treatment. However for the empty beam a very good agreement of the data is observed in the frequency range. These results reveal the limitation of the linear model for a beam with damping treatment and indicate nonlinear behavior in higher frequencies.

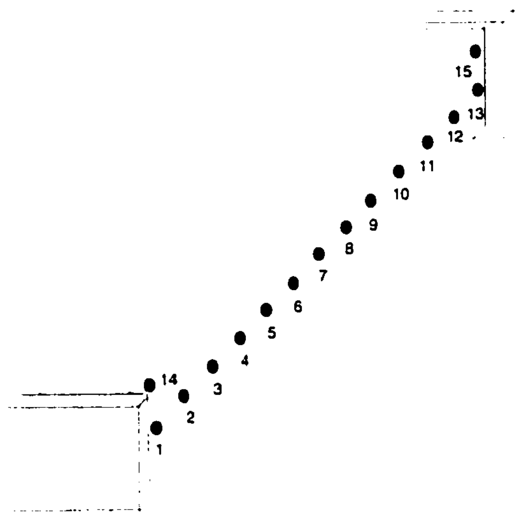

Figure 5.31: Scheme of the measurement nodes along the beam

Figure 5.32 shows that the velocity magnitude at node 15 differs significantly compared to that at node 13 if the frequency is larger than 200 Hz (see Figure 5.31). This also can be observed although is less distinct when the node 1 is compared with node 14 (Figure 5.33). The plots are prepared for the beam filled with damping treatment and excited at the short side. If the filled beam is subject to a long-side impact the difference becomes drastic and for the considered trial the 1D model is inapplicable after the first resonance (Figures 5.34–5.35). If one repeats this procedure for empty beam one sees that the 1D Euler-Bernoulli model is valid in the

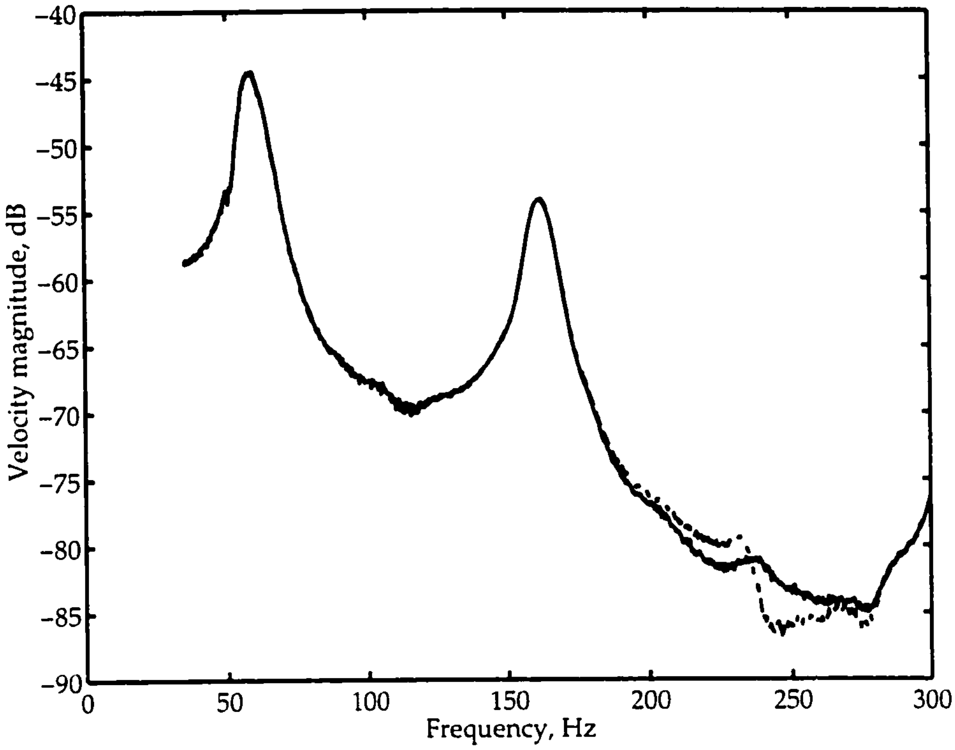

Figure 5.32: Comparison between the velocity at the node 13 and the velocity at node 15 for trial 9. Node 13 —: Node 15 - - -.

considered frequency range as it can be seen from Figures 5.35 and 5.34.

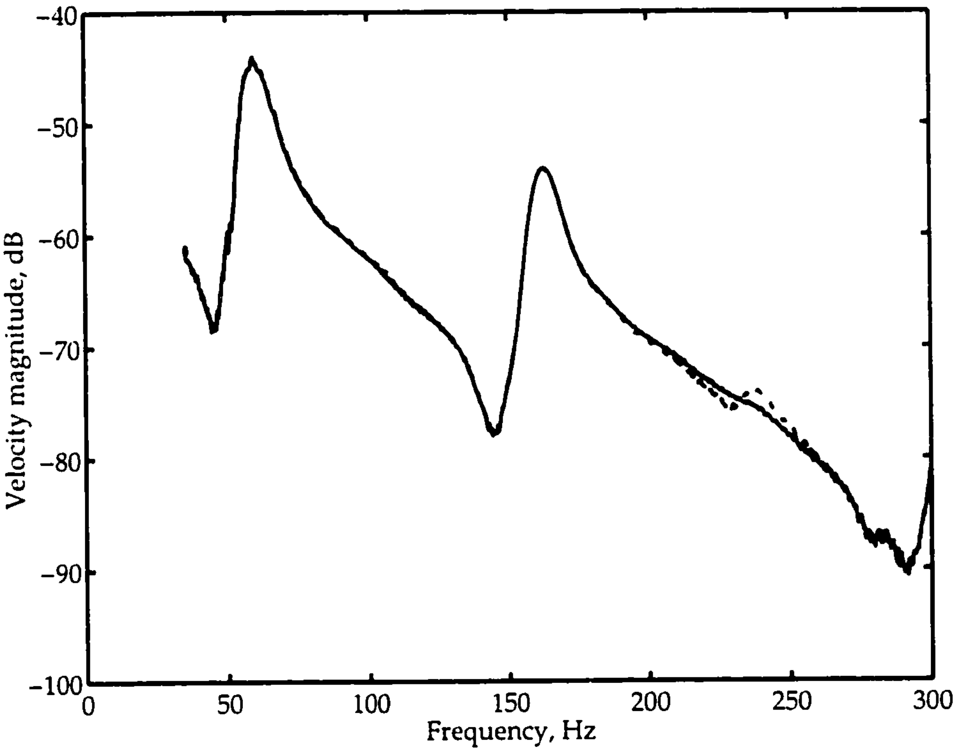

Figure 5.33: Comparison between the velocity magnitude at the node 1 and that at the node 14 for trial 9. The force is applied at the short side of the cross-section and the beam is filled with damping treatment. Node 1 —: Node 14 - - -.

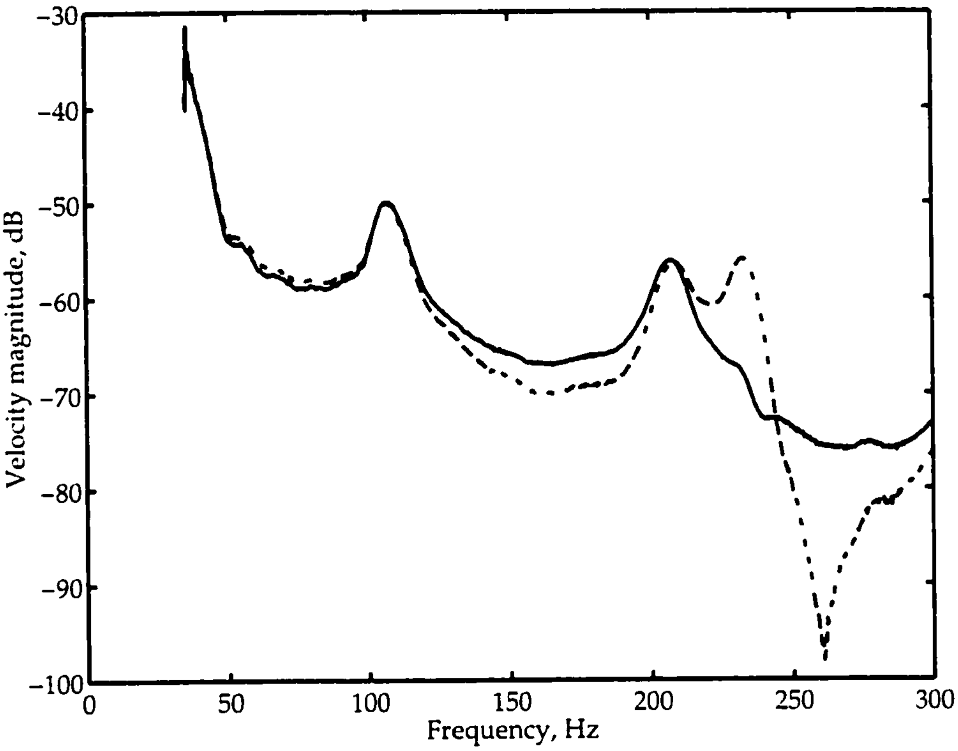

Figure 5.34: Comparison between the velocity at the node 13 and the velocity at node 15 for trial 9. The force is applied at the long side of the cross-section and the beam is filled with damping treatment. Node 13 —: Node 15 - - - .

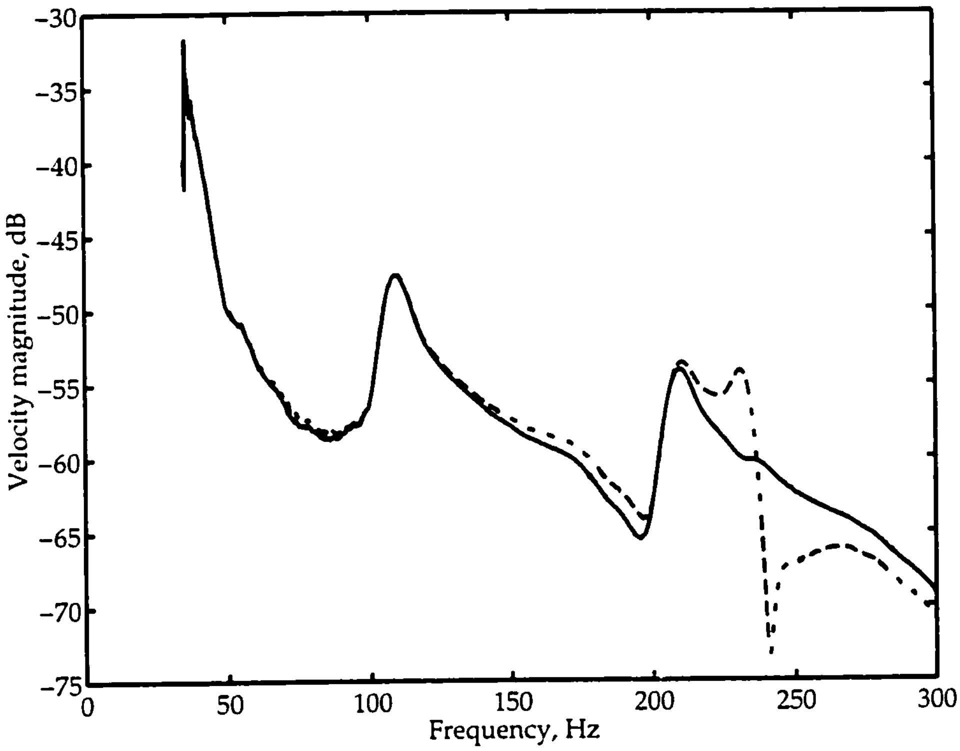

Figure 5.35: Comparison between the velocity magnitude at the node 1 and that at the node 14 for trial 9. The force is applied at the long side of the cross-section and beam is filled with damping treatment. Node 1 —; Node 14 - - - .

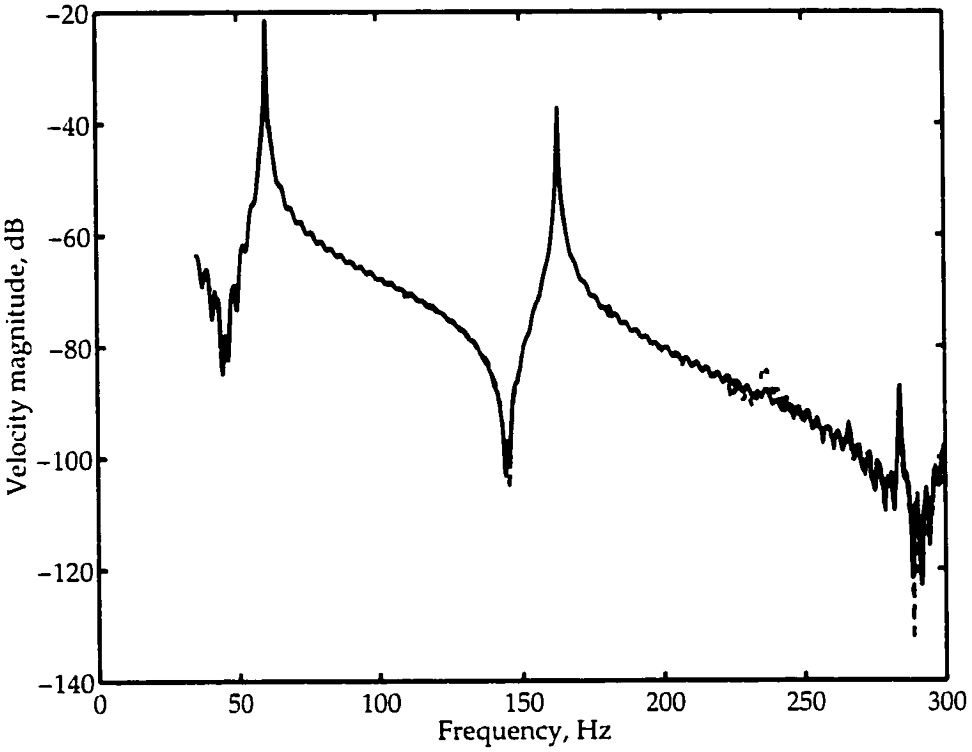

Figure 5.36: Comparison between the velocity magnitude at the node 1 and that at the node 14 for trial 9. The force is applied at the short side of the cross-section and the beam is without damping treatment. Node 1 —: Node 14 - - -.

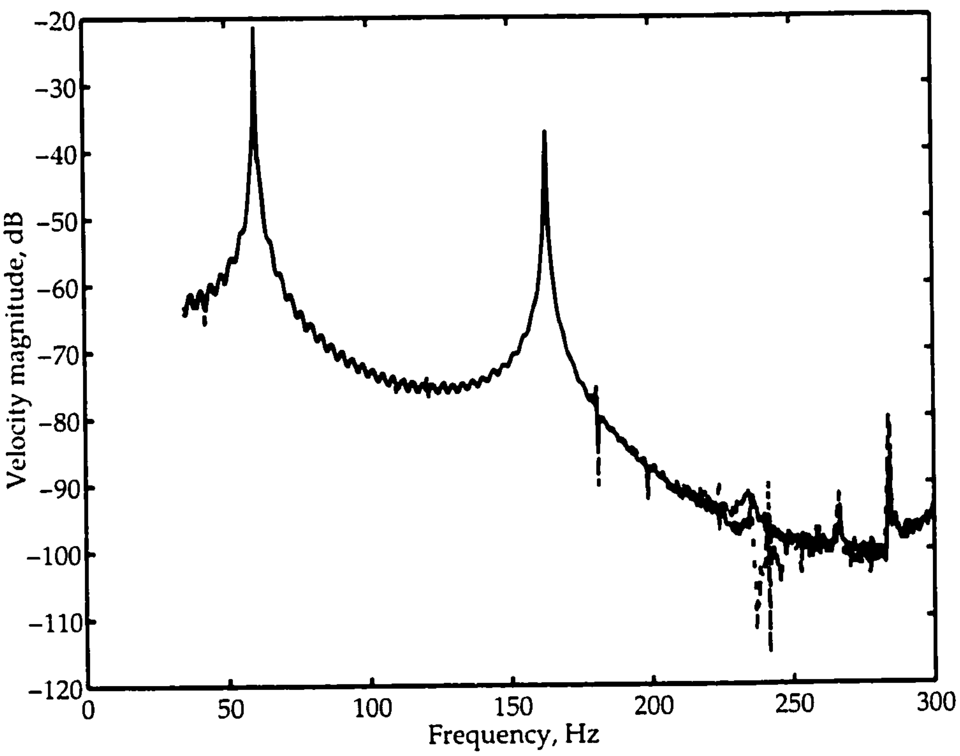

Figure 5.37: Comparison between the velocity magnitude at the node 13 and the velocity at node 15 for trial 9. The force is applied at the short side of the cross-section and the beam is without damping treatment . Node 13 —: Node 15 - - -.

5.6 Chapter summary

A new model for damping treatments is presented and applied to experimental data. The array impedance and loss factor of the damped structure are obtained using an optimization procedure that matches the finite element model prediction with the measured data in the frequency domain. The computed response shows very good agreement with the measured data, both in the frequency and time domains. The array impedance is approximated by a rational function such that the model becomes linear with reduced order. On the basis of this approximation, a time-domain FE model can built in which the model matrices can be constructed on the basis of the FE matrices for the empty beam and the coefficients of the rational fit.

Chapter 6

Conclusions

Analytic treatment of the dispersion relations and the response of infinite periodic structures with multiple arrays of attachments has resulted in a new recursive procedure for the computation of the Floquet wavenumbers and structural response. This procedure is a generalization of the approach presented by Mace to two-array structures [20]. The main contributions associated with this work are the closed-form expressions of the dispersion relations for the case of two or more arrays and expressions for the spatial structural response. Investigation into the attenuation associated with shifting one array with respect to another. producing an offset. have suggested a class of optimal isolation structures.

A new design of a MEMS resonator with high Q factor on the basis of nonuniform periodic structure was achieved by these analytical studies. To evluate the new design. the connection between the energy localization phenomenon and the structural Q factor was formalized. A design procedure is proposed which renders periodically-designed resonators with optimal performance. The design parameters (the length of the uniform sector. the ribs mass. and the array spacing) can be selected such that the high Q factor is achieved in a given resonance frequency. Realistic designs. fully integrated on chip level for high Q MEMS resonators are developed and evaluated on the basis of 2D finite element model. Here it is studied the effect of the rib number, shape, and material on the Q factor. It is observed, contrary to the intuition, that adding a tin cover on the rib top does not necessarily increases the Q factor. Four different periodic designs for high Q MEMS resonators are selected and proposed for manufacture.

As a recommendation for future investigations into more complex periodic structures should be analyzed for high Q MEMS resonators. These may render better performance than the ones considered in this thesis. For instance, periodic structures formed by two arrays of attachments may lead to broader attenuation bands in the frequency range of interest. Three dimensional FEM may be used taking into account the technological constraints when such resonators are built. Additionally, the influence of the surrounding gas on the resonator damping should be incorporated in the FEM which will lead to a more realistic estimate of the Q factor.

Partial homogenization concept for complex periodic structures is introduced in Chapter 4. This approach allows periodic structures with multiple arrays to be simplified significantly over practical frequency ranges. Low-frequency expansions were developed for the leading and second order terms of the Floquet wavenumber and the structural response at the cell boundary for the case of attachments modeled as pure masses. Error bounds were derived and the parameters controlling the homogenization error were identified. Through examples, we found that the latter expansions were relevant for attachments such as dashpots and springs. The partial homogenization concept can be applied to structures such as hulls and aircraft fuselages formed by multiple arrays of ribs which will result in simple computation procedure using relevant approximations for the structural wavenumbers. As a recommendation for future investigation one should consider formalizing the partial homogenization procedure for arbitrary impedance attachments (not only pure masses).

In Chapter 5 a new periodic model for damping treatment was presented and a procedure for estimating the structural loss factor was described. Array impedances and loss factors of the considered structure are obtained on the basis of optimization procedure matching the computed beam response with the measured data in frequency domain and using FE method. The computed response showed very good agreement with the measured data both in frequency and time domain. The array impedance was approximated by a rational function such that the model becomes linear with reduced order. On the basis of rational fraction approximation a time-domain FE model can be built where the model matrices can be constructed on the basis of the FE matrices for the empty beam and the coefficients of the rational fit. However, a good rational fit was not found and it should be a subject to a future investigation. Additionally, a physics-based approximation was proposed which models the damping treatment as a fluid column with low sound speed. It was observed that this simplified fluid model does not agree well with the complex nature of the damping treatment. As a future research topic, more accurate models for the beam with granular fill should be investigated. Additionally, the accuracy of the optimization procedure should be better understood.

More complicated periodic structures have not been used in real engineering systems because they have not been well understood. This thesis has developed an understanding of the design parameters and how they control the wave propagation in structures with multiple arrays of attachments and has illustrated the use of this understanding in two example applications.

Appendix A

Dispersion relation of piecewise periodic structure

Let us consider an infinite chain of multicoupled identical elastic substructures. In this Appendix we will derive the dispersion relation for the problem shown in Figure A.1.

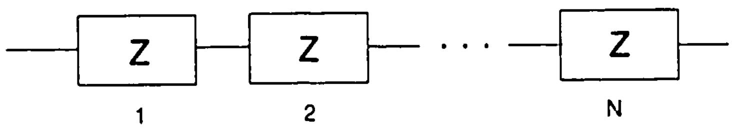

Figure A.1: Infinite chain of identical substructures

Let us consider a single element from the chain as shown on Figure A.2.

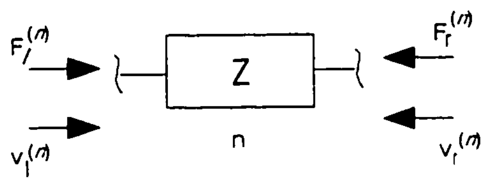

Figure A.2: Single substructure from the chain

Throughout the chapter, the subscripts l and r shall relate the corresponding quantity to the left and right boundary of the element accordingly. The superscript (n) relates the quantity to the nth substructure. Note that the forces $F_l^{(n)}$, $F_r^{(n)}$ and velocities $v_l^{(n)}$, $v_r^{(n)}$ on the element boundaries will be M-vectors for M coupled problem. For the case of flexure of Euler-Bernoulli beam M is equal to 2. Let us partition the impedance matrix $[Z]$ of the substructure in the following form

$$[Z] = \begin{bmatrix} Z_{ll} & Z_{li} & Z_{lr} \\ Z_{il} & Z_{ii} & Z_{ir} \\ Z_{rl} & Z_{ri} & Z_{rr} \end{bmatrix} \tag{A.1}$$

where the subscript i denotes the internal DOF which are not coupled with other substructures.

Then the equation of motion of the nth substructure becomes

$$[Z] \begin{Bmatrix} v_l^{(n)} \\ v_i^{(n)} \\ v_r^{(n)} \end{Bmatrix} = \begin{Bmatrix} F_l^{(n)} \\ 0 \\ -F_r^{(n)} \end{Bmatrix} \tag{A.2}$$

After eliminating the internal DOF from Equation (A.2) one obtains the reduced system

$$Z_{11} v_l^{(n)} + Z_{12} v_r^{(n)} = F_l^{(n)} \tag{A.3}$$

$$Z_{21} v_l^{(n)} + Z_{22} v_r^{(n)} = -F_r^{(n)} \tag{A.4}$$

where the condensed impedance matrices Z_{11}, Z_{12}, Z_{21}, and Z_{22} are given with

$$Z_{11} = Z_{ll} - Z_{li}Z_{ii}^{-1}Z_{il}; \quad Z_{12} = Z_{lr} - Z_{li}Z_{ii}^{-1}Z_{ir} \tag{A.5}$$

$$Z_{21} = Z_{rl} - Z_{ri}Z_{ii}^{-1}Z_{il}; \quad Z_{22} = Z_{rr} - Z_{ri}Z_{ii}^{-1}Z_{ir} \tag{A.6}$$

Note that $Z_{12} = Z_{21}{}^T$ which follows from Equation (A.6).

Assuming Floquet theorem with respect to boundary forces and velocities as

$$F_r{}^{(n)} = e^{\mu}F_l{}^{(n)}; \quad v_r{}^{(n)} = e^{\mu}v_l{}^{(n)} \tag{A.7}$$

and substituting the latter into Equation (A.4) results in

$$Z_{ll}v_l{}^{(n)} + Z_{lr}e^{\mu}v_l{}^{(n)} = F_l{}^{(n)} \tag{A.8}$$

$$Z_{rl}v_l{}^{(n)} + Z_{rr}e^{\mu}v_l{}^{(n)} = -e^{\mu}F_l{}^{(n)} \tag{A.9}$$

and after eliminating the force vector $F_l{}^{(n)}$ we obtain the homogeneous equation

$$(Z_{ll} + Z_{rl}e^{\mu} + Z_{rl}e^{-\mu} + Z_{rr})v_l{}^{(n)} = 0 \tag{A.10}$$

In order to obtain nontrivial solution of Equation (A.10) the following has to be fulfilled

$$\left|Z_{ll} + Z_{rl}e^{\mu} + Z_{rl}e^{-\mu} + Z_rr\right| = 0 \tag{A.11}$$

The latter represent the dispersion relation of the chain of elastic substructures. Note that it is a polynomial with $2M$ order with respect to the quantity e^{μ}.

Appendix B

Finite element model for the transverse vibrations of thin Euler-Bernoulli beam

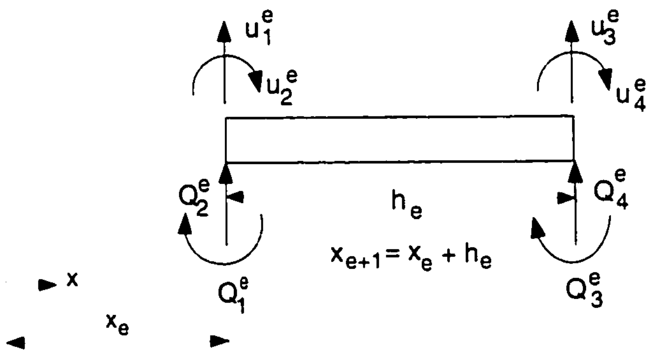

Figure B.1: Euler-Bernoulli beam element

The beam displacement can be expressed as

$$w^e(x) = u_1{}^e\phi_1{}^e + u_2{}^e\phi_2{}^e + u_3{}^e\phi_3{}^e + u_4{}^e\phi_4{}^e \tag{B.1}$$

where u_m are the nodal displacements and $\phi_m{}^e$, $m = 1, ..., 4$ are the Hermite interpolation functions. It is required that the beam's transversal and rotational displacements are equal to the corresponding nodal displacements as shown below

$$w^e|_{x=x_e} = u_1{}^e; \quad \left.\frac{dw^e}{dx}\right|_{x=x_e} = -u_2{}^e; \quad w^e|_{x=x_{e+1}} = u_3{}^e; \quad \left.\frac{dw^e}{dx}\right|_{x=x_{e+1}} = -u_4{}^e \quad (B.2)$$

The interpolation functions $\phi_m{}^e$, $m = 1, ..., 4$ will satisfy the following properties

$$\phi_1{}^e(x_e) = 1; \qquad \phi_m{}^e(x_e) = 0 \quad (m \neq 1) \tag{B.3}$$

$$\phi_3{}^e(x_{e+1}) = 1; \qquad \phi_m{}^e(x_{e+1}) = 0 \quad (m \neq 3) \tag{B.4}$$

$$-\left.\frac{d\phi_2{}^e}{dx}\right|_{x=x_e} = 1; \qquad -\left.\frac{d\phi_m{}^e}{dx}\right|_{x=x_e} = 0 \quad (m \neq 2) \tag{B.5}$$

$$-\left.\frac{d\phi_4{}^e}{dx}\right|_{x=x_{e+1}} = 1; \qquad -\left.\frac{d\phi_m{}^e}{dx}\right|_{x=x_{e+1}} = 0 \quad (m \neq 4) \tag{B.6}$$

Using (B.3) - (B.6) and restricting the order of the interpolation function to be equal or less than 3 one can obtain the following expressions

$$\phi_1{}^e = 1 - 3\xi^2 + 2\xi^3; \qquad \phi_2{}^e = -\xi(1-\xi)^2 \tag{B.7}$$

$$\phi_3{}^e = 3\xi^2 - 2\xi^3; \qquad \phi_4{}^e = -\xi(\xi^2 - \xi) \tag{B.8}$$

Here ξ is the local coordinate and it is given by

$$\xi = \frac{x - x_e}{h_e} \tag{B.9}$$

The element stiffness and mass matrices are expressed in terms of the Hermite interpolation functions as

$$K_{mn}{}^e = EI \int_{x_e}^{x_{e+1}} \frac{d^2\phi_m{}^e}{dx^2} \frac{d^2\phi_n{}^e}{dx^2} dx; \qquad M_{mn}{}^e = \rho t_e A_e \int_{x_e}^{x_{e+1}} \phi_m{}^e \phi_n{}^e dx \tag{B.10}$$

Appendix C

Two dimensional FE model for high Q MEMS resonator

The element stiffness and mass matrices are computed by using the well-known relations

$$[K^e] = \int_A [B]^T[D][B]tdA \qquad [M^e] = \rho \int_A [N]^T[N]tdA \tag{C.1}$$

where $[N]$ is the shape functions matrix and $[B]$ is the strain matrix of the element, relating element strain and nodal variables. Turner-Clough shape function matrix provides bilinear displacement approximation superimposed by bubble functions in order to create a linear stress field over the element. The displacement field is expressed in terms of the nodal variables

$$\{u\} = [N]\{q\} \tag{C.2}$$

where

$$\{u\} = \begin{bmatrix} u_x \\ u_y \end{bmatrix} \qquad \{q\} = \begin{bmatrix} q_1 \\ q_2 \\ \vdots \\ q_8 \end{bmatrix} \qquad [N] = \begin{bmatrix} N_1 & N_5 & N_2 & N_5 & N_3 & N_5 & N_4 & N_5 \\ N_6 & N_1 & N_6 & N_2 & N_6 & N_3 & N_6 & N_4 \end{bmatrix} \tag{C.3}$$

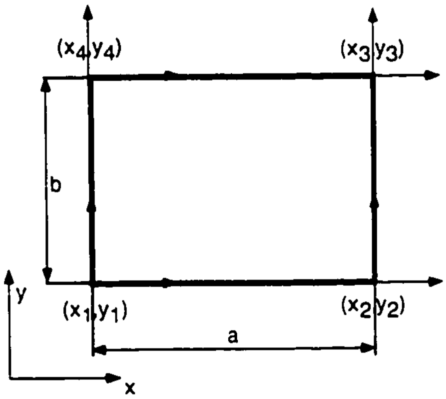

Figure C.1: Turner-Clough solid element

With a local coordinate system located at the center of the element (fig. C.1), the element shape functions $N_1, \ldots, N_6$ are obtained as

$$N_1 = \frac{1}{4ab}(a-x)(b-y) \qquad N_2 = \frac{1}{4ab}(a+x)(b-y) \qquad N_3 = \frac{1}{4ab}(a+x)(b+y)$$
$$N_4 = \frac{1}{4ab}(a-x)(b+y) \quad N_5 = \frac{1}{8ab}[(b^2-y^2)+\nu(a^2-x^2)] \quad N_6 = \frac{1}{8ab}[(a^2-x^2)+\nu(b^2-y^2)] \tag{C.4}$$

where

$$a = \frac{1}{2}(x_3 - x_1) \qquad b = \frac{1}{2}(y_3 - y_1) \tag{C.5}$$

The strain matrix $[B]$ is obtained as

$$[B] = \nabla[N] \tag{C.6}$$

where

$$\nabla = \begin{bmatrix} \frac{\partial}{\partial x} & 0 \\ 0 & \frac{\partial}{\partial y} \\ \frac{\partial}{\partial y} & \frac{\partial}{\partial x} \end{bmatrix} \tag{C.7}$$

Evaluation of the integrals for Turner-Clough element can be done either analytical or numerical by use of a 2×2 point Gauss integration scheme.

Appendix D

Expansions and derivation details

$$\sqrt{1-z} \sim 1 - \frac{z}{2} - \frac{z^2}{8} - \frac{z^3}{16} + \mathcal{O}\left[z^4\right] \tag{D.1}$$

$$\frac{1}{6\sqrt{2}} B^{3/2} {\Omega_1}^{3^{3/2}} \sim \frac{1}{24} {\Omega_1}^3 + \mathcal{O}\left[{\Omega_1}^5\right] \tag{D.2}$$

$$B^{5/2} {\Omega_1}^{5^{5/2}} \sim \frac{1}{2^{3/2}} {\Omega_1}^5 + \mathcal{O}\left[{\Omega_1}^7\right] \tag{D.3}$$

After applying cosine and sine functions on the both sides of Equation (4.24) we approximate

$$\cos(kd) \sim \cos(\Omega_1) - \sin(\Omega_1) K + \mathcal{O}\left[{\Omega_1}^5\right] \tag{D.4}$$

$$\sin(kd) \sim \sin(\Omega_1) + \cos(\Omega_1) K + \mathcal{O}\left[{\Omega_1}^5\right] \tag{D.5}$$

With the assumption that Ω_1 is small enough, the expansions hold

$$\cos(\Omega_1) \sim 1 - \frac{{\Omega_1}^2}{2} + \frac{{\Omega_1}^4}{24} + \mathcal{O}\left[{\Omega_1}^6\right] \quad \text{and} \tag{D.6}$$

$$\sin(\Omega_1) \sim \Omega_1 - \frac{{\Omega_1}^3}{6} + \mathcal{O}\left[{\Omega_1}^5\right]. \tag{D.7}$$

Substituting Equation (D.6) and (D.7) into (D.4) and (D.5) renders

$$\cos(kd) \sim 1 - {\Omega_1}^2 + \frac{1+2\zeta}{24(1+\zeta)}{\Omega_1}^4 + \mathcal{O}\left[{\Omega_1}^5\right] \quad \text{and} \tag{D.8}$$

$$\sin(kd) \sim \Omega_1 - \frac{3\zeta^2+4\zeta+4}{24(1+\zeta)^2}{\Omega_1}^3 + \mathcal{O}\left[{\Omega_1}^5\right] \tag{D.9}$$

. Using Equation (D.8) and (D.9) and the expansion for $\cos(\Omega)$ given in (4.18). we obtain

$$\frac{\cos(kd)-\cos(\Omega)}{\sin(kd)d} \sim -\frac{\zeta}{2d(1+\zeta)} \times \frac{\Omega_1 - p(\zeta){\Omega_1}^3 + \mathcal{O}\left[{\Omega_1}^5\right]}{1 - q(\zeta){\Omega_1}^2 + \mathcal{O}\left[{\Omega_1}^4\right]} \tag{D.10}$$

where

$$p(\zeta) = \frac{1}{6(1+\zeta)^2}; \quad q(\zeta) = \frac{3\zeta^3+4\zeta+4}{24(1+\zeta)^2} \tag{D.11}$$

Substituting the geometric series

$$\frac{1}{1-z} = 1 + z + z^2 + \mathcal{O}\left[z^3\right] \tag{D.12}$$

in the right side of Equation (D.10) transforms it to

$$-\frac{\zeta}{2d(1+\zeta)}\Omega_1 - \frac{\zeta^2(4+3\zeta)}{48d(1+\zeta)^3}{\Omega_1}^3 + \mathcal{O}\left[{\Omega_1}^5\right] \tag{D.13}$$

The coefficient C is

$$C = -n_2\frac{2\zeta_1^3+3\zeta_1^2\zeta_2+2\zeta_1^2+4\zeta_1\zeta_2}{48(1+\zeta_1)^3}\sin(\Omega_1 n_2) - n_2^2\Omega_1\frac{\zeta_1^2\zeta_2}{48(1+\zeta_1)^3}\cos(\Omega_1 n_2) \tag{D.14}$$

$$\cos^{-1}(\alpha+z) \sim \cos^{-1}(\alpha) - \frac{1}{\sqrt{1-\alpha^2}}z - \frac{\alpha}{2(1-\alpha^2)^{3/2}}z^2 - \frac{2\alpha^2+1}{6(1-\alpha^2)^{5/2}}z^3 + \mathcal{O}\left[z^4\right]; \quad |\alpha| \neq 1 \tag{D.15}$$

The coefficient K_1 is

$$K_1 = -\frac{C}{\sin(\kappa_1)} \tag{D.16}$$

The coefficient A_1 in the Ω_1-expansion of a_3 is

$$A_1 = -\alpha_1 \frac{\cos(\kappa_1)}{\sin(\kappa_1)} K_1 - \frac{1}{-i\zeta_2 m\omega d_2}\left[K_1 - \frac{\sin(\Omega_1 n_2)}{\sin(\kappa_1)} \frac{n_2 \zeta_1^2}{24\sqrt{1+\zeta_1}}\right] \tag{D.17}$$

The $\Omega_1 n_2$-expansions of the coefficients C and K_1 when $\Omega_1 n_2$ is small become

$$C \sim -\frac{n_2(\zeta_1^2 + 2\zeta_1\zeta_2)}{24(1+\zeta_1)^{1/2}}(\Omega_1 n_2) - \frac{n_2(\zeta_1^3 + \zeta_1^2 - 3\zeta_1^2\zeta_2 - 2\zeta_1\zeta_2)}{144(1+\zeta_1)^{3/2}}(\Omega_1 n_2)^3 + \\ + \mathcal{O}\left[(\Omega_1 n_2)^5\right] \tag{D.18}$$

$$K_1 = \frac{n_2}{24}\frac{\zeta_1^2 + 2\zeta_1\zeta_2}{\sqrt{1+\zeta_1+\zeta_2}} - \frac{n_2}{144}\frac{\zeta_1^3 + \zeta_1^2 - 3\zeta_1^2\zeta_2 - 2\zeta_1\zeta_2}{\sqrt{(1+\zeta_1+\zeta_2)(1+\zeta_1)}}(\Omega_1 n_2)^2 + \\ + \mathcal{O}\left[(\Omega_1 n_2)^4\right] \tag{D.19}$$

Appendix E

Transverse vibrations of thin Euler-Bernoulli beam

In this Appendix a wave model for the transverse vibrations of thin Euler-Bernoulli beam will be presented.

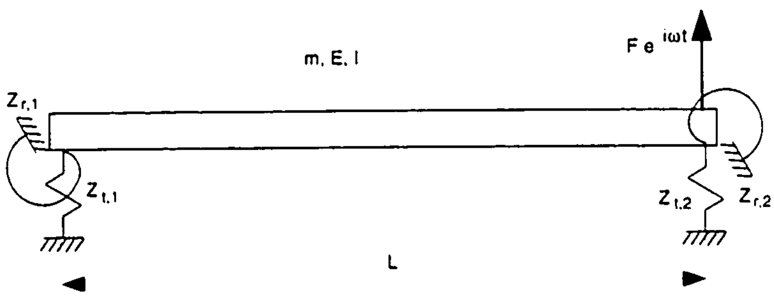

Figure E.1: Schematic of a beam on impedance supports

The beam response can be constructed as a superposition of four waves :

$$v(x) = c_1 e^{ikx} + c_2 e^{-ikx} + c_3 e^{kx} + c_4 e^{-kx} \tag{E.1}$$

The first, second and third derivatives are given with

$$\frac{dv}{dx} = c_1 ike^{ikx} - c_2 ike^{-ikx} + c_3 ke^{kx} - c_4 ke^{-kx} \tag{E.2}$$

$$\frac{d^2v}{dx^2} = -c_1 ike^{ikx} - c_2 ike^{-ikx} + c_3 ke^{kx} - c_4 ke^{-kx} \tag{E.3}$$

$$\frac{d^3v}{dx^3} = -c_1 ik^3 e^{ikx} + c_2 ik^3 e{-}ikx + c_3 k^3 e^{kx} - c_4 k^3 e^{-kx} \tag{E.4}$$

The boundary conditions are

$$\left.\frac{d^2v}{dx^2}\right|_{x=0} = \frac{i\omega Z_{r,1}}{EI}\left.\frac{dv}{dx}\right|_{x=0}; \qquad \left.\frac{d^2v}{dx^2}\right|_{x=L} = -\frac{i\omega Z_{r,2}}{EI}\left.\frac{dv}{dx}\right|_{x=L} \tag{E.5}$$

$$\left.\frac{d^3v}{dx^3}\right|_{x=0} = -\frac{i\omega Z_{t,1}}{EI}v|_{x=0}; \qquad \left.\frac{d^3v}{dx^3}\right|_{x=L} = \frac{-i\omega F}{EI} + \frac{i\omega Z_{t,2}}{EI}v|_{x=L} \tag{E.6}$$

In order to simplify the notation let

$$\psi_n = -\frac{i\omega Z_{t,n}}{EIk^3}; \qquad \varphi_n = \frac{i\omega Z_{r,n}}{EIk} \qquad n = 1, 2 \tag{E.7}$$

Upon defining the nondimensional parameter

$$\Omega = kL \tag{E.8}$$

we rewrite (E.7) as

$$\psi_n = \Omega\frac{M_n}{mL}; \qquad \varphi_n = -\Omega^3\frac{J_{c,n}}{mL^3} \tag{E.9}$$

where M_n and $J_{c,n}$ denote end cap mass and moment of inertia respectively.

From (E.5) it follows

$$c_1(-1 - i\varphi_1) + c_2(-1 + i\varphi_1) + c_3(1 - \varphi_1) + c_4(1 + \varphi_1) = 0 \tag{E.10}$$

Analogously the second relation in (E.5) leads to

$$c_1(-1 + i\varphi_2)e^{i\Omega} + c_2(-1 - i\varphi_2)e^{-i\Omega} + c_3(1 + \varphi_2)e^{\Omega} + c_4(1 - \varphi_2)e^{-\Omega} = 0 \tag{E.11}$$

From (E.6) it follows

$$c_1(-i - \psi_1) + c_2(i - \psi_1) + c_3(1 - \psi_1) + c_4(-1 - \psi_1) = 0 \tag{E.12}$$

and

$$c_1(-i + \psi_2)e^{i\Omega} + c_2(i + \psi_2)e^{-i\Omega} + c_3(1 + \psi_2)e^{\Omega} + c_4(-1 + \psi_2)e^{-\Omega} = -\frac{i\omega F}{EIk^3} \tag{E.13}$$

(E.10) – (E.13) represents a linear system with respect to the unknown wave constants c_1, c_2, c_3, and c_4. Its exact solution is shown below :

$$c_1 = -\frac{i\omega F}{EIk^3}\frac{1}{(-i + \psi_2)e^{i\Omega} + p(i + \psi_2)e^{-i\Omega} + (a + bp)(1 + \psi_2)e^{\Omega} + (c + dp)(-1 + \psi_2)e^{-\Omega}} \tag{E.14}$$

$$c_2 = pc_1; \qquad c_3 = (a + bp)c_1; \qquad c_4 = (c + dp)c_1 \tag{E.15}$$

where

$$a = \frac{(-1 - i\varphi_1)(1 + \psi_1) + (1 + \varphi_1)(-i - \psi_1)}{-(1 - \varphi_1)(1 + \psi_1) - (1 + \varphi_1)(1 - \psi_1)}; \quad b = \frac{(-1 + \varphi_1)(1 + \psi_1) + (1 + \phi_1)(i - \psi_1)}{-(1 - \phi_1)(1 + \psi_1) - (1 + \phi_1)(1 - \psi_1)} \tag{E.16}$$

$$c = a + \frac{-i - \psi_1}{1 + \psi_1}; \qquad d = b + \frac{i - \psi_1}{1 + \psi_1} \tag{E.17}$$

$$p = \frac{(-1 + i\varphi_2)e^{i\Omega} + a(1 + \phi_2)e^{\Omega} + c(1 - \varphi_2)e^{-\Omega}}{(1 + i\phi_2)e^{-i\Omega} - b(1 + \phi_2)e^{\Omega} - d(1 - \varphi_2)e^{-\Omega}} \tag{E.18}$$

Bibliography

[1] J.W. MILES 1956 *Proceedings of the American Society of Civil Engineers, Engineering Mechanics Division*, **EM** 1:1–9. Vibrations of beams on many supports.

[2] L. BRILLOUIN 1946 *Wave Propagation in Periodic Structures, Electric Filters and Crystal Lattices*. Second Edition. Dover Publications, Inc: New York.

[3] Y.K. LIN 1960 *Journal of Applied Mechanics* **27**, 669–676. Free vibration of continuous skin-stringer panels.

[4] Y.K. LIN 1962 *International Journal of Mechanical Science* **4**, 409–423. Free vibration of continuous beam on elastic supports.

[5] P.W. SMITH Jr. 1963 BBN Technical Report No. 976. Resonances of a periodically supported beam and its coupling to sound.

[6] M. HECKL 1961 *The Journal of the Acoustical Society of America* **33**, 640–651. Wave propagation on beam-plate systems.

[7] E.E. UNGAR 1961 *The Journal of the Acoustical Society of America* **33**, 633–639. Transmission of plate flexural waves through reinforcing beams; dynamic stress concentrations.

[8] E.E. UNGAR 1966 *The Journal of the Acoustical Society of America* **39**, 887–894. Steady-state responses of one-dimensional periodic flexural systems.

[9] Y.I. BOBROVNITSKII and V.P. MASLOV 1966 *Soviet Physics Acoustics* **12**, 150–154. Propagation of flexural waves along a beam with periodic point loading.

[10] D.J. MEAD 1970 *Journal of Sound and Vibration* **11**, 181–197. Free wave propagation in periodically supported, infinite beams.

[11] D.J. MEAD 1975 *Journal of Sound and Vibration* **40**, 1–18. Wave propagation and natural modes in periodic systems: I. Mono-coupled systems.

[12] D.J. MEAD 1975 *Journal of Sound and Vibration* **40**, 19–39. Wave propagation and natural modes in periodic systems: II. Multi-coupled systems.

[13] D.J. MEAD 1973 *Journal of Sound and Vibration* **27**, 235–260. A general theory of harmonic wave propagation in linear periodic systems with multiple coupling.

[14] D.J. MEAD 1991 *Journal of Sound and Vibration* **142**, 507–529. The response of infinite periodic beams to point harmonic forces : a flexural wave analysis.

[15] D.J. MEAD 1996 *Journal of Sound and Vibration* **190**, 495–524. Wave propagation in continuous periodic structures: Research contributions from Southampton, 1964–1995.

[16] V.N. ROMANOV 1971 *Soviet Physics Acoustics* **17**, 92–96. Radiation of sound by an infinite plate with reinforcing beams.

[17] V.N. EVSEEV 1973 *Soviet Physics Acoustics* **19**, 226–229. Sound radiation from an infinite plate with periodic inhomogeneities.

[18] M.L. RUMERMAN 1975 *The Journal of the Acoustical Society of America* **57**, 370–373. Vibration and wave propagation in ribbed plates.

[19] G.S. GUPTA 1972 *Journal of Sound and Vibration* **20**, 39–49. Propagation of flexural waves in doubly-periodic structures.

[20] B.R. MACE 1980 *Journal of Sound and Vibration* **71**, 435–441. Sound radiation from a plate reinforced by two sets of parallel stiffeners.

[21] B.R. MACE 1980 *Journal of Sound and Vibration* **73**, 473–485. Periodically stiffened fluid-loaded plates, I. Response to convected harmonic pressure and free wave propagation.

[22] C.B. BURROUGHS 1984 *The Journal of the Acoustical Society of America* **75**, 714–722. Acoustic radiation from fluid-loaded infinite circular cylinders with doubly periodic ring supports.

[23] B.A. CRAY 1994 *The Journal of the Acoustical Society of America* **95**, 256–264. Acoustic radiation from periodic and sectionally aperiodic rib-stiffened plates.

[24] A.H. NUTTALL 1992 *NUWC-NL Technical Report 10.015, Naval Undersea Warfare Detachment, New London, Connecticut.* Explicit solution of difference equation for the wavenumber response of fluid-loaded stiffened plate.

[25] B.A. CRAY 1997 *Fifth International Congress on Sound and Vibration*, Adelaide, South Australia. A formulation for the forced vibration of a multi-supported string.

[26] A. PAPOULIS 1962 *The Fourier Integral and Its Applications*. Electronic Science Series. McGraw-Hill Book Company, Inc: New York.

[27] B.R. Mace 1980 *Journal of Sound and Vibration* **73**, 473–486. Periodically stiffened fluid-loaded plates, I. Response to convected harmonic pressure and free wave propagation.

[28] D. Gueorguiev, J. G. McDaniel, P. DuPont, and L. B. Felsen 1999 *Journal of Sound and Vibration* (accepted for publishing) Analysis of Floquet Wave Generation and Propagation in A Plate With Multiple Arrays of Attachments

[29] W. C. Tang, C. Nguyen, and R. Howe 1989 *Sensors and Actuators*, **20**:25-32 Laterally Driven Polysilicon Resonant Microstructures

[30] Q. Meng, M. Mehregany 1993 *Journal of Microelectromechanical systems* **2**(3):128-137 Theoretical Modeling of Microfabricated Beams with Elastically Restrained Supports

[31] C. Nguyen, L. Katehi 1998 *Proceedings of the IEEE*, **86**(8):1756-1768 Micromachined devices for wireless communications

[32] C. Nguyen 1999 *IEEE Transactions on Microwave Theory and Techniques*, **47**(8):1486-1503 Frequency-Selective MEMS for Miniaturized Low-Power Communication Devices

[33] K. Wang, C. Nguyen 1999 *Journal of Microelectromechanical systems*, **8**(4):534-557 High-Order Medium Frequency Micromechanical Electronic Filters

[34] R.D. Cook, D.S. Malkus, M.E. Plesha 1989 *Concepts and Applications of Finite Element Analysis*, Third Edition John Wiley & Sons, Inc

[35] P. Bettess 1977 *International Journal for Numerical Methods in Engineering*, **11**, 53-64 Infinite elements

[36] C. ZHAO, S. VALLIAPPAN 1993 *International Journal for Numerical Methods in Engineering.* **36**,2567-2580 A Dynamic Infinite Element For Three-Dimensional Infinite-Domain Wave Problems

[37] R. L. MULLEN, M. MEHREGANY, M. P, Omar, and W. H. Ko 1991 *Proceedings of IEEE Micro Electro Mechanical Systems, Nara, Japan, 30 Jan-2 Feb, 1991* Theoretical Modeling of Boundary Conditions in Microfabricated Beams

[38] T. CORMAN, P. ENOKSSON, G. STEMME 1997 *Sensors and Actuators A* **61**.249-255 Gas damping of electrostatically excited resonators

[39] K. WANG, A. C. WONG, T. C. NGUYEN 2000 *Journal of Micromechanical Systems* **9** (3).347-359 VHF Free-free Beam High Q Micromechanical Resonators

[40] CALFEM A finite element toolbox to Matlab Version 3.2 *The Division of Structural Mechanics, Lund University, 1996*

[41] M. BORN and K. HUANG 1954 Dynamical Theory of Chrystal Lattices, chapter V, p. 229-236 *Oxford University Press, London*

[42] E. BEHRENS 1967 *The Journal of Acoustical Society of America* **42**(2), 378-383 Sound propagation in lamellar composite materials and averaged elastic constants

[43] E. BEHRENS 1967 *The Journal of Acoustical Society of America* **42** (2), 367-377 Elastic constants of filamentary composites with rectangular symmetry

[44] E. BEHRENS 1968 *The Journal of Acoustical Society of America* **45**(1), 102-108 Elastic constants of composite materials

[45] A. BENSOUSSAN, J-L. LIONS and G. PAPANICOLAU 1978 Asymptotic analysis for periodic structures *North-Holland, Amsterdam*

[46] D. CIORANESCU and J.S.J. PAULIN 1979 Homogenization in open sets with holes *Journal of mathematical analysis and application* 71, 590-607

[47] F. MIGNOT, J-P. PUEL and P-M. SUQUET 1980 Homogenization and bifurcation of perforated plates *Int. J. Engng Sci.* 18, 409-414

[48] R.V. KOHN and M. VOGELIUS 1984 A new model for thin plates with rapidly varying thickness *Int. J. Solids Structures* **20**(4), 333-350

[49] A. ERDELYI 1956 Asymptotic expansions, chapter I, p.5-25 *Dover Publications*

[50] A.N. NORRIS 1994 *Journal of Sound and Vibration* **169**(4),485-502 Low frequency bending waves in periodic plates

[51] N. BAKHALOV and G. PANASENKO 1990 Homogenization : averaging processes in periodic media Mathematics and its applications **36** *Kluwer Academic Publishers, Dordrecht*

[52] C. POTEL, J-F DE BELLEVAL, and Y. GARGOURI 1995 *The Journal of Acoustical Society of America* **97**(5), 2815-2825 Floquet waves and classical plane waves in an anisotropic periodically multilayered medium: Application to the validity domain of homogenization

[53] W. MEISENHOLDER 1996 *Acta Acustica* ***82*** *628-635* Low frequency sound transmission through periodically inhomogeneous plates with arbitrary local anisotropy and arbitrary global symmetry

[54] E. SANCHEZ-PALENCIA and A. ZAOUI 1985 Homogenization techniques for composite media *Lecture Notes in Physics* Lectures delivered at the CISM International Center for Mechanical Sciences, Udine, Italy, July 1-5 *Springer, Berlin*

[55] F. SANTOSA, M. VOGELIUS 1993 *SIAM J. Appl. Math.* **53**, 1636–1668. Low frequency sound transmission through periodically inhomogeneous plates with arbitrary local anisotropy and arbitrary global symmetry

[56] R. MORGAN, I. BABUSKA 1991 *SIAM J. Math. Anal.* **2**, 1–15 and 16–33. An approach for constructing families of homogenized equations for periodic media I, II

[57] C. SANTOSA, M. VANNINATHAN 1993 *SIAM J. Appl. Math.* **57**, 1639–1659. Homogenization of periodic structures via Bloch decomposition

[58] C. CASTRO and E. ZUAZUA 2000 *SIAM J. Appl. Math.* **60**, 1205-1233 Low frequency asymptotic analysis of a string with rapidly oscillating density

[59] G. ALLAIRE and C. CONCA 1998 *J. Math. Pures Appl.* **77**, 153-208 Bloch wave homogenization and spectral asymptotic analysis

[60] T. LEWINSKI and J.J. TELEGA 2000 Plates, laminates and shells: asymptotic analysis and homogenization Series on advances in mathematics for applied sciences **52** *River Edge, New Jersey*

[61] S.A. MEGUID and A.L. KALAMKAROV 1994 *International Journal of Solids and Structures* **31**(3), 303-316 Asymptotic homogenization of elastic composite materials with a regular structure

[62] A.G. KOLPAKOV 1998 *International Journal of Solids and Structures* **35**(22), 2847-2859 Application of homogenization method to justification of 1-D model for beam of periodic structure having initial stresses

[63] J.B. Castillero, J.A. Otero, R.R. Ramos 1998 *International Journal of Soldis and Structures* **35**(5-6), 527-541 Asymptotic homogenization of laminated piezocomposite materials

[64] N. Ohno, X. Wu, T. Matsuda 2000 *International Journal of Mechanical Sciences* **42**(8) 1519-1536 Homogenized properties of elastic-viscoelastic composites with periodic internal structures

[65] Y.M. Yi, S.H. Park, S.K. Youn 1998 *International Journal of Solids and Structures* **35** (17) 2039-2055 Asymptotic homogenization of viscoelastic composites with periodic microstructures

[66] H. Bufler 2000 *Acta Mechanica* **141** (1-2) 21-36 Planar elastic laminates and their homogenization

[67] K-T. Cheng and N. Olhoff 1981 *International Journal of Solids and Structures* **17** 305-323 An investigation concerning optimal design of solid elastic plates

[68] O. Sigmund 1994 *Internation Journal of Solids and Structures* **31**:(17) 2313-2329 Materials with prescribed constitutive parameters - an inverse homogenization problem

[69] Y.M. Yi, S.H. Park, S.K. Youn 2000 *International Journal of Solids and Structures* **37**(35) 4791-4810 Design of microstructures of viscoelastic composites for optimal damping characteristics

[70] D. Gueorguiev, J. G. McDaniel, and P. DuPont 1999 *In preparation for publishing in Journal of Sound and Vibration* Partial Homogenization of infinite elastic bar with multiple arrays of attachments

[71] L. W. Salvino, P. Dupont, and J. G. McDaniel 1998 *Proceedings of the 69th Shock and Vibration Simposium*, St. Paul. 12-16 October Evaluation of Granular-Fill Damping in Shock-Loaded Box Beam

[72] J. Vollmann 1997 *The Journal of the Acoustical Society of America* **102**(2):909-920 High-resolution analysis of the complex wave spectrum in a cylindrical shell containing a viscoelastic medium

[73] J. G. McDaniel, K. LePage, and N. C. Martin 1995 *The Journal of Acoustical Society of America* **98**(5):2889 Computation of complex wavenumbers and amplitudes of vibrating structures

[74] J. E. Phillips 1996 *Proceedings of the 16th Aerospace Testing Seminar*, pages 355-365 Vibration testing of titan IV-A instrumentation truss with polymeric bead damping

[75] J. R. House 1989 *Polymeric Materials: Science and Engineering. Proceedings of the ACS Division* . **60**:734-738 Damping hollow tubular structures with lightweight visco-elastic spheres

[76] J. G. McDaniel, K. D. LePage, and N. C. Martin 1995 *Journal of the Acoustical Society of America*, **98**(5) Computation of complex wavenumbers and amplitudes on vibrating structures from response data

[77] J. G. McDaniel, P. Dupont, and L. W. Salvino 1999 *Journal of Sound and Vibration* Evaluation of Granular-Fill Damping in Shock-Loaded Box Beam

[78] Simulation of the response of particulate filled beams due to shock excitation *Weidlinger Associates Report, July 1, 1999*

[79] G. Maidanik, J. Dickey 1996 *Journal of Sound and Vibration*, **99**(5):2766–2774 Loss factor of pipelike structures containing beads

[80] L. Hillstrom, M. Mossberg, and B. Lundberg 2000 *Journal of Sound and Vibration*, **230**(3):689–707 Identification of complex modulus from measured strains on an axially impacted bar using least squares

[81] G. A. Baker, Jr 1975 *Essentials of Pade Approximants* Academic Press, New York

[82] A. Bultheel, M. V. Barel 1986 *Journal of Computational and Applied Mathematics* **14**:401-438 Pade techniques for model reduction in linear system theory : a survey

[83] J. Shoukens, R. Pintelton, and J. Renneboog *IEEE Transactions on Instrumentation and Measurement* **37**(1):10–17 A maximum likelihood estimator for linear and nonlinear systems - a practical application of estimation techniques in measurement problems

[84] M. Longman 1974 *SIAM Journal of Mathematical Analysis* **5**(4):574–580 Best rational function approximation for Laplace transform inversion

[85] J.C. Lagarias, J.A. Reeds, M.H. Wright, P.E. Wright 1999 *SIAM Journal of Optimization*, **9**(1):112-147 Convergence Properties of the Nelder-Mead Simplex Algorithm in Low Dimensions

[86] E.C. Levi 1959 *IRE Transactions on Automatic Control*. **AC-4**:37-44 Complex Curve Fitting

[87] D.J. McTavish 1993 *Journal of Vibrations and Acoustics*, **115**:103-110 Modeling of linear viscoelastic space structures

[88] D.F. GOLLA and P.C. HUGHES 1985 *Journal of Applied Mechanics*, **52**:897-906 Dynamics of viscoelastic structures – a time-domain finite element formulation

[89] A.R. JOHNSON, A. TESSLER, and M. DAMBACH 1997 *Journal of Engineering Materials and Technology*, **119**:273-278 Dynamics of thick viscoelastic beams

[90] M.I. FRISWELL and D.J. INMAN 1999 *AIAA Journal*, **37**:1318-1325 Reduced-order models of structures with viscoelastic components

[91] E.A. GUILLEMIN Synthesis of passive networks: theory and methods appropriate to the realization and approximation problems *New York, John Wiley & sons 1957*

Curriculum Vitae of Dimitar Gueorguiev

OFFICE ADDRESS:

EMC Corp. 171 South Street, HOP1-2, Hopkinton, MA 01702

OFFICE PHONE: 508-435-100 ext.12871

E-MAIL: dpg@bu.edu

HOME ADDRESS:

Lulin, block 629, apt. 91, Sofia 1336, Bulgaria

FIELDS OF INTEREST:

Structural Acoustics, Vibrations, Wave Propagation, Computer modeling

EDUCATION:

Boston University, Class of 2003 Ph.D. in Mechanical Engineering:

Thesis title: Vibrations of elastic structures with muitiple arrays of attachments

Technical University - Sofia, Class of 1997. Postgraduate specialization in Applied Mathematics and Computer Science

Thesis title : Study of the movement of a vehicle on a rail in a curve

Technical University - Sofia, Class of 1994 M.S. in Mechanical Engineering

Thesis title : Freight vehicle bogie with elastically suspended vehicle body on the bogie frame

RESEARCH:

Periodic structures with multiple arrays of attachments. Funded by National Science Foundation under Grant Number CMS-9531399

Modeling damping treatments of thin box beam

Design of microelectromechanical resonators with high Q factor

Dynamic computation and design of freight vehicle bogie with elastically suspended vehicle body on the bogie frame

Study of the movement of a vehicle on rail in a curve

HONORS:

At Boston University

Best Student Paper Award at the 136th Meeting of the Acoustical Society of America on "Dispersion Relations for Waves on Doubly Periodic Beams" (1998)

John J. and Helen Carey Fitzgerald Award for outstanding research by a student in the Department of Aerospace and Mechanical Engineering, College of Engineering, Boston University (1999)

Dean's Fellowship (1997-1998)

At Technical University - Sofia

Scholarship Award of the Korean Foundation "For The Future" (1993-1994)

First place in the university competition of "Strength of Materials" (1991)

Third place in the university competition of "Dynamics and Vibrations" (1991)

PRESENTATIONS:

136th Meeting of the Acoustical Society of America, Norfolk, Virginia. Presentation on "Dispersion Relations for Waves on Doubly Periodic Beams"

1999 ASME Design Engineering Technical Conferences September 12-15, 1999, Las Vegas, Nevada. Presentation on "Simplified dispersion relations for Floquet waves in a plate with multiple arrays of attachments", Dimitar Gueorguiev, James G. McDaniel, Pierre DuPont

Brown bag seminar at Aerospace/Mechanical Engineering Department, Boston University on "Dispersion relations and derivation of explicit expression for the wavenumber response of doubly periodic structures"

Brown bag seminar at Aerospace/Mechanical Engineering Department, Boston University on "Partial homogenization of infinite elastic structures with multiple arrays of attachments and derivation of uniform and nonuniform asymptotic expansions for the Floquet wavenumber and response".

PUBLICATIONS:

Analysis of Floquet wave generation and propagation in a plate with multiple arrays of line attachments, Dimitar Gueorguiev, James G. McDaniel, Pierre DuPont, and Leopold Felsen, Journal of Sound and Vibration, 234(5), 819-840

Partial homogenization of infinite elastic bar with multiple arrays of attachments, Dimitar Gueorguiev, J. Gregory McDaniel, and Pierre DuPont, in preparation for publishing in Journal of Sound and Vibration

WORK AND TEACHING EXPERIENCE:

Senior Design Engineer at EMC Corporation: 2001-present

Full-time Assistant at Technical University - Sofia, Transport Faculty: 1996-1997